UNDERSTANDING RESERVOIR ENGINEERING ASPECTS OF SHALE GAS DEVELOPMENT ON THE ALASKA NORTH SLOPE

By

Anna Nyulund

RECOMMENDED:

Dr. Mohabbat Ahmadi
Advisory Committee Chair

Dr. Shirish Patil
Advisory Committee Co-Chair

Dr. Abhijit Dandekar,
Advisory Committee Co-Chair
Chair, Department of Petroleum Engineering

APPROVED:

Dr. Douglas Goering
Dean, College of Engineering and Mines

Dr. John Eichelberger
Dean of the Graduate School

20 November 2015
Date

This page intentionally left blank for the purposes of print publication.

UNDERSTANDING RESERVOIR ENGINEERING ASPECTS OF SHALE GAS DEVELOPMENT ON THE ALASKA NORTH SLOPE

A

THESIS

Presented to the Faculty

of the University of Alaska Fairbanks

in Partial Fulfillment of the Requirements

for the Degree of

MASTER OF SCIENCE

By

Anna Nyulund, B.S.

Fairbanks, Alaska

December 2015

Abstract

Horizontal drilling and multi-stage hydraulic fracturing made it possible to develop US shale resources. Shublik shale is one of such US shale resources – it is one of the largest source rocks for hydrocarbon accumulations located on the Alaska North Slope.

This study used the workflow introduced by Mirzaei and Cipolla in 2012 to investigate the effects of fracturing fluid flowback; shale porosity; matrix, fracture and unpropped zone permeability; hydraulic fracture spacing; permeability anisotropy; non-Darcy flow; gas adsorption/desorption using the complex-fracture-network model, referred to as an Unconventional Fracture Model (UFM), and Voronoi grid on well performance in the Shublik shale formation. In addition, the effects of natural fracture network orientation, fracture spacing and length were examined using a single porosity model with incorporated Discrete Fracture Network (DFN). The Schlumberger Mangrove Plug-In for Petrel platform was used to conduct the study. Mangrove has the DFN feature, which can be deactivated in the single porosity model.

The results suggested that ignoring fracturing fluid flowback and non-Darcy effects can lead to overestimation of the gas recovery factor. Neglecting gas adsorption/desorption effects leads to underestimation of the gas recovery factor. In addition, smaller fracture spacing leads to a higher gas recovery factor. DFN orientation, fracture spacing and length affect the propped fracture area and should be incorporated into analysis from shale plays since it can result in either overestimation or underestimation of the gas recovery factor depending on fracture network propagation. Finally, examining multiple hydraulic fractures instead of one fracture is more accurate due to the stress shadowing effects and fracture network propagation.

Dedicated to:

My Daughter

Acknowledgements

I would like to thank my adviser, Dr. Ahmadi, for his patient and kind guidance through my thesis research and classes at UAF. I also would like to thank him for volunteering to be my adviser and believing in me before I believed in myself. I really appreciate professor Ahmadi for teaching me many things about reservoir engineering. Thank you for your dedication and generosity.

I would like to thank my department chair, Dr. Dandekar for giving me a chance by accepting me to the graduate school and for guiding me through the process. I also would like to thank Dr. Patil for telling me that it is possible to attend the grad school and helping me with the first step.

I would like to thank my UAF graduate school friends: Shruti Oza, John Cheshire, Jonathon Sheppard, Quinn Sawyer, Arya Narayan, Bakul Mathur, Neha Agarwal, Mohit Paryani, Tejas Ghorpade, Aditya Nikam, Srichand Poludasu, Kishan Joshi and Ojo Omoruwi for the emotional support, good technical insights and making learning more fun. I also would like to express my gratitude to Dr. Farrokh Sheibani for giving me an encouragement during my time in grad school.

I would like to thank my Schlumberger mentor, Edward Evans, for all of his Petrel, Intersect and Mangrove support and for sticking with me to the end. I appreciate his willingness to work hard and to answer questions not only during the day, but also at night and on the weekends. I also appreciate his willingness to go extra mile to get things done and for giving me encouragement to continue working when I was feeling down.

I would like to thank David Seabrook - SIS NAM Vice President - for providing a laptop with Mangrove, Petrel and Intersect license for the duration of the study.

I would like to thank Martin Neudecker and Peter Forster – my Schlumberger supervisors during my Schlumberger internship for doing all logistics. I worked for Martin in the summer, and think that Martin is the best supervisor I had.

I would like to thank all Schlumberger employees that helped me with advise on my thesis: Gunther Rutzinger, Alejandro Vasquez Martinez, Han Xue, April Wisebaker, Amanda Joyce Blades, Dr. Kresse and Dr. Weng.

I would like to thank the Dean of Students – Dr. Foley – for his impeccable talent to resolve any complex student situations in which I ended being from time to time.

I would like to thank UAF counseling and health center for keeping me healthy in Alaska.

I would like to thank my stepfather – Arnold Dacks - for providing me with food, shelter, transportation and emotional support during my time in college.

I would like to thank my mom for bringing me to this world, raising my brother and I alone without any financial support and for her entrepreneurial spirit that kept us fed and dressed.

I would like to thank my dad for teaching me to recognize an intelligent design and humor in most difficult situations.

And finally and most importantly, I would like to thank my daughter for giving me endless inspiration; for being a source of joy, peace and strength; and for her big wide smile, which can instantly lighten up the room even on the most miserable and hopeless days.

Table of Contents

Page

This page intentionally left blank for the purposes of print publication.

List of Figures

List of Tables

Page

List of Appendices

This page intentionally left blank for the purposes of print publication.

Chapter 1 Introduction

1.1 Overview

In the past decade, horizontal drilling combined with hydraulic fracturing allowed U.S. oil companies to extract vast quantities of natural gas trapped in once-inaccessible shale plays. The resulting surge in production led to lower U.S. oil and gas prices in the second half of 2014. The Eagle Ford Formation (also called the Eagle Ford shale) is an example of unconventional, nano-Darcy permeability shale resources. The Eagle Ford Formation is a sedimentary rock, which underlies most of South Texas. The Eagle Ford shale was one of the most actively drilled targets for oil and gas in the Unites States in 2010. In the first half of 2013, 2.69 billion cubic feet of gas and 599,000 barrels of oil and condensate per day were extracted from the Eagle Ford Formation; the oil production represented an increase of 51% over the average for 2012. By the end of 2013, production had increased to more than 1,000,000 boe/day (EIA, 2015). Eagle Ford shale is believed to be the closest analog to the Alaska Shublik shale.

Ikewun (2012) thesis presented a reservoir model that correlated production performance with completion method (horizontal leg/stages of fracture) and length of horizontal leg, which used data from the Eagle Ford shale. Ikewun did not include variation of conductivity in hydraulic fracture and ignored the presence of the fracture fluid in the hydraulic fracture and the surrounding matrix. It was found by Zanganeh (2014) that assuming constant permeability in the fracture and ignoring the fracturing fluid will lead to overestimation of well rate and recovery. Further studies need to be done to create a better simulation model to more accurately estimate well rate and recovery.

1.2 Objective

According to United States Geological Survey (Housknecht et al., 2012) Alaska's North Slope geology will yield bountiful untapped resources as vast as the unconventional oil plays at Texas's Eagle Ford and North Dakota's Bakken shale fields. That source could contain up to 2 billion barrels of technically recoverable oil and up to 80 trillion cubic feet of natural gas. The North Slope shales stretch from the Chukchi Sea on the west to the Arctic National Wildlife Refuge on the east. This thesis presents a simulation study of gas production from a typical shale gas window using data from the Eagle Ford shale, analogous to the Shublik shale. The objectives of this study are:

- To investigate the importance of the adsorbed gas and non-Darcy effects
- To see the effects of the fracturing fluid flowback on well performance
- To investigate the importance of natural fractures in the gas production
- To do technical sensitivity studies to further investigate the effect of reservoir parameters on well production rate and recovery factor

Chapter 2 Literature Review

2.1 US Shale

Production from US shale gases is rapidly increasing. Shales are fine-grained sedimentary rocks, which contain oil and natural gas. The development of its sources is led by applications of hydraulic fracturing technology and horizontal drilling propelled the major increases in reserves of US natural gas by 35 percent higher in 2008 than in 2006 (Madden and Vossoghi, 2013).

Figure 1 shows the wet natural gas proved reserves by state/area in 2012. EIA no longer publishes an estimate of dry natural gas proved reserves since dry natural gas is the volume of gas that remains after natural gas liquids and non-hydrocarbon impurities are removed from the natural gas stream.

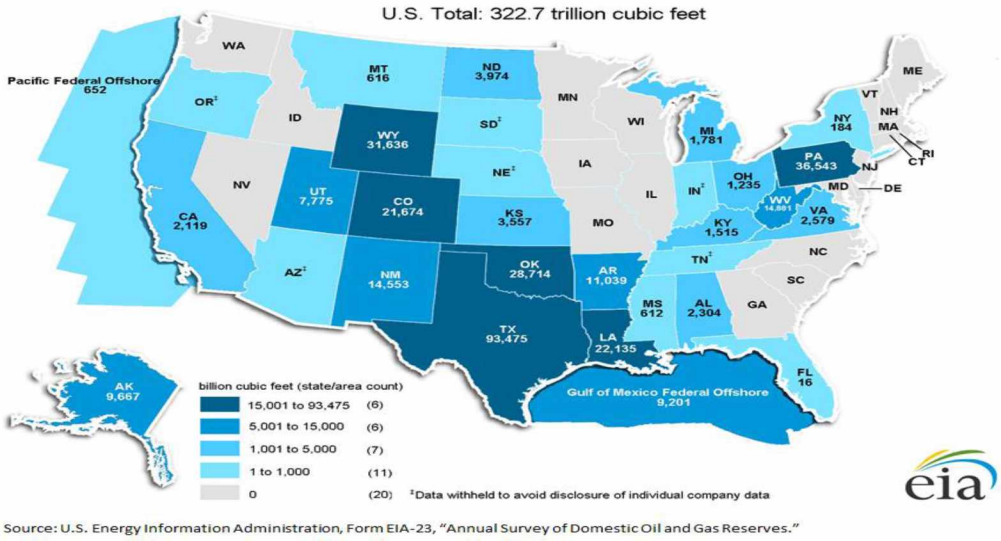

Figure 1: Wet natural gas proved reserves by state/area in 2012

Gas reserves estimates vary sufficiently based on such factors as completion efficiency, reservoir pressure, water removal efficiency and well spacing. Additional factors including but not limited to effects of non-Darcy flow, fracturing fluid flowback, gas desorption and water evaporation would also affect wells reserves. The major development sites are Barnett Shale in

North-Central Texas, Fayetteville Shale in Arkansas, Marcellus, Bakken, Haynesville, Woodford and Eagle Ford shales (EIA U.S. shale report, 2015).

2.2 Shublik Formation

The Shublik Formation has been mapped along the northern Brooks Range from just east of the U.S. – Canada border to Mount Doonerak (Moore et al., 1994). The Shublik Formation is Upper Triassic (Carnian-Norian) on the basis of mollusks. The field criterion for distinguishing the Shublik from underlying and overlying formations in outcrop is the presence of carbonate (limestone and carbonate cement), which varies throughout the formation but is lacking in overlying and underlying formations. The Shublik Formation forms part of a succession of rocks on the North Slope termed the "Ellesmerian sequence", which is lower Carboniferous to Lower Cretaceous. Units in this succession are defined by an unconformity marked by the Cretaceous "pebble shale unit", which is succeeded by Cretaceous and Cenozoic rock sourced from the south.

The Shublik Formation has heterogeneous lithology (Parrish, 1987; Parrish et al., 2001). This formation is composed of phosphatic rocks (Patton and Matzko, 1959; Detterman, 1970) and organic-rich rocks which are source beds for the Prudhoe Bay oil (Tailleur, 1964; Hughes et al., 1983; Magoon and Claypool, 1983; Magoon and Bird 1988; Kupecz, 1995). The USGS made an appraisal of three rock components: the Triassic Shublik Formation, the lower part of the Jurassic – Lower Cretaceous Kingak Shale and the Cretaceous Brookian Shale. These rock components are located along Alaska's north coast. They dip towards the south and reach a depth of over 20,000 feet in the Brooks Range foothills. The rocks can yield oil but their thermal maturity increases down dip into the dry gas window in the foothills. Figure 2 shows USGS assessment map of the Triassic Shublik formation.

Shublik Formation consists of five lithofaces (Parrish et al., 2001):

(1) nonglauconitic sandstone – thin- to medium-bedded, fine quartzose, calcareous to noncalcareous sandstone or silty to muddy sandstone, fossiliferous in places;

(2) glauconitic – thin- to medium-bedded, fine, quartzose sandstone, muddy sand-stone, or siltstone containing 10% to > 50% glauconite grains
(3) phosphatic – thin- to medium-bedded siltstone or sandstone or laminated, black silty limestone or limestone containing phosphate nodules; and
(4) organic-rich – laminated, black limestone, marl, and mudstone
(5) nonphosphatic, nonorganic-rich limestone – bioclastic wackerstone, or argillaceous grainstone and packstone or graded grainstone and packstone.

There are three middle members that are associated with the Shublik Formation (Blome, 1986; Blome, 1987): the informal chert, limestone members and the overlying formal Karen Creek Member. The chert member consists of rhythmically interbedded radiolarian chert, silicified mudstone, limestone, and shale (Bodnar, 1984). The limestone member consists of rhythmically interbedded limestone cherty limestone, and black or gray-green shale (Bodnar, 1984). The Karen Creek Member consists of siltstone and is directly correlative with the Karen Creek Sandstone, which is the upper member of the Shublik Formation at Fire Creek (Detterman, 1970; Bodnar 1984).

Kupecz (1995) segregated breaking the Shublik Formation into four zones (D through A, bottom to top). Basal zone D is massive, fine- to medium-grained phosphatic sandstone in the Prudhoe Bay area, outside of which it consists of calcareous shale, bioclastic limestone, siltstone, and sandstone with variable amounts of phosphatic components (Hulm, 1999). Zone C is composed predominantly of black shale and dark to light gray limestone with the latter dominating upwards. The shale is very organic rich and extremely fossiliferous, with abundant fossils of the bivalve Halobia (Dingus, 1984). Zone B is characterized by phosphorite and phosphatic carbonate and siliciclastic rocks. Zone A is lithologically similar to zone C. The base of zone A is comprised of black shale that grades upward into dark-gray limestone with abundant Monotis bivalve fossils (Dingus, 1984).

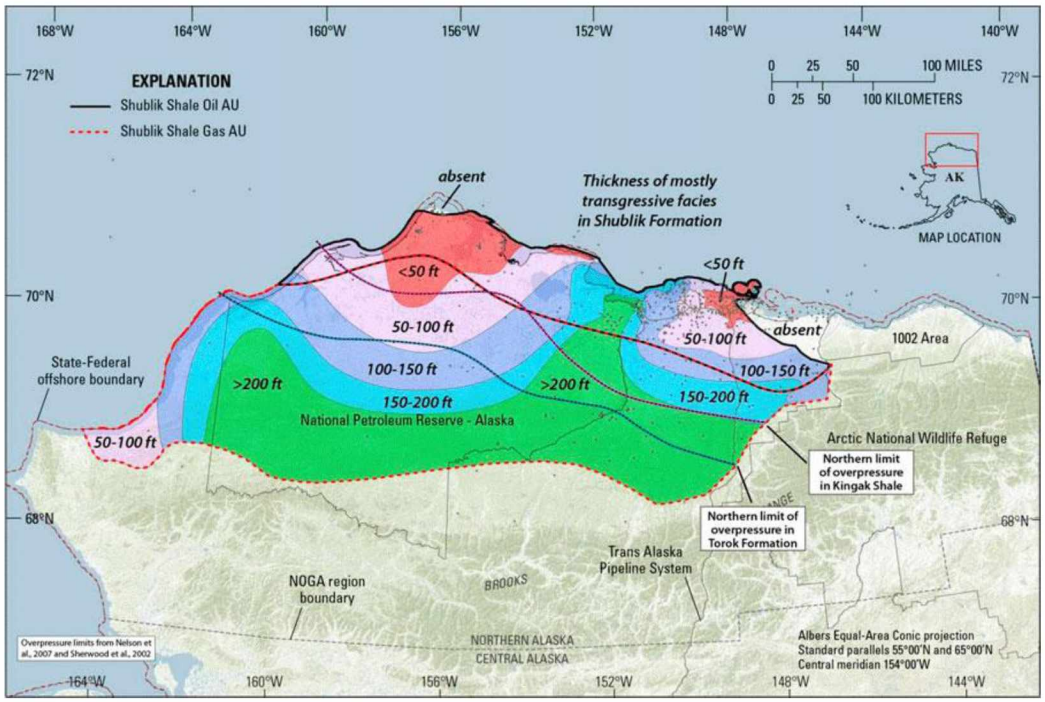

Figure 2: USGS assesment map of the Triassik Shublik formation

The USGS (Houseknecht et al., 2012) completed the first appraisal of technically recoverable shale-oil and shale-gas resources in northern Alaska. Aggregate estimates for all three source rocks range from 0 to 2 billion barrels of oil and 0 to 80 trillion cubic feet of gas (TCFG), with the ranges representing a 95- to 5-percent probability of occurrence (Houseknecht D.W., 2012b). Estimates for each source rock system include 0 to 928 million barrels of oil (MMBO) and 0 to 72 TCFG for the Shublik formation. The Shublik is estimated to contain the greatest oil and gas resource potential per unit area, with values that rank among the top few source-rock systems in the United States (Table 1).

Table 1: Key assessment input data for shale-oil and shale-gas assessment units of Alaska North Slope (USGS)

[EUR (estimated ultimate recovery per well), cell size, and success ratios are based on U.S. lower-48 shale-oil and shale-gas analogs. MMBO, million barrels of oil; BCFG, billion cubic feet of gas; AU, assessment unit; %, percent, Min., minimum; Max., maximum. For the average EUR variables, the mode columns contain the medians of the EUR distributions.]

Assessment input data	Shublik Shale Oil AU				Shublik Shale Gas AU				Brookian Shale Oil AU				Brookian Shale Gas AU				Kingak Shale Oil AU			
	Min.	Mode	Max.	Mean	Min.	Mode	Max.	Mean	Min.	Mode	Max.	Mean	Min.	Mode	Max.	Mean	Min.	Mode	Max.	Mean
Potential production area (million acres)	5.0	7.3	7.5	6.6	20.0	25.6	30.0	25.2	14.0	18.2	20.0	17.4	14.0	17.3	20.0	17.1	5.0	7.4	8.0	6.8
Average drainage area of wells (acres)	100	160	400	220	75	150	200	142	100	200	400	233	120	150	180	150	100	160	400	220
Percentage of AU in sweet spots (%)	0.5	15.0	40.0	18.5	2.0	20.0	50.0	24.0	0.2	10.0	40.0	16.8	0.5	5.0	10.0	5.2	0.0	0.0	10.0	3.3
Input for inside sweet spots																				
Average EUR (MMBO, oil; BCFG, gas)	0.020	0.050	0.250	0.061	0.200	0.800	2.500	0.887	0.010	0.040	0.100	0.043	0.040	0.400	1.000	0.426	0.010	0.040	0.100	0.043
Success ratio (%)	70	85	95	83	50	80	95	75	50	70	95	72	40	65	95	67	50	70	95	72
Input for outside sweet spots																				
Average EUR (MMBO, oil; BCFG, gas)	0.010	0.025	0.125	0.031	0.100	0.400	1.250	0.444	0.005	0.010	0.060	0.013	0.040	0.200	0.500	0.214	0.005	0.010	0.060	0.013
Success ratio (%)	0	10	70	27	1	10	50	20	0	10	30	13	0	0	10	3	0	5	25	10

2.3 Eagle Ford Formation

The Eagle Ford shale extends from the Mexican border north of the Maverick basin through northeast to the Sabine uplift. Eagle Ford Shale thickness varies between 50 ft on the north east side to 330 ft on the southwest side and has the elevation range between 1,500 ft and 14,000 ft. (Waite, 2009). The area is composed of an oil zone, a condensate zone, and a dry gas zone. Figure 3 shows Eagle Ford zone geographic locations.

The Eagle Ford oil and gas shale play was first discovered by Petrohawk in 2008 (Texas RRC). The first well was drilled in the Hawkville field in LaSalle County, Texas. According to the Railroad Commission of Texas there were 2,521 producing oil leases on schedule in 2013; 1,262 producing oil leases on schedule in 2012; 368 producing oil leases on schedule in 2011; 72 producing oil leases in 2010; and 40 producing oil leases in 2009. There were 2,418 producing gas well on schedule in 2013; 875 producing gas well on schedule in 2012; 550 producing gas wells in 2011; 158 producing gas wells in 2010; and 67 producing gas wells in 2009.

The Eagle Ford Shale is equivalent to the Boquillas formation in the Maverick basin and Tuscaloosa Shale in Louisiana and Mississippi (Figure 4) (Lock and Peschier, 2006). Eagle Ford is a Late-Cretaceous (Cenomanian-Turonian) formation that overlies the Buda limestone and is overlain by the Austin Chalk (Figure 5).

Approximate mineral content of the Eagle Ford shale is 20% quartz, 50% calcite, 20% clay, and 10% kerogen. Effective porosity ranges between 3% and 10% with a mean of 6%. Permeability ranges between 3nd and 405 nd, with an average value of 180 nd. The pressure

gradient in the Eagle Ford Shale varies from 0.55 to 0.85 psi/ft (Martin et al., 2011; Chaudhary et al., 2011).

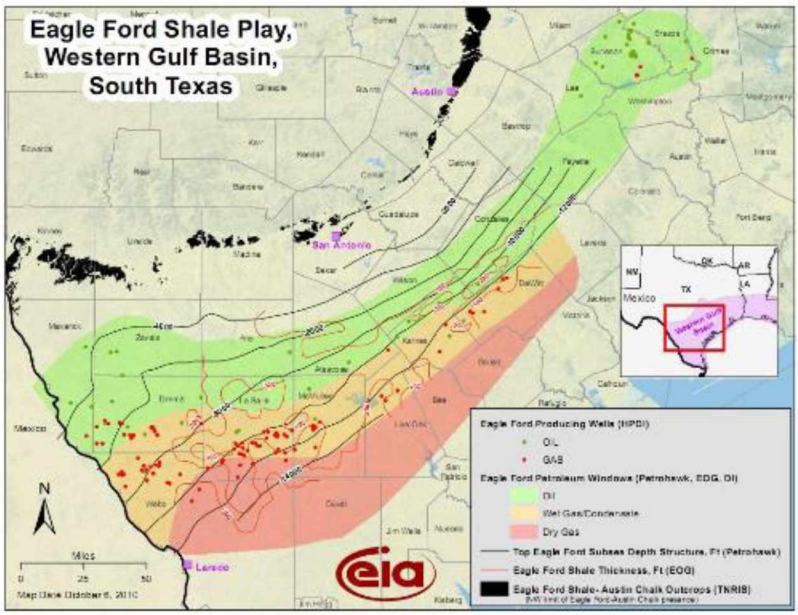

Figure 3: Eagle Ford Zones (Energy Information Administration)

Eagle Ford Shale completions consist mostly of horizontal wells with several fractures. The number of stages has increased from 14 to 20 over the years of the Eagle Ford shale development. The usage of treatment fluid progressed from slickwater to cross-linked get tail-in. The average stage has about 11,000 bbl of fluid and 260,000 lbm of proppant. Proppant sizes vary between 100 mesh, 30/50 and 40/70. In some cases, 20/40 or 16/30 mesh size proppant is tailed in to help minimize pressure drop across the tail-in and to reduce proppant flowback in softer formations (Barasia and Pankaj, 2014). Some wells use low strength ceramic or resin-coated sand with majority of wells incorporating sand (IHS, 2011).

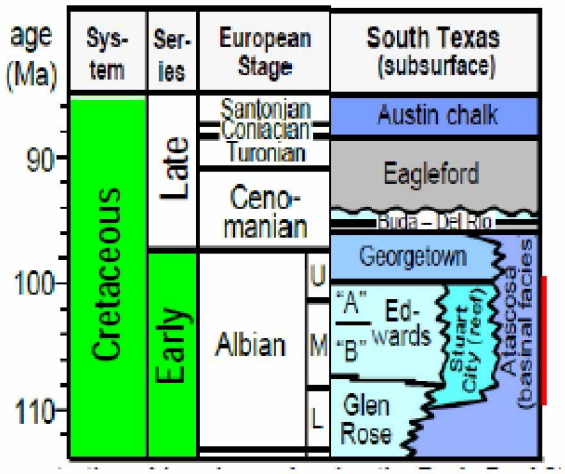

Figure 4: Upper Cretaceous stratigraphic column showing the Eagle Ford Shale (Dawson, 2000)

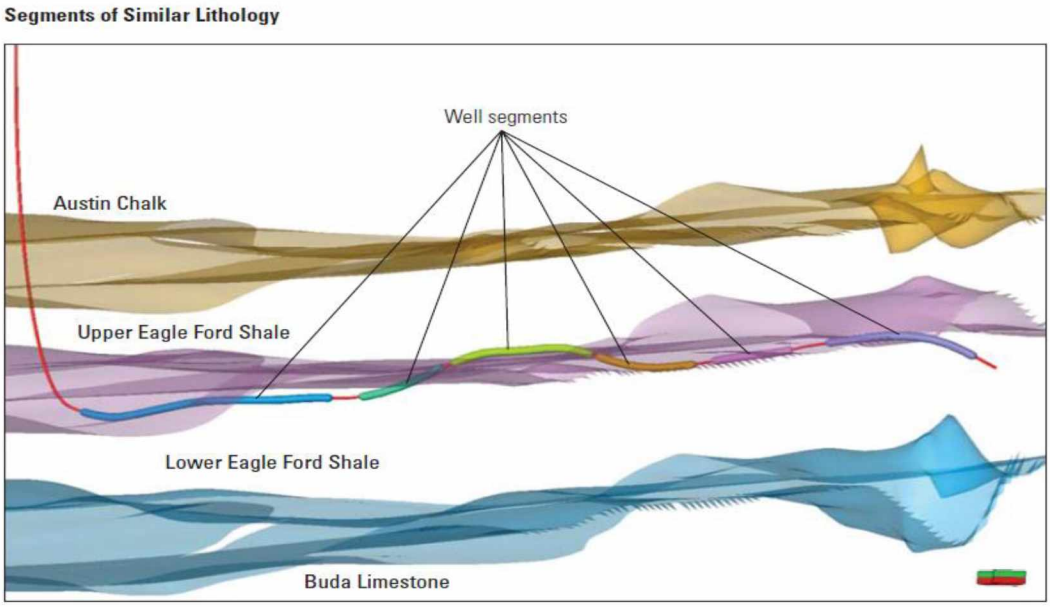

Figure 5: Formation layers in Eagle Ford (Ajayi et al., 2013)

2.4 The Eagle Ford Shale as a Proposed Analog for the Shublik Shale

Hutton et al. (2012) proposed the Eagle Ford shale to be a close analog to the Shublik Formation. The Eagle Ford shale and the Shublik shale appeared to have similar kerogen types, TOC, thermal maturity and mechanical values, some of which are listed in Table 2. There is a possibility of Shublik shale fracture propagation to be similar to ones in Eagle Ford shale with

the same hydraulic fracture treatments. However, Shublik may require different completion and simulation strategies due to differences in age, lithology, in situ stress orientation, and depths (Hutton et al., 2012).

Table 2: Similar characteristics of the Eagle Ford Shale and the Shublik shale (Hutton et al., 2012)

	Eagle Ford	**Shublik**
Total Organic Carbon (TOC), %	2 - 7	2 - 4
Main Kerogen Types	I/II (oil)	I/II (oil)
Oil Gravity, ^{0} API	30 - 50	24
Thickness, ft	50 - 250	0 - 600
Thermal Maturity	Immature – Oil - Gas	Immature – Oil - Gas
Lithology and Variability	Shale – Siltstone - Shale	Shale – Siltstone - Limestone
Brittleness	Yes -Quartz	Yes - Calcite
Overpressure	Yes	Locally

2.5 Hydraulic Fracturing

Fracturing stimulation treatment is routinely performed on wells in low-permeability reservoirs. Specially engineered fluids are pumped at high pressure and at a high rate into the reservoir interval to be treated, causing a vertical fracture to open.

The wings of the fracture extend away from the wellbore in opposing directions according to the natural stresses within the formation. Proppant, such as grains of sand of particular size, is mixed with the treatment fluid to keep the fracture open when the treatment is complete. Hydraulic fracturing creates high-conductivity communication with a large area of formation and bypasses any damage that may exist in the near-wellbore area (Schlumberger Oilfield Glossary).

2.6 The Important Role of Natural Fractures in Shale Gas Production

Multi-stage hydraulic fracturing of long horizontal wells enhanced commercial exploitation of low permeability gas reservoirs due to enlarged fracture surface area in contact with shale matrix where natural fractures play a critical role. Hydraulic fracture system is usually complex due to the interaction of the hydraulic fracture system with the natural fracture network.

In majority of shale gas reservoirs most of the reservoir fluid is stored in the matrix and the main flow path is from the matrix into the fractures and then into the wellbore (Walton and McLennan, 2013). There are two methods of characterizing a fractured reservoir: discrete fracture network (DFN) and dual porosity/dual permeability models. Dual porosity model is not applicable to disconnected fracture media and is not suitable to model a small amount of fractures (Chong et al., 2004). The fractures in DFN are explicitly defined in terms of their location in the reservoir, their connectivity to one another and to the wellbore as well as their production characteristics, such as permeability and conductivity (Walton and McLennan, 2013). To avoid these limitations, Unconventional Fracture Model (UFM), which utilizes DFN, combined with Voronoi grid system was used in this study.

2.7 Propped and Unpropped Zones

Cipolla (2009) proposed to assign the total fracture height into three different zones: arch zone, propped zone and unpropped zone (Figure 6). When slickwater is used as a fracturing fluid, the proppant settles in the bottom of the fracture. Due to this phenomenon, the bottom part of hydraulic fracture stays open after pressure release. Top and side sections of the fracture have smaller distribution of the proppant and hence close after pressure release, which results in lower conductivity values in the unpropped zones compared to propped zones. The difference in width between the bottom and top sections causes an open zone with very high conductivity – the arch zone (Cipolla, 2009). Closing stress is important in fluid flow modeling.

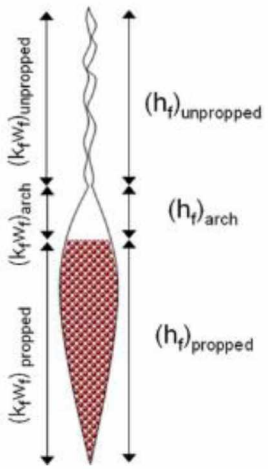

Figure 6: Vertical proppant distirbution in a hydraulic fracture (Cipolla, 2009)

2.8 Voronoi Grid

In the past 50 years, a variety of methods for the spatial discretization of hydrocarbon reservoirs were developed for flow simulation. In the early years, reservoirs were modeled using Cartesian grids where the resolution of the simulation model was limited to a few thousand blocks due to the limitation of CPU-time and available memory. With a progress of computer hardware development the resolution of simulation models became finer and number of grid blocks increased. A demand rose for new gridding techniques to accurately represent the flow within the model and to reflect complex geological features at the same time (Palagi and Aziz, 1994).

Unstructured/irregular gridding techniques were developed to meet the demand in the middle of the 1980s. Various kinds of unstructured grids were presented at that time: hybrid grids (Pedrosa and Aziz, 1986), CVFE (Control Volume Finite Element) grids (Forsyth, 1990), PEBI (Perpendicular Bisector), or Voronoi grids (Heinemann and Brand, 1998) and triangular grids (Gunasekera et al.,1997). Voronoi grids seemed attractive, since this grid type combines the advantages of structured and unstructured grids. In addition, Voronoi grid allowed a correct use of two-point flux approximation methods (Palagi and Aziz, 1994).

A noteworthy benefit of this grid is that individual grid points can be defined at any place inside the domain regardless of the position of any other points. Grid points are effortlessly

created by utilizing modules of known geometry and can be placed, scaled or pivoted in any position. Physical properties are specified that are independent of the computational grid (Palagi and Aziz, 1994). Voronoi grid is utilized in many areas such as physical science, crystallography, rock characterization, petroleum engineering, electrical engineering and fluid mechanics. Voronoi grid blocks are also called Wigner-Seitz cells or PEBI grid.

In order to perform a simulation of petroleum reservoir, the area in question is divided into grid blocks where the fluid flow between the blocks is calculated by discretized manifestation of Darcy's law. Calculations are done by locally applying conservation laws for every fluid component in the system and using permeability and PVT equations.

A Voronoi block is defined as the region of space that is closer to its grid point than to any other grid point, where the set of points is specified beforehand (Figure 7). Each block is associated with a grid point and series of neighboring blocks. Material balance equations are defined for each of these grid bocks, accounting for the fluids accumulation and flow through the boundaries. This method is known as the integral method of discretization and sometimes is referred to as the control volume finite difference (CVFD) method. Pairs of points, which are located closer together are picked to create Voronoi diagram. Then the equidistant line is drawn between them, which is perpendicular to the line connecting them. Hence, Voronoi grid is also called the perpendicular bisection (PEBI) grid in the petroleum literature. In addition, this grid can be viewed as a generalized point-distributed grid due to its dissection method (Aurenhammer, 1991).

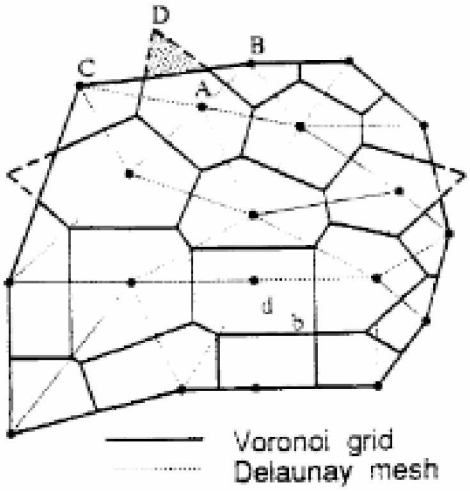

Figure 7: Voronoi grid and Delaunay mesh (Palagi and Aziz, 1994)

The Voronoi diagram is dual to its Delaunay Triangulation (Figure 7). A line in the Delaunay mesh means that there can be flow between the connected grid points. Consequently, the mesh of connections can be formed by lines, triangles, rectangles and polygons, which can be considered as a modified Delaunay mesh. Usually, reservoir engineers are more interested in the Voronoi blocks than the Delaunay mesh (Palagi and Aziz, 1994).

Grid systems, most often used in petroleum engineering, can be shown as special cases or at least very close approximations of the Voronoi grid: Cartesian, cylindrical, curvilinear, hexagonal, locally refined Cartesian and hybrid-Cartesian (Figure 8). Voronoi block is slightly different from the curved-boundary blocks in radial and cylindrical grids with straight sides and a curved-boundary block like the ones in curvilinear or cylindrical geometries, because it has straight lines. However, the results are very close. The Voronoi grid provides a natural way to connect the locally refined grid with the base coarse grid (Figure 8b). In addition, connections between two different types of grids are handled automatically. Consequently, any combination of grids shown in Figure 8 and other grids can be used in a single area, which significantly increases the flexibility for representing major reservoir features and flow around vertical and

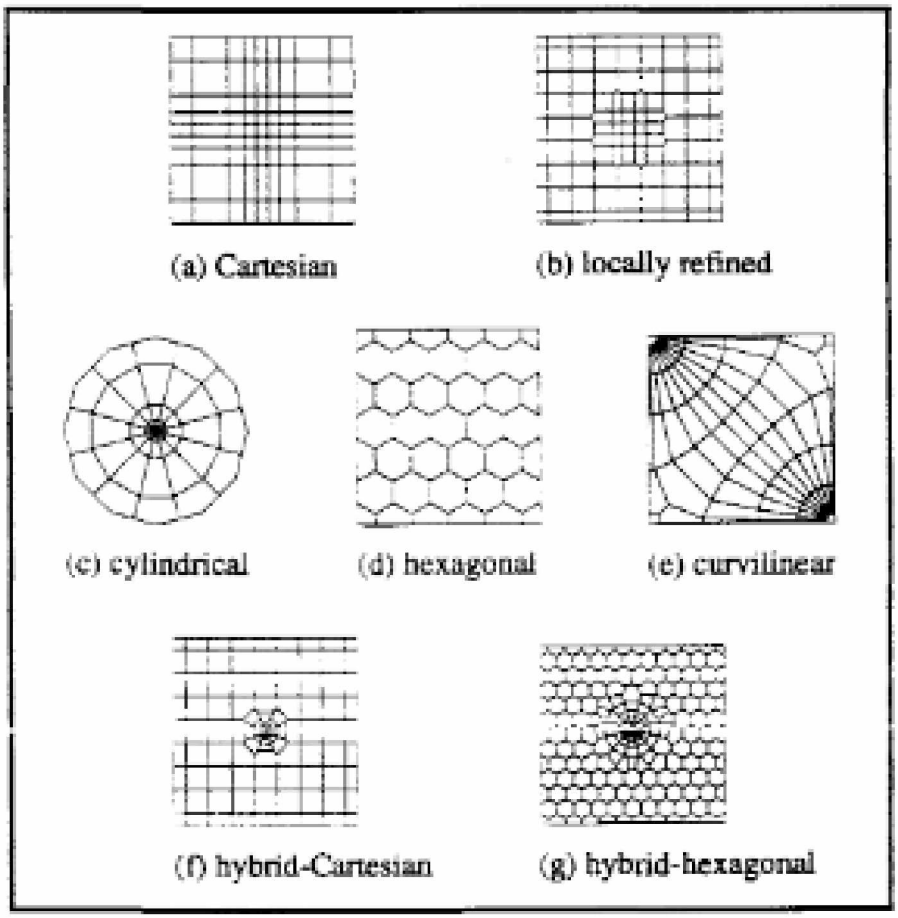

Figure 8: Some special cases of the Voronoi grid (Palagi and Aziz, 1994)

horizontal wells. After the geometry of the grid is defined, the cells are assigned physical properties to each cell and its connections. In conventional simulators each property is specified for a given cell. Then connection properties such as permeability are averaged between each pair of adjacent values. Voronoi gridding technique is based on the specification of physical properties (horizontal and vertical permeability, porosity, thickness, depth at each layer) at points (property-point), which do not depend on grid points. A property-point is defined by its location (x-y coordinates) and the value of the property.

2.9 Modeling of Hydraulic-Fracture-Network Propagation in a Naturally Fractured Formation

Microseismic monitoring proved that hydraulic fracturing of shale wells usually contributes to a development of complex fracture network (Fisher et al., 2002; Maxwell et al.,

2002; Daniels et al., 2007; Le Calvez et al., 2007). Conventional bi-wing planar fracture simulation is not sufficient enough to accurately design fracture treatment in a shale gas formation with complex fracture network. A hydraulic fracture model – referred as "wiremesh" - was developed to surpass the restriction of the conventional fracture models (Xu et al., 2009; Xu et al., 2010; Meyer and Bazan, 2011). Figure 9 demonstrates wiremesh model, which consists of two orthogonal sets of parallel and uniformly spaced fractures.

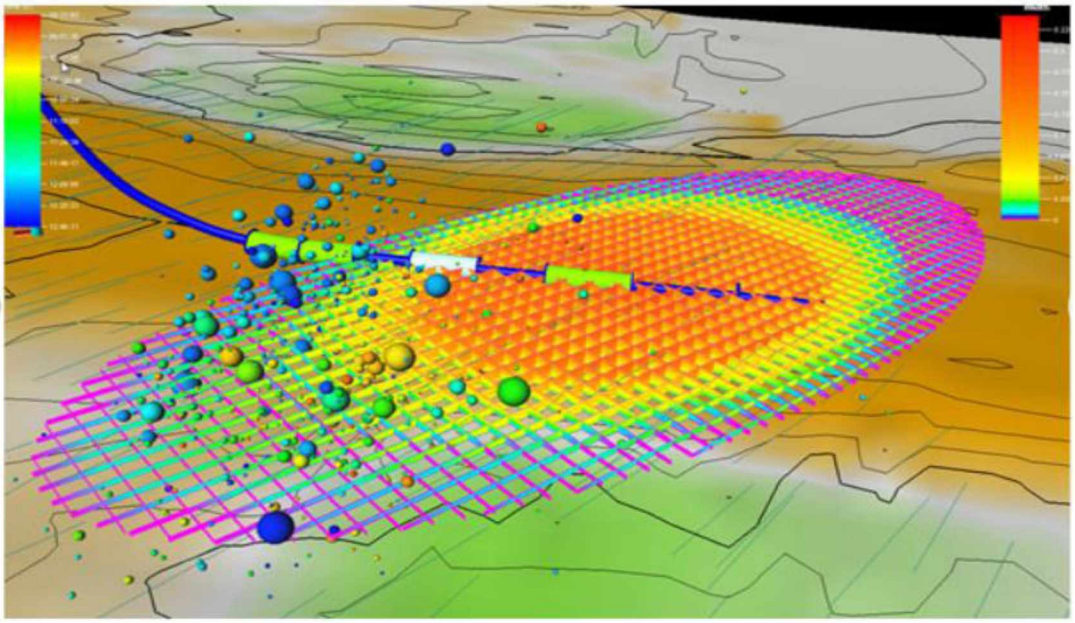

Figure 9: Wiremesh grid (courtesy of Schlumberger)

Zhang et al. (2007) introduced a thorough hydraulic-fracture model, which included a full solution of coupled elasticity and fluid. However, this model is limited to the 2D plane-strain conditions and hence is not suitable for general field applications where fractures are often contained in height. Moreover, the model is computationally intensive and is not well suited for engineering design applications (Weng et al., 2011). A complex-fracture-network model, which is capable of predicting hydraulic-fracture propagation and interaction with pre-existing natural fractures, was introduced by Olson (2008). But this model is based on only fracture mechanics and does not include fluid flow and proppant transport. In addition, this model's ability to accurately simulate actual hydraulic fracture treatments is limited due to an assumption of a constant fracturing pressure (Weng et al., 2011).

Weng et al. (2011) presented a new hydraulic-fracture model, which simulates the propagation of complex fractures in a formation with pre-existing natural fractures. The model addressed fracture deformation, height growth, fluid flow, and proppant transport in a complex fracture network with multiple propagating fracture tips. In addition, this model accounts for the interaction between hydraulic fractures and pre-existing natural fractures.

2.10 Unconventional Fracture Model

An unconventional fracture model (UFM) simulates the propagation, deformation, and fluid flow in a complex network of fractures (Kresse et al., 2011). This model uses assumptions, similar to the ones of conventional pseudo-3D fracture models to solve the fully coupled problem of fluid flow in the fracture network and the elastic deformation of the fractures. However, UFM solves the equations for the complex fracture network instead of solving them for a single planar fracture. Fracture-height growth is modeled in the same manner as in conventional pseudo-3D models. Transport equations are solved for each component of the fluids and proppants pumped. The main difference between UFM and the conventional planar-fracture model is its "ability to simulate the interaction of hydraulic fractures with pre-existing natural fractures (i.e., determining whether it subsequently propagates along the natural fracture)" (Wu et al., 2012). The branching of the hydraulic fracture at the intersection with the natural fracture gives rise to the development of a nonplanar, complex fracture pattern (Kresse et al., 2011). A crossing model has been developed (Gu and Weng, 2010) and validated against the experimental data (Gu et al. 2011), and it is included in the UFM. This crossing model is extended from the Renshaw and Pollard (1995) interface crossing criterion, applicable to any intersection angle (Wu et al., 2012). Moreover, the UFM also takes into the account the interaction among adjacent hydraulic-fracture branches by computing the stress-shadow effect on each fracture by the adjacent fractures in addition to the hydraulic-fracture/natural-fracture interactions (Kresse et al., 2011).

2.11 Fracturing Fluid Flowback

Slickwater hydraulic fracturing is one of the main techniques used to simulate shale gas wells. Tens of thousands of barrels of water are injected into a single well during a typical treatment out of which only 10 to 50% is recovered during production (King, 2012). Most of the water recovery occurs during the clean-up of the well and initial period of production (several weeks). The retained water is the sum of water that imbibes into the formation and water that is trapped in a fracture network. There is no proven explanation of which of the two mechanisms is dominant, and why so much treatment water is retained by the reservoir (Jurus et al., 2013).

Since the leak-off into the formation is finite, most of the pumped water remains either in fractures as an immobile "propping" phase, or in unpropped zone (Fan et al., 2010; Ehlig-Economides, 2011). This is a reasonable assumption since the mobility of water in ultra-tight shale formation is too low to produce sufficient amount of water leaking-off into the rock. Furthermore, some shale formations are partly oil-wet systems due to the high content of organic material (Andrade et al., 2010).

Water retention could be due to the imbibition of water into shale rock since shale formations are considered to be mostly water wet. King (2012) suggested that shale formations can contain less water than would be expected in a connate condition leading to increased water entrapment. Production of entrapped water reduces fracture conductivity and results in lower gas production. Some recent field tests and observations show that post fracturing shut-in may reduce water recovery and help gain higher production rates (King, 2012).

2.12 Non-Darcy Flow

Usually the flow pattern in recovery processes is governed by Darcy's Law, which describes a linear relationship between pressure gradient and velocity as follows:

$$u = -\frac{K}{\mu}\frac{\partial P}{\partial x} \tag{1}$$

Where u is superficial velocity, K is permeability, P is pressure, μ is viscosity and x is dimension in x direction (Li and Engler, 2001).

Forchheimer added a non-Darcy term to the equation above to account for turbulent flow:

$$-\frac{dP}{dx} = \frac{\mu}{K}u + \beta\rho u^2 \quad (2)$$

Empirical correlations available for non-Darcy coefficient for one phase are listed in Table 3. In the equations below porosity is used in a fraction and τ stands for well tortuosity – the arc-chord ratio: the ratio of the length of the well path to the distance between the ends of it.

Table 3: Empirical Correlations for Non-Darcy coefficient (Li and Engler, 2001)

Flow	**Correlation**	**Description**	
One-Phase	$\beta = ab^{-\frac{1}{2}}(10^{-8}K)^{--\frac{1}{2}}\varphi^{-\frac{3}{2}}$	a=1.75, b=150, K(darcy), β(1/cm) Gasses: carbon dioxide, nitrogen, methane, hydrogen	Thauvin and Mohanty
	$\beta = ab^{-\frac{1}{2}}(10^{-8}K)^{--\frac{1}{2}}\varphi^{-\frac{3}{2}}$	a=1.8 to 4, b=180	McDonald et al.
	$\beta = 1.82 * 10^{8}K^{\frac{-5}{4}}\varphi^{-\frac{3}{4}}$	K (md), β (1/cm) For natural porous media	Janicek and Katz
	$\beta = bK^{-a}$	a and b are based on proppant types, K(darcy)	Cooke
	$\beta = \frac{0.005}{K^{0.5}\varphi^{5.5}}$	K (cm^2), β (1/cm) For unconsolidated sandstones, consolidated sandstones, limestones and dolomites	Geertsma
	$\beta = \frac{4.8 * 10^{12}}{K^{1.176}}$	K(md), β(1/m)	Pascal et al.
	$\beta = \frac{6.15 * 10^{10}}{K^{1.55}}$	K(md), β (1/ft)	Jones
	$\beta = 8.91 * 10^{8}K^{-1}\varphi^{-1}\tau$	K(md), β(1/ft)	Liu et al.
	$\beta = \frac{1.55 * 10^{4}\tau^{3.35}}{K^{0.98}\varphi^{0.29}}$	K(Darcy), β (1/cm)	Thauvin and Mohanty
	$\beta = \frac{1.07 * 10^{12} * \varphi^{0.449}}{K^{1.88}}$ $\beta = \frac{2.49 * 10^{11}\varphi^{0.537}}{K^{1.79}}$	K (md), β (1/ft)	Coles and Hartman
	$\beta = \frac{11500}{K\varphi}$	K(Darcy), β (1/cm) For Berea sandstone	Li et al.
	$\beta = \frac{1.485x10^{9}}{k^{1.021}}$	K (md), β (1/ft)	Civan and Evans

Proppants are essential to the success of hydraulic fractures and often account for a significant portion of the cost of the treatment. Cooke (1973) developed a relationship to account

for the turbulent flow using constants for different proppant mesh sizes, which are listed in Table 4.

Table 4: Constants for different mesh sizes (Cooke, 1973)

Proppant Size, mesh	A	B
8 to 12	1.240	17,423
10 to 40	1.340	27,539
20 to 40	1.540	110,470
40 to 60	1.600	69,405

2.13 Gas Adsorption/Desorption

Gas exists in both adsorbed and free phase in the shale gases. Ignoring gas desorption in calculations may result in underestimation of ultimate gas recovery factor. A large portion of gas is stored as adsorbed phase inside kerogen (Mengal and Wattenbarger, 2011; EIA, 2011; Wu et al., 2012). As the reservoir depletes and pressure drops, the adsorbed gas releases from kerogen surface and contributes to production. Adsorption capacity of shale formations depends on the surface area, pressure, temperature, composition, pore size and sorption affinity (Leahy-Dios et al., 2011). Different studies have been conducted in literature to assess impact of gas desorption on gas production from shale gas reservoirs (e.g., Cipolla et al., 2010; Thompson et al., 2011; Mengal and Wattenbarger, 2011; Yu and Sepehrnoori, 2014; Haghshenas et al., 2014).

The BDDT theory (Brunauer et al., 1940) lists the adsorption isotherms into five types as shown in Figure 10. Kerogen pore geometry affects the complexity and the size of the curves. Type I is the classical Langmuir isotherm. Due to the high heterogeneity and multiple adsorption layers, the actual adsorption shape may be different from the classic Langmuir isotherm (Wu et al., 2012). Langmuir isotherms for Eagle Ford shale are present in the literature and are used in this study.

Langmuir Isotherm model (Langmuir, 1916) accounts for the amount of adsorbed phase at a given pore pressure by the following equation:

$$G = \frac{V_L P}{P + P_L} \tag{3}$$

Where G is the adsorbed volume of gas in scf/ton, V_L is the Langmuir volume and P and P_L are the pressure and Langmuir pressure in psi, respectively. V_L is the gas volume at the infinite pressure and represents the maximum storage for gas. Langmuir pressure is the corresponding pressure to one-half Langmuir volume as shown on Figure 11 (Freeman et al., 2010).

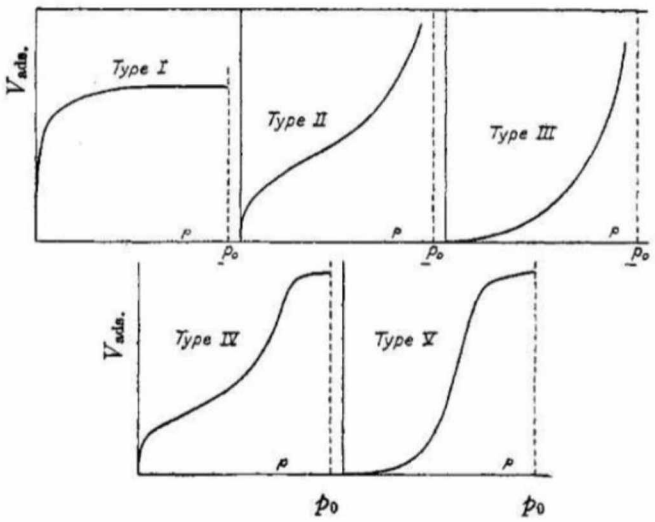

Figure 10: Five types of adsorption istotherms (taken from Wang (2013))

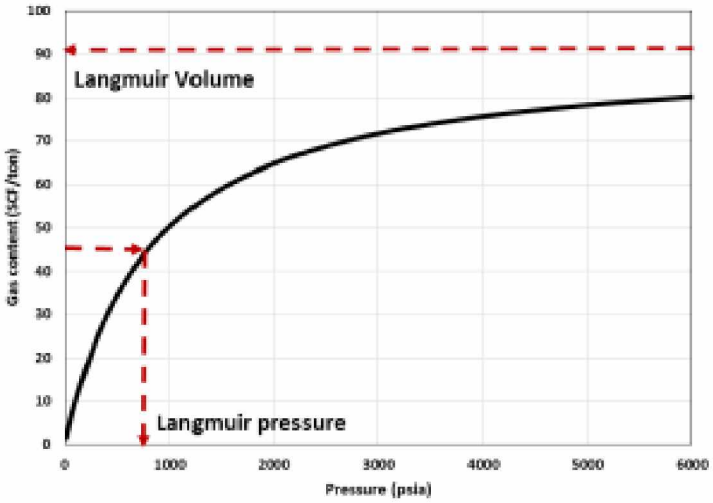

Figure 11: Langmuir isotherm curve (Freeman et al., 2010)

2.14 Reservoir Simulator Description

2.14.1 Mangrove

The Mangrove is a reservoir-centric stimulation design software with a seismic-to-stimulation workflow. The software has been developed after extensive theoretical and experimental work to fill the void in complex fracture design tool modeling capability. Its key function is using UFM to model the interaction between hydraulic fractures and natural fractures in the reservoir described by a discrete fracture network (DFN) geological model. The software analytically models this interaction in terms of various parameters, including angle of incidence, net pressure, fluid viscosity, and minimum-to maximum stress contrast in the reservoir. Mangrove workflow is rooted in reservoir characterization. The software leverages the science of the Petrel E&P software platform to build multidomain and multisource cross-validated reservoir models to account for heterogeneity that dictates completion and stimulation in unconventional reservoirs (Sobernheim, 2012).

2.14.2 INTERSECT

INTERSECT was developed in partnership with Chevron and combines the extensive simulator development experience and global oil and gas reservoir management expertise of both companies. The INTERSECT simulator has been designed to make field development planning and risk mitigation of larger and more complex fields more efficient – to provide greater certainty in reserves estimation and management. INTERSECT is much faster than the current generation of reservoir simulators on large and heterogeneous models, with the ability to rapidly simulate tens of millions of cells and thousands of wells. The main advantage of INTESECT is that it is capable of simulating unstructured gridding necessary in modeling of DFN (Petrel reference manual, 2013).

2.14.3 Petrel

Petrel is a Schlumberger owned E and P software platform that provides an integrated solution from exploration to production. It allows the user to interpret seismic data, perform well correlation, build reservoir models suitable for simulation, submit and visualize simulation

results, calculate volumes, produce maps and design development strategies to maximize reservoir exploitation. It addresses the need for a single application able to support the "seismic-to-simulation" workflow, reducing the need for a multitude of highly specialized tools. By bringing the whole workflow into a single application risk and uncertainty can be assessed throughout the life of the reservoir (Petrel reference manual, 2013).

This page intentionally left blank for the purposes of print publication.

Chapter 3 Methodology and Model Construction

While a robust predictive fracture model is a key to analyze Shublik shale play, it is technically challenging to achieve. Additional challenges make predicting well performances difficult, even in the short term. These include:

- No obvious relationship between number of hydraulic fractures and production
- Wide geographical variability related to more or less developed fracture systems
- Rapidly changing production over time
- Limited production history
- Complexity associated with modeling fluid flow

Ultralow-permeability shale reservoirs require a large fracture network to maximize well performance. Microseismic fracture mapping has shown that large fracture networks can be generated in many shale reservoirs. In conventional reservoirs and tight gas sands, single-plane-fracture half-length and conductivity are the key drivers for stimulation performance. In shale reservoirs, where complex fracture network are created in multiple planes, the concepts of single-fracture half-length and conductivity are insufficient to describe stimulation performance. This is the reason for the concept of using stimulated reservoir volume (SRV) as a correlation parameter for the well performance. The size of the created fracture network can be approximated as the 3D volume (stimulated reservoir volume) of the microseismic-event cloud (Mayerhofer et al., 2010). However, SRV is not the only driver of well performance. Hydraulic and natural fracture spacing and conductivity within a given SRV can affect production rate deceleration and ultimate recovery.

In the first part of the study, a single planar fracture was examined without the effect of natural fracture network. In the second part of the study, the effects of natural fracture network were included for the same SRV for consistent results.

3.1 Hydraulic Fracture Design

To create the fracture, a fluid is pumped into the wellbore at a high rate to increase the pressure in the wellbore at the perforations to a level greater than the breakdown pressure of the formation. The breakdown pressure is generally believed to be the sum of the in-situ stress and the tensile strength of the rock. Once the formation is broken and the fracture initiated, the fracture can be extended at a pressure called the fracture-propagation pressure. The fracture-propagation pressure is equal to the sum of the in-situ stress, the net pressure drop and the near-wellbore pressure drop. The net pressure drop is equal to the pressure drop down the fracture as the result of viscous fluid flow in the fracture, plus any pressure increase caused by fracture tip effects. The near-wellbore pressure drop can be a combination of the pressure drop of the viscous fluid flowing through the perforations and /or the pressure drop resulting from tortuosity between the wellbore and the propagating fracture.

Modified workflow introduced by Mirzaei and Cipolla (2012) is used in this study (Figure 12).

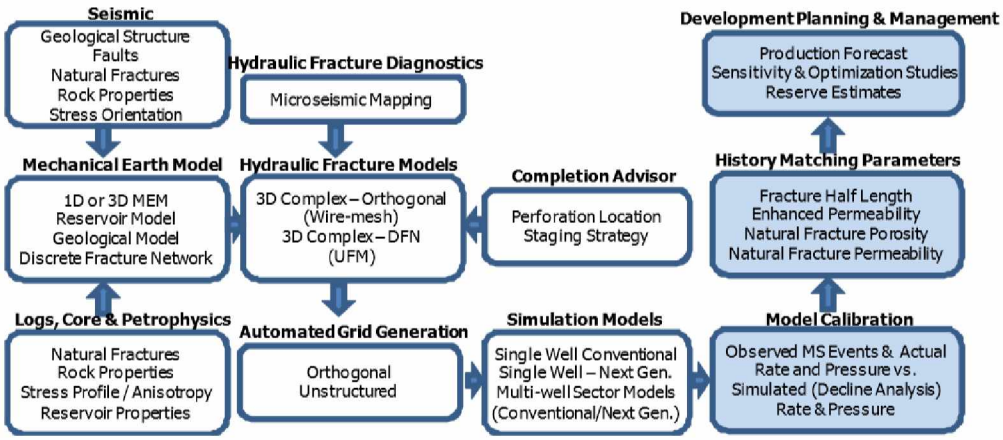

Figure 12: Worklfow for modeling, simulaiton, and ultimate recovery forecast of a well with hydraulic fracture in an unconventional shale gas reservoier (Mirzaei and Cipolla, 2012)

Due to absence of micro seismic and lateral data, seismic and hydraulic fracture diagnostics steps were omitted. First step in this study began at logs, core and petro physics step. Logs for Petrohawk Martin Dora 1 exploration dry gas well in La Salle County, TX were obtained from DrillingInfo database and loaded into Petrel (Figure 13). A synthetic lateral well

was designed based on the exploration well. A 200-ft thick shale layer was added into the lateral section. Lateral section well path was based on the directional surveys for the Petrohawk Martin Dora 2.

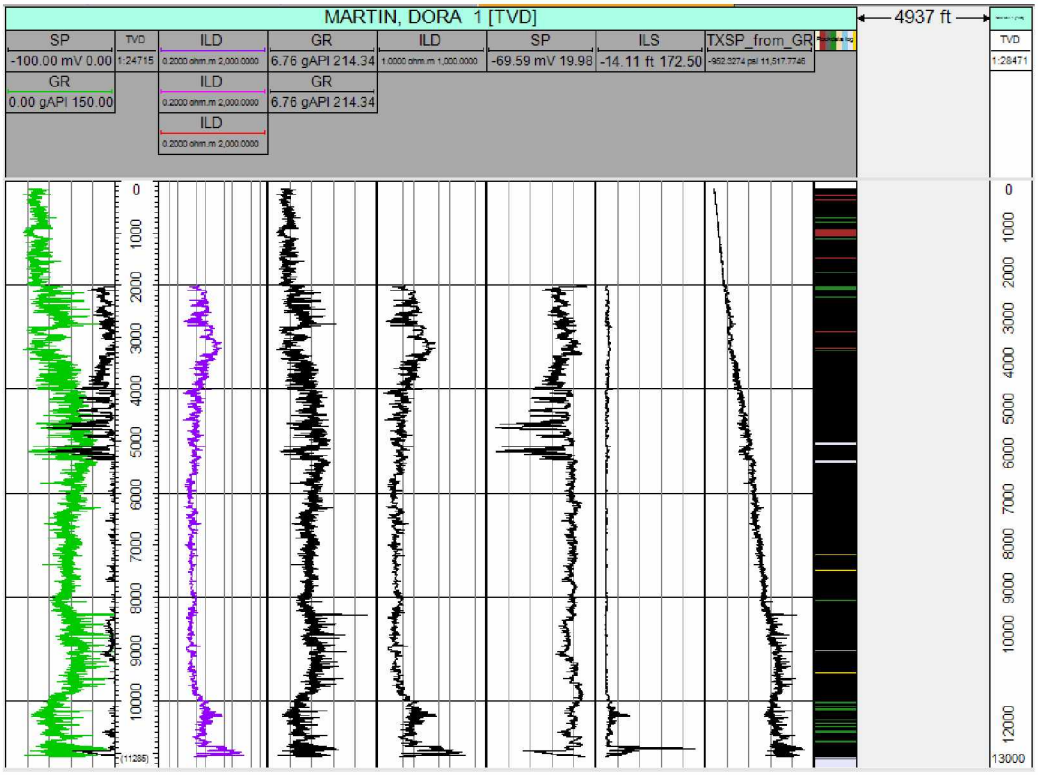

Figure 13: Logs for Martin Dora 1

3.1.1 Single Hydraulic Fracture Simulation

First, one single fracture was modeled in this study (Model I). The rest of the properties and dimensions of this model are based on published studies on the Eagle Ford Shale are listed in Table 5 (Inamdar et al., 2010; Bazan et al., 2010; Murphy et al., 2013). Completions data and directional surveys used in this study were taken from Drilling info and are shown in Table 6. The deviation of the lateral was higher than 90 degrees to provide larger exposure of the well length to the paying formation layer.

Completion and stimulation design was done by using the geometric method – the deviated wellbore length was divided evenly into the number of planned intervals, or stages, designated for fracture treatment. The stage with the perforation was placed at the center of the

deviated wellbore length; and its length was limited to 2 ft since only one single perforation was used. During a typical hydraulic fracturing treatment, engineers design stages with two to eight perforation clusters distributed uniformly along the stage length to promote fracture growth from multiple starting points (Ajayi et al., 2013).

Table 5: Parameters for single well simulation (Base Case, Model I)

Reservoir Data		
Reservoir thickness	200	ft
Initial reservoir pressure	8594	psia
Rock porosity	0.06	fraction
Rock permeability in all directions ($_{i,j,k}$)	200	nDarcy
Reservoir temperature	269	^{O}F
Well Data		
Total MD	15503	ft
Fracture spacing	200	ft
Stage start TVD	11156.7	ft
Stage end TVD	11156.8	ft
Stage start MD	13046	ft
Stage end MD	13048	ft
Shut in time	6	hours

Table 6: Completions data for Martin Dora 1

Top MD (ft)	**Bottom MD (ft)**	**OD (in)**	**ID (in)**	**Weight (lb/ft)**	**Grade**	**Collapse pressure (psi)**	**Burst pressure (psi)**
0	2028	10.75	9.95	45.50	C75	2410	4880
0	10752	7.63	6.88	29.70	C95	5120	8180
0	15503	4.5	3.83	15.10	P110	14320	14420

Pumping schedule was modified from Weng et al. (2011) for the single fracture for the reservoir pressure present and is shown in Table 7. Proppant settling was calculated using the Schiller and Naumann correlation to provide more accurate settling velocity calculation in low viscosity liquid (slickwater) as recommended by Mangrove manual. Shut-in time of 6 hours was used.

Table 7: Treatment schedule for Base Case simulation

Step name	Pump rate (bbl/min)	Fluid	Fluid volume (gal)	Proppant	Prop.conc. (PPA)	Prop.mass (lb)	Slurry volume (bbl)	Pump time (min)
Pad	60.	Slickwater	2000		0	0	47.62	0.79
0.4 PPA	60.	Slickwater	4000	CarboLite 20/40	0.4	1600	96.91	1.62
0.6 PPA	60.	Slickwater	5000	CarboLite 20/40	0.6	3000	122.17	2.04
0.8 PPA	60.	Slickwater	6000	CarboLite 20/40	0.8	4800	147.86	2.46
Flush	60.	Slickwater	7791.6		0	0	185.51	3.09

Totals

Avg. pump rate (bbl/min)	Volume weighted avg. rate (bbl/min)	Fluid volume (bbl)	Prop. mass (lb)	Slurry volume (bbl)	Pump time (min)
60.	60.	590	9400	414.56	6.91

Mangrove manual suggests using auto shut-in option. When this option is selected, the fracture closure time is estimated by the simulator and the simulation runs until the fracture is closed. Therefore, it is not necessary to estimate shut-in time on a trial-and-error basis in order to simulate fracture closure. Shut-in time specifies the time interval that is to be estimated after pumping ends. The value entered for shut-in time should be long enough to allow the fracture to close completely. A good estimate of the shut-in times is 3*(pump time) (Mangrove reference manual, 2014). In this study shut in time selection was based on Zanganeh (2014), who demonstrated that shut in time of 6 hours achieves optimum conductivity.

Eagle Ford formation has elevated temperatures, which reduces the conductivity of sand-based proppant. CarboLite 20/40 was the chosen proppant in this study since ceramic proppants are unaffected by temperature (Palisch, 2012). It is recommended to use 30/70 and 100 Mesh for the slickwater systems due to its smaller settling rate (Palisch, 2012), however CarboLite 20/40 provided the most optimum results and was used in this study.

Volume of slickwater and proppant concentration were reduced until dimensionless fracture conductivity (Fcd) was less than 10. If the dimensionless fracture conductivity is equal to 10 or greater, the hydraulic fracture will essentially act as if it is an infinitely conductive fracture (Prats, 1961). Dimensionless fracture conductivity is calculated the following way:

$$F_{CD} = \frac{K_f w}{K\, x_f} \tag{4}$$

Where $K_f w$ is fracture conductivity (mD-ft), K is reservoir permeability (mD) and x_f is fracture half-length. Equation 4 yielded the following result:

$$F_{CD} = \frac{47.06\ mD * 0.12\ in}{200\ nD *\ 406.49\ ft} = 5.78 \tag{5}$$

Dimensionless conductivity F_{CD} is not the only main driver for the hydraulic fracture design. A smaller size proppant can be chosen to allow proppant to transport further toward the tips of fracture to ensure greater propped length and increase the treatment volume to get more width/conductivity. The first priority is usually to achieve longer fracture length in ultra low

permeability rock and then proppant can be chosen to satisfy F_{CD} requirement. However, proppant size 20/40 was chosen based on the study done by Zanganeh (2014).

The "half length" for UFM actually represents the half distance between the fracture tips along the max horizontal stress direction, rather than the true fracture length along the curved fracture path. Therefore, the half lengths from UFM for the two outmost fractures, which have the greatest curvature, are shorter than the corresponding PKN fractures that are assumed straight (Wu et al., 2012).

An injection rate of 60 bpm was selected to reduce an injection time and hence to obtain more efficient fracture propagation, since fluid leakoff is proportional to the square root of the execution time (Economides et al., 1994).

Figures 14 - 16 show the fracture propagation stages. Figure 14 shows conductivity plots for each stage. Figure 15 shows proppant areal distribution. Figure 16 shows width contour for each stage. Purple horizontal planes indicate zone set produced by Mangrove based on logs. Fracture growth is limited to only shale layer. The fracture looks stretched horizontally due to scaling in Petrel. Vertical axis is scaled 1:5 in default settings of Petrel. Magenta color represents the unpropped fracture area. Unpropped area has very low conductivity in the fracture simulation. However, unpropped zone conductivity is specified manually in the later stage (0.01 mD-ft for the Base Case) of the simulation in order to obtain the flow. Purple horizontal plans represent zone sets based on logs. Figures 14-15 show direct correlation between fracture conductivity and proppant areal distribution and evidence of proppant settlement due to slickwater use. One of the main concerns with the slickwater fracturing is its low carrying capacity, which increases proppant settling velocity. Vertical coverage of the hydraulic fracture with proppant is critical to transport, but may not occur due to the proppant settling (Britt et al., 2006). This adds a dimension to the slickwater fractures of propped vs. hydraulic measurements for width, height, and length (King, 2012). Using a hybrid fluid of slickwater to open the fissures and a more viscous fluid to place the main body of the proppant eliminates this phenomenon (King, 2012). Figure 16 shows that the fracture is wider near the wellbore and gets narrower closer to the fracture tips.

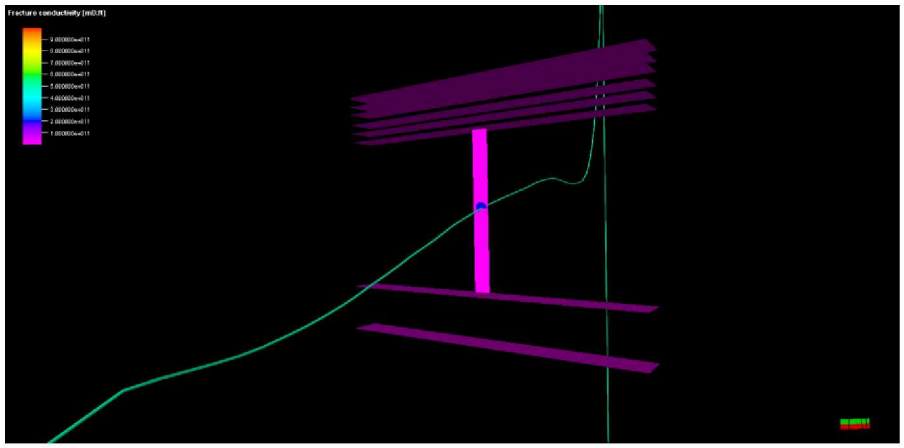

(a)

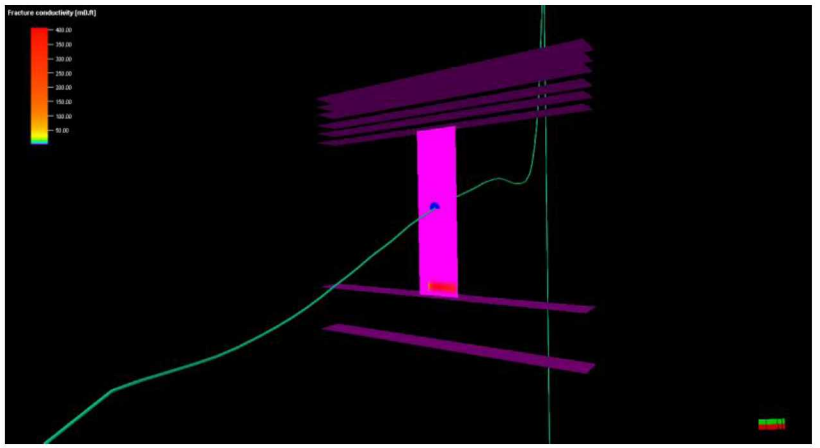

(b)

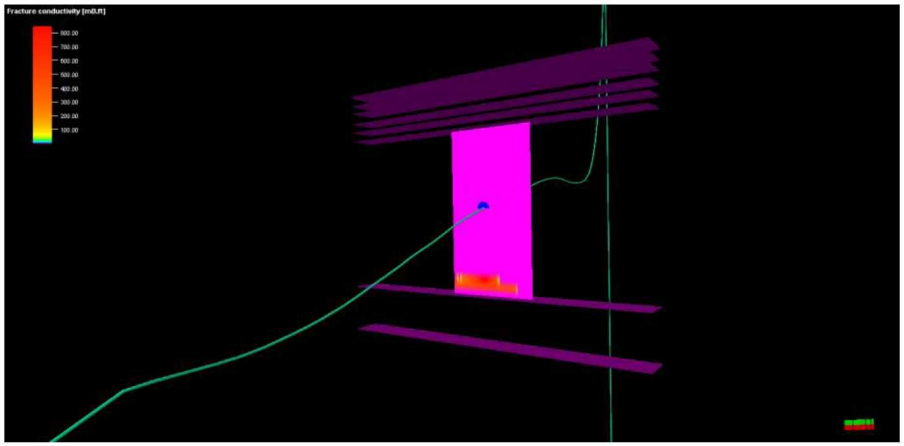

(c)

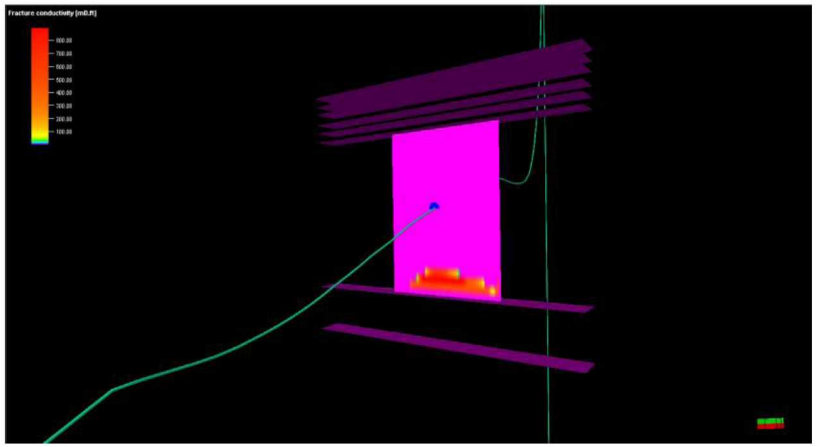

(d)

Figure 14: Conductivity [mD-ft] for a) Pad; b) 0.4 PPA; c) 0.6 PPA; d) 0.8 PPA

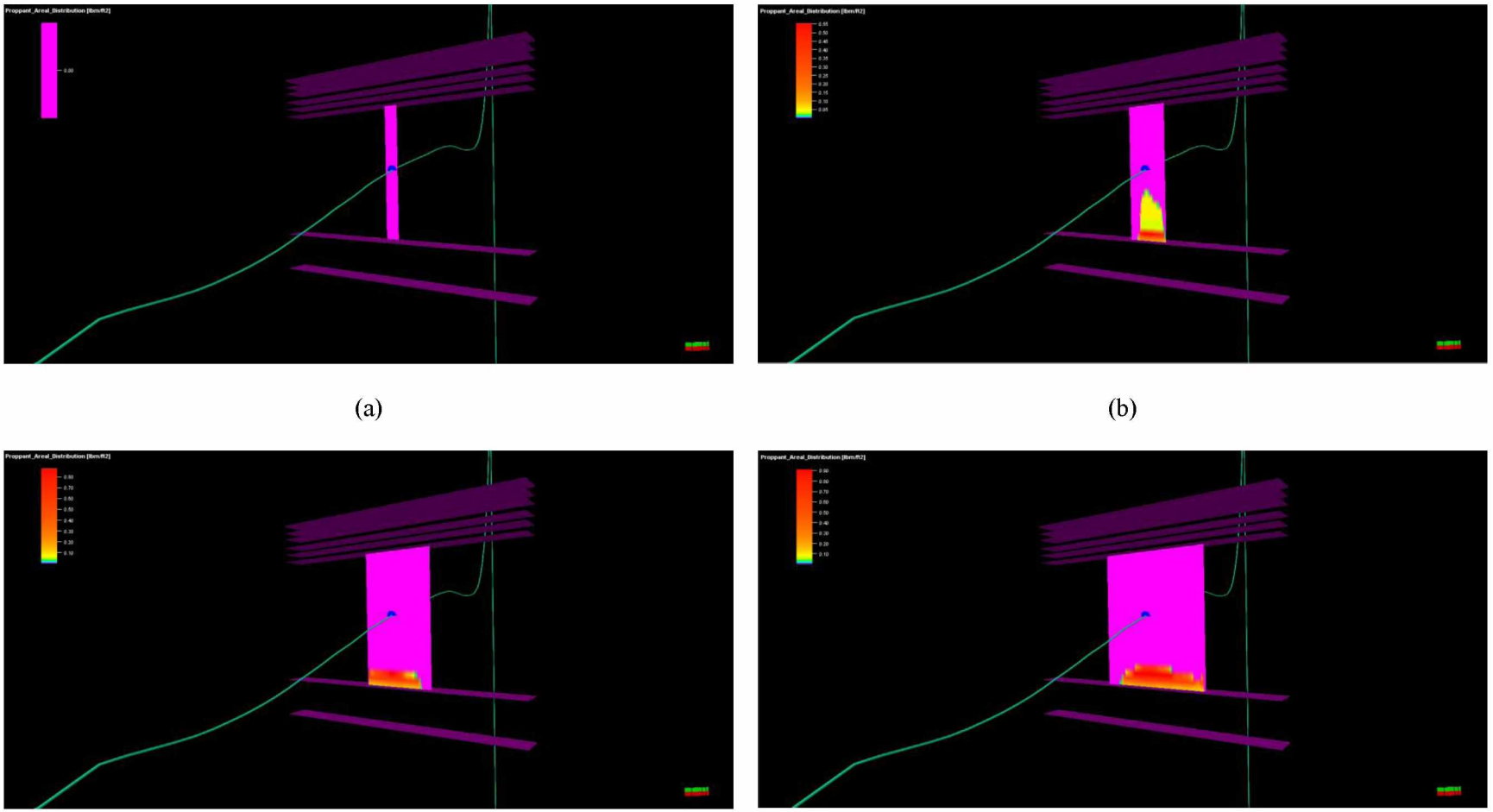

(a) (b)

(c) (d)

Figure 15: Proppant areal distribution for a) Pad; b) 0.4 PPA; c) 0.6 PPA; d) 0.8 PPA

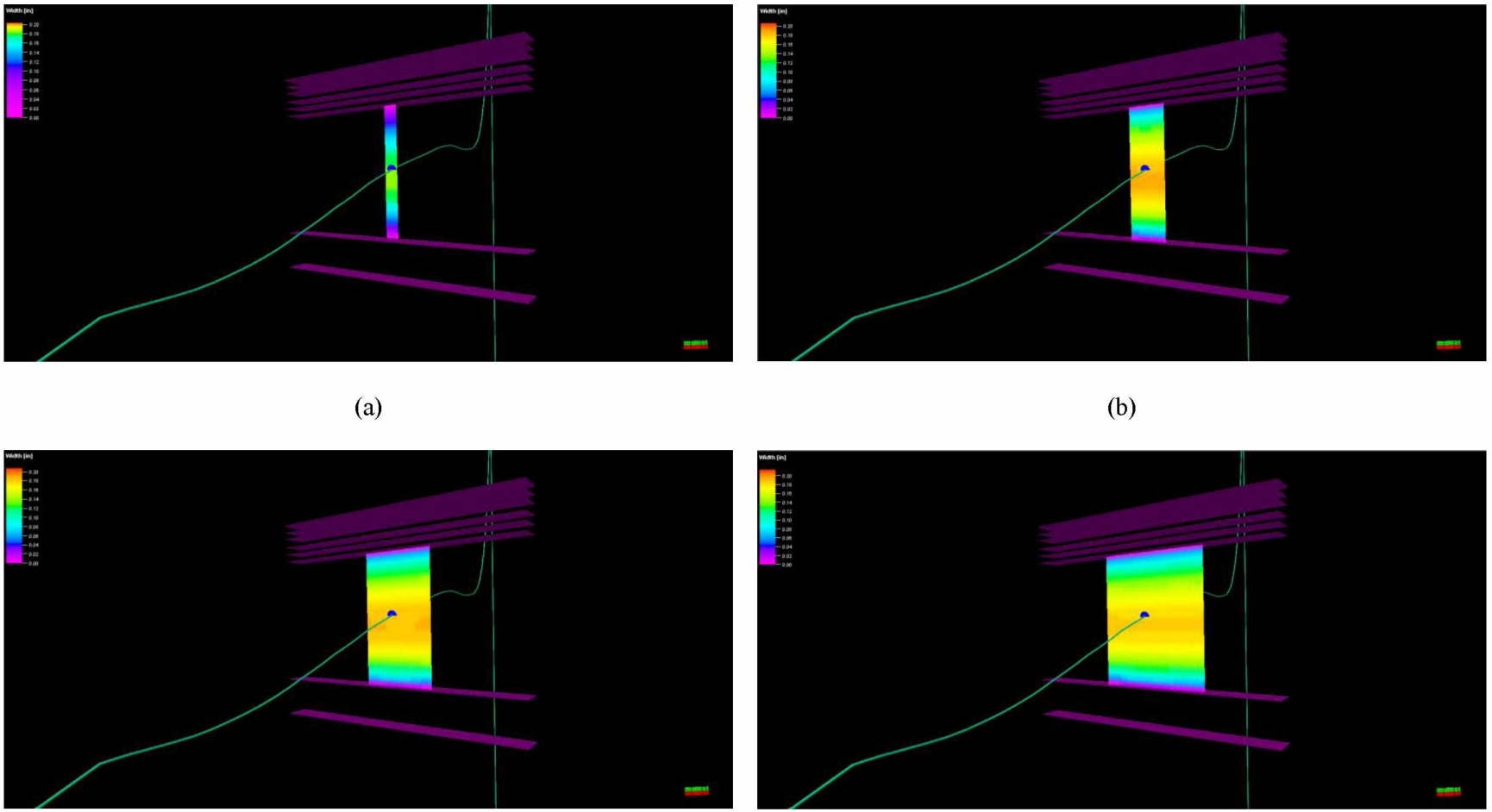

(a) (b)

(c) (d)

Figure 16: Width for a) Pad; b) 0.4 PPA; c) 0.6 PPA; d) 0.8 PPA

Table 8 displays the hydraulic fracture parameters results after the hydraulic fracture simulation run per each stage. After pad was injected, slickwater was injected with the proppant concentration starting at 0.4 PPA (proppant added per gallon) and increased 0.2 PPA each stage until reaching 0.8 PPA. All definitions for the table are listed in the Appendix A.

Table 8: Hydraulic fracture results for the hydraulic fracture simulation by stage

Hydraulic fracture results produced by Mangrove				
	Pad	0.4 PPA	0.6 PPA	0.8 PPA
Total fracture volume [ft^3]	257	759	1369	2081
Total fracture surface area [ft^2]	26556.4	77700.7	139914.7	211478.6
Maximum surface pressure [psi]	12416	12501	12440	12433
Estimated closure time [min]	360	931	4173	12
Total propped fracture surface area [ft^2]	0	27105.0	37073.0	59149.5
Maximum BH pressure [psi]	14077	14217	14217	14217
Efficiency [%]	96.2	93.6	91.5	89.4
Hydraulic fracture geometry				
	Pad	0.4 PPA	0.6 PPA	0.8 PPA
Final extension of HFN in the direction of max stress [ft]	100.6	298.1	536.6	813.0
Final extension of HFN in the direction of min stress [ft]	0	0	0	0
Maximum fracture height [ft]	258.3	258.3	258.3	258.23
Average fracture height [ft]	200	200	200	200
Total fracture surface area [ft^2]	25566.4	77700.7	139914.7	211478.6
Fracture width at wellbore [in]	0.20	0.20	0.21	0.21
Average fracture width [in]	0.11	0.11	0.12	0.12
Total fracture volume [ft^3]	242	736	1342	2078
Propped fracture geometry				
	Pad	0.4 PPA	0.6 PPA	0.8 PPA
Final extension of HFN in the direction of maximum stress [ft]	0	236.2	452.8	689.0
Final extension of HFN in the direction of minimum stress [ft]	0	0	0	0
Total propped fracture surface area [ft^3]	0	27105.0	37073.0	58556.0
Average propped fracture height [ft]	0	110.2	80.1	83.8
Fracture width at wellbore [in]	0	0.06	0.09	0.10
Average fracture width [in]	0	6.42E-3	0.01	0.02
Average fracture conductivity [mD.ft]	0	24.9	80.0	110.8

Time to closure, closure pressure, and fluid efficiency were estimated by Mangrove based on the fracture volume divided by the pumped slurry volume. Using the time at closure event (12.34 min in this study), Mangrove estimated the fluid efficiency and therefore the leak off volume, which later was converted to the leak off rate.

Total fracture volume is the volume of fluid injected minus the volume of fluid that leaks off into the formation. Productive fracture surface area is the area of the fractures in contact with the reservoir that serve as channels that convey gas to the wellbore. In the base case model natural fractures were not used, hence the area only accounts for propped and unpropped hydraulic fractures.

Leak off volume is the volume of the fluid absorbed by the formation. Efficiency is related to leakoff volume, hence low leak off signifies high efficiency.

Fluid efficiency is the ratio of the stored volume within the fracture to the total fluid injected. If too much fluid leaks off, the fluid has low efficiency (10 to 20%), and the created fracture volume will be only a small fraction of the total volume injected. If the fluid efficiency is too high (80 to 90%), the fracture will not close rapidly after the treatment. Ideally, fluid efficiency of 40 to 60% will provide an optimum balance between creating the fracture and having the fracture close down after the treatment. However, controlling the efficiency to 40-60% is difficult, especially with a low viscosity fracturing fluid since it causes a long fracture closure time. The model in this study has high efficiency due to low viscosity of the slickwater, which increases leak off into the formation.

Closure stress is the pressure at which the fracture closes after the fracturing pressure is relaxed. It is usually between 80 and 90% of breakdown pressure.

3.1.2 Multiple Hydraulic Fractures Simulation

Sometimes complex nonplanar hydraulic fractures are generally modeled as a single planar fracture to simplify the modeling process. This modeling method may result in higher net pressure values, lower values for the propped length and the width of individual fractures, which leads to potential for screen-outs. Screen-outs may lead to, higher values of fluid leak-off and lower values of the reliable fracture confinement within a payzone (Nolte and Economides,

1991). Such inaccurate results can cause a poor hydraulic fracturing jobs and lower resulting recovery factor (e.g., Hallam and Last, 1991).

After a single fracture simulation was constructed, nine fractures were added to investigate the difference between a single fracture and ten fracture simulations. All parameters were left the same as in the model with a single fracture. Pumping treatment schedule for Model II was kept the same as for Model I. Table 9 displays the parameters for a multiple fractures simulation. Resulted hydraulic fracture network for Model II is displayed in Figures 17 and 18. Proppant settling due to use of slickwater is present as in Model I. Hydraulic fracture parameters for Model II are listed in Table 10. Resulting fractures are not planar as in Model I due to a pressure drop across the cluster of the fractures and stress shadow effect accounted by UFM. Planar hydraulic fractures are unlikely to occur in unconventional plays. "If there are few natural fractures – or if these are tight with narrow initial apertures – whether pumped simultaneously (as in multiple clusters per frac stage) or sequentially (one stage pumped after the other), the stress shadow effect will force subsequent fractures to grow away from the first fracture. Alternatively, if there are many, hydraulically open fractures, the stress shadow effect may be muted by many open natural fractures and reduced length and aperture of the main hydraulic fracture" (Nagel et al., 2013). The fractures propagated not only in the direction of the maximum horizontal stress, but also in the direction of the minimum stress relative to each other.

Table 9: Parameters for single well simulation (Base Case, Model II)

Reservoir Data		
Reservoir thickness	200	ft
Initial reservoir pressure	8594	psia
Rock porosity	0.06	fraction
Rock permeability in all directions ($_{i,j,k}$)	200	nDarcy
Reservoir temperature	269	^{o}F
Well Data		
Total MD	15503	ft
Fracture spacing	200	ft
Stage start MD	13046	ft
Stage end MD	13048	ft
Shut in time	6	hours

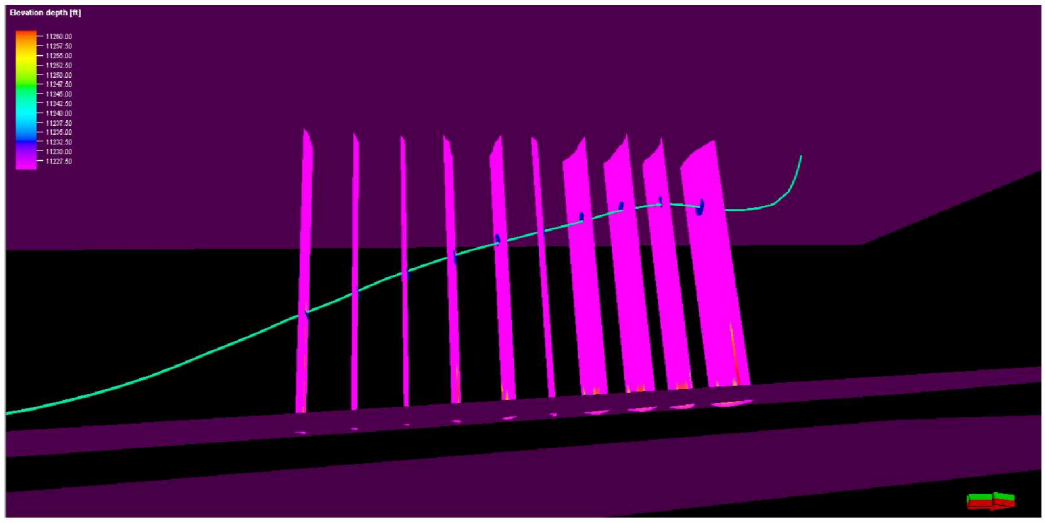

Figure 17: Conductivity profile for Model II [mD-ft] (Bottom view)

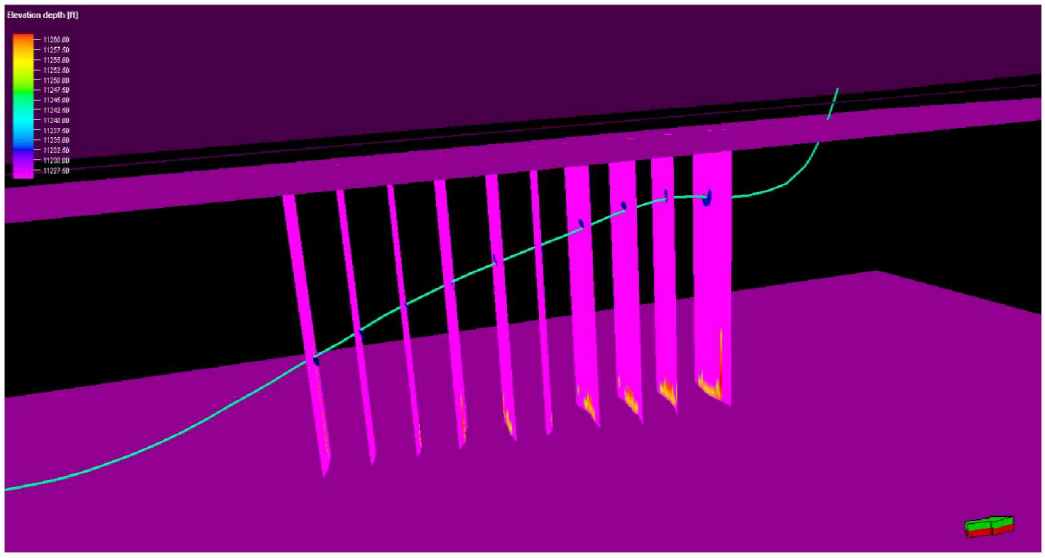

Figure 18: Conductivity profile for Model II [mD-ft] (Top view)

Table 10: Hydraulic fracture results for Model II

Hydraulic fracture results Model II	
Total fracture volume [ft^3]	1352
Total fracture surface area [ft^2]	581291.0
Maximum surface pressure [psi]	7597
Estimated closure time [min]	21.82

Table 10: Hydraulic fracture results for Model II continued

Total propped fracture surface area [ft^2]	40407.4
Maximum BH pressure [psi]	9367
Efficiency [%]	58.08
Hydraulic fracture geometry	
Final extension of HFN in the direction of max stress [ft]	309.7
Final extension of HFN in the direction of min stress [ft]	39.1
Maximum fracture height [ft]	226.9
Average fracture height [ft]	200
Total fracture surface area [ft^2]	73520.1
Fracture width at wellbore [in]	0.07
Average fracture width [in]	0.03
Total fracture volume [ft^3]	193
Propped fracture geometry	
Final extension of HFN in the direction of maximum stress [ft]	247.5
Final extension of HFN in the direction of minimum stress [ft]	23.6
Total propped fracture surface area [ft^3]	5190.5
Average propped fracture height [ft]	19.5
Fracture width at wellbore [in]	0.03
Average fracture width [in]	0.03
Average fracture conductivity [mD.ft]	36.5

3.2 Model Description

Mirzaei and Cipolla (2012) showed that Voronoi grid accurately models flow from a fractured shale reservoir. Rubin (2010) used locally refined grids with fracture cells represented using approximately 2.0 ft. wide cells for a hydraulic fracture.

This study used unstructured grid with fracture cells of 2 ft and rectangular bulk cells of 5 ft *5ft to model fracture flow, matrix to fracture flow, saturation and pressure. The azimuth of the well was altered to align it with the matrix grid. Mangrove eliminates the necessity of aligning the grid with the wellbore by deploying Voronoi grid. SRV, however, should be aligned with the well in order to accurately predict the drainage. Mangrove gives an option to align the orientation of the zoneset polygon, which dictates the dimensions of SRV, along the well. In this study the whole grid was aligned with the well to avoid any potential uncertainties.

The simulation was run over the period of 10,000 days with a bottom hole pressure (BHP) of 1000 psia. Mangrove gives an option to control either gas production rate or BHP, so the last one was chosen as a control for the simulation. These conditions were kept the same throughout technical sensitivity studies as well.

3.2.1 Model I

The simulated segment for Model I is shown in Figure 19. The simulation model consists of 31,188 cells. Natural fracture network is excluded from this model and is examined later in the study. Fracture closure is included in all simulation models in this study and is described in detail in Section 3.2.3. Gas desorption was not included in this study and was later added in technical sensitivity studies in section 4.12.

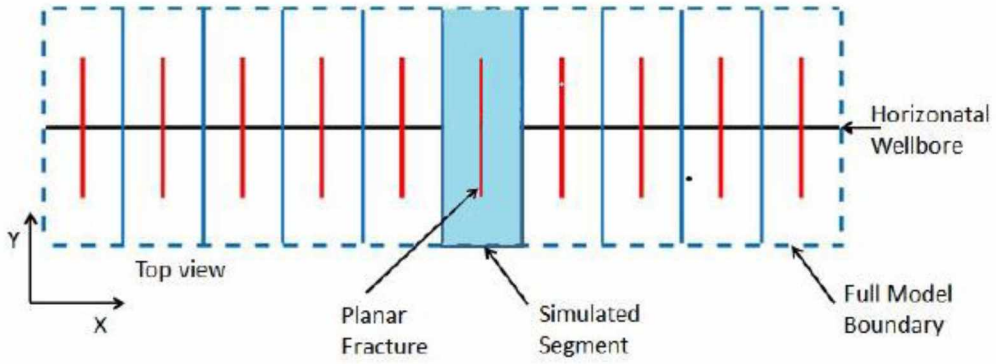

Figure 19: Well model for planar geometry (Model I)

Figure 20 shows top and side views of the single hydraulic fracture model built using Petrel, Mangrove and Intersect. Note that fracture spacing and formation thickness are both 200ft – however they are displayed 1:5 default ratio in Petrel. The grid dimensions are determined based on the fracture as following: fracture spacing*$2X_f$*thickness, which adds up to be 200ft*1220ft*200ft – total bulk volume of 48800000 ft^3. Pore volume of this model is 517210 RB. Average model porosity is 0.0595. Matrix porosity is 0.06. Fracture porosity was calculated by Mangrove and was in a range of 0.006-0.002 (Figure 21).

The governing factors of fracture porosity are fracture aperture, spacing, surface toughness, area and filling. The aperture is the average distance between the walls of the fracture.

The fracture porosity is defined as the ratio of fracture volume to the volume of rock specimen (Sen, 1995):

$$\varphi_f = \frac{La}{A} \tag{6}$$

Where φ_f is fracture porosity, L is length of the fracture, a is fracture aperture and A is the surface area of the rock. Hence, the fracture porosity is usually smaller than the matrix porosity due to small values of the fracture aperture and large values of the fracture surface area.

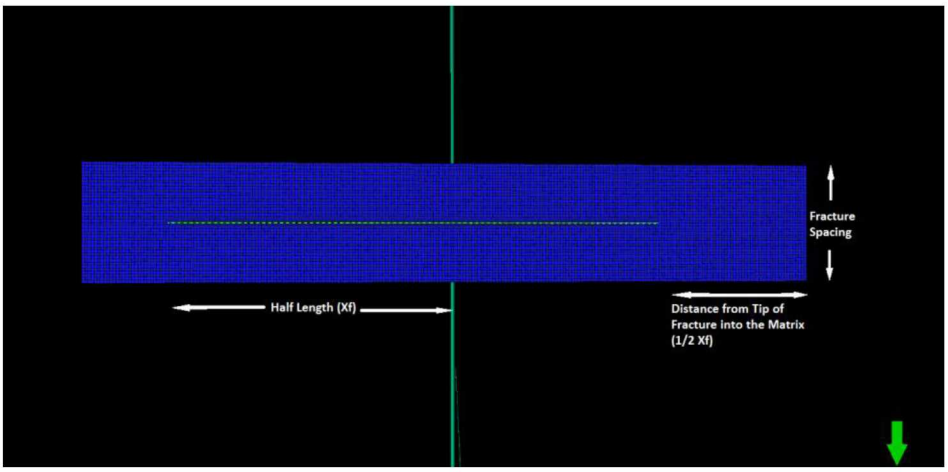

(a)

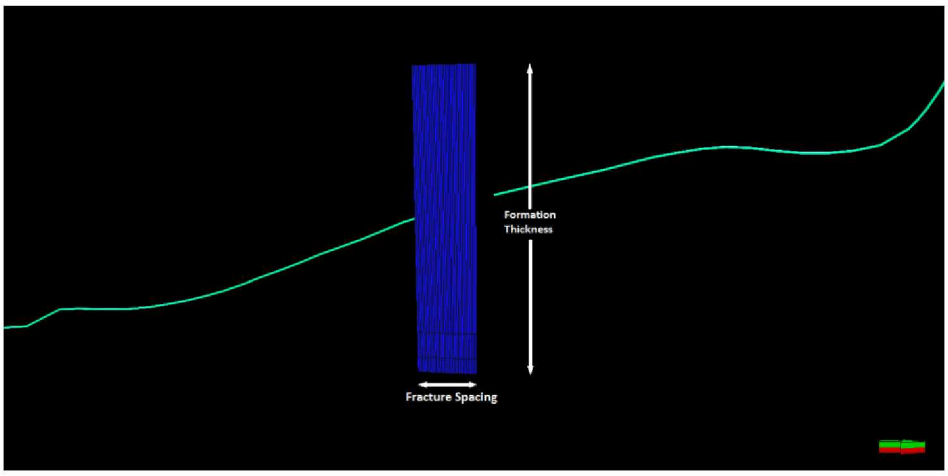

(b)

Figure 20: Top and side views of the model

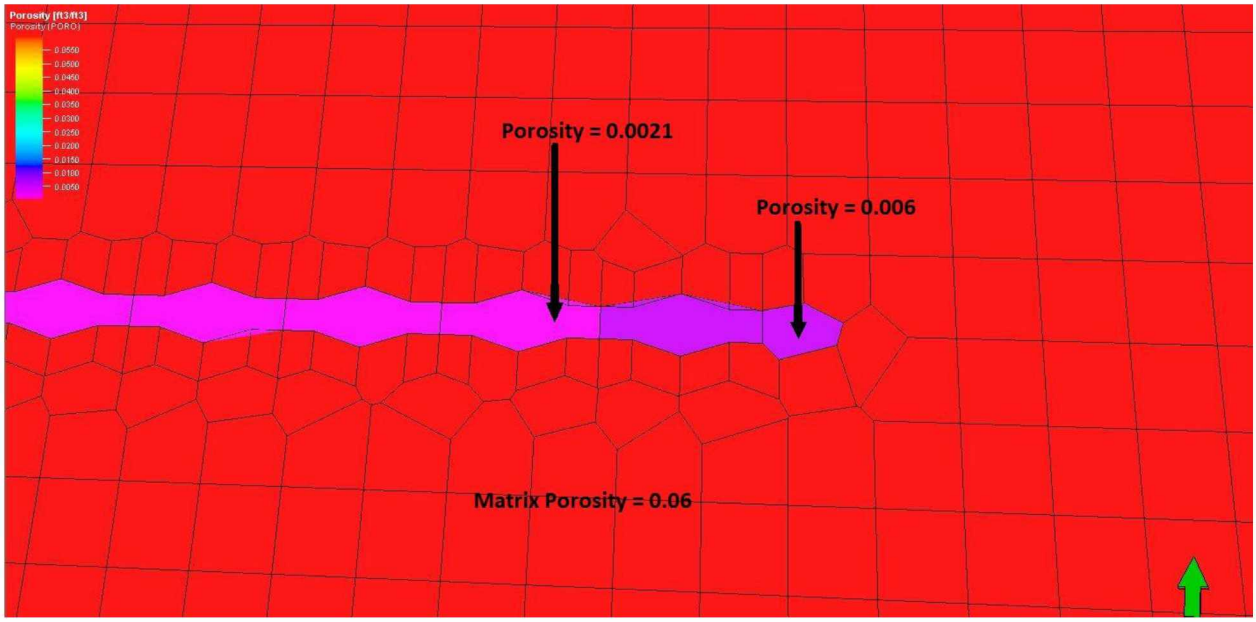

Figure 21: Porosity

3.2.2 Model II

Since the resulting fractures were smaller than a single fracture due to much smaller treatment volume for each fracture, new zone set polygon for smaller SRV was constructed using the same methodology as in Model I (Figure 22 and Figure 23).

Figures 24 and 25 show top and side views of the single hydraulic fracture model built using Petrel, Mangrove and Intersect. Note that fracture spacing and formation thickness are the same length – 200 ft – however they are displayed 1:5 default ratio in Petrel. The grid dimensions are determined based on the fracture as following: fracture spacing*$2X_f$*thickness which adds up to be 200 ft*619.32 ft*200 ft – total bulk volume of 247728000 ft^3. Pore volume of this model is 2941964 RB. Average porosity is 0.0596.

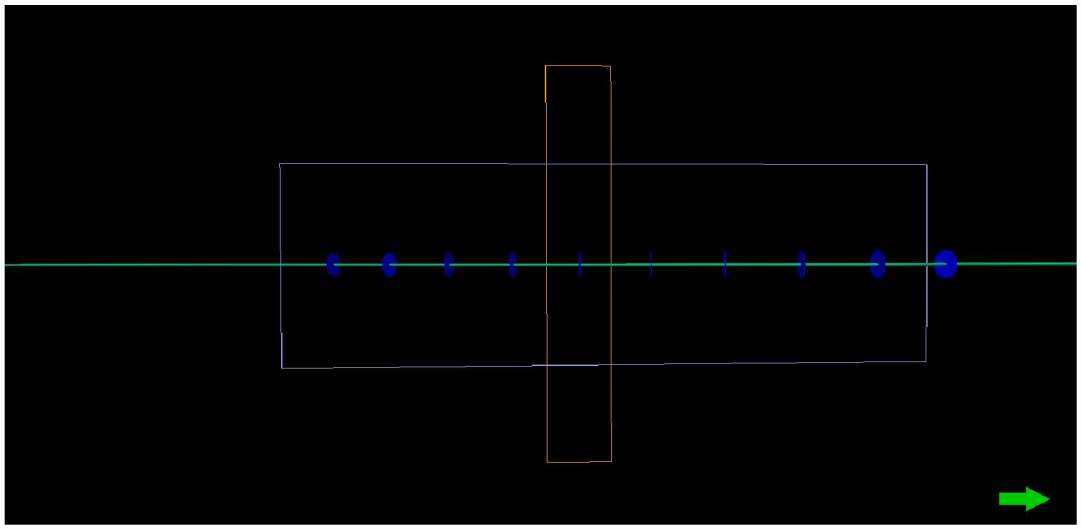

Figure 22: Simulated zone set polygons - top view

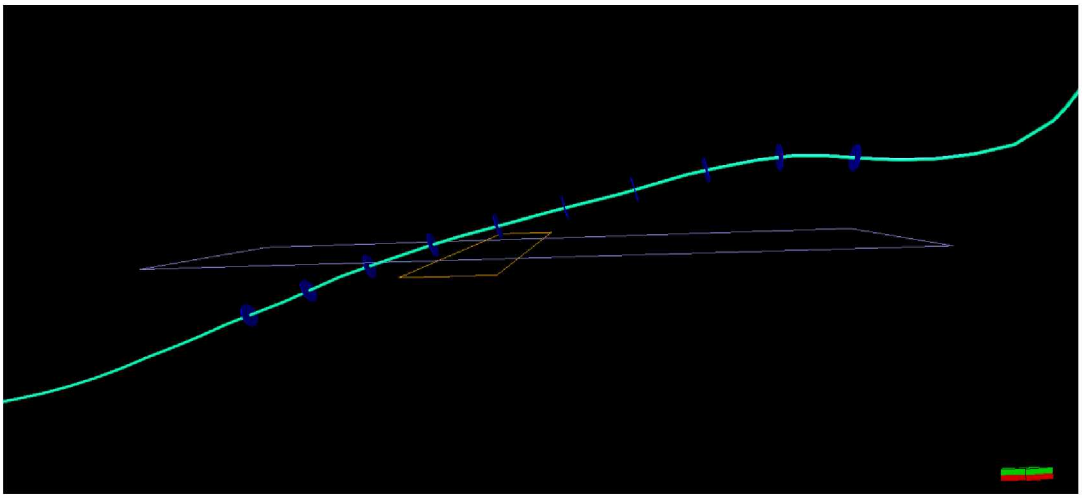

Figure 23: Simulated zoneset polygons - side view

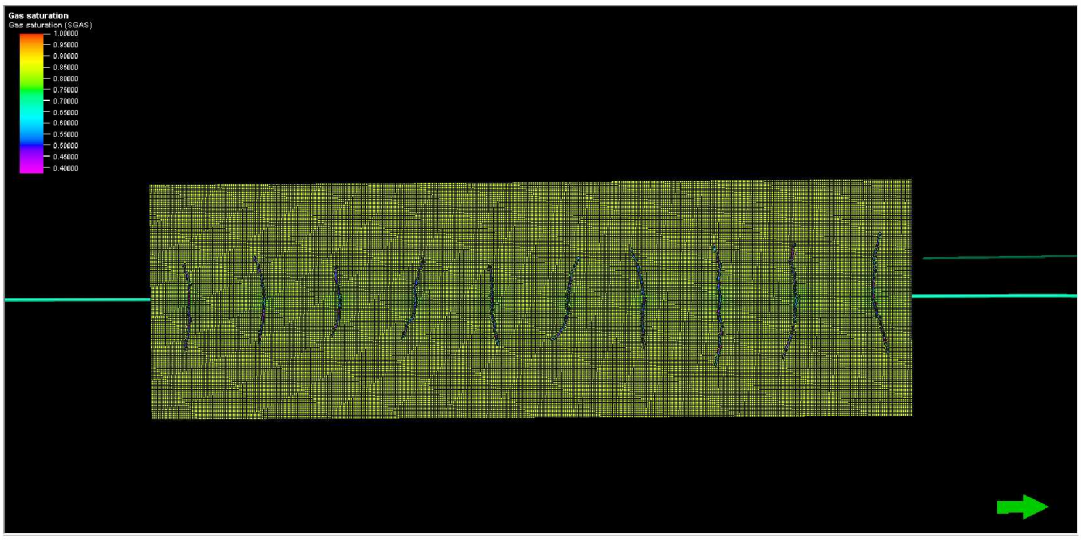

Figure 24: Top view Model II (Base Case)

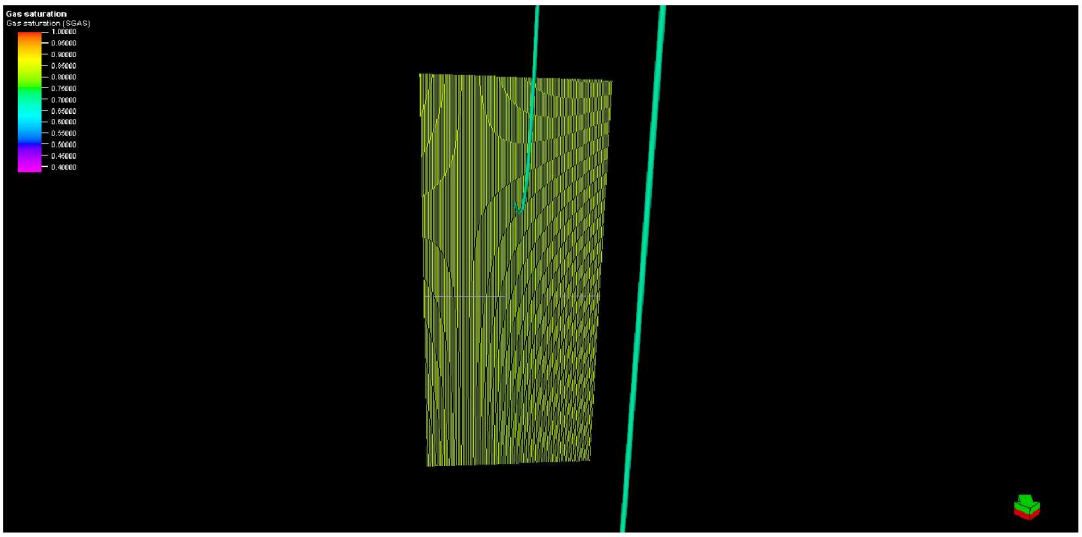

Figure 25: Side view Model II (Base Case)

3.2.3 Fluid Model

Black oil fluid model was used in this study. Table 11 lists the values for the fluid model. Figures 26 and 27 display gas formation factor and gas viscosity plots used in this model.

Table 11: Fluid model parameters

Gas Gravity	0.64	
Water Salinity	20000	ppm
Reservoir Pressure	8594	psia
Water Contact depth	-13000	ft
Datum	-11257.4	ft
Minimum pressure	14.7	psia
Maximum pressure	9205.0	psia

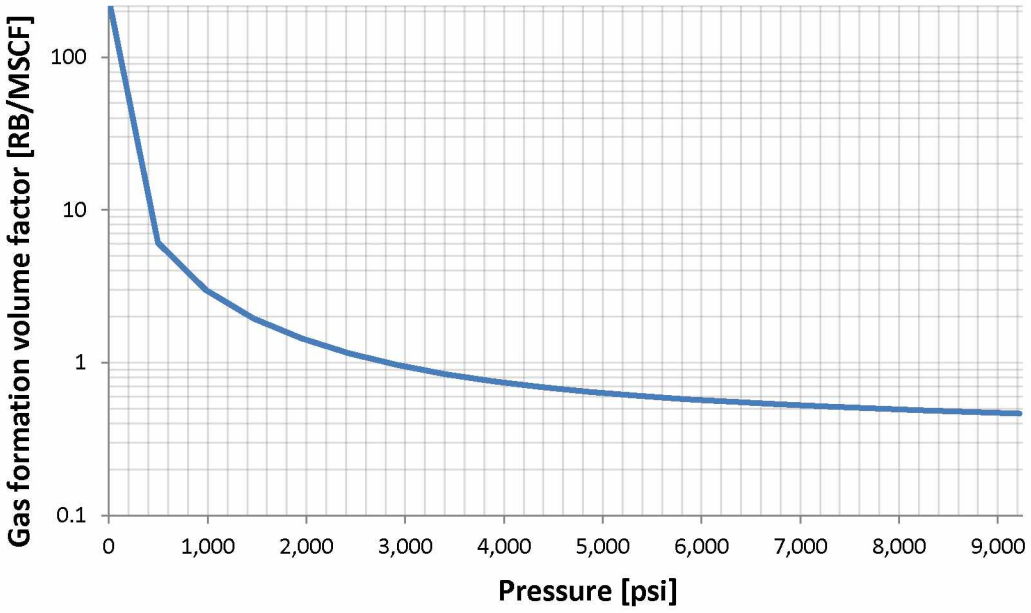

Figure 26: Gas formation factor

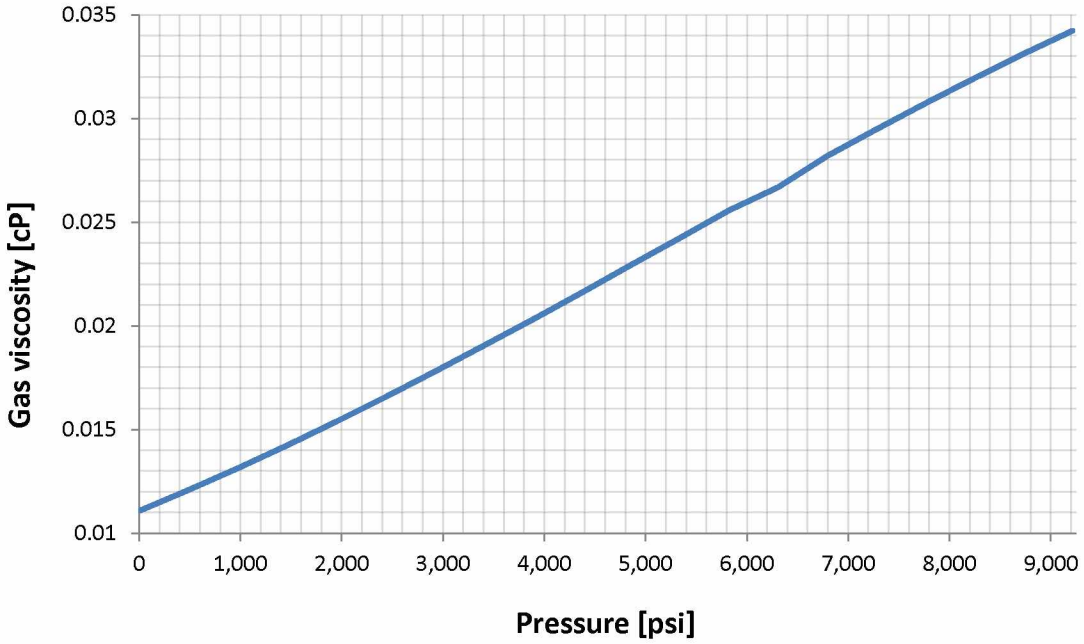

Figure 27: Gas viscosity

3.2.4 Relative Permeability Curves

Relative permeability curves used in the simulations of matrix and fracture are generated using the Corey Model (1954) for gas-water system (Equation 7 and Equation 8). Table 12 lists values for matrix relative permeability curves. Due to the absence of the core data and end points model for a dry gas shale Eagle ford model, relative permeability end points were assigned based on Inamdar et al. (2010) (Figure 28).

$$k_{rg} = \left[\frac{S_g}{1 - S_{iw}}\right]^{Ng} \left[1 - \left(\frac{1 - S_g - S_{iw}}{1 - S_{iw}}\right)^2\right] \quad (7)$$

$$k_{rw} = \left[\frac{S_w - S_{iw}}{1 - S_{iw}}\right]^{Nw} \quad (8)$$

Where k_{rg} is gas relative permeability at minimum water saturation; S_g is gas saturation; S_{iw} is initial water saturation; k_{rw} is water relative permeability at residual gas and S_w is water saturation.

In the fracture model, relative permeability curves approach the straight-line form assumed in many reservoir simulators due to large values of dimensionless parameter H_D, which quantifies the extent of gravity segregation and is described by:

$$H_D = \frac{\Delta\rho g H}{(\frac{\gamma}{b_O})} \tag{9}$$

Where $\Delta\rho$ is density difference between phases, g is gravitational acceleration, H is fracture height, γ is interfacial tension and b_O is mean half-aperture of the fracture (Rossen and Kumar, 1994) (Figure 29).

Table 12: Relative permeability curves for the matrix (Base Case)

Matrix relative permeability curves		
Connate water	S_{wcr}	0.16
Critical gas	S_{gcr}	0.05
Minimum water saturation	S_{wmin}	0.16
Gas relative permeability	K_{rg} at S_{wmin}	0.84
Gas relative permeability	K_{rg} at S_{orw}	1
Water relative permeability	K_{rw} at S_w=1	1
Corey gas exponent	N_g	2
Corey water exponent	N_w	4

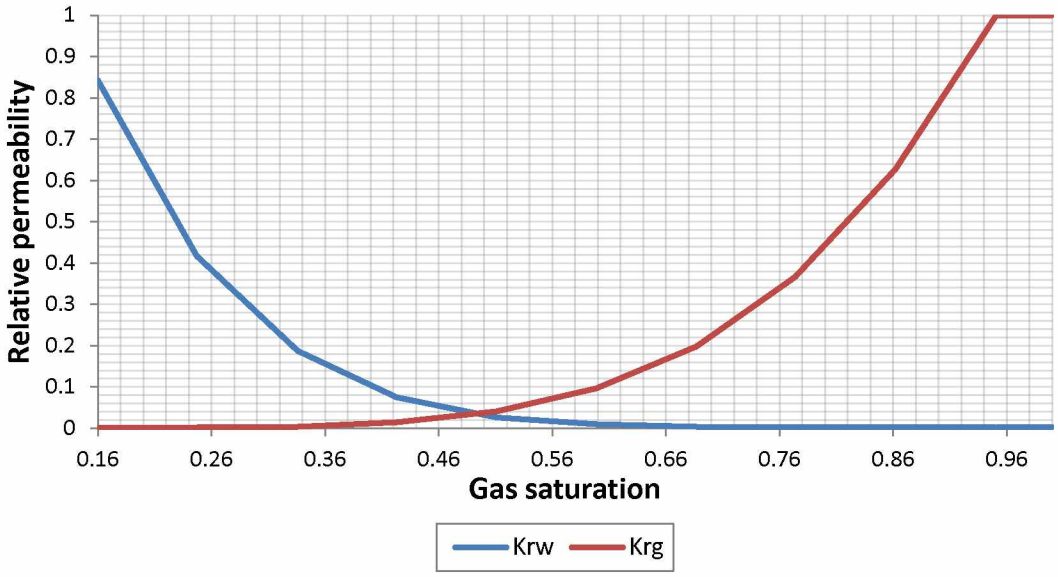

Figure 28: Relative permeability curves for the matrix

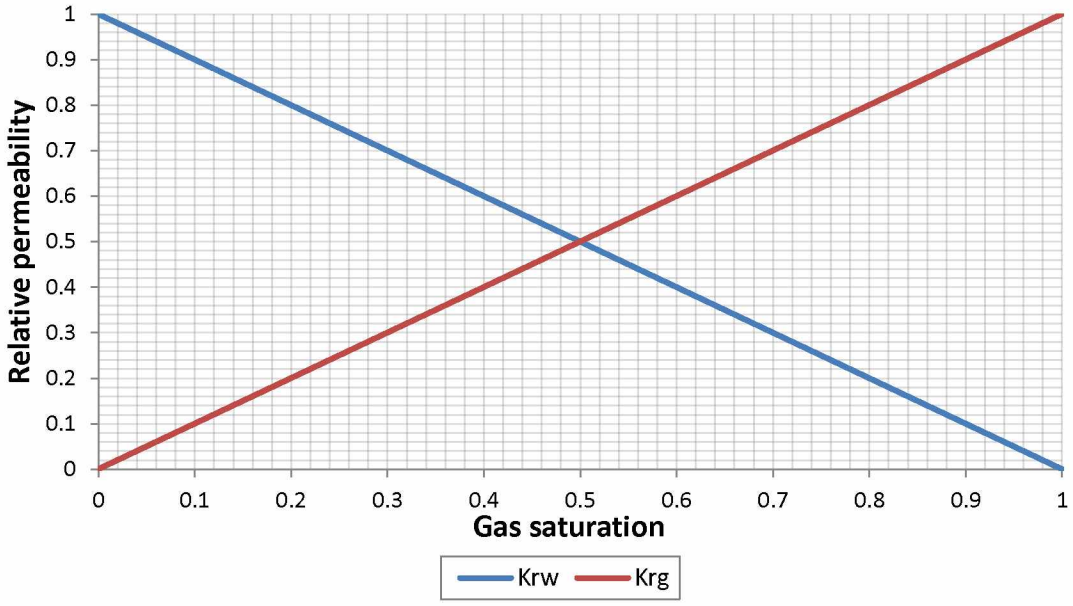

Figure 29: Relative permeability curves for the fracture

3.2.5 Rock Compaction Functions

Reservoir pressure decrease during depletion can result in rock and proppant compaction, which can reduce matrix and fracture permeability (Warpinski, 2009). Figures 30-32 display rock compaction function plots used in the simulation. Tm stands for transmissibility multiplier and Pm stands for pore volume multiplier. Mangrove calculated the functions based on rock type and region (matrix, unpropped, CarboLite20/40). Transmissibility multiplier is held constant since there are no faults present in the model.

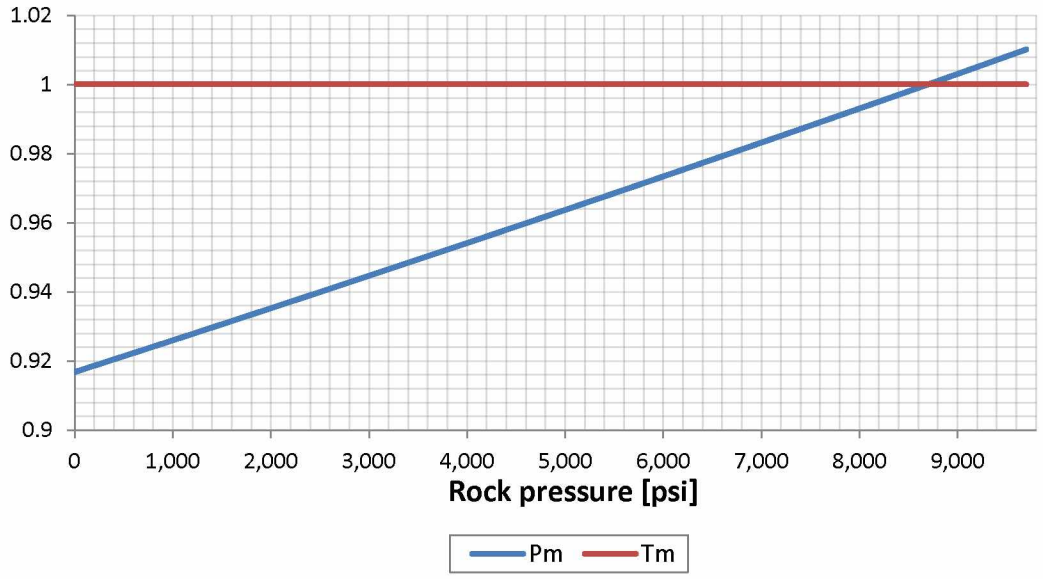

Figure 30: Rock compaction function plot for the matrix

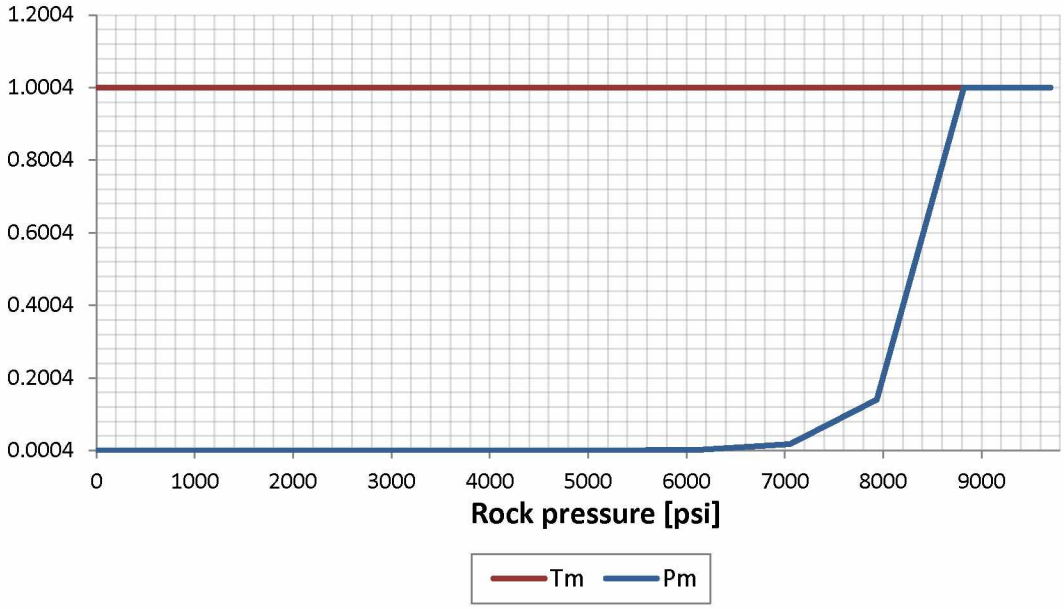

Figure 31: Rock compaction function plot for the unpropped fracture

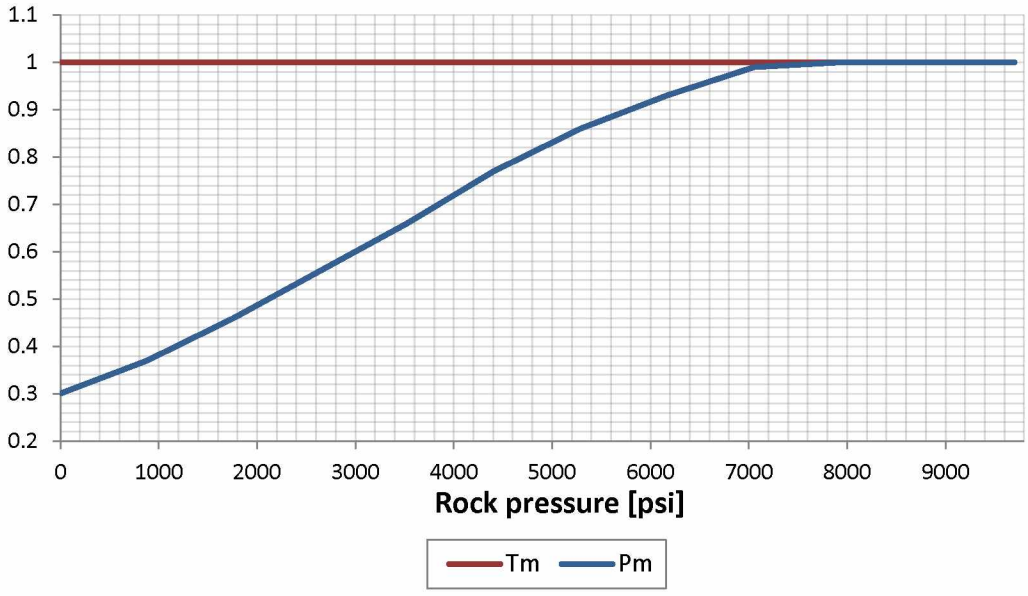

Figure 32: Rock compaction function plot for hydraulic fracture (CarboLite 20/40)

3.3 Model Description With Included Discrete Fracture Network (DFN).

Separate models had to be constructed to investigate the effects of natural fractures. Due to the absence of microseismic data, artificial DFN profiles were created. First, the profiles for varied DFN orientation (0 and 45 degrees with respect to wellbore), DFN natural fracture spacing (1, 10 and 100 ft) and DFN length (25, 50 and 75 ft) for the single fracture model (Model I) were created. DFN orientation of 90 degrees was omitted, since it recreated the base case – planar model. Then the same DFN profiles were created for the model with 10 fractures (Model II).

3.3.1 Effects of DFN orientation

Two natural fracture sets were built for this case – 45 degrees and 0 degrees. DFN orientation of 0 degrees is parallel to the wellbore. The fracture set of 90 degrees resulted in the same planar fracture and was omitted in this study. DFN fracture spacing and DFN length for this study was set at 10 ft and 50 ft, respectively. Standard deviation for all parameters was set to zero to more accurately examine geometry effects.

3.3.1.1 Model I

Figure 33 shows DFN orientation of 0 and 45 degrees for Model I.

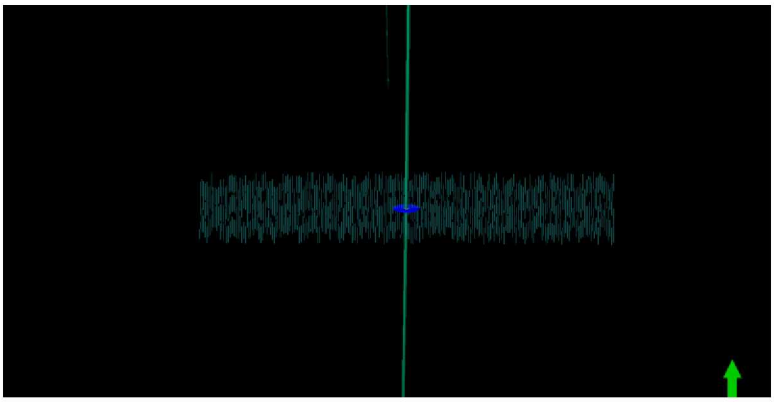

(a) 0 degrees

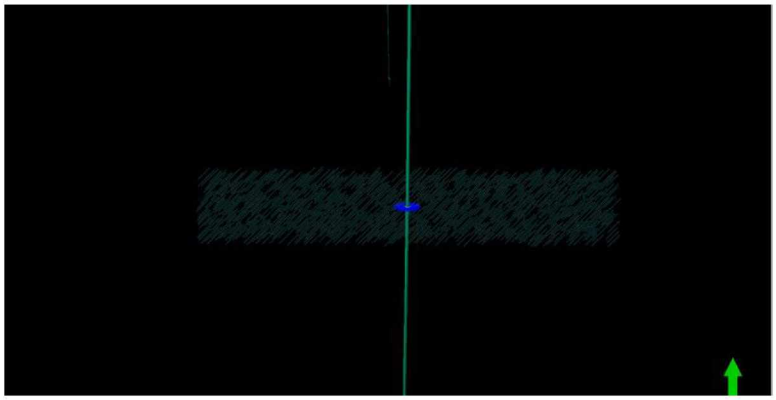

(b) 45 degrees

Figure 33: DFN profile for varied orientation (Model I)

Figure 34 shows resulting fracture network for assigned DFN profiles. The fractures stayed within the shale zone in both cases; proppant settlement is present. The fracture did not propagate as far in the case of the orientation of 0 degrees than in the case of 45 degrees because they were terminated by DFN. In this case DFN of 45 provided the largest fracture area, but the Base Case has the largest propped fracture area. Base Case has a planar fracture due to absence of natural fractures - a planar crack penetrated by a well or propagated from a well by hydraulic fracturing with nonzero pressure drop in the fracture during production (Schlumberger Oilfield Glossary). The larger propped fracture area could be due to the uncertainty of using DFN, proppant size and low fracturing fluid viscosity.

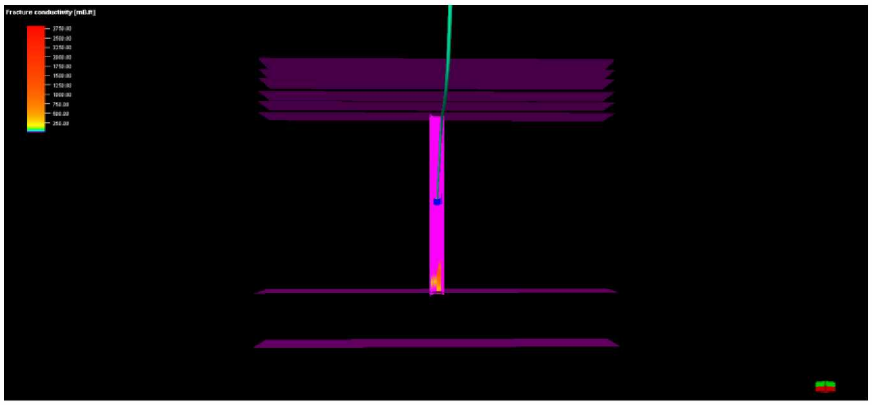

(a) 0 degrees

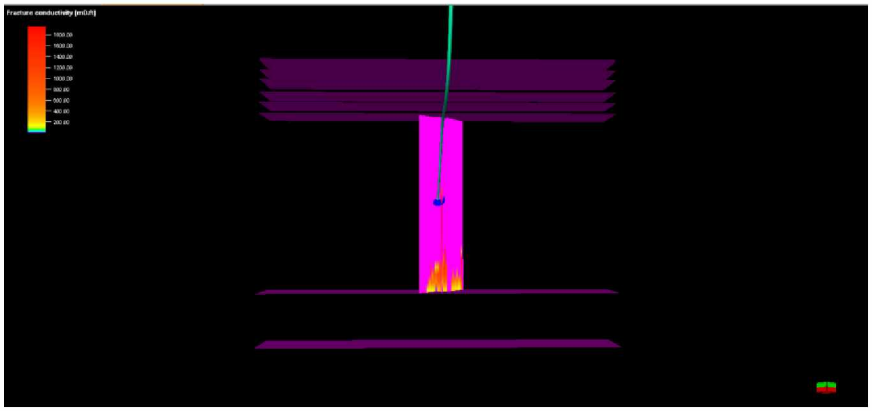

(b) 45 degrees

Figure 34: Conductivity profile for varied DFN orientation [mD-ft] (Model I)

In case of DFN, the natural fracture systems are stochastically generated, so there is some built in randomness in the DFN generated. Even for the same average parameters (length, spacing and orientation) and with standard deviation set to zero, two realizations of the DFN generated will not have identical natural structures. For each realization of DFN, the fracture geometry is unique, which results in slightly different hydraulic fracture network each time. As a consequence, the predicted fracture network geometry for each set of average DFN has certain uncertainty.

Another cause of possible uncertainty is the proppant size. Very large proppant size 20/40 is used in this study. If proppant size is large relative to the fracture width, (fracture width/ proppant diameter >2.5) it would bridge. The bridging would add an uncertainty to the results. Also, for low viscosity fluid, the proppant tends to settle to the bottom, which may cause the proppant bank to lose connection with perforations and hence have little contribution of the fracture to production.

Figure 35 displays top view of the resulted grid constructed using Base Case zoneset polygon for given DFN orientation. Fracture network in both cases initiates in the direction of the minimum horizontal stress, but then propagates in the same direction as DFN.

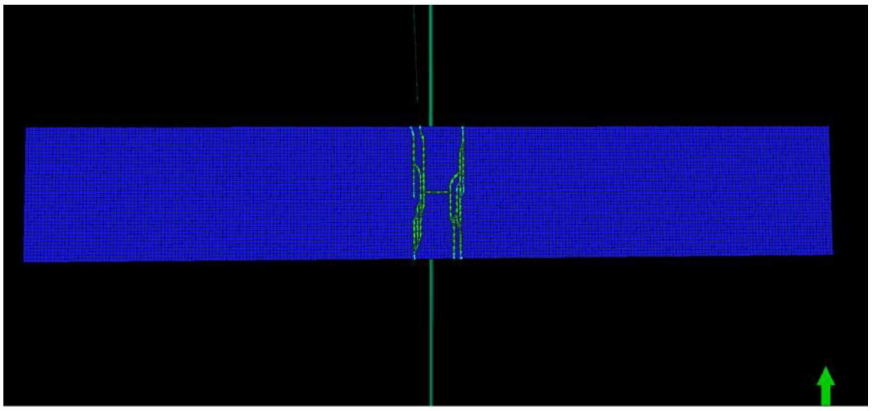

(a) DFN 0 degrees

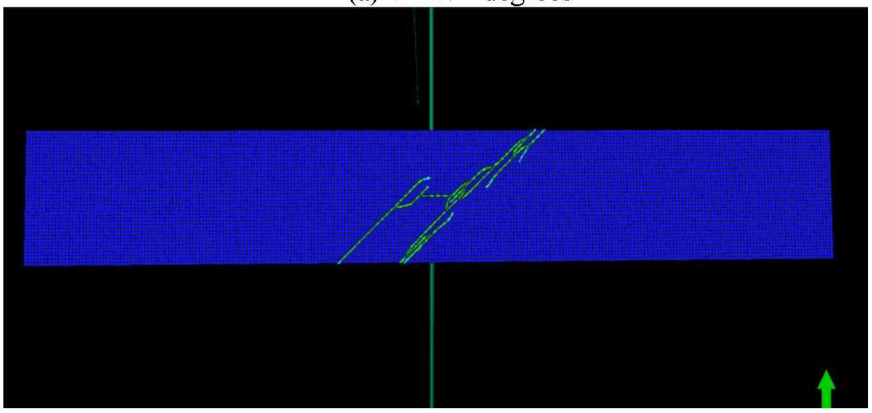

(b) DFN 45 degrees

Figure 35: Top view for models with varied DFN orientation (Model I)

Hydraulic fracture parameters for the fracture network in this case are listed in Table 13. All terminology is defined in Appendix B.

Table 13: Hydraulic fracture results for varied orienation (Model I)

Hydraulic fracture results for varied DFN orientation (Model I)			
	Base Case (Planar)	0 degrees	45 degrees
Total fracture volume [ft^3]	2081	1026	1106
Total fracture surface area [ft^2]	211478.6	228605	239225.8
Maximum surface pressure [psi]	12433	12313	12317
Total leak-off volume [ft^3]	1013	1302	1221
Total propped fracture surface area [ft^2]	59149.52	190237	195619
Maximum BH pressure [psi]	14217	14108	14105
Efficiency [%]	89.4	44.1	47.5
Hydraulic fracture geometry			
Final extension of HFN in the direction of max stress [ft]	813.0	76.8	309.2
Final extension of HFN in the direction of min stress [ft]	0	195.1	197.9
Maximum fracture height [ft]	258.3	212.5	212.5
Total fracture surface area [ft^2]	211478.6	228605	239225.8
Fracture width at wellbore [in]	0.21	0.26	0.26
Average fracture width [in]	0.12	0.05	0.06
Total fracture volume [ft^3]	2078	1034	1102
Total leak-off volume [ft^3]	1013	1302	1221
Propped fracture geometry			
Final extension of HFN in the direction of maximum stress [ft]	689.0	75.0	285.1
Final extension of HFN in the direction of minimum stress [ft]	0	189.9	189.7
Total propped fracture surface area [ft^3]	58555.9	185281.3	195619
Average propped fracture height [ft]	83.8	196.0	196.1
Fracture width at wellbore [in]	0.10	0.04	0.03
Average fracture width [in]	0.02	4.90E-003	4.49E-003
Average fracture conductivity [mD.ft]	110.8	46.3	39.8

3.3.1.2 Model II

Figure 36 displays DFN fracture network for orientations of 0 and 45 degrees populated using Model II zoneset polygon.

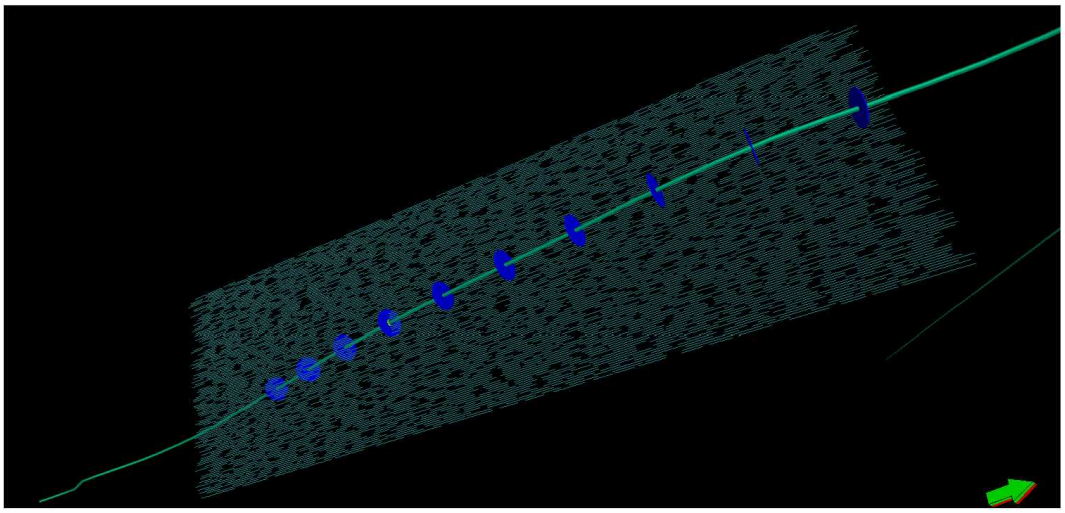

(a) DFN orientation 0 degrees

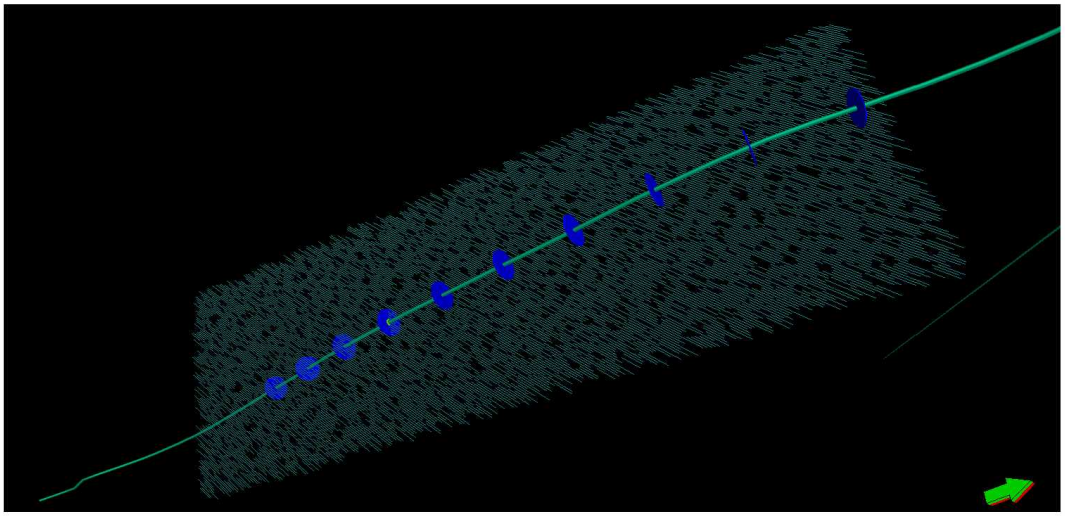

(b) DFN orientation 45 degrees

Figure 36: DFN profile for varied orientation (Model II)

Figure 37 displays resulted fracture network propagation for varied DFN orientation of 0 and 45 degrees. Fracture network stayed within the shale zone. DFN of 0 degrees resulted in the largest total fracture area; however, the Base Case Model II had the largest propped fracture area as Base Case Model I.

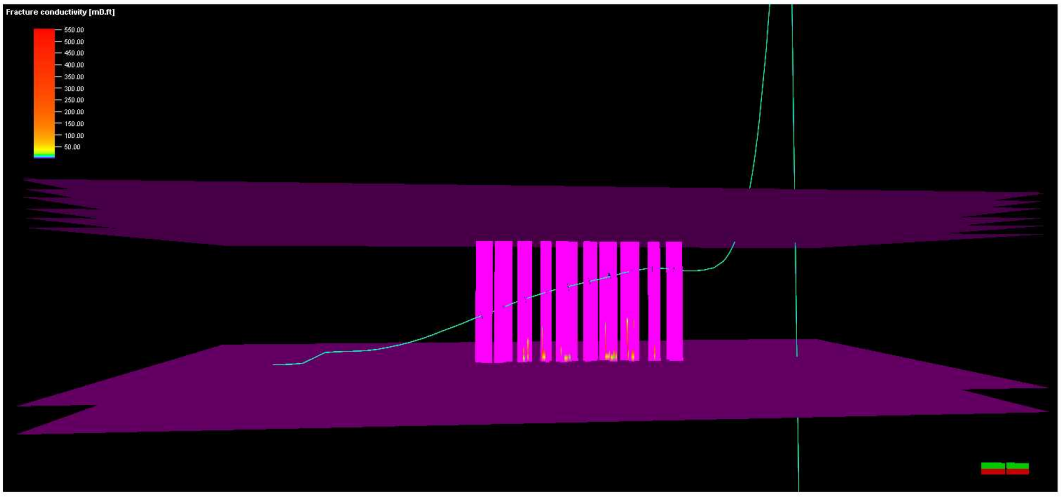

(a) DFN orientation 0 degrees

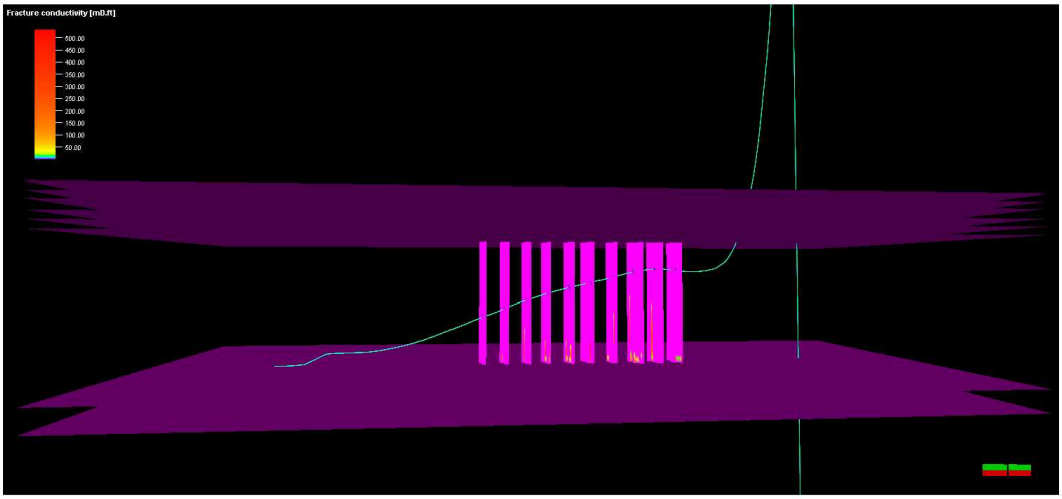

(b) DFN orientation 0 degrees

Figure 37: Conductivity profile for varied DFN orientation [mD-ft] (Model II)

Figure 38 displays top view for different DFN fracture sets. Resulting fracture propagation mimicked the orientation of DFN.

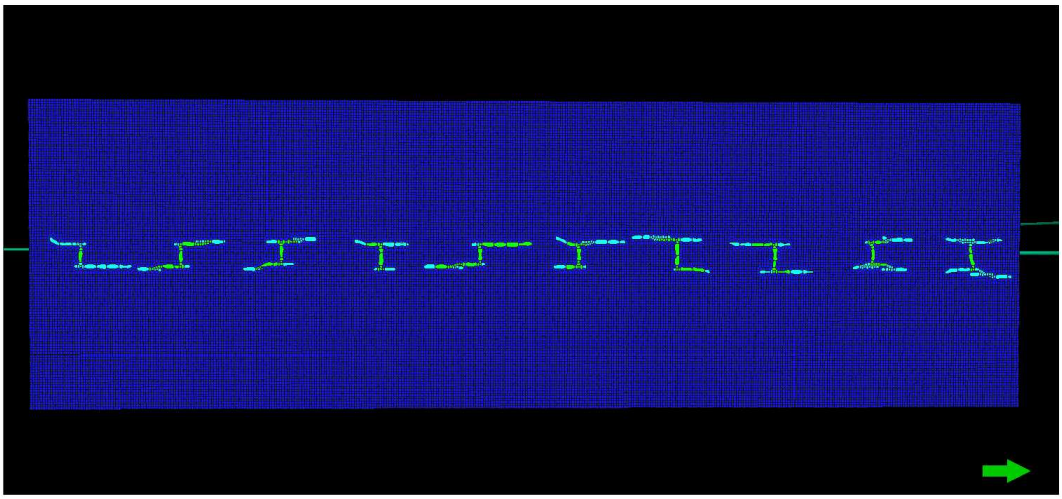

(a) DFN orientation 0 degrees

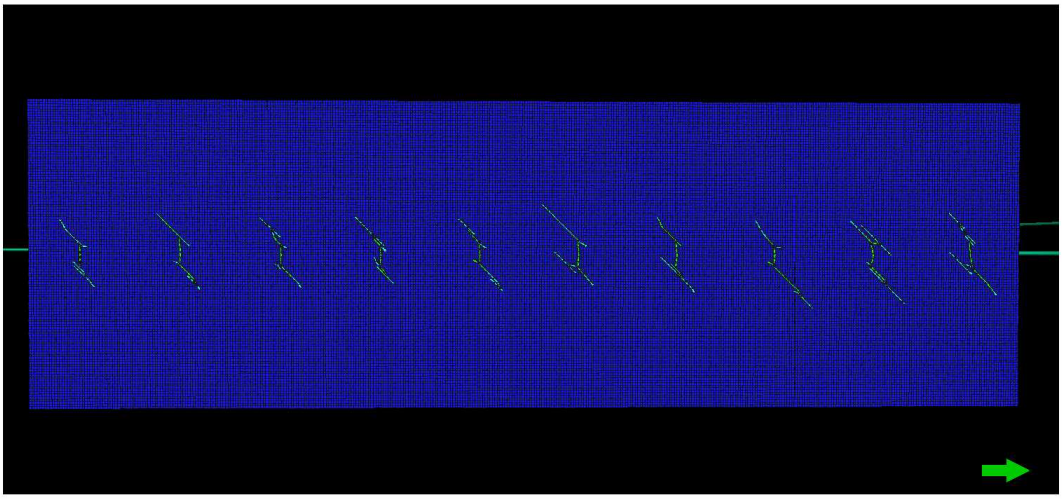

(b) DFN orientation 45 degrees

Figure 38: Top view for models with varied DFN orientation (Model II)

Table 14 displays hydraulic fracture results for varied DFN orientation. All definitions are listed in Appendix B. The Base Case model has the largest final extension of Hydraulic Fracture Network (HFN) in the direction of maximum stress due to absence of natural fractures. The largest fracture area ensures the highest leak-off since the fracturing fluid leak-off is correlated to the fracture length and width (Mikhailov et al., 2011).

Table 14: Hydraulic fracture results for varied DFN orientation (Model II)

Hydraulic fracture results for varied DFN orientation (Model II)			
	Planar	0 degrees	45 degrees
Total fracture volume [ft^3]	1352	1266	1269
Total fracture surface area [ft^2]	581291.0	631681.2	624122.7
Maximum surface pressure [psi]	7597	7595	7601
Total leak-off volume [ft^3]	976	1062	1059
Total propped fracture surface area [ft^2]	40407.4	32542.8	31551.2
Maximum BH pressure [psi]	9367	9369	9367
Efficiency [%]	58.08	54.39	54.52
Hydraulic fracture geometry			
Final extension of HFN in the direction of max stress [ft]	309.66	76.02	165.23
Final extension of HFN in the direction of min stress [ft]	39.1	127.1	96.7
Maximum fracture height [ft]	225.9	224.0	225.0
Total fracture surface area [ft^2]	73520.1	86334.4	77864.7
Fracture width at wellbore [in]	0.07	0.08	0.07
Average fracture width [in]	0.03	0.02	0.03
Total fracture volume [ft^3]	193	157	165
Total leak-off volume [ft^3]	123	131	128
Propped fracture geometry			
Final extension of HFN in the direction of maximum stress [ft]	247.5	39.8	92.1
Final extension of HFN in the direction of minimum stress [ft]	23.6	19.0	48.1
Total propped fracture surface area [ft^3]	5190.5	4898.3	4836.2
Average propped fracture height [ft]	19.5	66.4	39.4
Fracture width at wellbore [in]	0.03	0.04	0.04
Average fracture width [in]	0.03	0.03	0.03
Average fracture conductivity [mD.ft]	36.5	140.0	26

3.3.2 Effects of DFN Fracture Spacing

In order to investigate the effects of DFN fracture spacing on gas recovery factor, three profiles for DFN were selected: 1 ft, 10 ft and 100 ft. Hydraulic spacing is important since small natural fracture spacing can terminate the propagation of a hydraulic fracture in horizontal direction and encourage its growth out of the boundary zone set. In addition an uncertainty increases if DFN has spacing much greater than length since there is a lot of void space between adjacent fractures. Whether a hydraulic fracture hits or misses a natural fracture, causes significant difference in the resulting hydraulic fracture network. DFN orientation and DFN length for this set was set at 0 degrees and 50 ft respectively. Standard deviation for all parameters was set to zero to more accurately examine geometry effects.

3.3.2.1 Model I

Figure 39 displays DFN with varied fracture spacing.

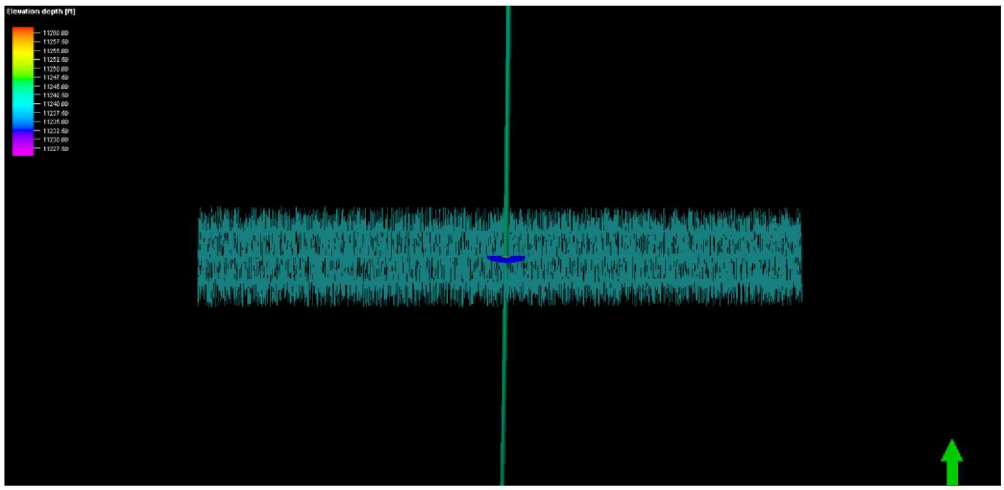

(a) Fracture spacing 1 ft

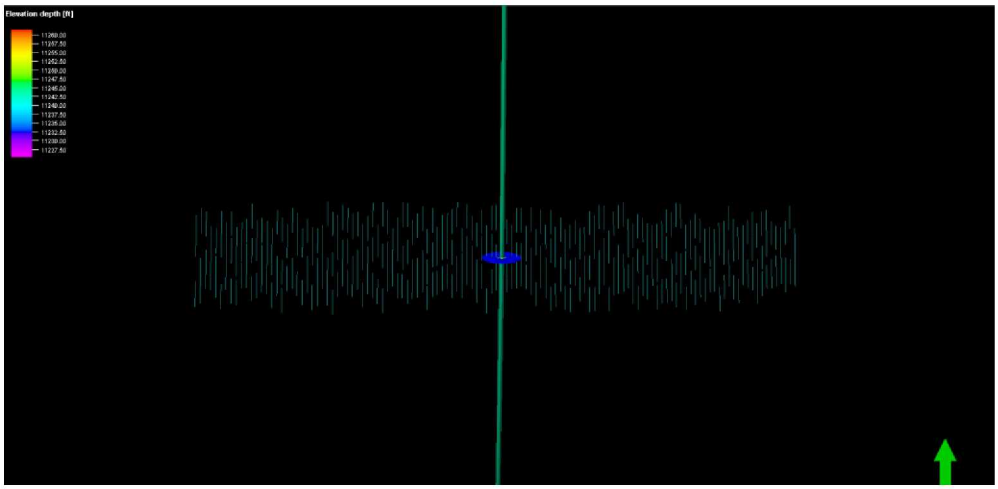

(b) Fracture spacing 10 ft

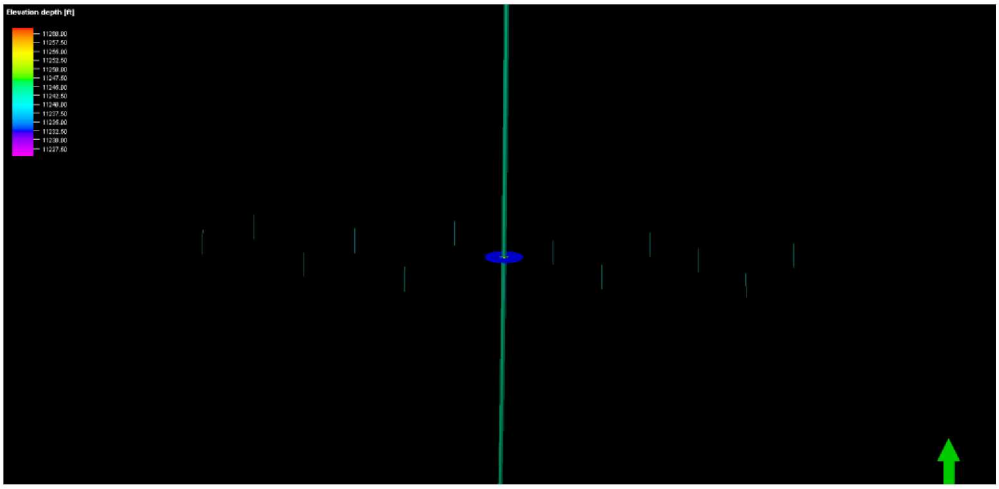

(c) Fracture spacing 100 ft

Figure 39: DFN profile for varied fracture spacing (Model I)

Figure 40 displays resulting fracture propagation for given DFN fracture spacing profiles. Fracture spacing of 10 ft yield the largest total fracture area, largest propped fracture area and the highest resulting average conductivity.

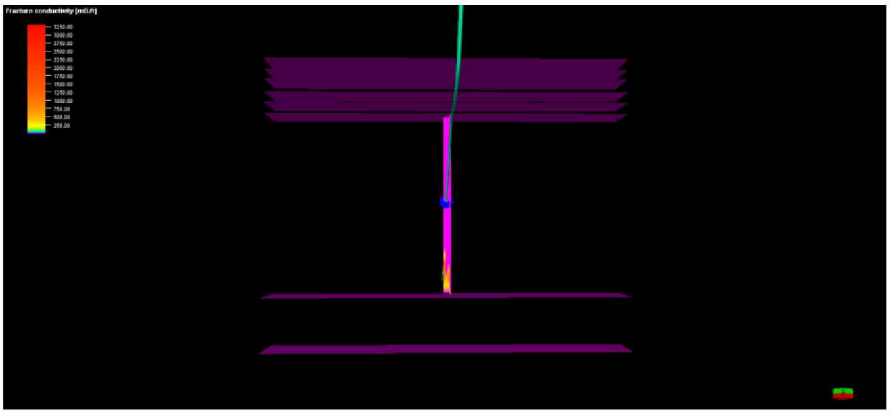

(a) Fracture spacing 1 ft

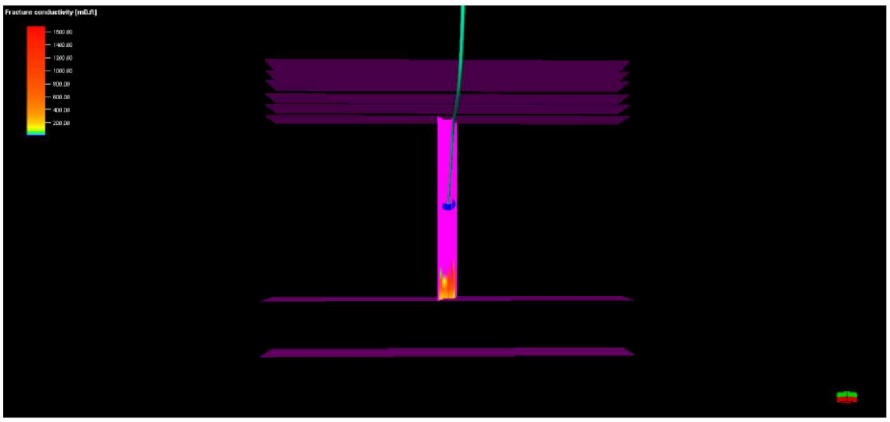

(b) Fracture spacing 10 ft

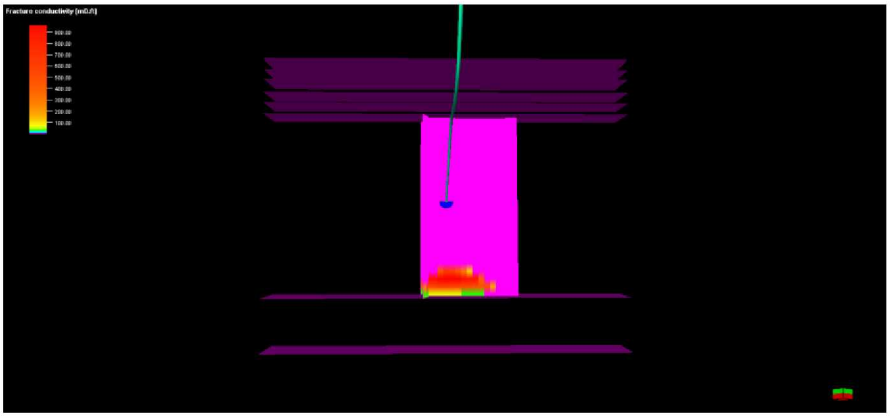

(c) Fracture spacing 100 ft

Figure 40: Conductivity profile for varied DFN fracture spacing [mD-ft] (Model I)

Figure 41 displays the top view for varied DFN fracture set. DFN fracture spacing of 100 ft results in the largest propagation of the fracture network due to low density.

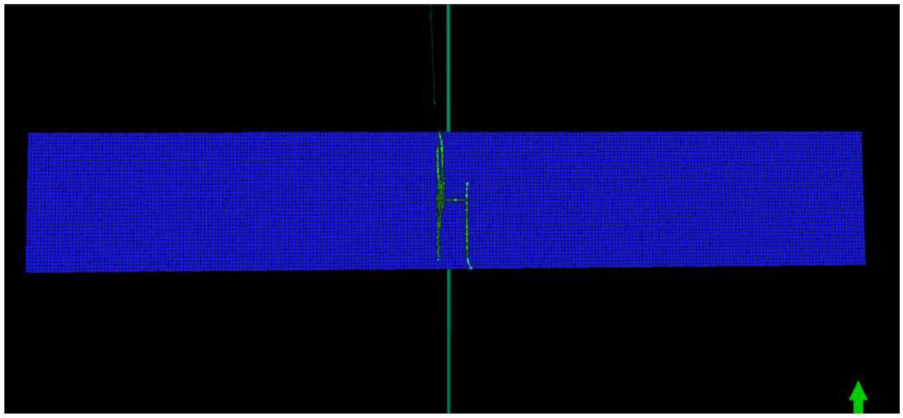

(a) Fracture spacing 1 ft

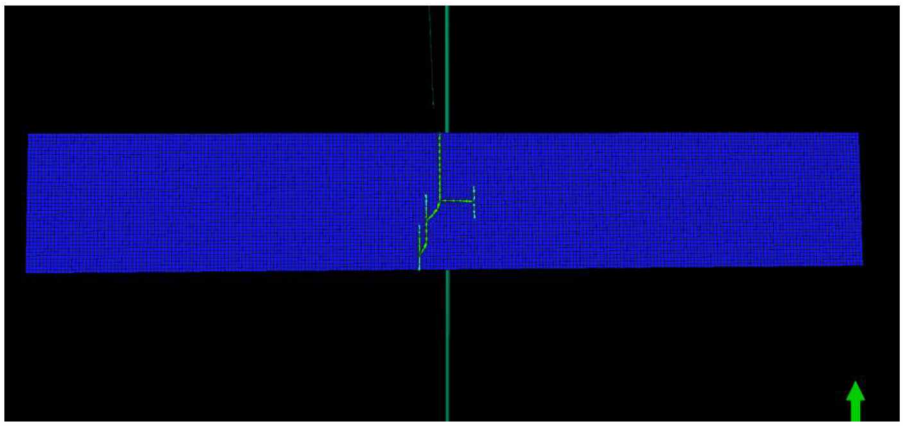

(b) Fracture spacing 10 ft

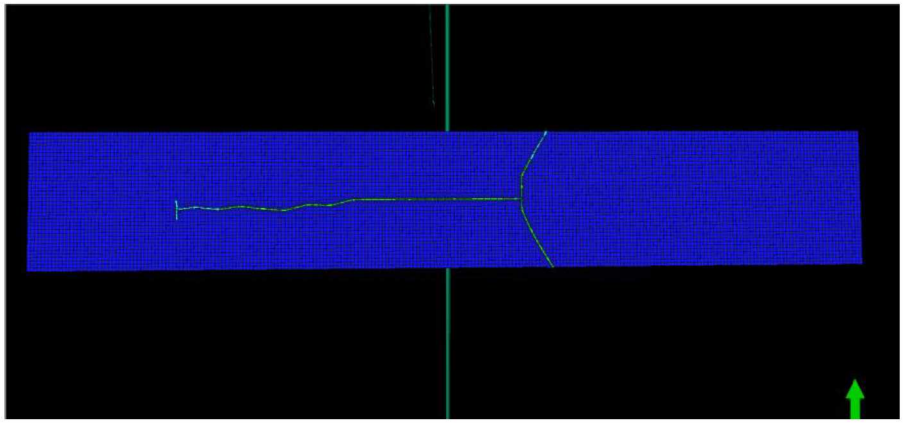

(c) Fracture spacing 100 ft

Figure 41: Top view for models with varied DFN fracture spacing (Model I)

Table 15 shows the fracture propagation results for the given set. DFN with a fracture set of 10 ft has the highest leak-off since it is the most optimal DFN length selection. The leak-off can be characterized by several parameters including the fluid path for the fracture fluid to travel, the stress concentration at the fracture tips and uncertainty. In order for the hydraulic fracture to propagate into the natural fractures and create a fracture network, natural fractures have to have enough stress concentration at its tips. In the case of the fracture spacing of 1 ft, there is not a lot of stress concentration at the natural fracture tips. In the case of the fracture of 100 ft, the stress concentration at the fracture tips is high. However, the path for the fracture fluid is much smaller due to large natural fracture spacing. Hence, the fracture spacing of 10 ft has enough stress concentration at the natural fracture tips in order for the hydraulic fracture to travel and sufficient enough fluid path for the fracture fluid to travel. Hence the DFN length of 10 ft has the highest leak-off and the highest fracture area. Ultimately the higher the fracture surface area, the higher is a leak-off (Mikhailov et al., 2011).

Table 15: Hydraulic fracture results for varied DFN fracture spacing (Model I)

Hydraulic fracture results for varied DFN fracture spacing (Model I)				
	Planar	1 ft	10 ft	100 ft
Total fracture volume [ft^3]	2081	1340	1145	1306
Total fracture surface area [ft^2]	211478.6	167678.0	243543.2	196050.5
Maximum surface pressure [psi]	12433	12315	12304	12327
Total leak-off volume [ft^3]	1013	987	1183	1022
Total propped fracture surface area [ft^2]	59149.5	133872.9	161700.8	165116.2
Maximum BH pressure [psi]	14217	14102	14096	14112
Efficiency [%]	89.4	57.6	49.2	56.1
Hydraulic fracture geometry				
Final extension of HFN in the direction of max stress [ft]	813.0	41.2	132.8	558.0
Final extension of HFN in the direction of min stress [ft]	0	189.5	196.7	198.9
Maximum fracture height [ft]	258.3	212.5	212.5	212.5
Total fracture surface area [ft^2]	211478.6	167678.0	243543.2	196050.6
Fracture width at wellbore [in]	0.21	0.06	0.28	0.25
Average fracture width [in]	0.12	0.1	0.06	0.08
Total fracture volume [ft^3]	2078	132	1124	1240
Total leak-off volume [ft^3]	1013	987	1183	1022
Propped fracture geometry				
Final extension of HFN in the direction of maximum stress [ft]	689.0	40	122.7	524.9
Final extension of HFN in the direction of minimum stress [ft]	0	169.7	189.3	141.0
Total propped fracture surface area [ft^3]	58555.9	132799.7	159888.2	158842.0
Average propped fracture height [ft]	83.8	189.5	193.6	207.8
Fracture width at wellbore [in]	0.10	7.77E-003	0.05	0.11
Average fracture width [in]	0.02	5.74E-003	5.89E-003	5.65E-003
Average fracture conductivity [mD.ft]	110.8	62.3	64.0	60.7

3.3.2.2 Model II

Figure 42 displays DFN fracture spacing sets for zoneset polygon used in Model II.

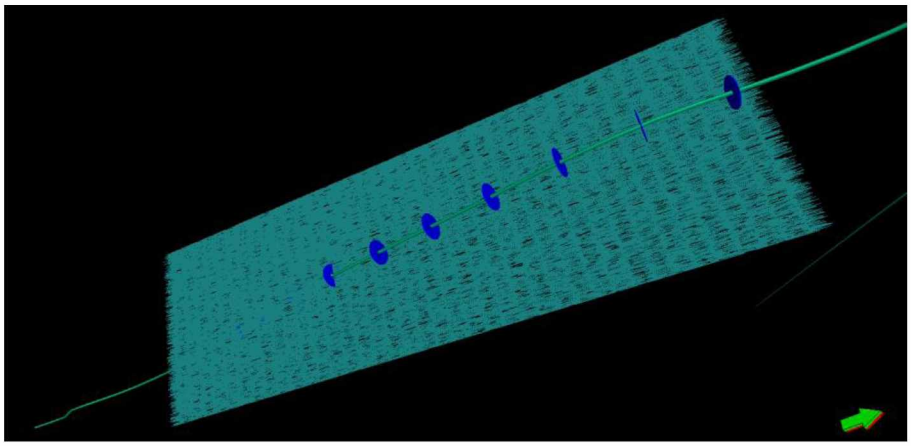

(a) DFN fracture spacing 1 ft

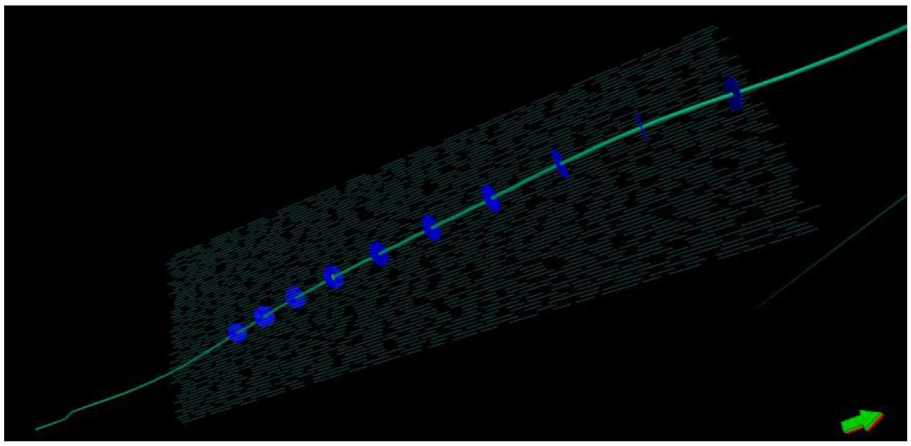

(b) DFN fracture spacing 10 ft

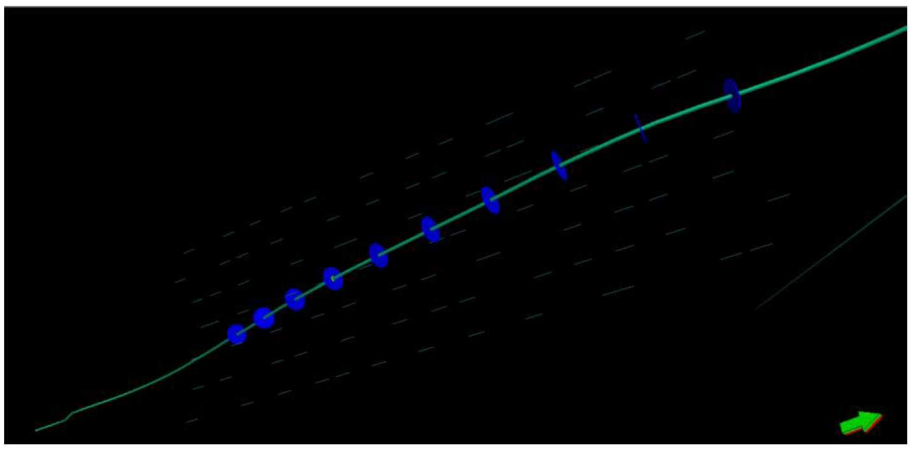

(c) DFN fracture spacing 100 ft

Figure 42: DFN profile for varied fracture spacing (Model II)

Figure 43 displays resulting fracture propagation profiles. DFN spacing resulted in the highest total fracture area, and Base Case resulted in the highest propped fracture area. However, DFN fracture spacing of 10 ft resulted in highest conductivity. This phenomena occurred since grid cells vary in size and hence conductivity for each case. Few small cells with very high conductivity could offset the values for the average conductivity.

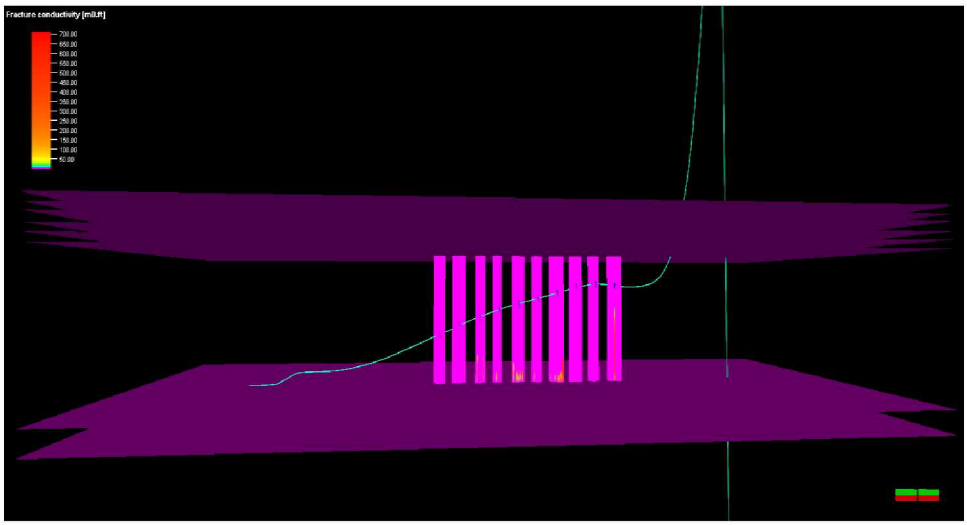

(a) DFN fracture spacing 1 ft

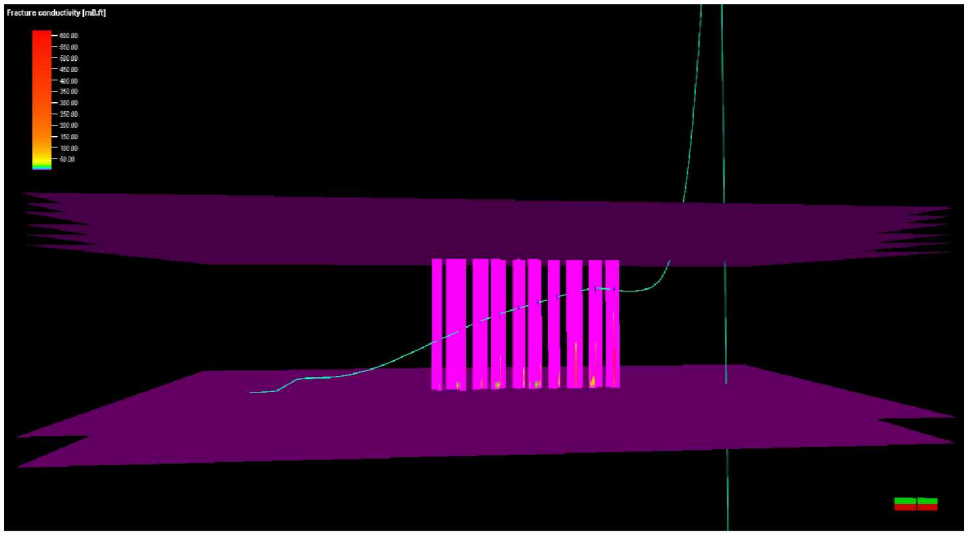

(b) DFN fracture spacing 10 ft

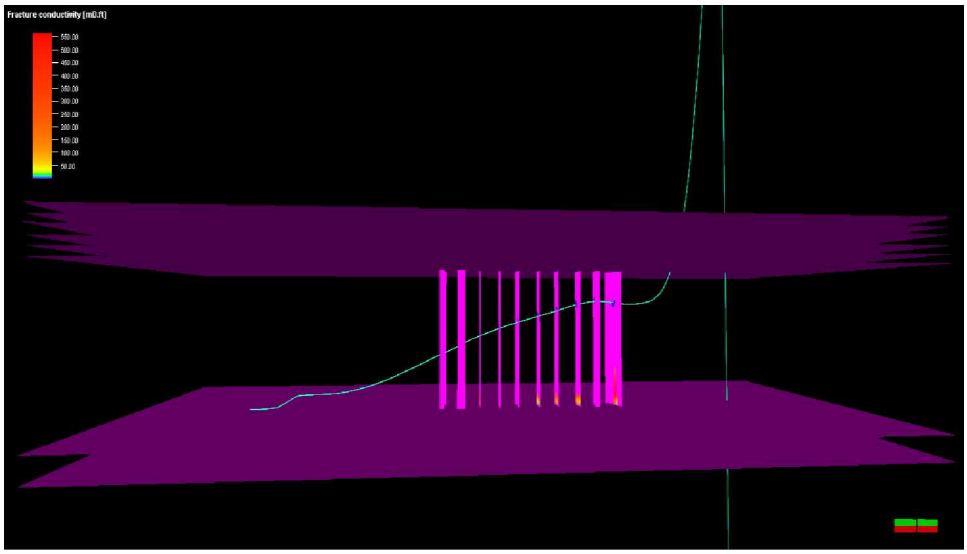

(d) DFN fracture spacing 100 ft

Figure 43: Conductivity profile for DFN fracture spacing [mD-ft] (Model II)

Figure 44 displays resulting grid set for varied DFN fracture spacing. DFN fracture spacing of 100 ft gives the highest fracture propagation due to low density.

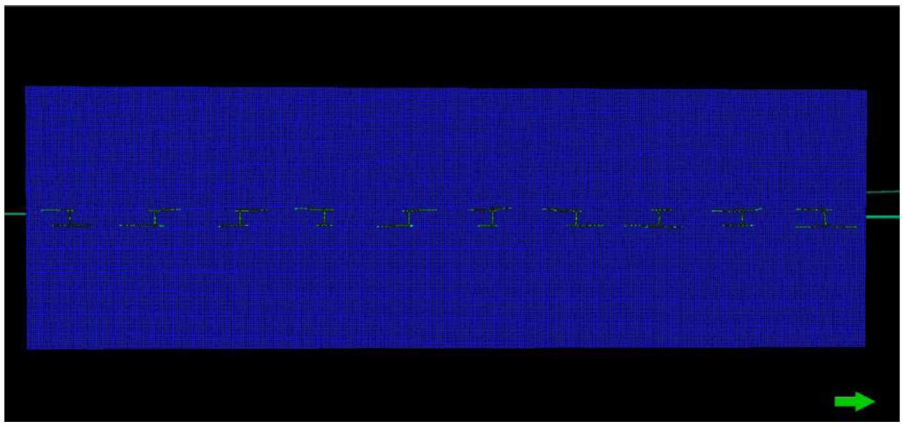

(a) DFN fracture spacing 1 ft

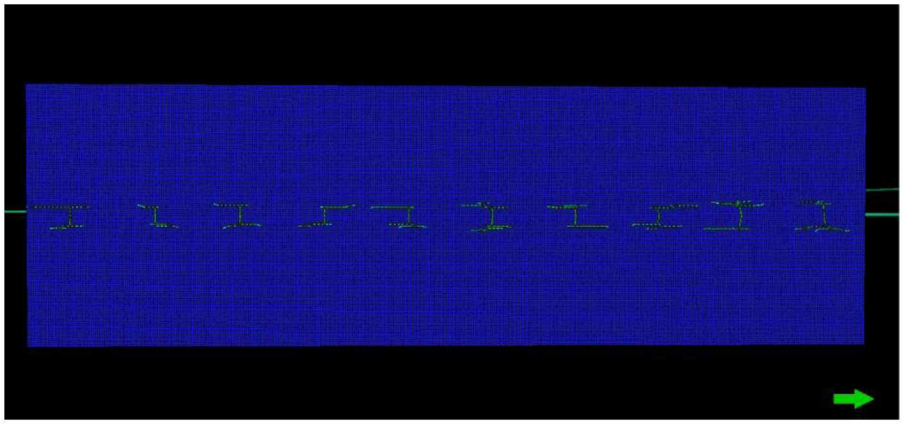

(b) DFN fracture spacing 10 ft

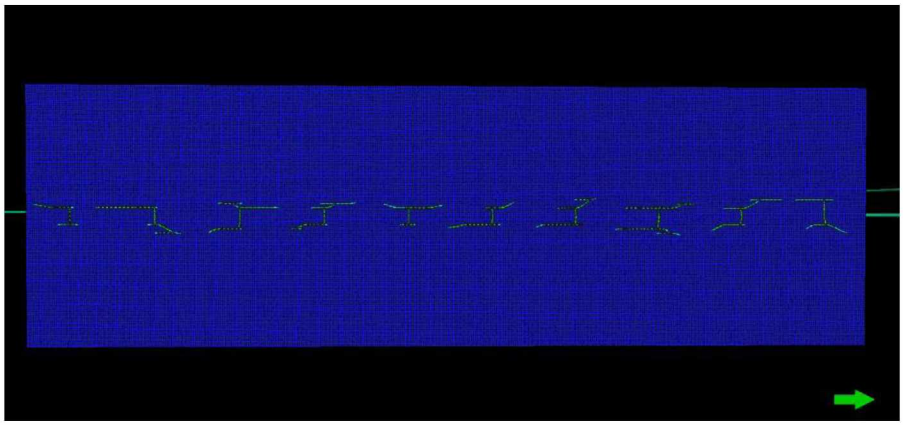

(c) DFN fracture spacing 100 ft

Figure 44: Top view for models with varied DFN fracture spacing (Model II)

Table 16 displays all hydraulic fracture results for varied DFN fracture spacing. All parameters in the table are defined in Appendix B. The case with DFN fracture spacing of 10 ft resulted with the highest leak-off due to the largest total fracture surface area. In this case the largest fracture surface area provided the highest conductivity.

Table 16: Hydralic fracture results for varied DFN fracture spacing (Model II)

Hydraulic fracture results for DFN fracture spacing (Model II)				
	Planar	1 ft	10 ft	100 ft
Total fracture volume [ft^3]	1352	1254	1278	1441
Total fracture surface area [ft^2]	581291.0	618427.5	618596.6	538699.3
Maximum surface pressure [psi]	7597	7609	7602	7606
Total leak-off volume [ft^3]	976	1073	1050	887
Total propped fracture surface area [ft^2]	40407.4	32611.2	32910.4	30495.7
Maximum BH pressure [psi]	9367	9381	9369	9375
Efficiency [%]	58.1	53.9	54.9	61.9
Hydraulic fracture geometry				
Final extension of HFN in the direction of max stress [ft]	309.7	44.0	78.0	214.6
Final extension of HFN in the direction of min stress [ft]	39.1	140.6	113.6	91.1
Maximum fracture height [ft]	225.9	223.8	223.9	226.6
Total fracture surface area [ft^2]	73520.1	82461.5	55861.0	70371.5
Fracture width at wellbore [in]	0.07	0.05	0.07	0.07
Average fracture width [in]	0.03	0.02	0.03	0.04
Total fracture volume [ft^3]	193	164	130	214
Total leak-off volume [ft^3]	123	136	93	112
Propped fracture geometry				
Final extension of HFN in the direction of maximum stress [ft]	247.5	41	41.3	185.2
Final extension of HFN in the direction of minimum stress [ft]	23.6	77.9	16.8	66.1
Total propped fracture surface area [ft^3]	5190.5	4706.5	4184.8	4872.2
Average propped fracture height [ft]	19.5	28.0	58.0	20.9
Fracture width at wellbore [in]	0.03	0.04	0.05	0.07
Average fracture width [in]	0.03	0.03	0.04	0.04
Average fracture conductivity [mD.ft]	36.5	117.7	174.4	162.4

3.3.3 Effects of DFN Length

In order to investigate the effects of DFN length on gas recovery factor, three profiles for DFN were selected: 25 ft, 50 ft and 75 ft. DFN orientation and DFN fracture spacing for this set was set at 0 degrees and 10 ft respectively. Standard deviation for all parameters was set to zero to more accurately examine geometry effects.

3.3.3.1 Model I

Figure 45 displays sets for DFN of 25, 50 and 75 ft.

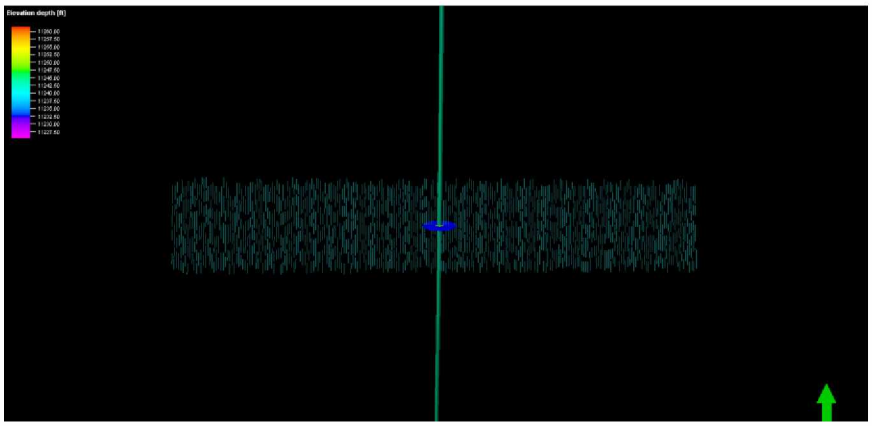

a) DFN length 25 ft

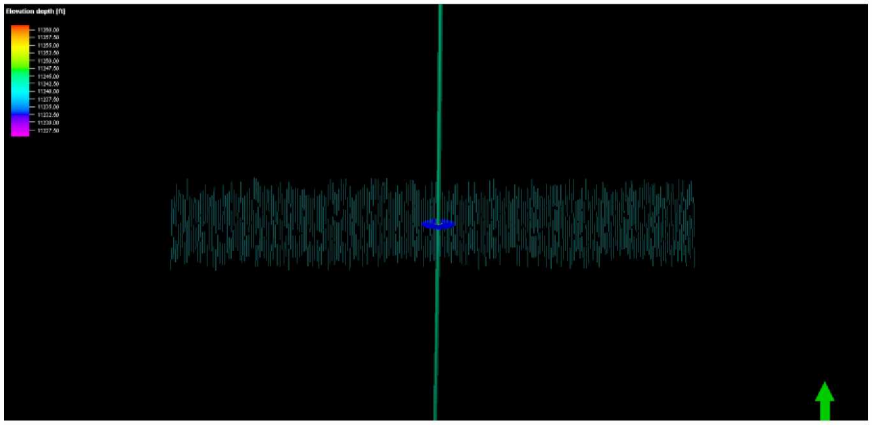

b) DFN length 50 ft

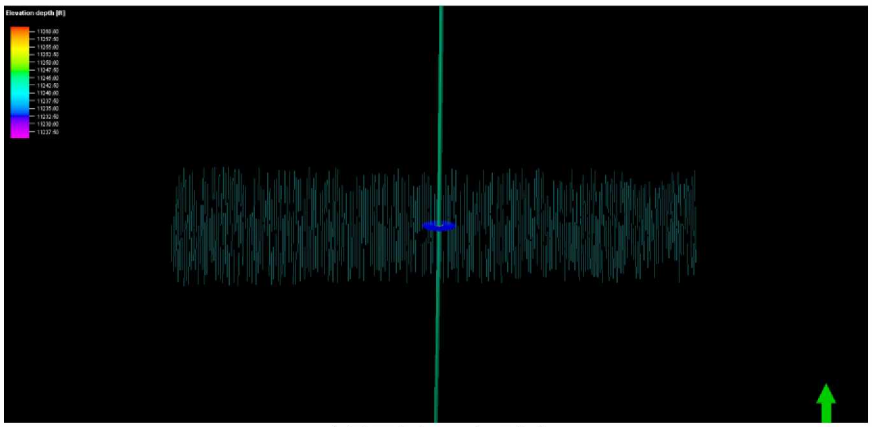

c) DFN length 75 ft

Figure 45: DFN profile for varied length (Model I)

Figure 46 displays the resulting fracture propagation for the given DFN sets. DFN length of 50 ft resulted in the largest fracture area. The largest fracture area resulted due to the most optimal concentration of the fracture stress at the fracture tips resulted from the natural fracture length and the most optimal fluid path for the fracture fluid to travel. However, DFN length of 25 ft resulted in the highest value of average conductivity, which could be explained by few small fracture cells with very high values of conductivity offsetting the average conductivity.

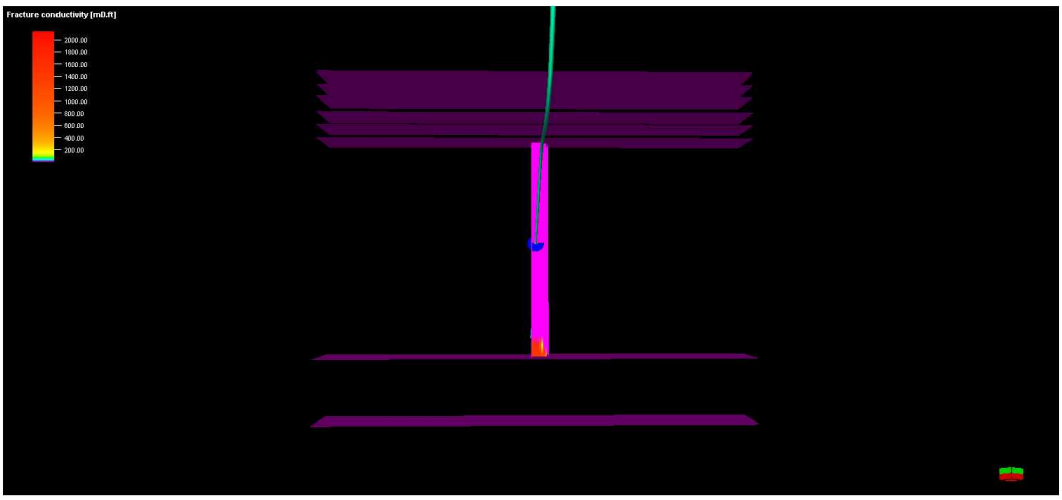

a) DFN length 25 ft

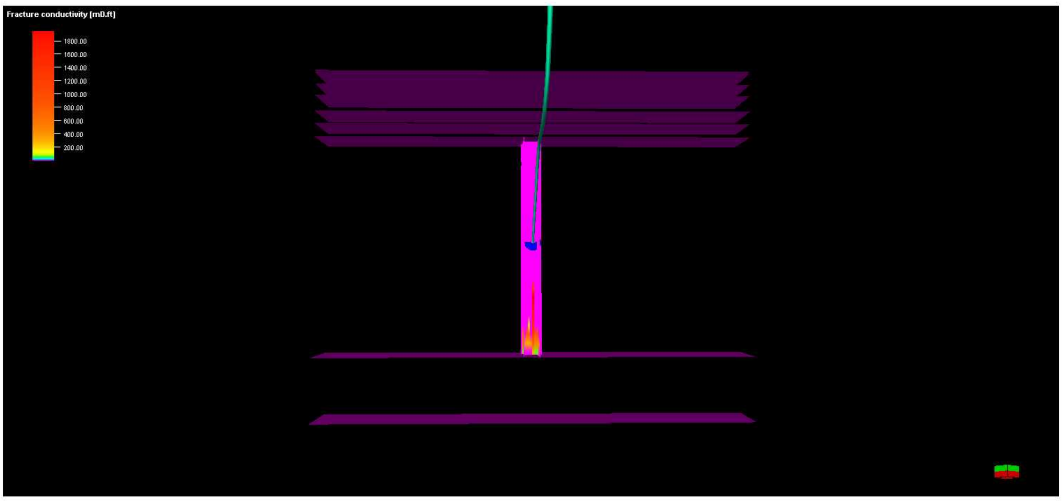

b) DFN length 50 ft

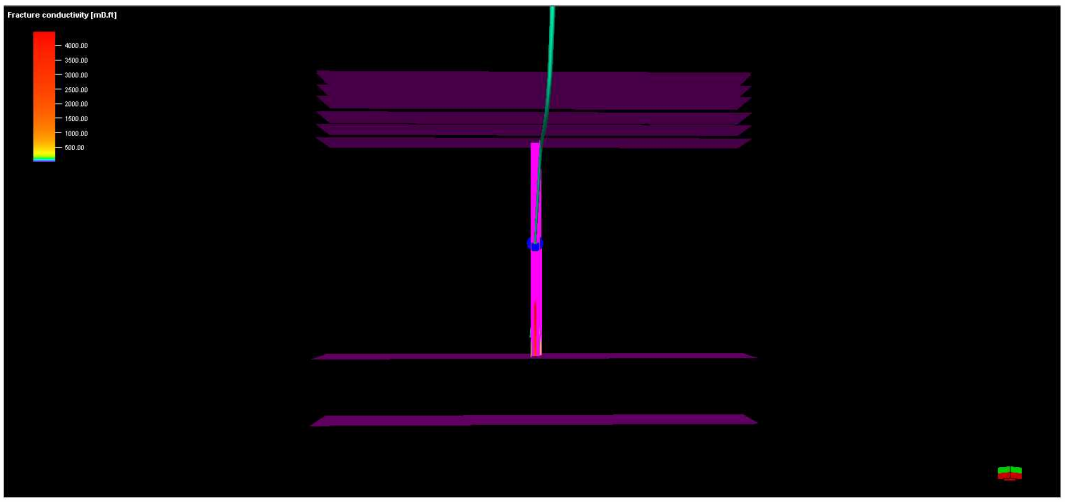

c) DFN length 75 ft

Figure 46: Conductivity profile for varied DFN length [mD-ft] (Model I)

Figure 47 displays top view for varied DFN length sets. No obvious geometric trend between the fracture propagation and DFN fracture length is visible at this time due to the uncertainty involved with a generation of stochastic natural fracture model.

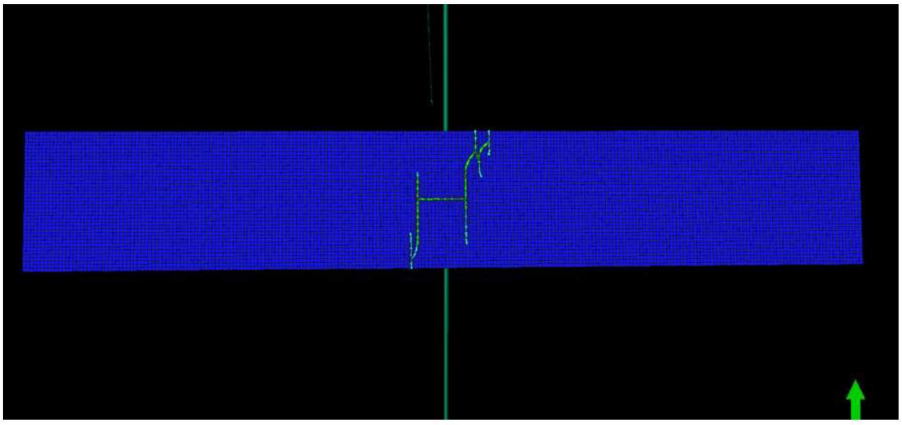

a) DFN length 25 ft

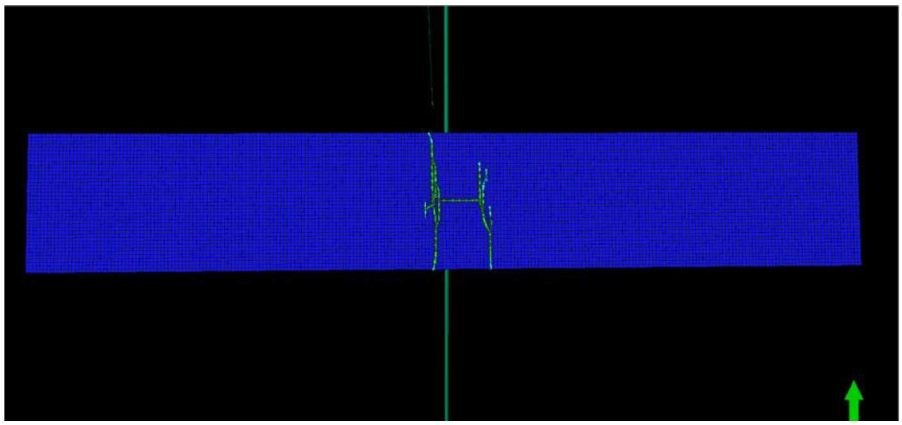

b) DFN length 50 ft

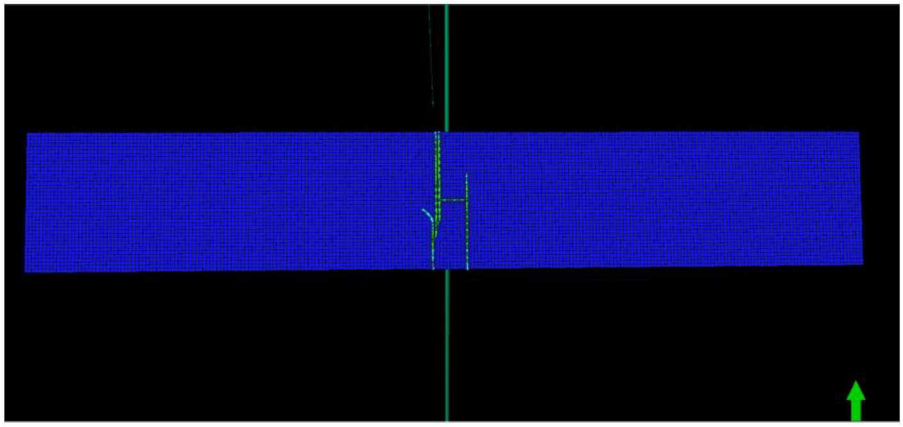

c) DFN length 75 ft

Figure 47: Top view for models with varied DFN length (Model I)

Table 17 displays all fracture parameters for the given sets. The case with DFN of 50 ft length resulted in the smallest fracture area, but the largest total fracture volume due to the smallest fracture width at the wellbore. The width depends on the fluid pressure (*Pcp*, Equation 10), which is solved from the overall discretized network system at each time step.

$$w(z) = \frac{4}{E'}\left[P_{cp} - \sigma_n + \rho_f g(h_{cp} - z)\right]\sqrt{z(h-z)} + \frac{4}{\pi E'}\sum_{i=1}^{n-1}(\sigma_{i+1} - \sigma_i)\left[(h_i - z)cosh^{-1}\frac{z\left(\frac{h-2h_i}{h}\right)+h}{|z-h_i|}\right] + \sqrt{z(h-z)}arccos\left(\frac{h-2h_f}{h}\right) \quad (10)$$

Where $w(z)$ is the width at depth z, σ_n and σ_i are the in-situ stressed at the top tip and the *i*-th layer, respectively, h is the fracture height and h_i is the height from the lower tip to the tow of the *i*-th layer (Kresse et al., 2011).

Since the resulting maximum height is the same for all DFN varied length profiles, different width in the case with 50 ft length could be a result of screen out. A condition that occurs when the solids carried in a treatment fluid, such as proppant in a fracture fluid, create a bridge across the perforations or similar restricted flow area. This creates a sudden and significant restriction to fluid flow that causes a rapid rise in pump pressure (Schlumberger Oilfield Glossary). If screen out occurs early in the fracture, it causes the pumping pressure and fracture width to increase.

Table 17: Hydraulic fracture results for varied DFN length (Model I)

Hydraulic fracture results for DFN length (Model I)				
	Planar	75 ft	50 ft	25 ft
Total fracture volume [ft^3]	2081	1241	985	1337
Total fracture surface area [ft^2]	211478.6	204126.8	263038.8	180120.0
Maximum surface pressure [psi]	12433	12336	12329	12341
Total leak-off volume [ft^3]	1013	1086	1342	991
Total propped fracture surface area [ft^2]	59149.5	133872.9	217084.4	154038.0
Maximum BH pressure [psi]	14217	14112	14109	14120
Efficiency [%]	89.4	53.3	42.3	57.4

Table 17: Hydraulic fracture results for varied DFN length (Model I) continued

Hydraulic fracture geometry				
Final extension of HFN in the direction of max stress [ft]	813.0	87.5	124.0	131.1
Final extension of HFN in the direction of min stress [ft]	0	197.3	193.4	192.6
Maximum fracture height [ft]	258.3	212.5	212.5	212.5
Total fracture surface area [ft^2]	211478.6	204126.8	263038.8	180120.0
Fracture width at wellbore [in]	0.21	0.25	0.24	0.27
Average fracture width [in]	0.12	0.07	0.04	0.09
Total fracture volume [ft^3]	2078	1253	986	1323
Total leak-off volume [ft^3]	1013	1086	1342	991
Propped fracture geometry				
Final extension of HFN in the direction of maximum stress [ft]	688.98	85	120	130.51
Final extension of HFN in the direction of minimum stress [ft]	0	185.19	180.3	178.11
Total propped fracture surface area [ft^3]	58555.9	73697.9	217084.4	154038.0
Average propped fracture height [ft]	83.8	86.8	201.1	197.4
Fracture width at wellbore [in]	0.10	0.19	0.03	0.04
Average fracture width [in]	0.02	0.01	3.81E-003	5.44E-003
Average fracture conductivity [mD.ft]	110.8	118	104	140

3.3.3.2 Model II

Figure 48 displays varied DFN length for the zoneset polygon used for Model II.

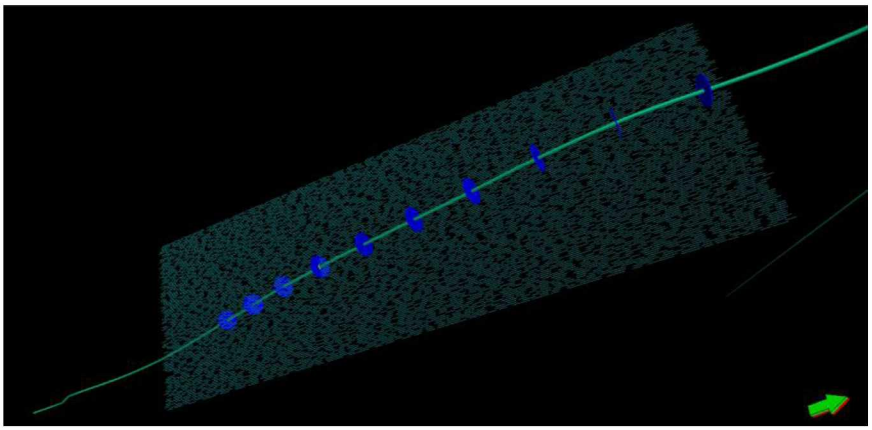

a) DFN length 25 ft

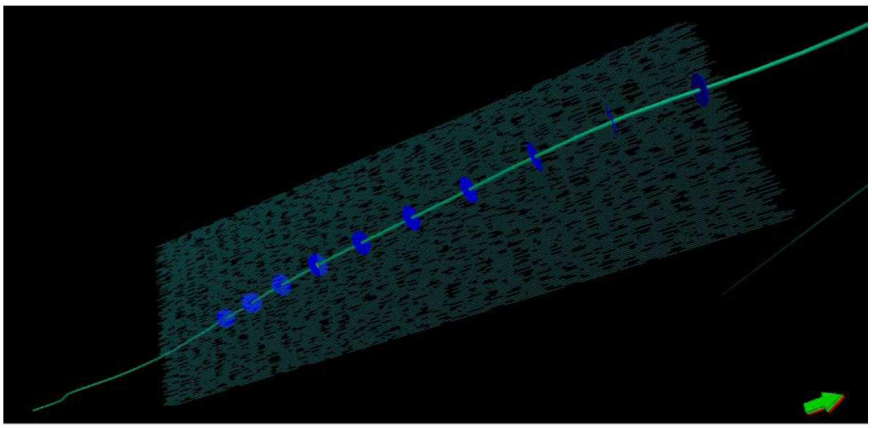

b) DFN length 50 ft

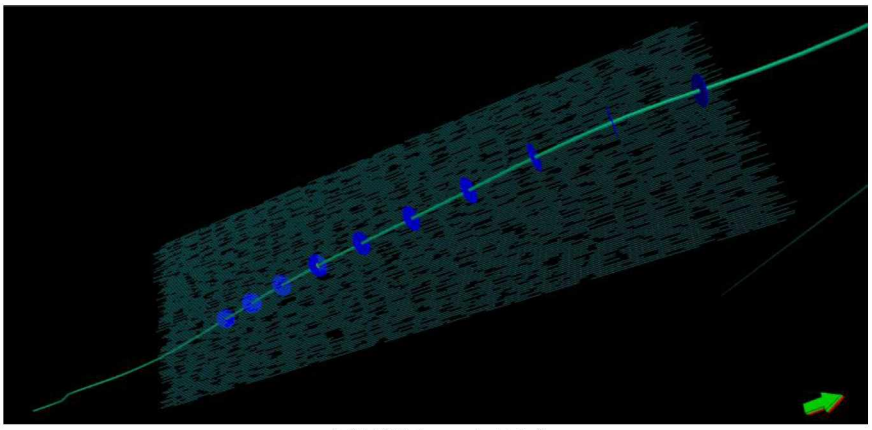

c) DFN length 75 ft

Figure 48: DFN profile for varied length (Model II)

Figure 49 displays resulting fracture network for the given sets. DFN length of 50 ft resulted in the largest fracture area and the largest propped fracture area.

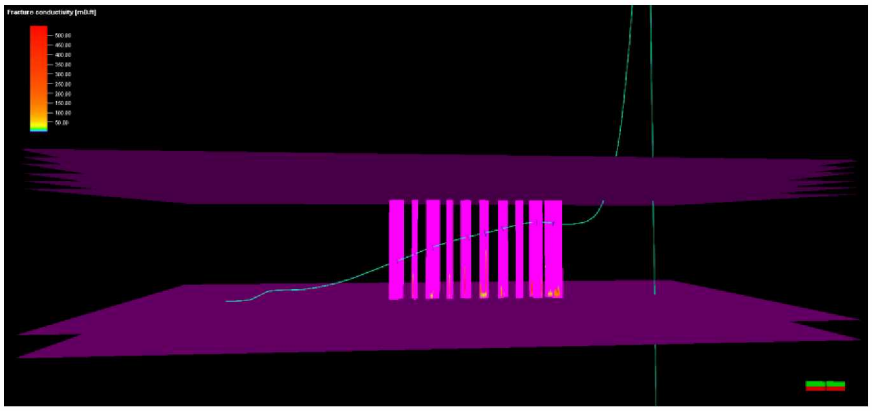

a) DFN length 25 ft

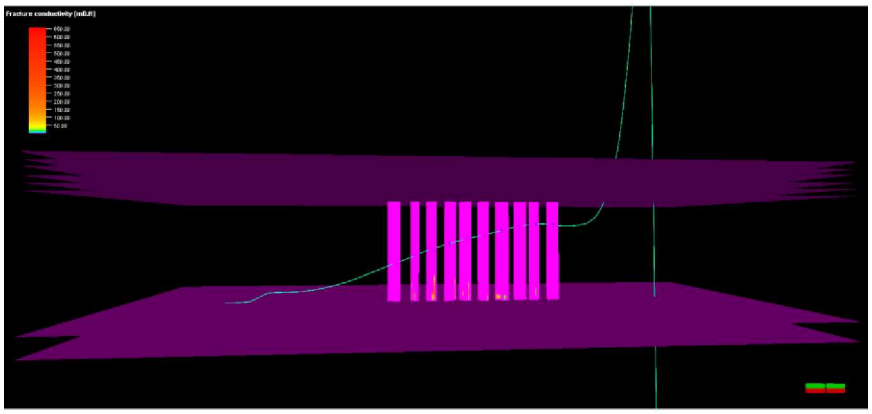

b) DFN length 50 ft

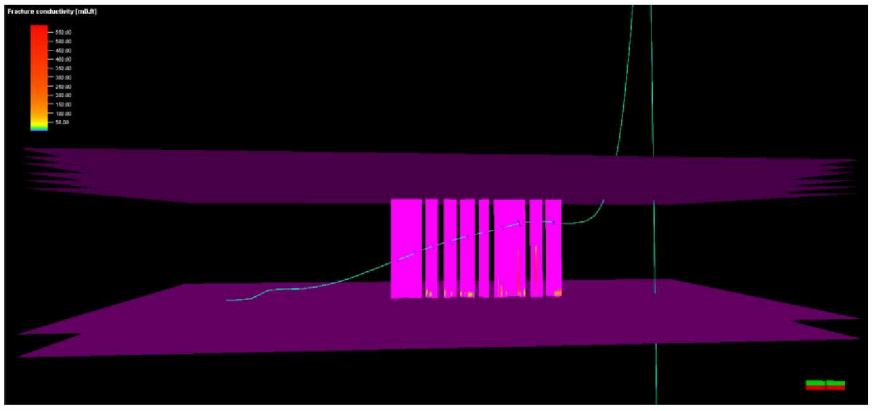

c) DFN length 75 ft

Figure 49: Conductivity profile for varied DFN length [mD-ft] (Model II)

Figure 50 displays top view for varied DFN lengths parameters. DFN length of 75 ft has the largest propagation perpendicular to the well, which could not be seen in the Model I case due to smaller SRV defined by hydraulic fracture spacing.

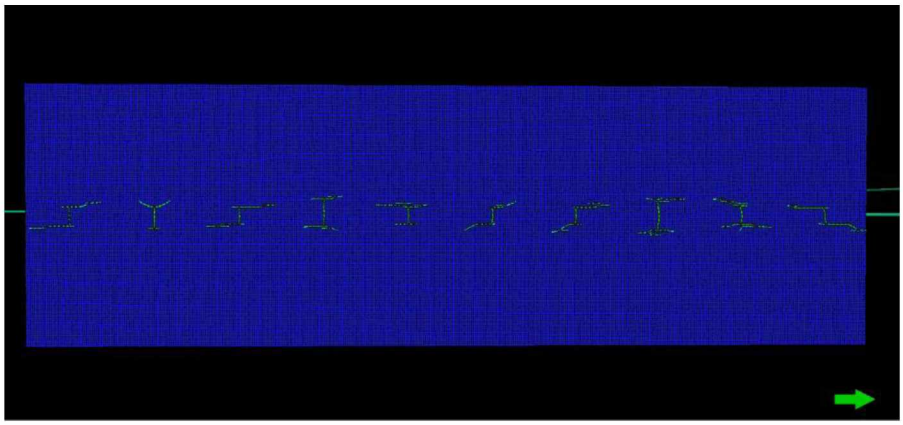

a) DFN length 25 ft

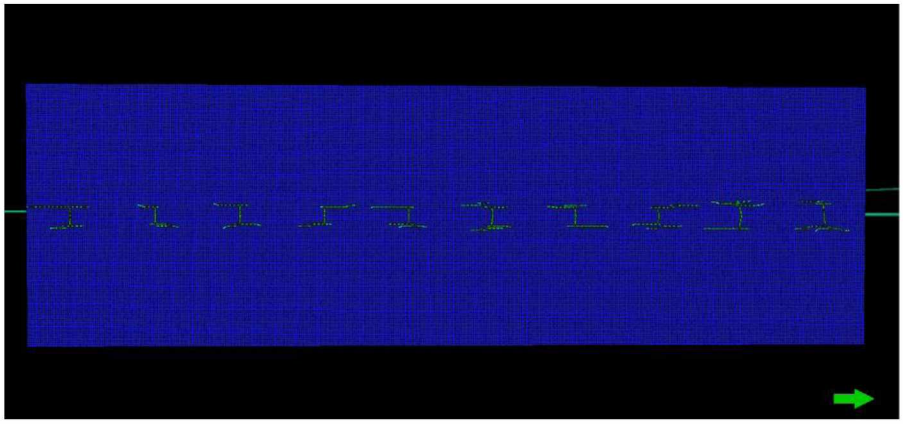

b) DFN length 50 ft

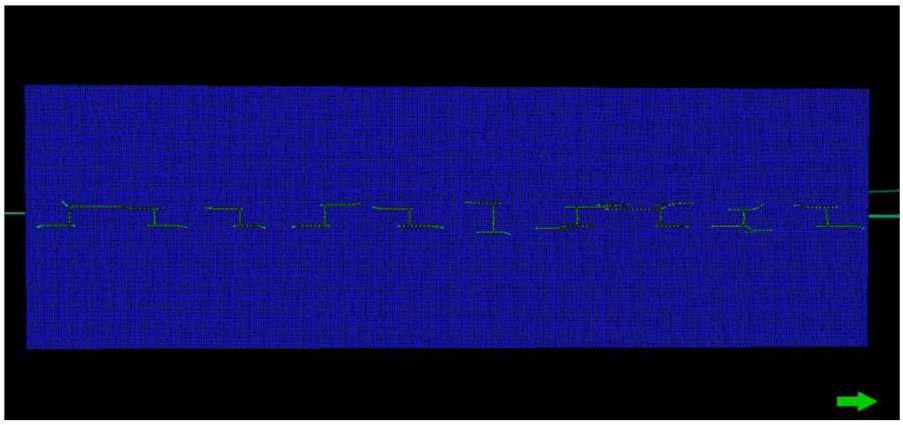

c) DFN length 75 ft

Figure 50: Top view for models with varied DFN length (Model II)

Hydraulic fracture results are shown in Table 18. As in the case with a single fracture, DFN length of 50 ft was the most optimum length to provide the largest total fracture area.

Table 18: Hydraulic fracture results for varied DFN length (Model II)

Hydraulic fracture results for varied DFN length (Model II)				
	Planar	75 ft	50 ft	25 ft
Total fracture volume [ft^3]	1352	1267	1222	1275
Total fracture surface area [ft^2]	581291.0	623485.5	645650.6	601702.6
Maximum surface pressure [psi]	7597	7596	7599	7606
Total leak-off volume [ft^3]	976	1060	1106	1053
Total propped fracture surface area [ft^2]	40407.4	364742.5	32884.3	28142.6
Maximum BH pressure [psi]	9367	9368	9369	9386
Efficiency [%]	58.1	54.5	52.5	54.9
Hydraulic fracture geometry				
Final extension of HFN in the direction of max stress [ft]	309.7	55.2	70.0	60.1
Final extension of HFN in the direction of min stress [ft]	39.1	162.8	120.9	185.4
Maximum fracture height [ft]	225.9	225.2	223.7	225.5
Total fracture surface area [ft^2]	73520.1	62843.1	81354.7	67230.3
Fracture width at wellbore [in]	0.07	0.08	0.07	0.07
Average fracture width [in]	0.03	0.03	0.02	0.03
Total fracture volume [ft^3]	193	154	156	170
Total leak-off volume [ft^3]	123	110	126	115
Propped fracture geometry				
Final extension of HFN in the direction of maximum stress [ft]	247.54	31.61	60	50.66
Final extension of HFN in the direction of minimum stress [ft]	23.6	89.6	40.0	154.2
Total propped fracture surface area [ft^3]	5190.4	4488.8	4720.5	4273.4
Average propped fracture height [ft]	19.5	33.2	34.3	21.3
Fracture width at wellbore [in]	0.03	0.05	0.04	0.05
Average fracture width [in]	0.03	0.03	0.03	0.03
Average fracture conductivity [mD.ft]	36.5	129.5	148.2	75.1

Chapter 4 Results and Discussion

4.1 Injection Profiles during Treatment

To account for the presence of fracturing fluid (slickwater) in the hydraulic fracture and the matrix around the fracture, 590 barrels of water was injected into the simulation Model I after the fracture propagated for the time of the fracture treatment. Figure 51 shows cumulative water injection profile for Model I. Figure 52 shows water injection rate versus time for Model I. Water injection rate drops and then builds up again due to having only one constraint during water injection – bottomhole pressure of 10,000 psi. There was no injection rate constraint. Figure 53 shows average model pressure change during the injection. The injection pressure mimics the injection rate behavior – it drops and then increases again. The average model pressure increased slightly from 8677.093 psia to 8678.242 psia. Material Balance calculations for this case are included in Appendix D. There is not much pressure build up since the water was injected into the fracture network, which already propagated. Figure 54 shows average water saturation change during the injection. Water saturation increased slightly from 0.159998 to 0.160041.

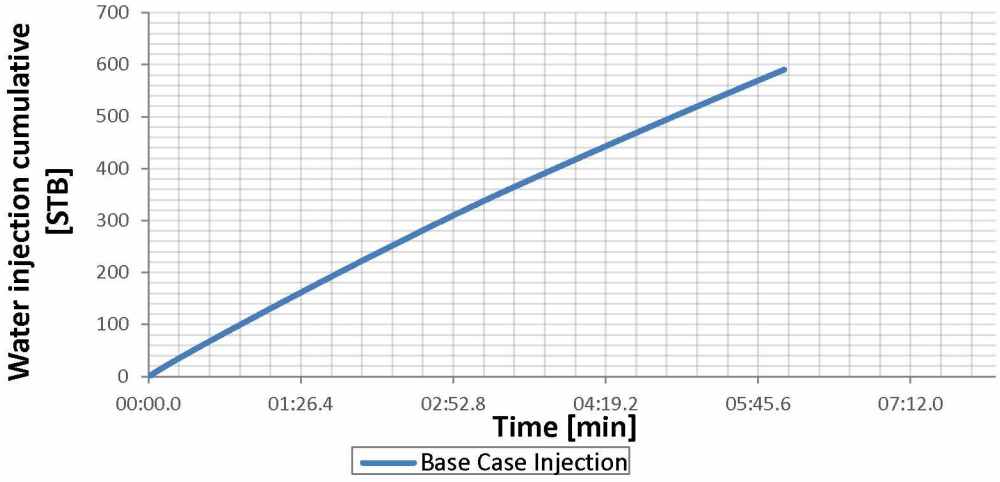

Figure 51: Water injection cumulative [STB]

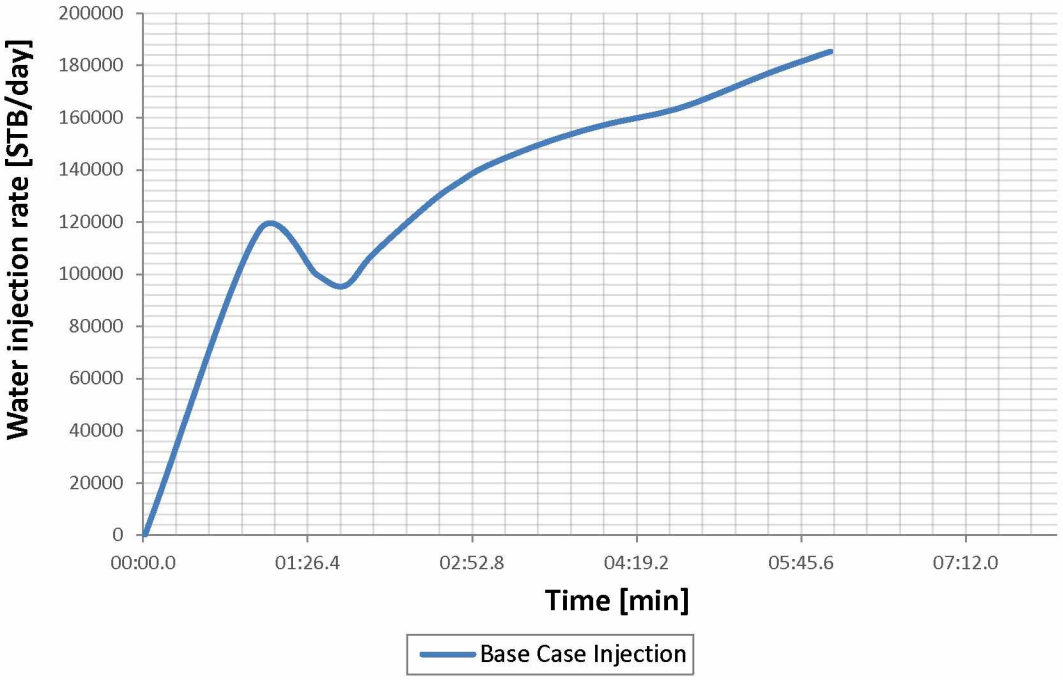

Figure 52: Water injection rate [STB/day]

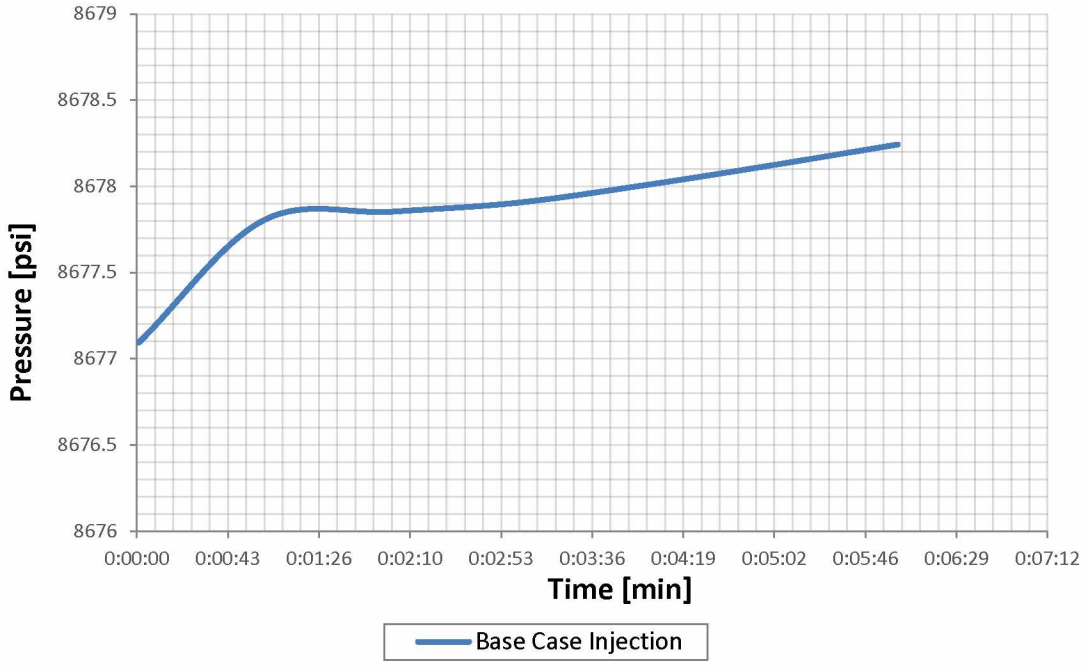

Figure 53: Average model pressure during water injection [psi]

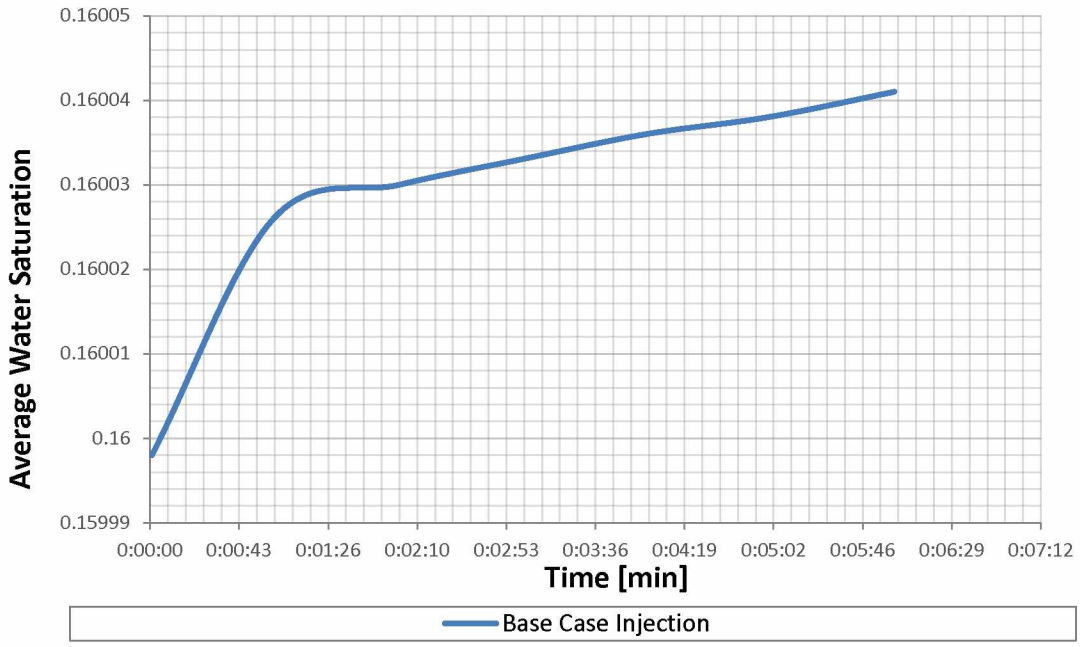

Figure 54: Average water saturation during water injection

4.2 Production Trends

Figure 55 shows cumulative gas production for the Base Case and the case with including presence of fracturing water. Less gas was produced when fracturing fluid was included in the model mainly due to reduction in gas saturation and relative permeability in the near fracture matrix. Gas production and cumulative gas production is higher for the base case with lower initial water saturation that results in higher gas relative permeability in the area around the fracture. Figure 56 shows gas production rate when fracturing fluid is included. Initially, the well is producing 100% water. After gas breakthrough gas rate increases and then eventually slightly decreases due to reservoir depletion. Figure 57 shows water production rate versus time. Most of the water is produced during the first two days of the production.

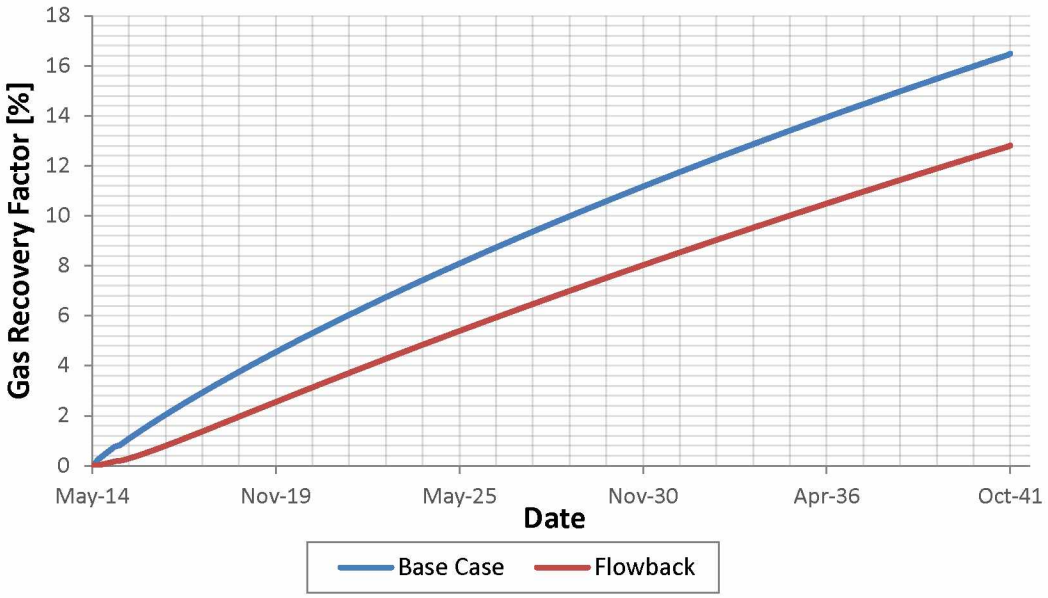

Figure 55: Effect of including fracturing water on gas production cumulative [%]

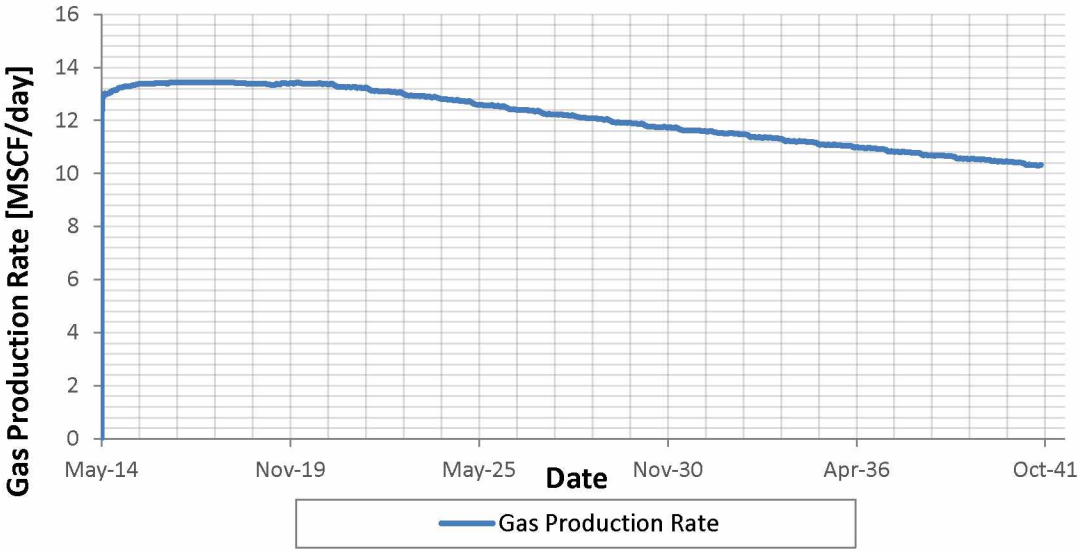

Figure 56: Effect of presence of fracturing fluid on gas production rate [MSCF/day]

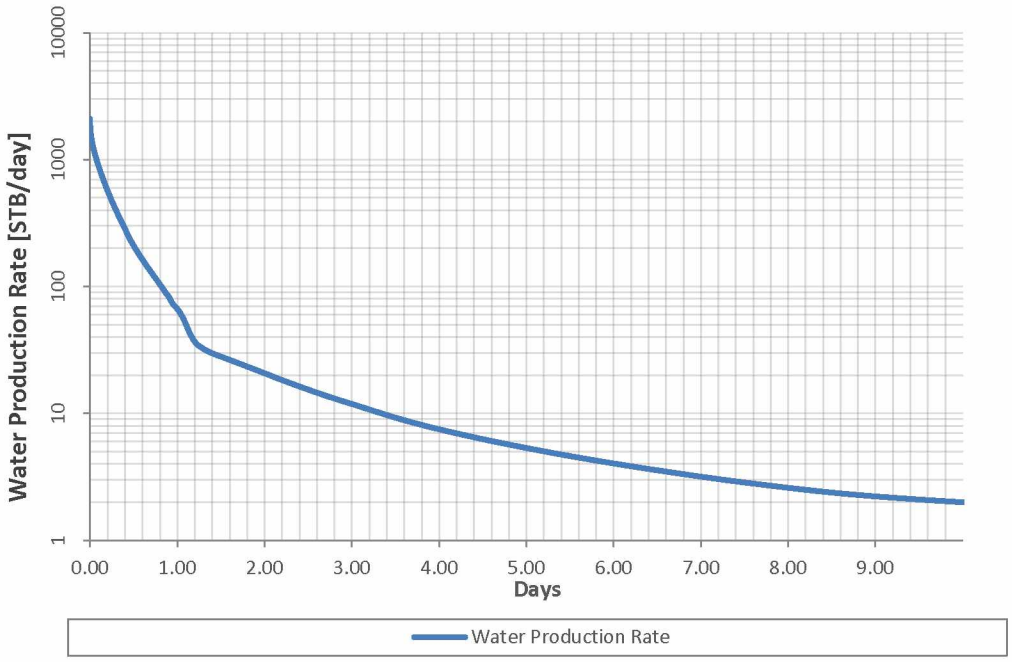

Figure 57: Water production rate during flowback [STB/day]

4.3 Effect of Fracturing Fluid Flowback

Figure 58 shows the gas recovery factor for base case and a case when fracturing water is included in the model. Recovery factor for the Base Case was 16.5 % over approximately 30 years which is 12.8 % when fracturing fluid is present and modeled. This leads to the conclusion that ignoring the presence of fracturing water in simulation leads to the overestimation of the gas recovery factor by ~ 30%.

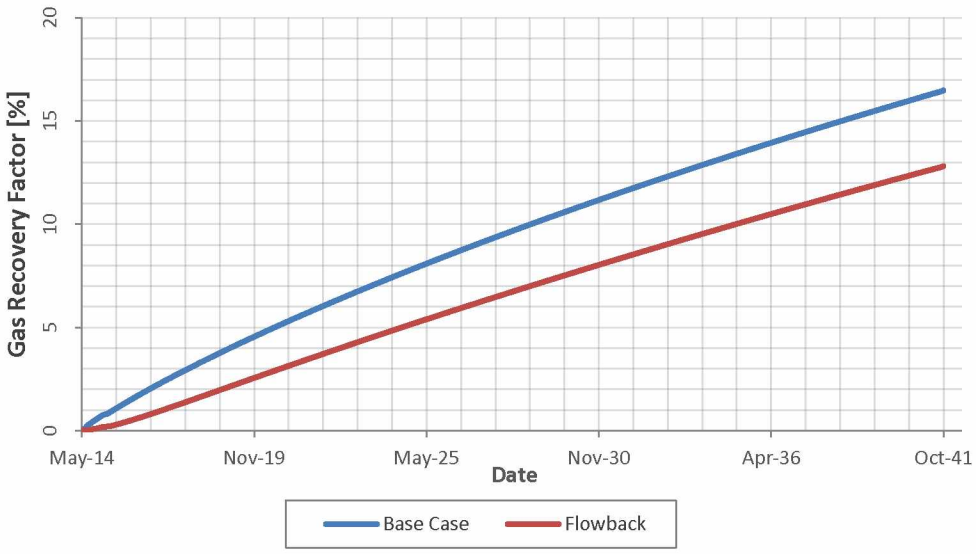

Figure 58: Gas recovery factor with and without considering precense of fracturing fluid[%]

4.4 Fracturing Fluid Recovery

Figure 59 shows cumulative water production over approximately 30 years. Total of 523 barrels of water is recovered. The water recovered is high since all of the water was injected after the fracture was already propagated instead being injected stage-by-stage. Hence there was less time for the water to leak off into the formation. Figure 60 shows the percentage of water recovered, which adds up to 88.6 percent.

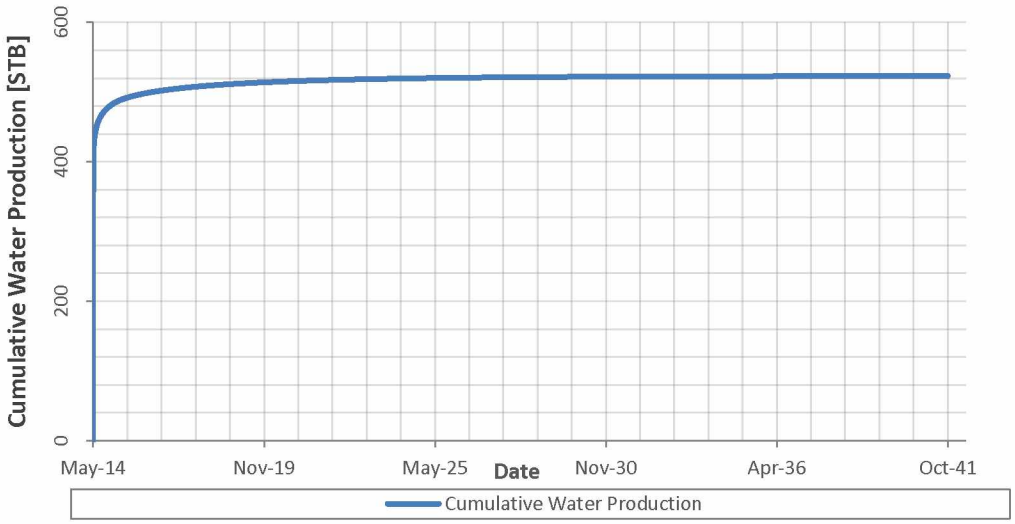

Figure 59: Cumulative water production versus time [STB]

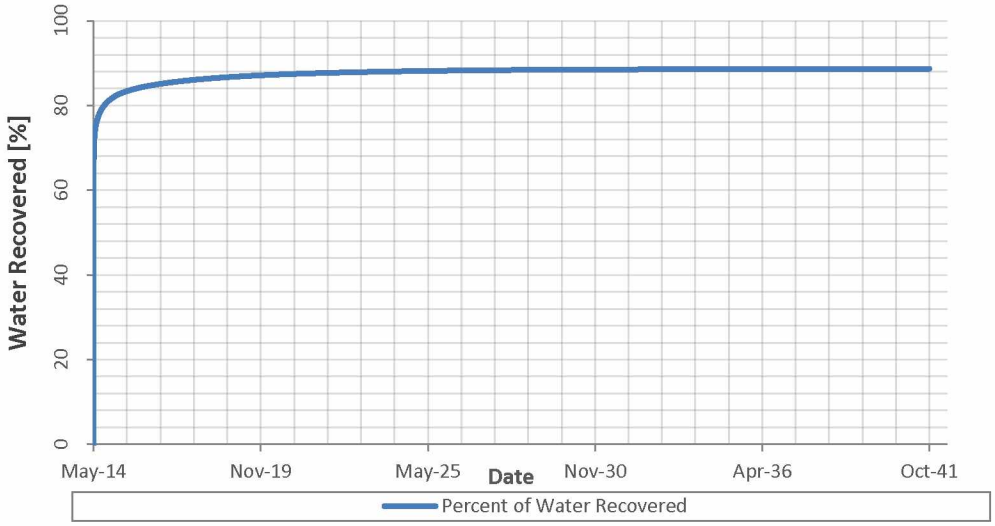

Figure 60: Percent of water recovered versus time [%]

4.5 Effect of Matrix Porosity on Rate and Recovery Factor

Figure 61 shows the effect of matrix porosity on the gas recovery factor. As porosity of the matrix decreases, the gas recovery factor increases. The case with highest porosity has the lowest recovery factor due to the lowest reservoir pressure drop (Figure 62). Bottom hole pressure of 1000 psi was assigned for production for all cases. The simulation duration was 30 years and there was no minimum production rate applied – Mangrove has only one option for production constraint – either BHP or gas production rate. Since there was larger gas in place as porosity increased, it took longer to drain SRV for the highest porosity case.

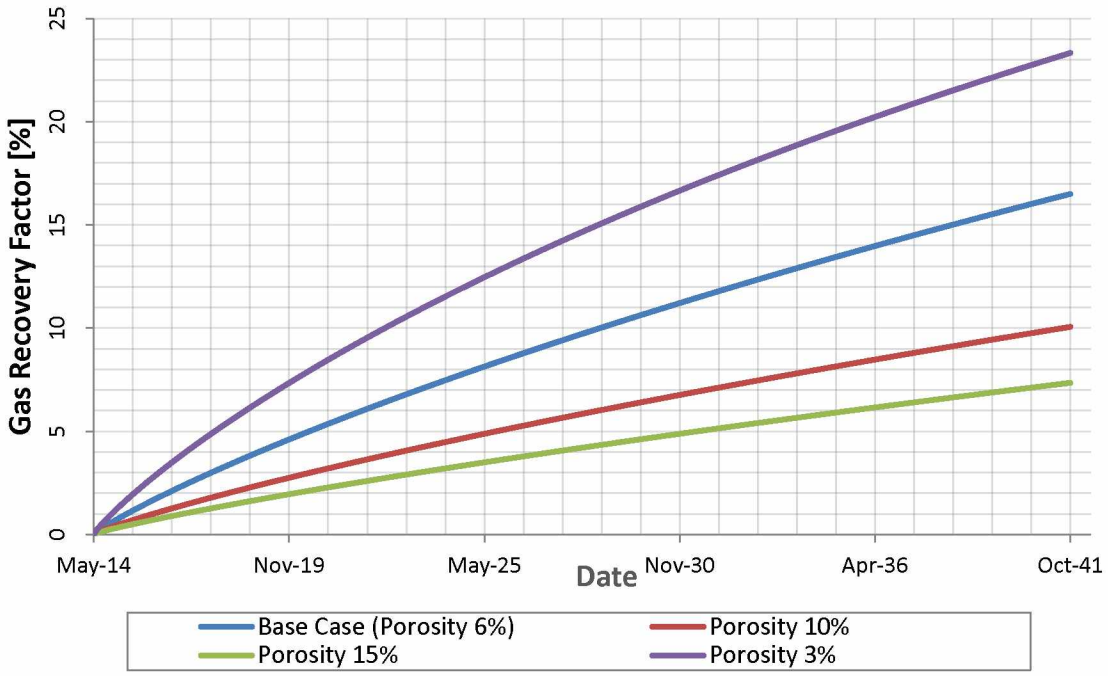

Figure 61: Effect of porosity on gas recovery factor [%]

Figure 62 shows pressure drop for varied matrix porosity. The case with the highest porosity has the lowest pressure drop. Initial and final pressure values are listed in Table 19.

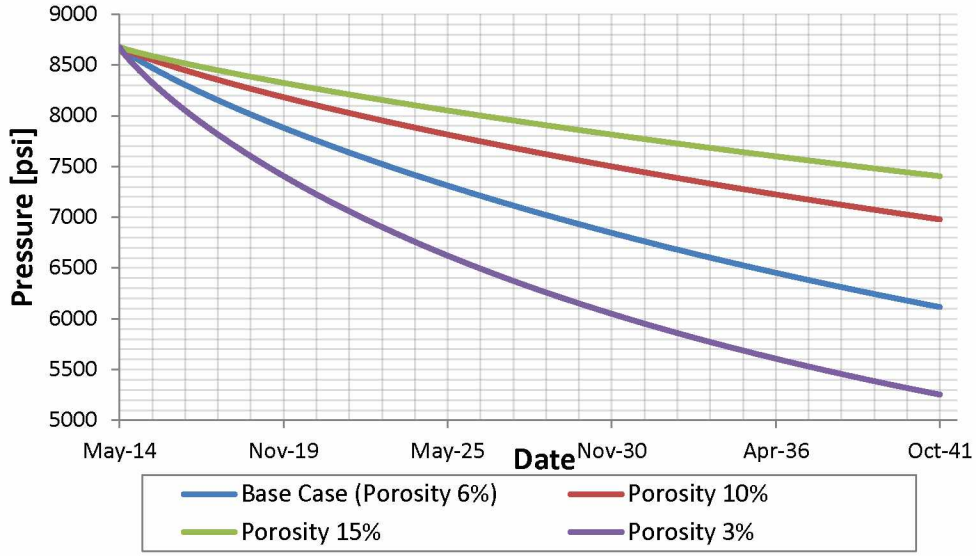

Figure 62: Average model pressure versus time for varied porosity cases [psi]

Figure 63 shows cumulative gas production for varied matrix porosity. As porosity increases, cumulative gas production increases.

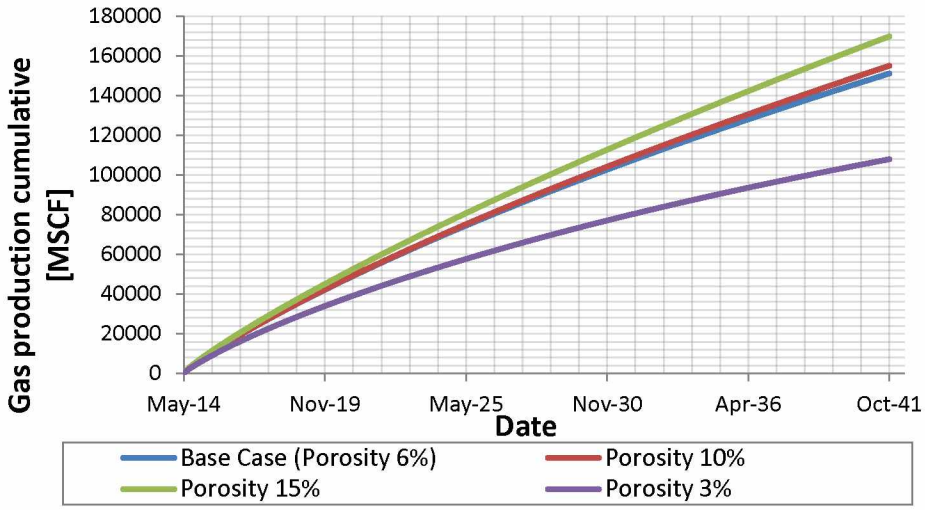

Figure 63: Cumulative gas production versus timec for varied porosity cases [MSCF]

Figure 64 shows gas production rate for varied matrix porosity cases. The highest porosity gives the highest production rate as expected.

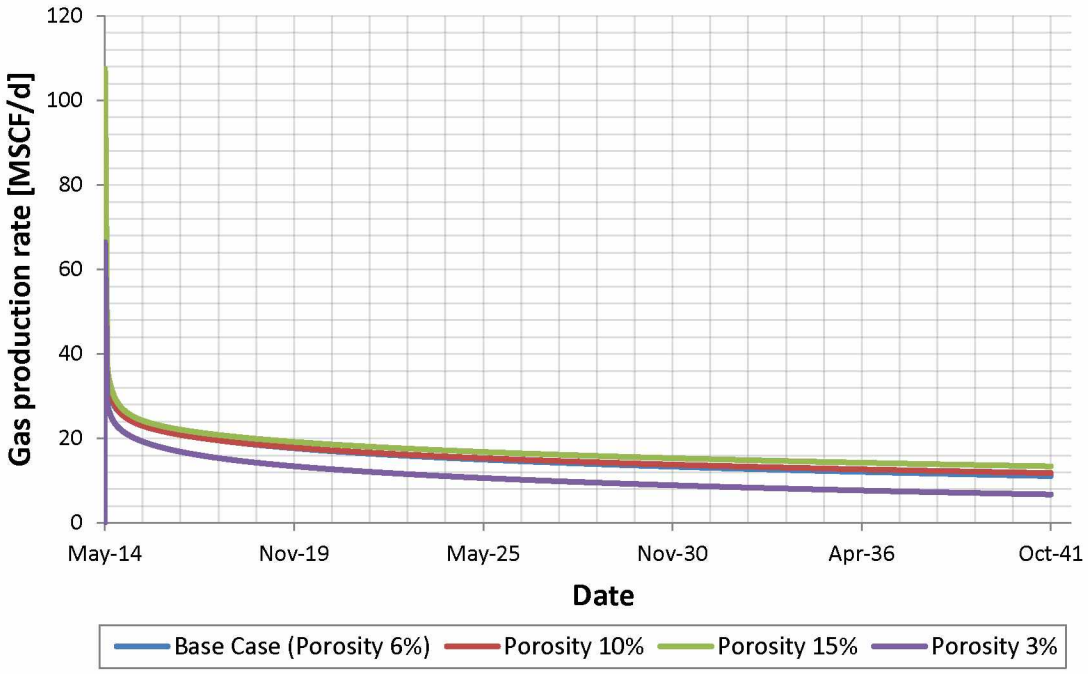

Figure 64: Gas production rate versus time for varied porosity cases [MSCF/day]

Figure 65 shows gas in place for varied matrix porosity. Highest porosity gives the highest gas in place as expected since gas in place calculation using volumetric method is directly proportional to the porosity of the rock:

$$GIP = \frac{V_b \varphi (1 - S_{wi})}{B_g} \tag{11}$$

Where GIP is gas in place (SCF), V_b is bulk reservoir volume (ft^3), S_{wi} is initial water saturation (fraction) and B_g is gas formation volume factor (reservoir ft^3/SCF).

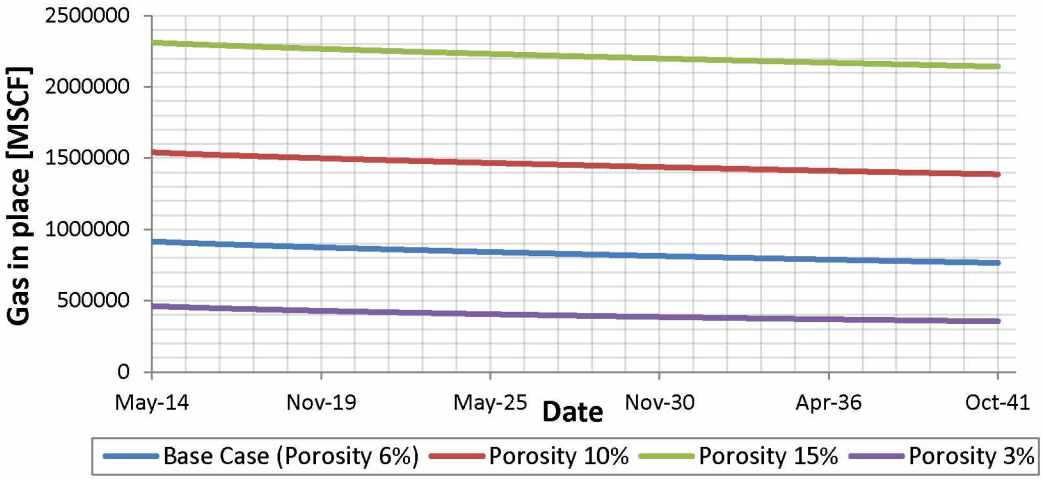

Figure 65: Gas in place versus time for varied porosity cases [MSCF]

Table 19: Simulation results for the varied porosities (Model I)

	Porosity 15 %	**Porosity 10 %**	**Porosity 3%**	**Base Case (Porosity 6%)**
Pressure [psi]				
Initial value	8676.6	8676.6	8676.6	8676.6
Final value	7403.7	6977.9	5252.3	6114.1
Cumulative gas production [MMSCF]				
Final value	169.7	154.9	107.8	151.0
Gas production rate [MSCF/day]				
Maximum value	107.0	94.3	65.9	59.3
Final value	13.4	11.8	6.7	11.1
Gas in place [BSCF]				
Initial value	2.3	1.5	0.46	0.92
Final value	2.1	1.4	0.35	0.76
Recovery factor [%]				
Final value	8.7	6.7	23.9	17.4

4.6 Effect of Matrix Permeability

To examine the effect of matrix permeability on the gas recovery factor, filter feature with different matrix permeability values (50 nD, 500 nD and 1000nD) was applied for the Base Case (200 nD).

Figure 66 shows significant effect of matrix permeability on the gas recovery factor. Higher matrix permeability produces higher recovery factor. Base Case permeability of 200 nD yields recovery factor of 17.4 %; permeability of 50 nd yields recovery factor of 8.7 %;

permeability of 500 md yields recovery of 27.2 % and finally permeability of 1000 nd yields recovery factor of 34.7 %. All simulation results are summarized in Table 20. Figures 67 - 69 show effect of matrix permeability on average model pressure, cumulative gas production and gas production rate. All plots show the same trend: as matrix permeability increases, it gets easier to deplete the model, higher gas production rate and higher recovery factors.

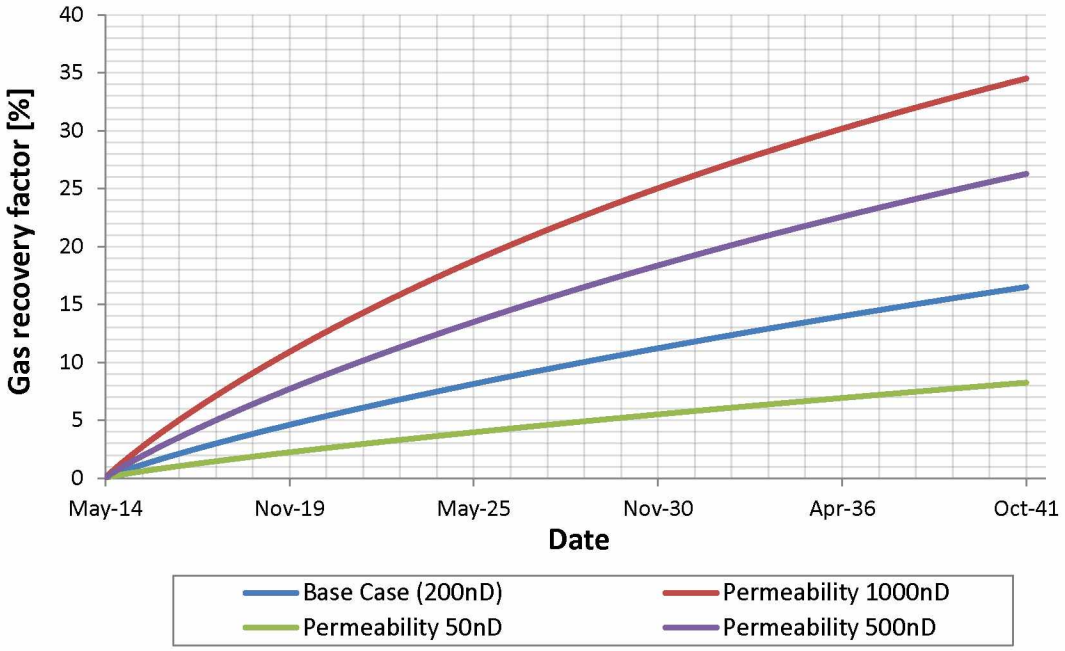

Figure 66: Effect of matrix permeability on gas recovery factor [%]

Table 20: Simulation results for varied matrix permeability

	Permeability 1000nD	**Permeability 500nD**	**Permeability 50ndD**	**Base Case**
Pressure [psi]				
Initial value	8676.6	8676.6	8676.6	8676.6
Final value	4455.5	5259.5	7502.5	6114.1
Cumulative gas production [MMSCF]				
Final value	315.7	240.3	75.4	151.0
Gas production rate [MSCF/day]				
Maximum value	99.5	81.7	36.0	59.3
Final value	18.27	15.91	5.87	11.08
Gas in place [BSCF]				
Initial value	0.92	0.92	0.92	0.92
Final value	0.60	0.67	0.84	0.76
Recovery factor [%]				
Final value	34.7	27.2	8.7	17.4

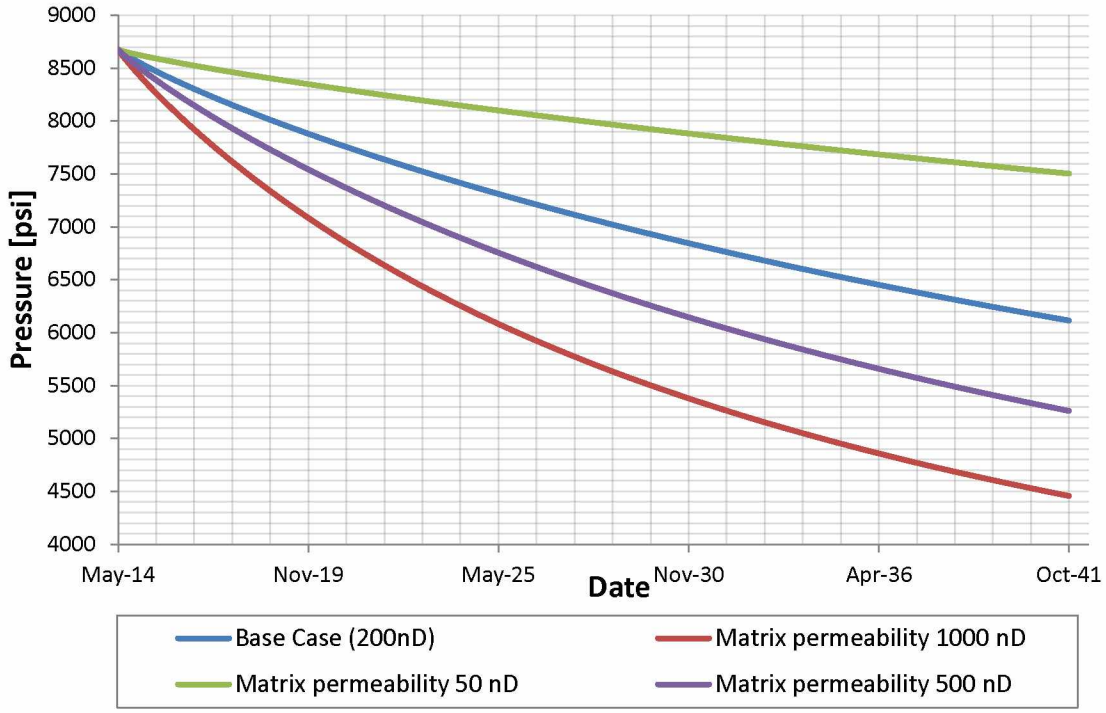

Figure 67: Average model pressure versus time in varied matrix permeability cases [psi]

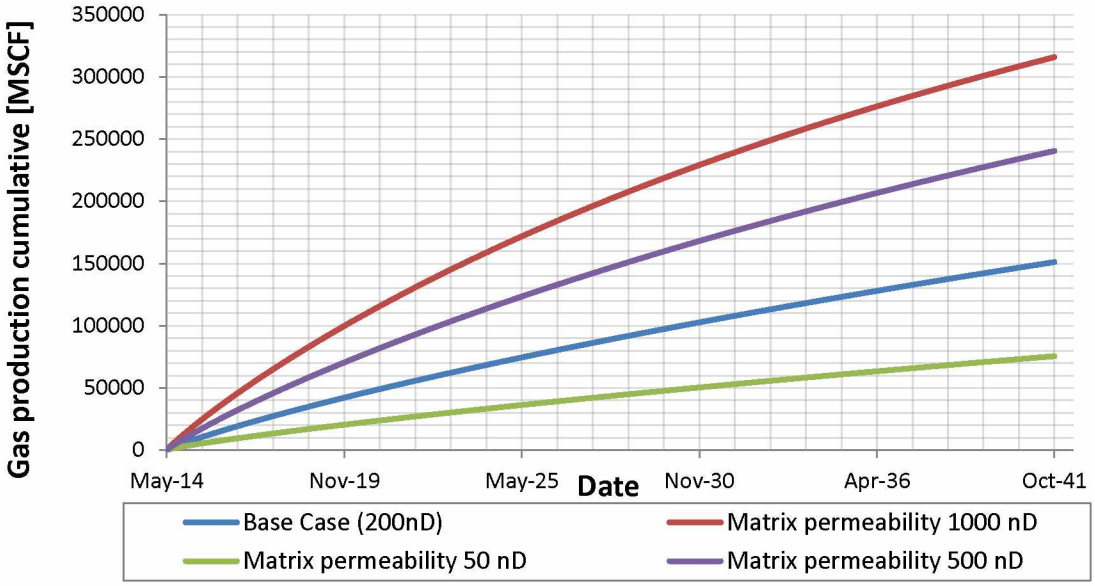

Figure 68: Cumulative gas production versus time in varied matrix permeability cases [MSCF]

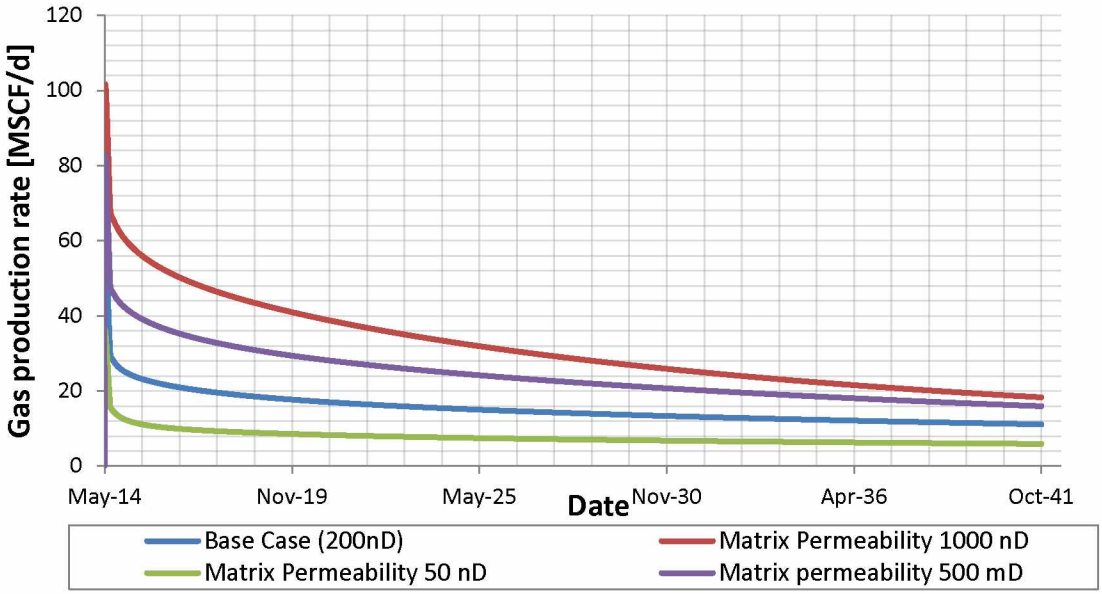

Figure 69: Gas production rate versus time in varied matrix permeablity cases [MSCF/day]

4.7 Effect of Hydraulic Fracture Permeability

To examine the effect of hydraulic fracture permeability, filter with different multiplier for the maximum fracture permeability was applied to reach the permeability values 1mD, 10 mD, 100 mD, 500 mD, 1000 mD, 2000 mD and 5000mD. Base Case permeability is 47 mD. Hence, to get permeability of 100 mD, Base Case maximum permeability had a filter with a multiplier of 2.12766. The same procedure was applied multiple times to achieve above maximum permeability values. The filter was applied to the cells with permeability values higher than 0.0002 mD to exclude matrix permeability cells. Since the permeability in the fracture cells varies with size and location, the largest permeability values are listed. Fracture closure is included in this model and is described in Section 3.2.3.

Figure 70 shows gas recovery factor for varied fracture permeability. All fractures resulted in non-zero pressure drop and hence all are finitely conductive. As fracture conductivity increases, the gas recovery factor increases as well.

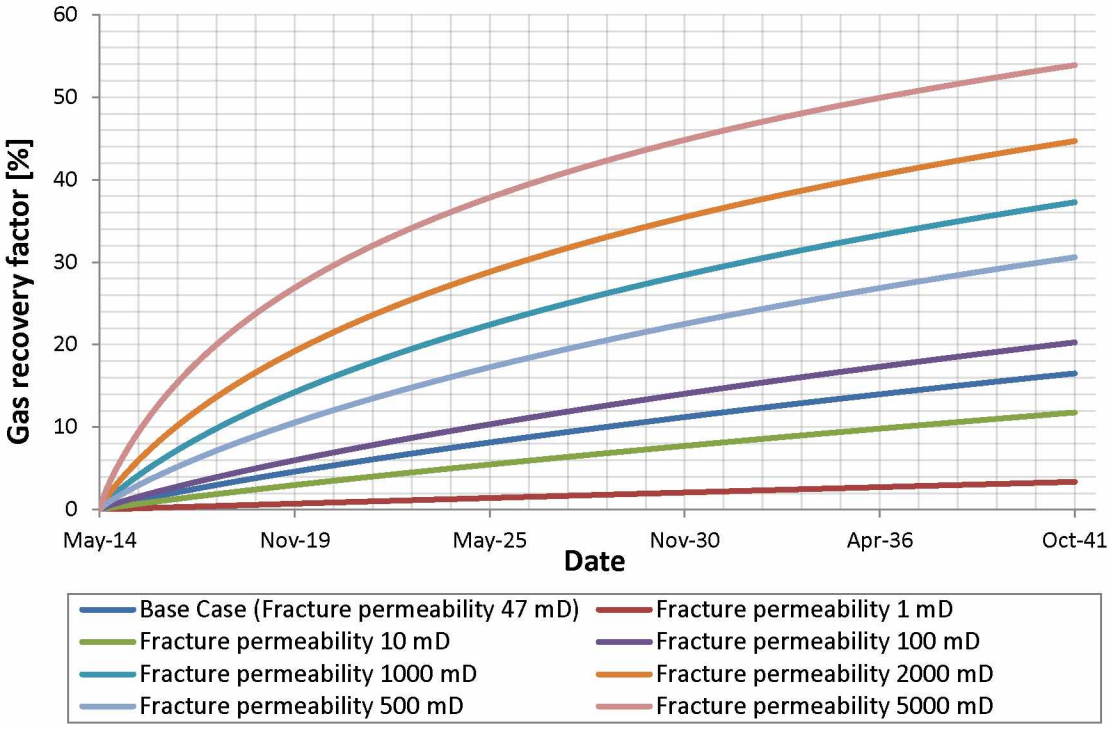

Figure 70: Effect of fracture permeability on the gas recovery factor

Figure 71 displays the model average pressure drop for varied fracture permeability. Higher permeability yields more depletion consequently higher pressure drop. Figure 72 shows cumulative gas production with the same trend – higher permeability results in higher gas production. Figure 73 displays gas production rate, which decreases as the model is being depleted.

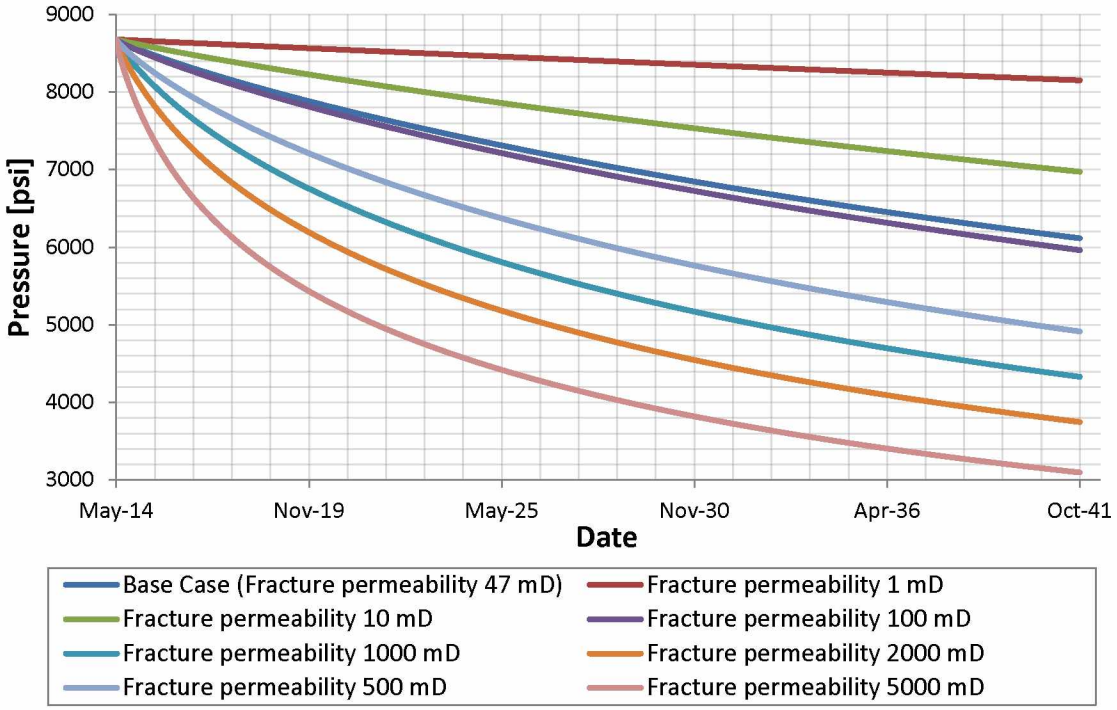

Figure 71: Model average pressure results for varied fracture permeability [psi]

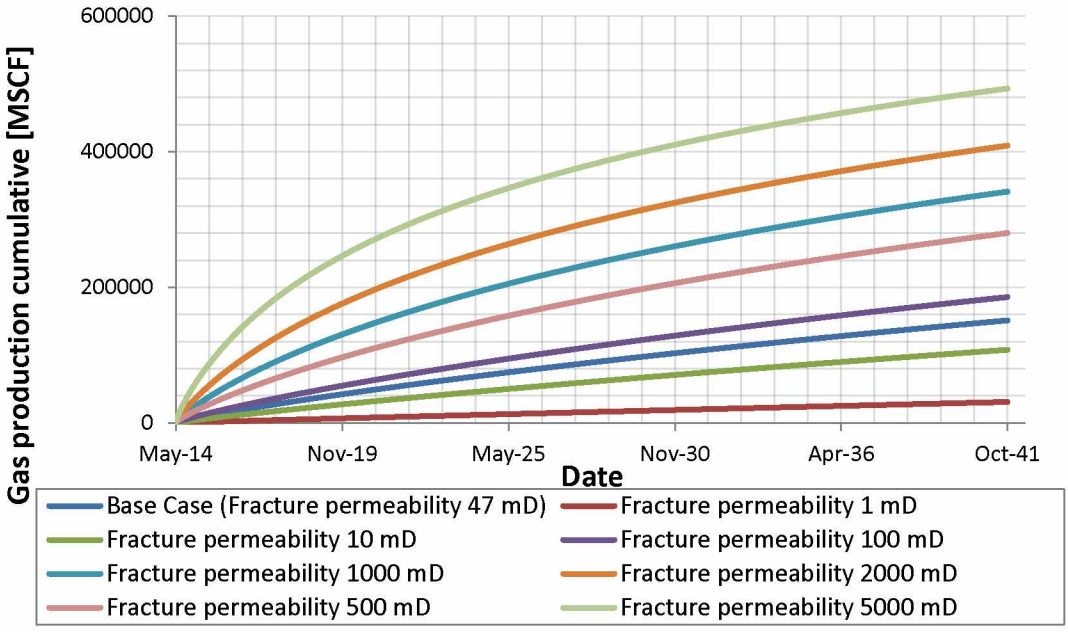

Figure 72: Gas production cumulative results for varied fracture permeability [MSCF]

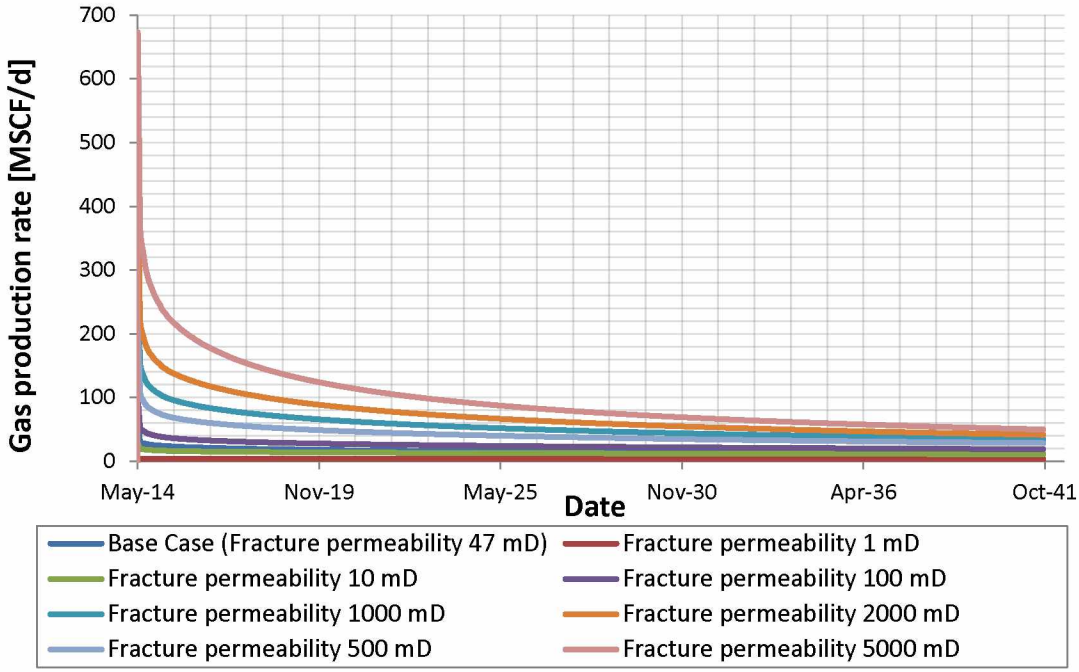

Figure 73: Gas production rate results for varied hydraulic fracture permeability [MSCF/day]

Table 21 and Table 22 display all simulation results for varied fracture permeability simulations.

Table 21: Simulation results for varied fracture permeability (Part I)

	Fracture Permeability 1000 mD	**Fracture Permeability 2000 mD**	**Fracture Permeability 5000 mD**	**Fracture Permeability 500 mD**
Pressure [psi]				
Initial value	8676.6	8676.6	8676.6	8676.6
Final value	4328.9	3746.5	3095.9	4913.7
Cumulative gas production [MMSCF]				
Final value	340.9	408.8	0.493	0.28
Gas production rate [MSCF/day]				
Maximum value	288.4	409.9	665.1	204.5
Final value	34.3	41.2	49.7	28.2
Gas in place [BSCF]				
Initial value	0.92	0.92	0.92	0.92
Final value	0.57	0.51	0.42	0.63
Recovery factor [%]				
Final value	38.0	44.6	54.3	31.5

Table 22: Simulation results for varied fracture permeability (Part II)

	Fracture Permeability 1mD	Fracture Permeability 10mD	Fracture Permeability 100mD	Base Case 47 mD
Pressure [psi]				
Initial value	8676.6	8676.6	8676.6	8676.6
Final value	8149.6	6971.7	5961.7	6114.1
Cumulative gas production [MMSCF]				
Final value	30.8	107.7	185.4	151.0
Gas production rate [MSCF/d]				
Maximum value	3.9	26.7	94	59.3
Final value	3.1	10.8	18.7	11.078
Gas in place [BSCF]				
Initial value	0.92	0.92	0.92	0.92
Final value	0.89	0.81	0.73	0.76
Recovery factor [%]				
Final value	3.3	12.0	20.7	17.4

4.8 Effect of Fracture Spacing

To investigate the effect of fracture spacing polygon zone sets with fracture spacing of 50 ft, 100 ft and 200 ft (Base Case) were simulated. Figure 74 displays zone set polygons used in the simulation.

Figure 75 shows the effect of different fracture spacing on the gas recovery factor. Pressure drop in 3D is displayed in Figure 76. Smaller fracture spacing gives smaller reservoir volume, which is easier to drain. Hence the gas recovery factor is higher for the smaller fracture spacing. Gas recovery factor was 17.4 %, 24.4% and 31.8% for the fracture spacing of 200 ft, 100 ft and 50 ft respectively.

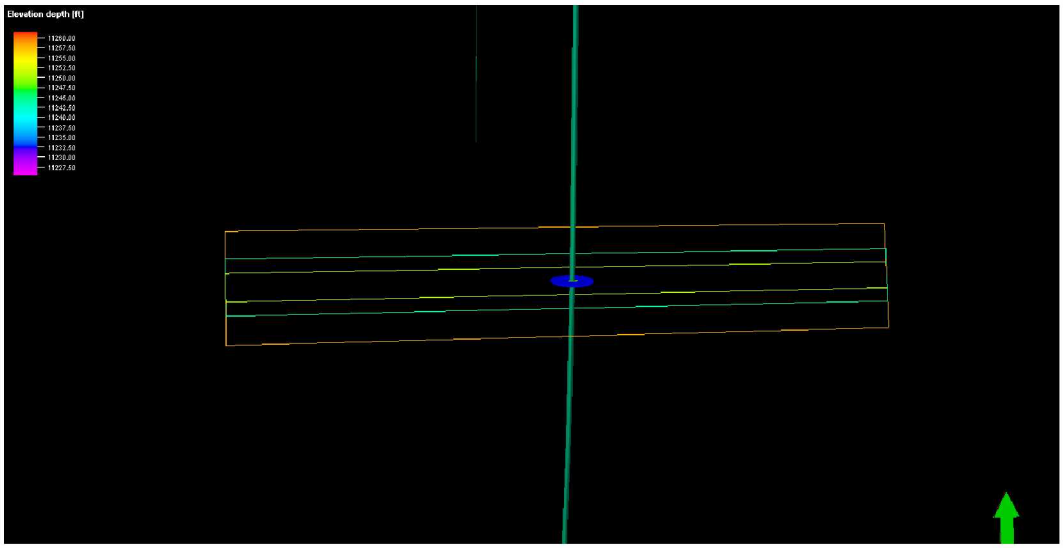

Figure 74: Fracture spacing zone set polygons (Top view)

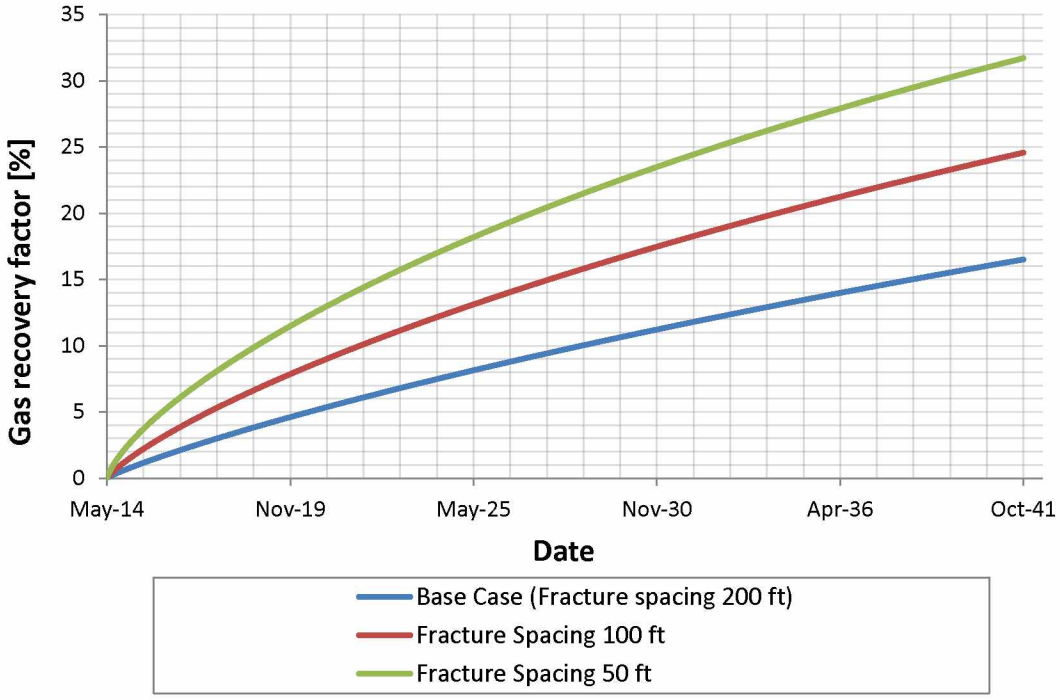

Figure 75: Effect of fracture spacing on gas recovery factor

Figures 77 through 80 show changes in pressure, gas production rate, cumulative gas production and gas in place for the different fracture spacing sizes. The results confirm the trend seen in the gas recovery factor.

Table 23: Simulation results for varied fracture spacing (Model I)

	Fracture Spacing 50 ft	**Fracture Spacing 100 ft**	**Base Case**
Pressure [psi]			
Initial value	8676.6	8676.6	8676.6
Final value	4835.9	5512.3	6114.1
Cumulative gas production [MMSCF]			
Final value	70.8	111.5	151.0
Gas production rate [MSCF/day]			
Maximum value	59.3	59.9	60.8
Final value	5.2	8.2	11.1
Gas in place [BSCF]			
Initial value	0.22	0.45	0.92
Final value	0.15	0.34	0.76
Recovery factor [%]			
Final value	31.8	24.4	17.4

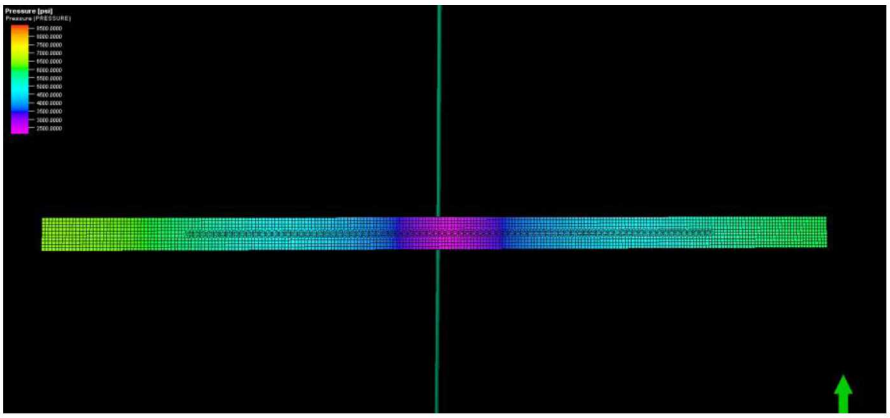

(a) Fracture spacing 50 ft

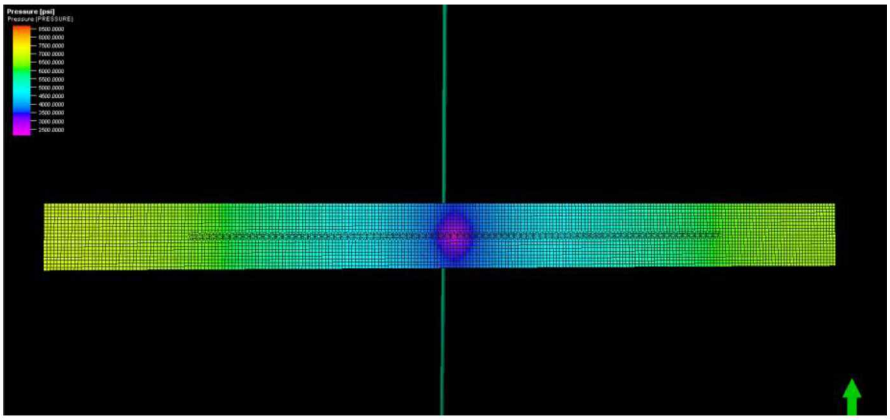

(b) Fracture spacing 100 ft

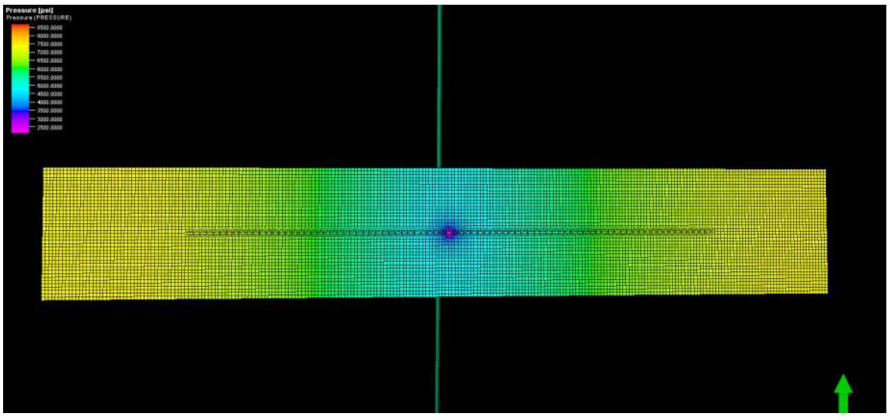

(c) Fracture spacing 200 ft

Figure 76: Pressure drop 3D results for varied fracture spacing at the end of the simulation (Top view)

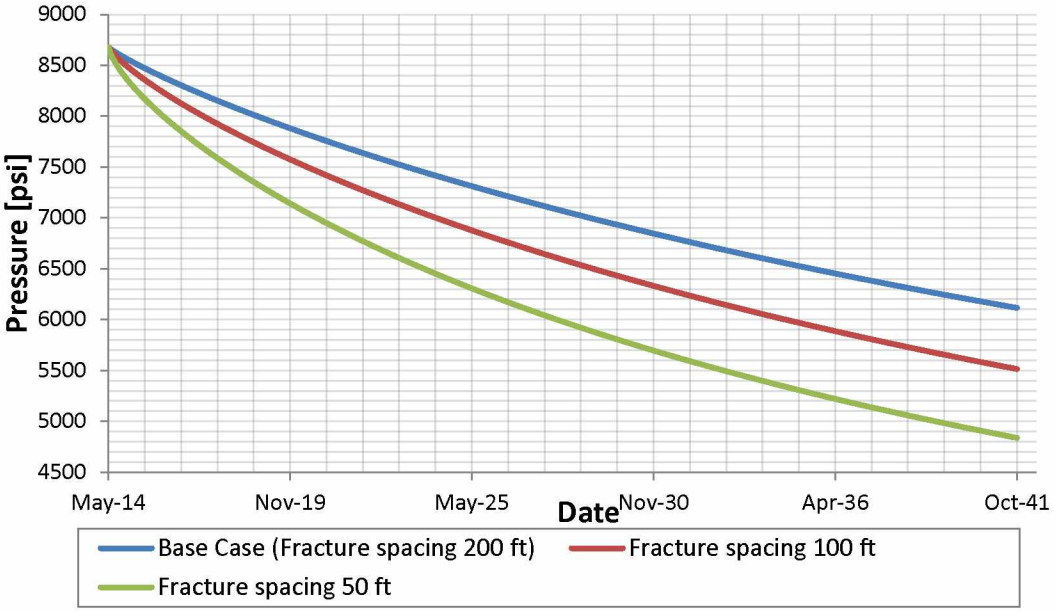

Figure 77: Model average pressure results for varied fracture spacing (Model I) [psi]

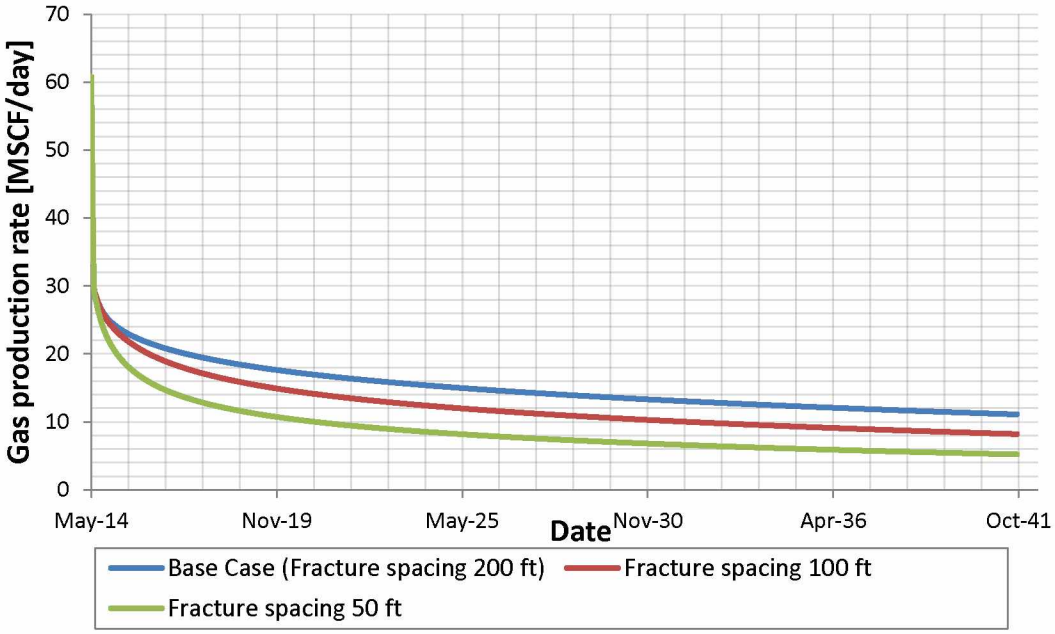

Figure 78: Gas production rate results for varied fracture spacing (Model I) [MSCF/day]

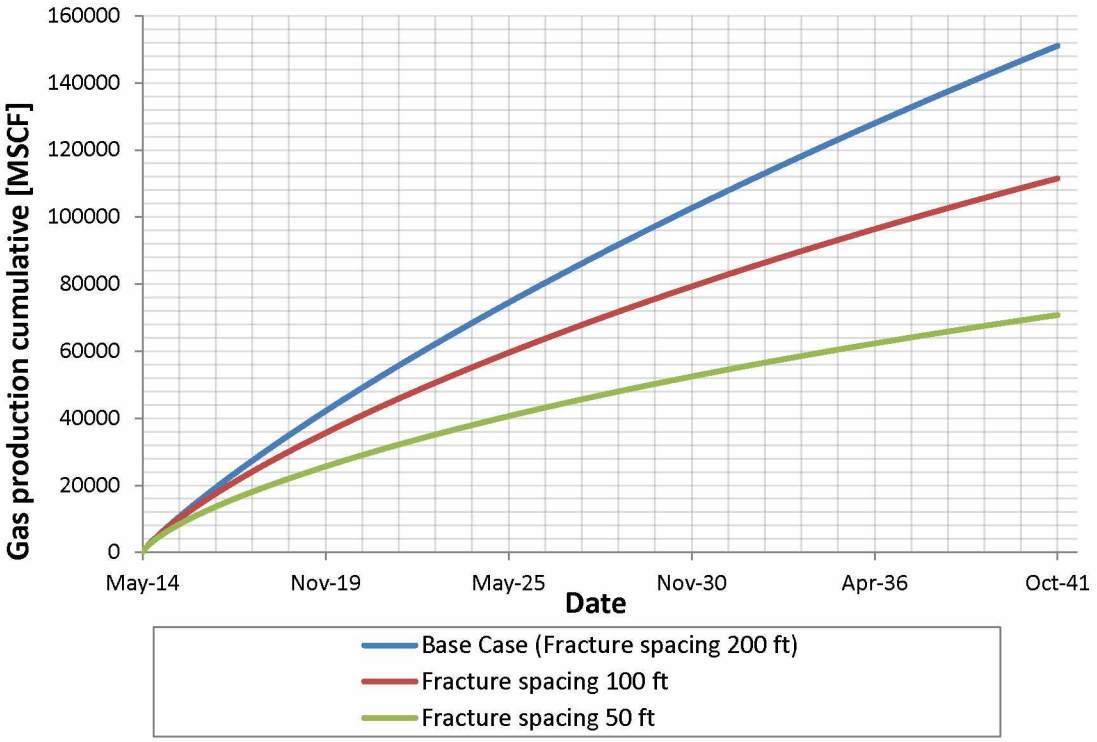

Figure 79: Cumulative gas production results for varied fracture spacing (Model I) [MSCF]

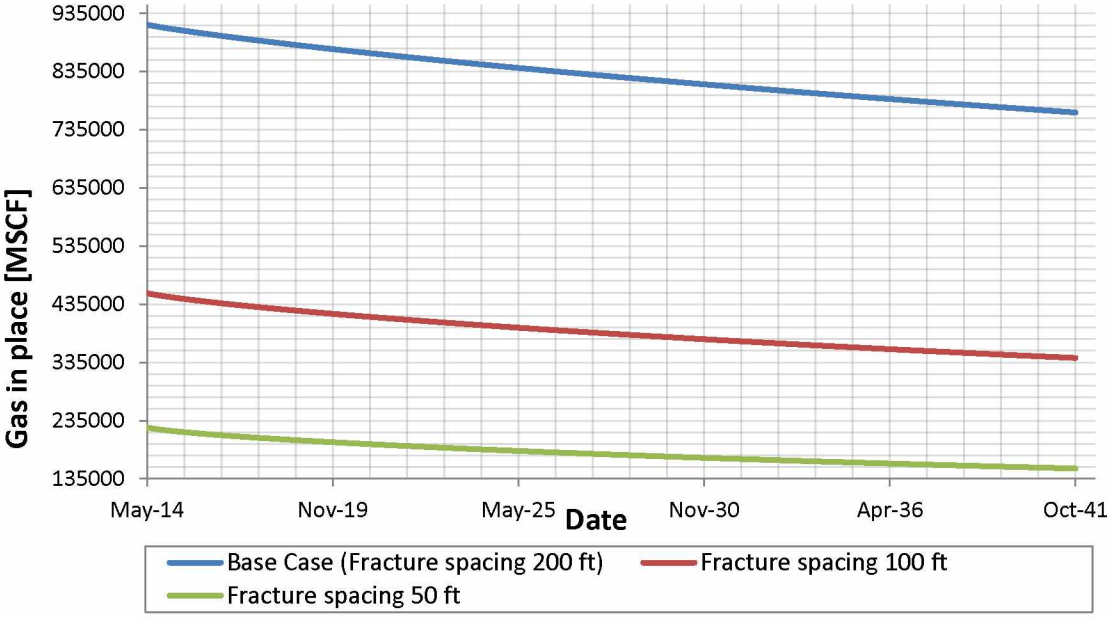

Figure 80: Changes in gas in place for varied fracture spacing (Model I) [MSCF]

4.9 Effect of Unpropped Zone Conductivity on Production Performance

Figure 81 shows the effects of unpropped zone conductivity on the gas recovery factor. Mangrove simulation has an option for unpropped zone conductivity, which can be specified before running the simulation. Fracture closure parameters are included in the Section 3.2.3 for the Base Case and were kept the same for all other cases. The highest unpropped zone conductivity yields the highest gas recovery factor.

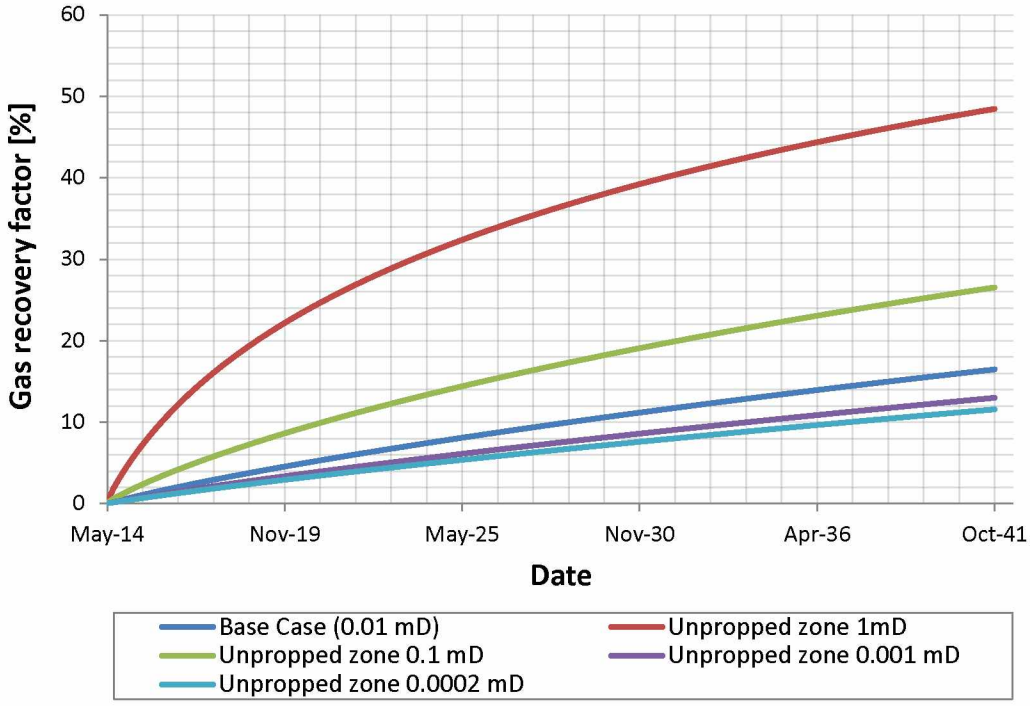

Figure 81: Gas recovery factor results for varied unpropped zone conductivity (Model I) [%]

Table 24 shows all simulation results. Figures 82 through 84 show average model pressure, gas production rate and cumulative produced gas results for varied unpropped zone simulations.

Table 24: Simulation results for varied unpropped zone conductivity (Model I)

	Unpropped Conductivity 0.001 mD-ft	**Unpropped Conductivity 1mD-ft**	**Unpropped Conductivity 0.0002 mD-ft**	**Unpropped Conductivity 0.1mD-ft**	**Unpropped Conductivity 0.01mD (Base Case)**
Pressure [psi]					
Initial value	8676.6	8676.6	8676.6	8676.6	8676.6
Final value	6816.6	3470.4	6996.8	5302.8	6114.1
Cumulative gas production [MMSCF]					
Final value	119.1	442.4	105.8	243.0	151.0

Table 24: Simulation results for varied zone conductivity (Model I) continued

Gas production rate [MSCF/d]					
Maximum value	33.2	498.1	23.4	159.4	59.9
Final value	9.4	16.9	8.5	15.0	11.9
Gas in place [BSCF]					
Initial value	0.92	0.92	0.92	0.92	0.92
Final value	0.80	0.47	0.81	0.67	0.76
Recovery factor [%]					
Final value	13.0	48.9	12.0	27.2	17.4

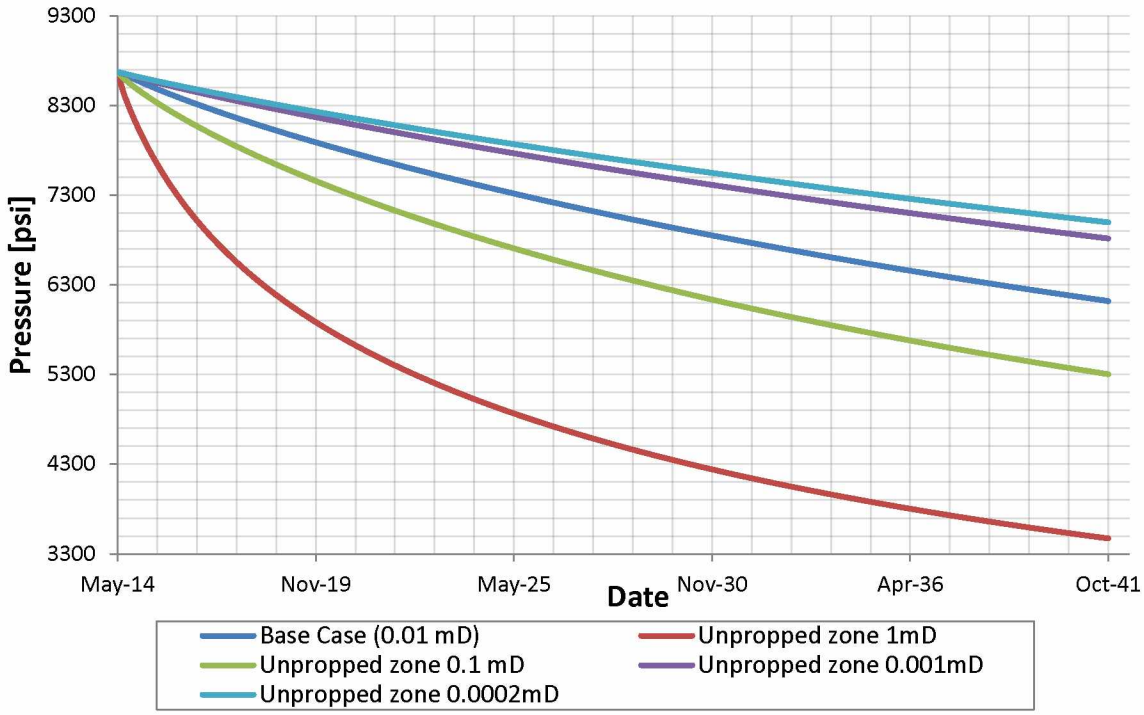

Figure 82: Model average pressure results for varied unpropped zone conductivity (Model I) [psi]

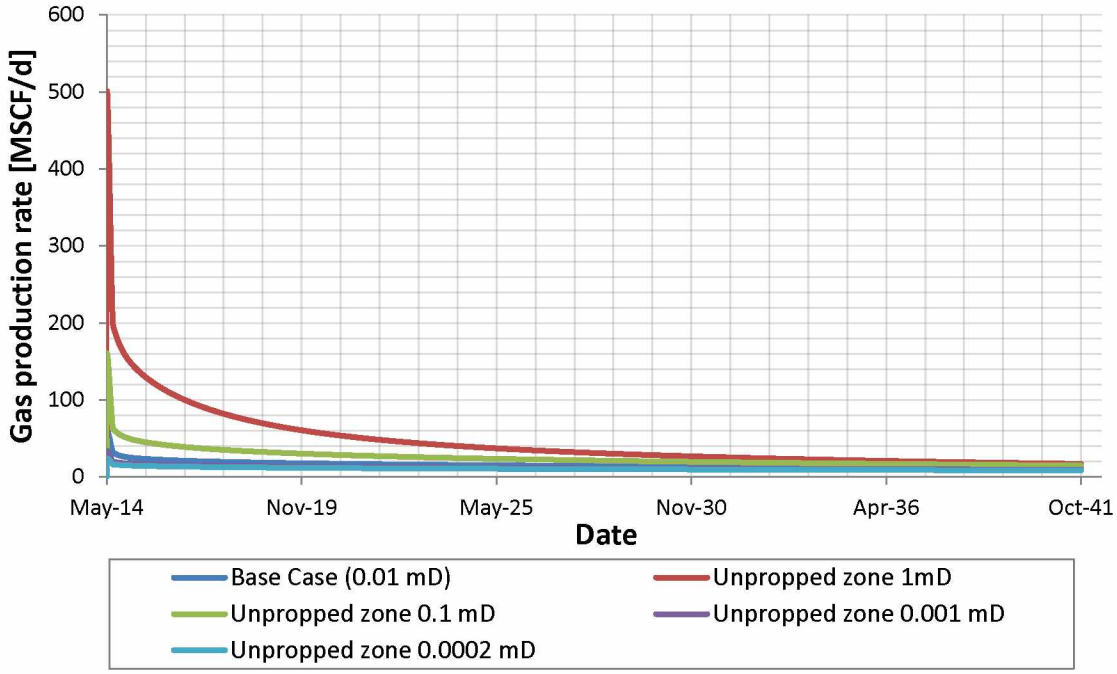

Figure 83: Gas production rate results for varied unpropped zone conductivity (Model I) [MSCF/day]

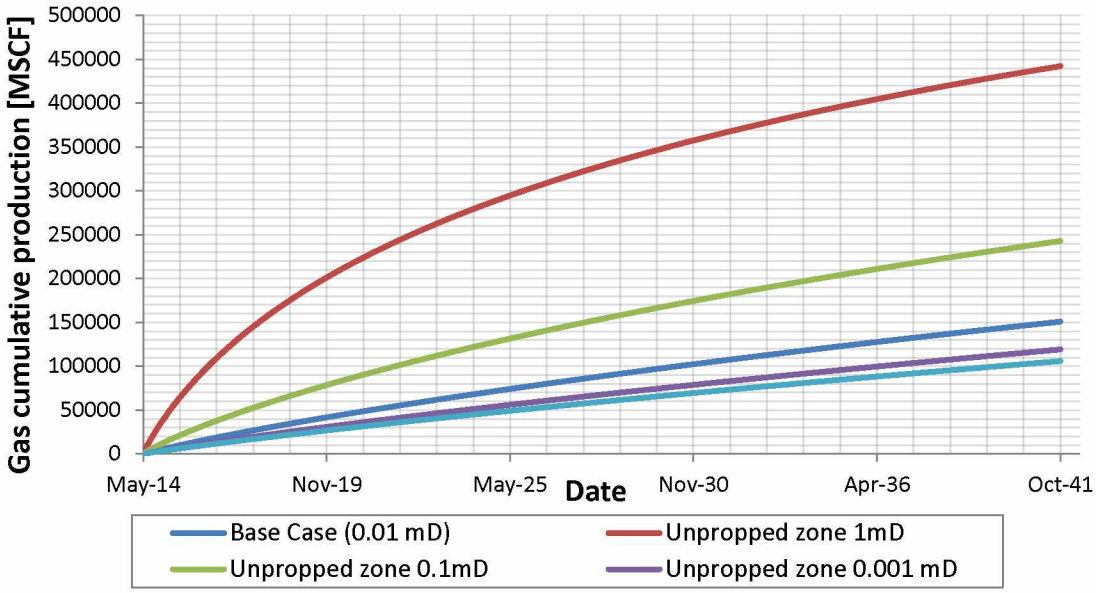

Figure 84: Cumulative gas production results for unpropped zone (Model I) [MSCF]

4.10 Effect of Non-Darcy Flow

Rubin (2010) indicated that non-Darcy flow was not occurring within the shale itself; therefore non-Darcy flow was ignored between matrix grids in the analysis. However, non-Darcy was included for flow through hydraulic fracture.

Non-Darcy coefficient was calculated using two different correlations: Cooke (1973) and Civan and Evans (1991).

The proppant type is CarboLite 20/40, so the constants for Cooke's correlation are a=1.540 and b=110,470. Maximum resulting permeability for the fracture for the Base Case is 47.06 mD. Cooke's correlation yielded the Forchheimer coefficient:

$$\beta = bK^{-a} = 110470 * (0.047D)^{-1.540} = 1.22281E07 \text{ ft}^{-1} \quad (12)$$

Civan and Evans correlation for the non-Darcy coefficient for the fracture yielded:

$$\beta = bK^{-a} = 1.485E10^{9} * (47.06mD)^{-1.021} = 2.91037E07 \text{ ft}^{-1} \quad (13)$$

Figure 85 shows the effect of non-Darcy flow on the recovery factor. While non-Darcy flow decreased the gas recovery due to the turbulent flow in the fracture, there was no significant difference between results whether using Cooke's or Civan and Evans correlations. With the increase in gas velocity, the inertial term in Forchheimer equation becomes important. This term also leads to the decrease in fracture conductivity (Wang, 2013). However, since the velocity term in the Forchheimer equation is squared, most previous studies were focused on high production rates, i.e. 10 MMSCF/day (Saboorian-Jooybari and Pourafshary, 2015). This study has very low production rate (Table 25), so the effects of non-Darcy flow are less significant, but still are present. The presence of non-Darcy effects in this case can be attributed to the fact that the contribution of the non-Darcy component is controlled by a combination of parameters including physical properties of the rock and flowing fluid and non-Darcy coefficient besides the velocity (flow rate) as a primary factor (Saboorian-Jooybari and Pourafshary, 2015). Figures 86-88 show the effect of non-Darcy flow on model average pressure, gas production rate and cumulative produced gas.

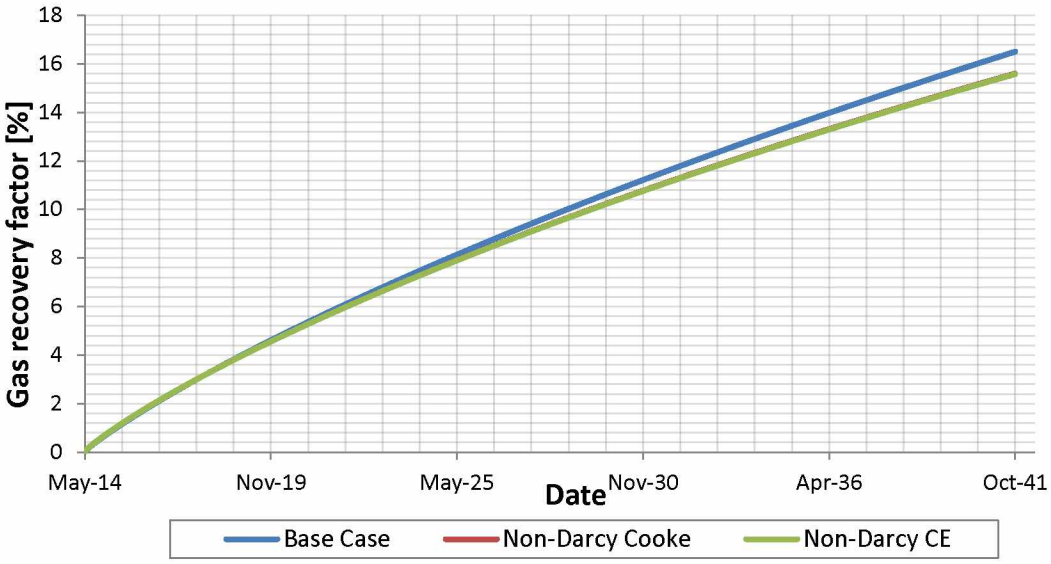

Figure 85: Effect of non-Darcy flow on the gas recovery factor

Table 25 lists all initial and final values for the simulation. Non-Darcy effect has a difference of 6.3% from the Base Case, which shows that Non-Darcy effect should be accounted for in the natural gas production.

Table 25: Simulation results for non-Darcy flow (Model I)

	Civan and Evans	**Cookes**	**Base Case**
Pressure [psi]			
Initial value	8676.6	8676.6	8676.6
Final value	6196.0	6193.2	6114.1
Cumulative gas production [MMSCF]			
Final value	142.6	142.8	151.0
Gas production rate [MSCF/day]			
Maximum value	74.4	74.3	59.3
Final value	10.0	10.0	11.1
Gas in place [BSCF]			
Initial value	0.92	0.92	0.92
Final value	0.77	0.77	0.76
Recovery factor [%]			
Final value	16.3	16.3	17.4

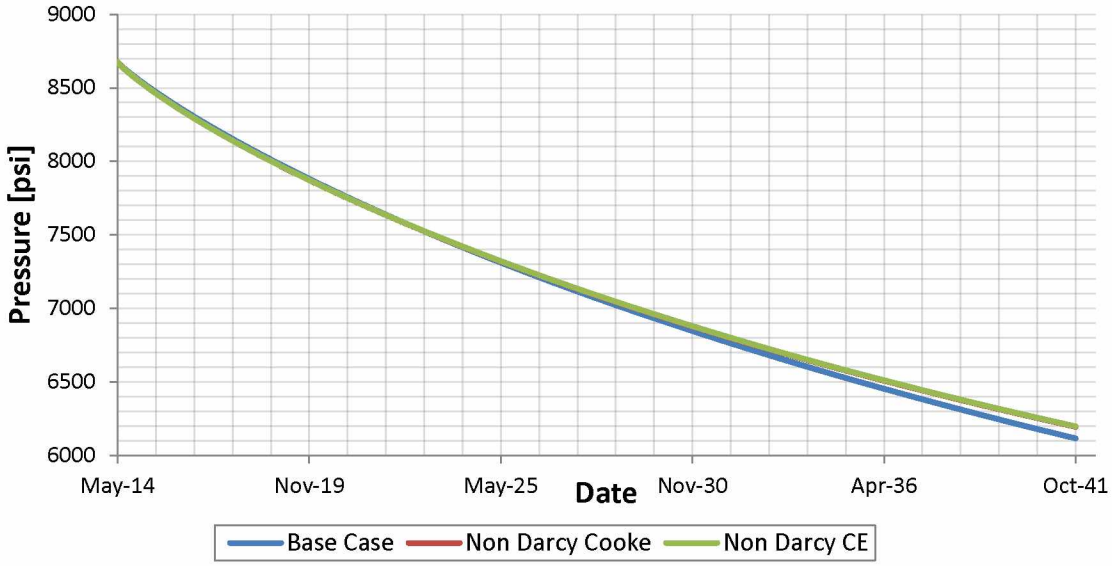

Figure 86: Model average pressure results for non-Darcy flow (Model I) [psia]

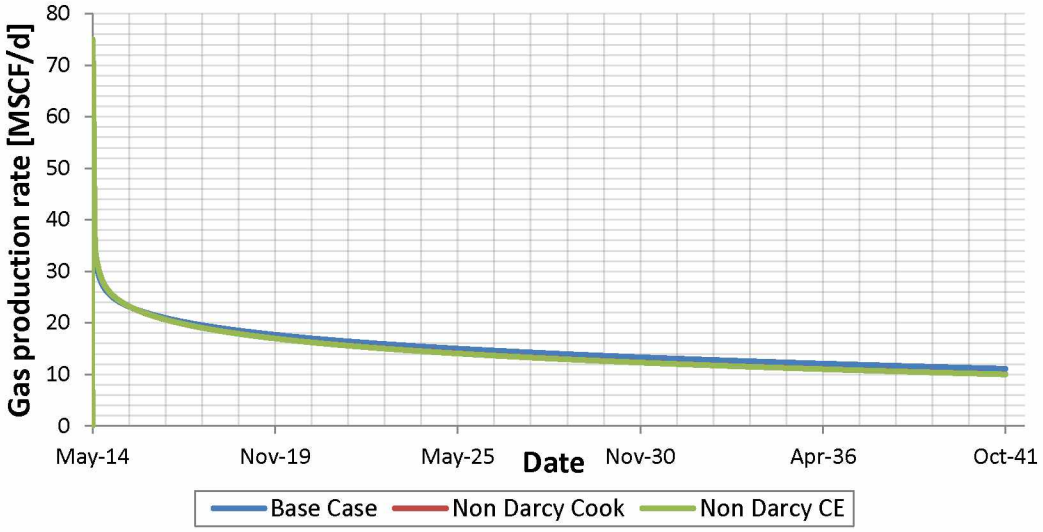

Figure 87: Gas production rate results for non-Darcy flow (Model I) [MSCF/day]

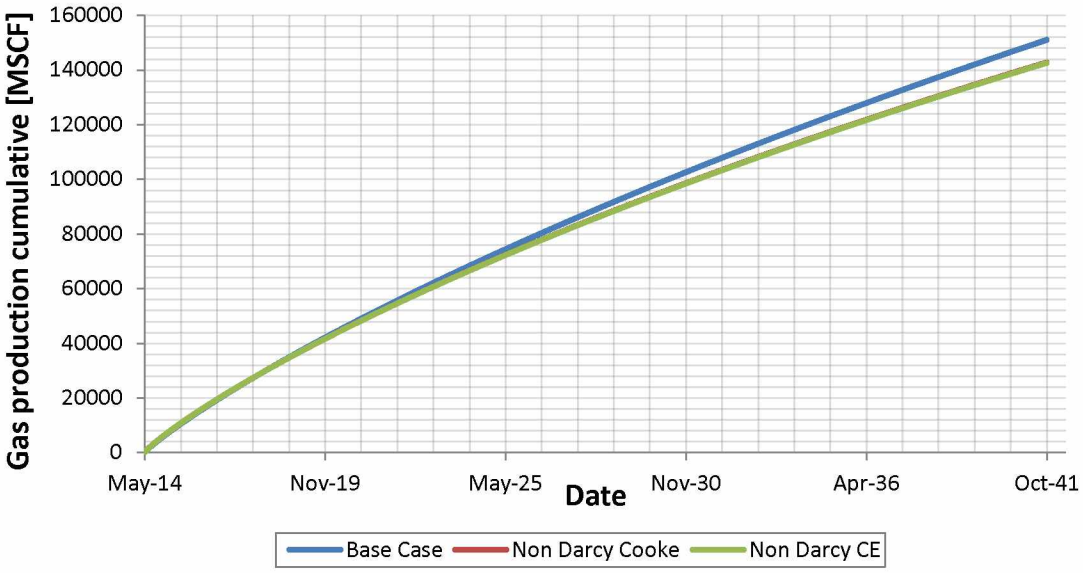

Figure 88: Cumulative gas production results for non-Darcy flow (Model I) [MSCF]

4.11 Effect of Gas Adsorption/Desorption

Langmuir isotherm parameters for Eagle Ford from Dong et al. (2012) are displayed in Table 26.

Table 26: Adsorption/desorption parameters for Eagle Ford (Dong et al., 2012)

Langmuir pressure [psia]	1000
Langmuir volume [scf/ton]	60

Figure 89 displays gas recovery factor for the Base Case and adsorption/desorption case. Recovery factors for gas adsorption/desorption were lower than in the Base Case because initial total gas in place is much larger than in the Base Case. Figures 90-93 show the gas in place, model average pressure, gas production rate, and cumulative gas production results. The reservoir pressure decreases faster in the Base Case since once the desorption process is triggered, it sends free gas to the pore space, which keeps the pressure at higher levels. Since the Langmuir volume constant used in this study is low, there is not any significant pressure support

from the adsorbed gas. There is a small change in the adsorbed gas in place during the production since the desorption process is not effectively activated. The reason for this is that adsorbed gas is released at very low pressures, and it is difficult to get into low-pressure values in shale formations especially away from the hydraulic fracture.

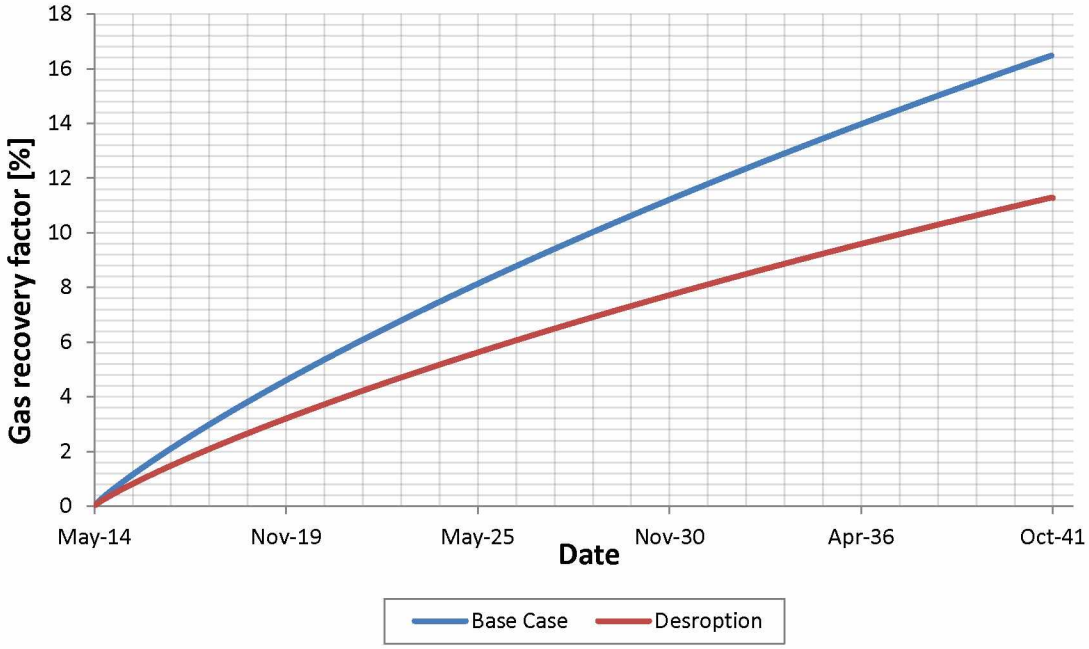

Figure 89: Effect of adsorption on gas recovery factor (Model I) [%]

Table 27: Simulation results for gas adsorpton case

	Desorption	**Base Case**
Pressure [psi]		
Initial value	8676.6	8676.6
Final value	6419.8	6114.1
Cumulative gas production [MMSCF]		
Final value	162.2	138.2
Gas production rate [MSCF/day]		
Maximum value	65.0	59.3
Final value	12.6	11.1
Free gas in place [BSCF]		
Initial value	0.92	0.92
Final value	0.76	0.76
Total gas in place [BSCF]		
Initial value	1.2	0.92
Final value	1.1	0.76
Recovery factor [%]		
Initial value	8.3	17.4

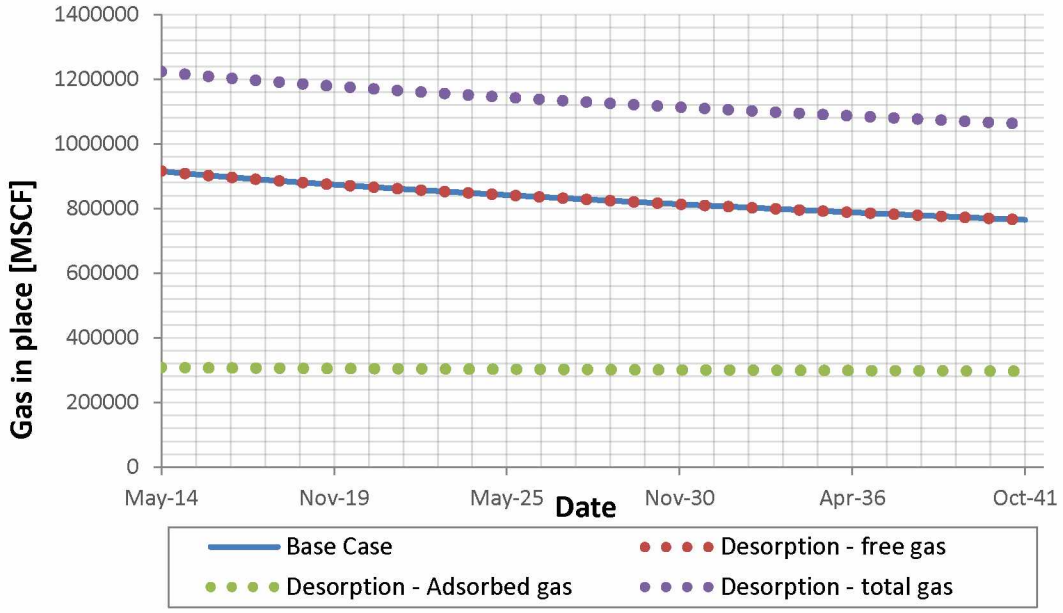

Figure 90: Changes in gas in place with gas adsorption (Model I) [MSCF]

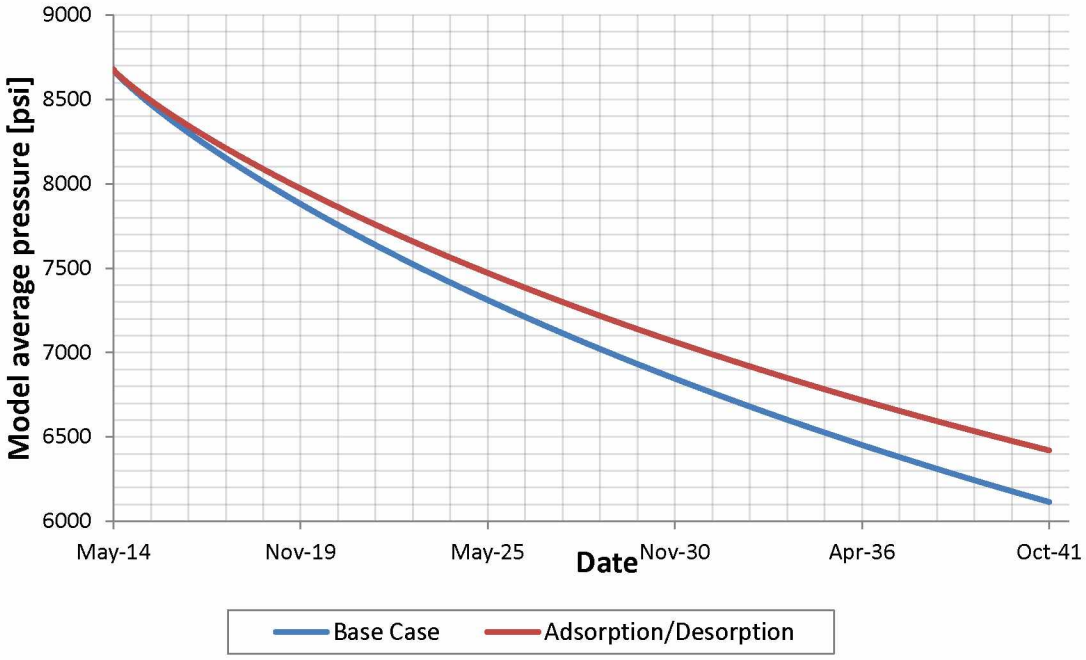

Figure 91: Model average pressure results for gas adsorption case (Model I) [psi]

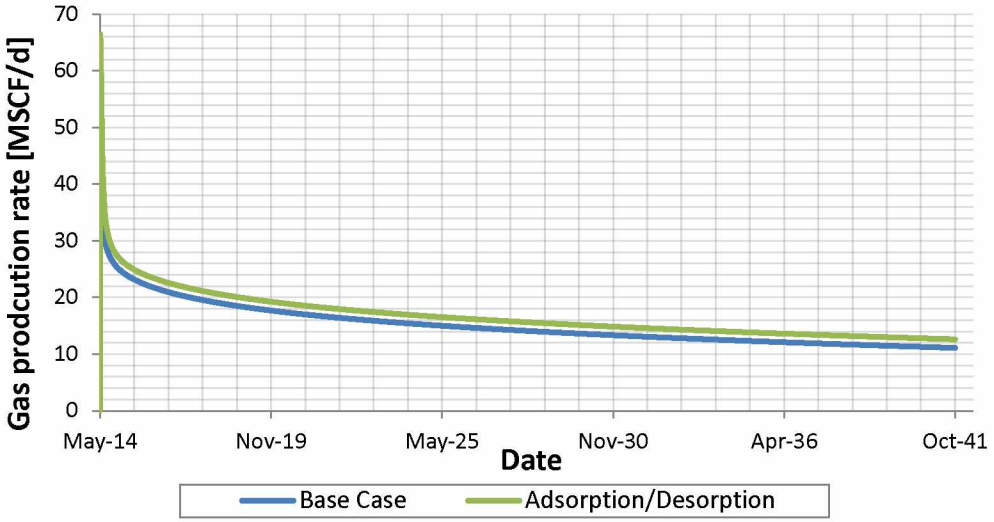

Figure 92: Gas production rate results for gas adsorption case (Model I) [MSCF/day]

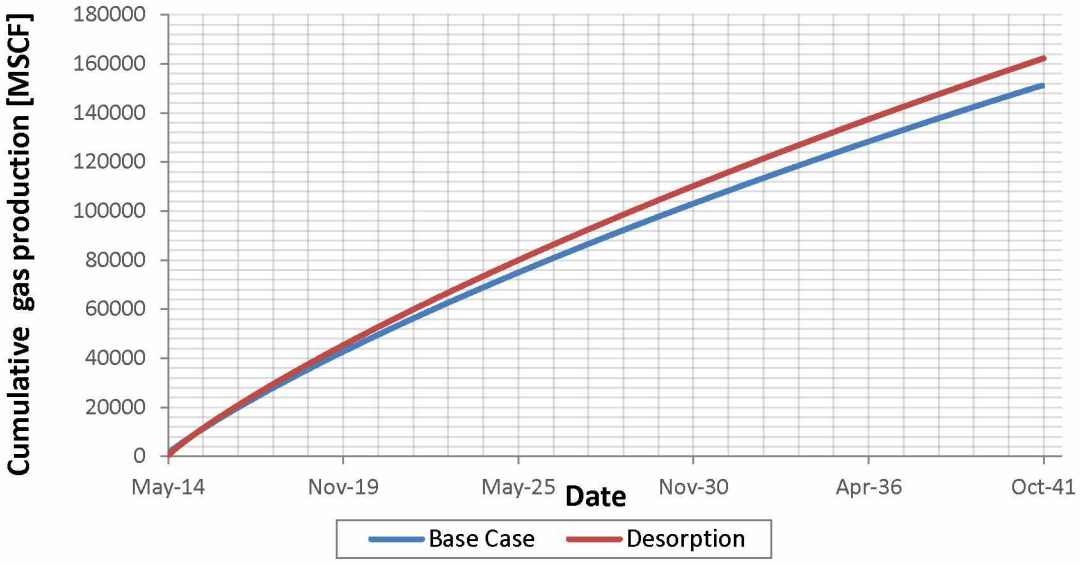

Figure 93: Cumulative gas production results for gas adsorption case (Model I) [MSCF]

4.12 Effect of DFN

4.12.1 Planar SRV

Figure 94 displays top view of pressure results at the end of the simulation for the base case Model I and Model II, respectively. Choosing larger number of fractures for the same stage

in Model II resulted in smaller fracture length. Elliptical drainage area is present. Pressure drop is more significant near the wellbore for both cases. The pressure drop is significantly larger in Model II due to the smaller SRV. As seen in the case with varied fracture spacing, smaller SRV produces higher reservoir pressure drop during production due to smaller area of the zoneset polygon. It should be noted that Model II has smaller SRV per well and need tighter well spacing, see gas in place in Table 28.

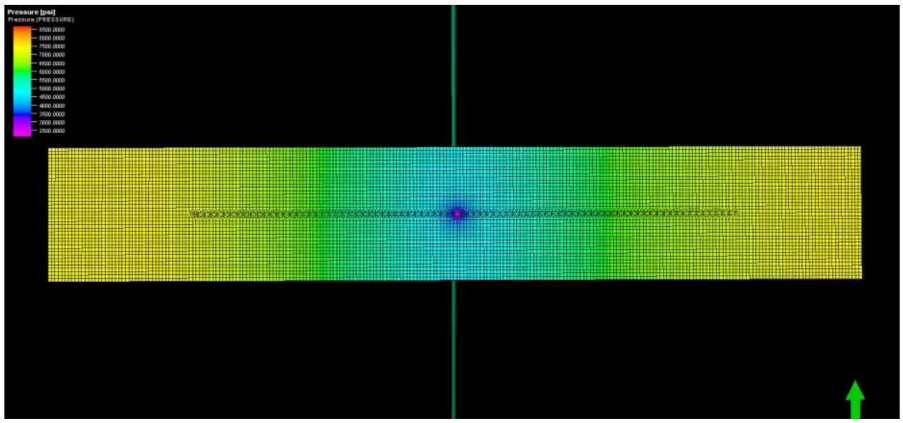

(a) Model I

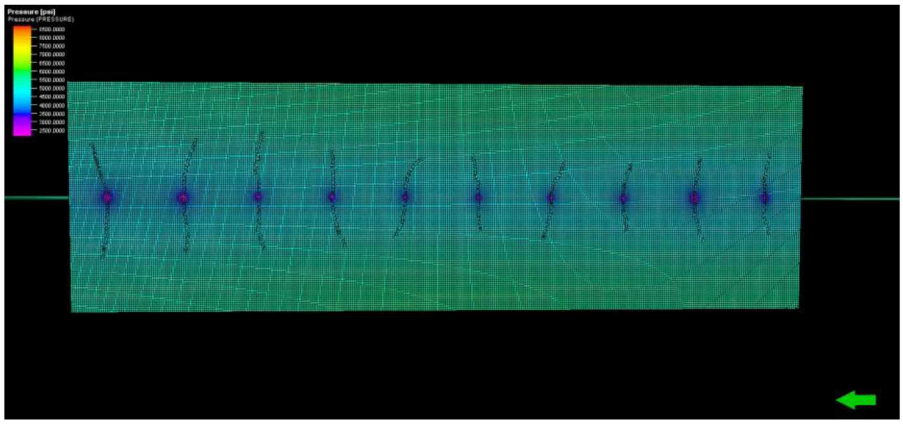

(b) Model II

Figure 94: Top view of 3D pressure results at the end of the simulation (Model I, Model II) [psi]

Figures 95 -98 show gas recovery factor, cumulative gas production, gas production rate and gas in place, respectively.

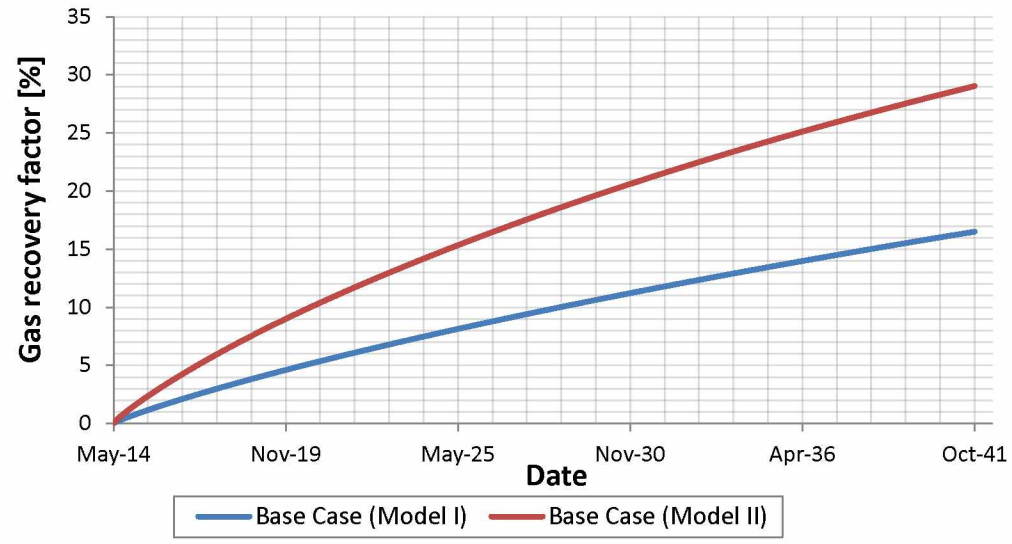

Figure 95: Model average pressure results for the Base Case (Model I and Model II) [psi]

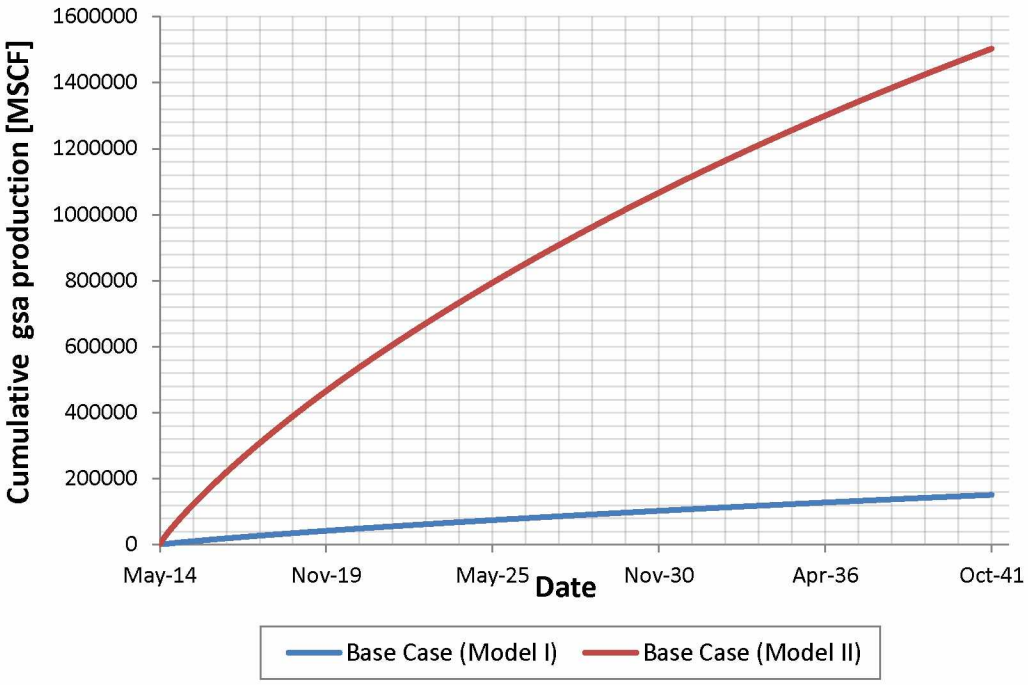

Figure 96: Cumulative gas production results for the Base Case (Model I and Model II) [MSCF]

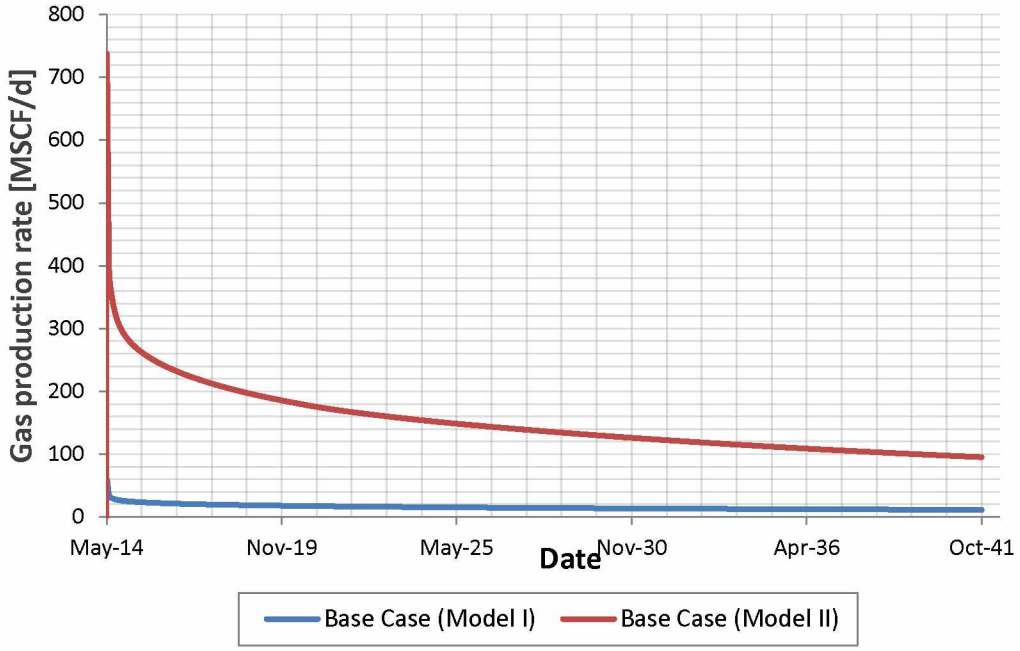

Figure 97: Gas production rate results for the Base Case (Model I and Model II) [MSCF/day]

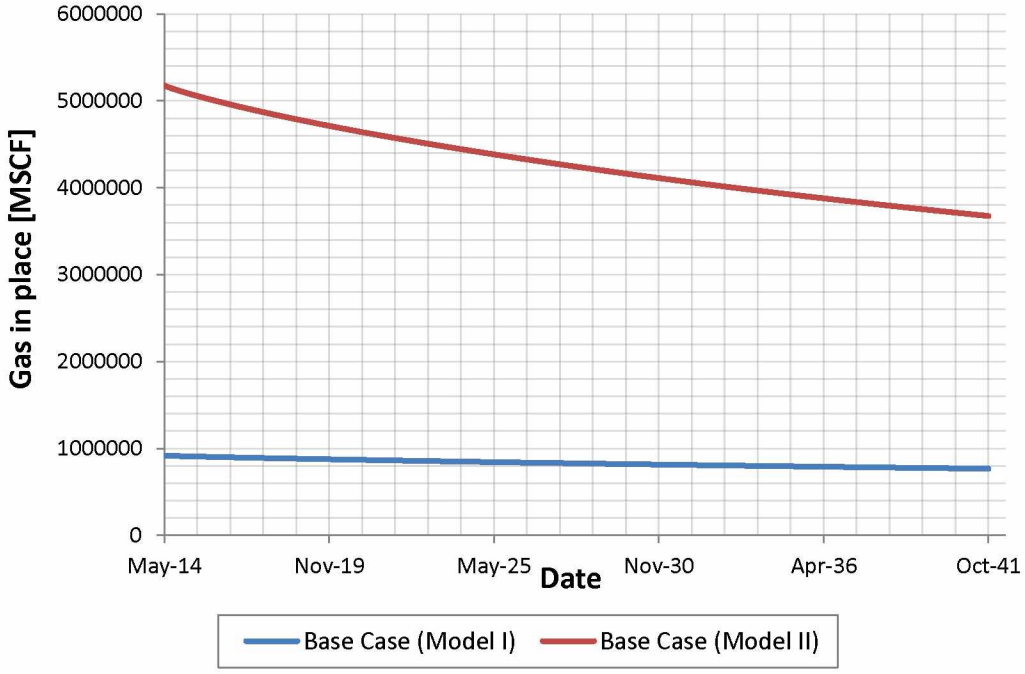

Figure 98: Model gas in place results for the Base Case (Model I and Model II) [MSCF]

Table 28 shows initial and final simulation results.

Table 28: Simulation results for the Base Case (Model I and Model II)

	Single Fracture (Model I)	Ten Fractures (Model II)
Pressure [psi]		
Initial value	8676.6	8688.0
Final value	6114.1	4905.6
Cumulative gas production [MMSCF]		
Final value	151.0	1502.8
Gas production [MSCF/day]		
Maximum value	59.3	729.3
Final value	11.1	95.0
Gas in place [BSCF]		
Initial value	0.92	5.2
Final value	0.76	3.7
Recovery factor [%]		
Final value	17.4	28.8

4.12.2 Effect of DFN Orientation

4.12.2.1 Model I

Figure 99 displays top view results for pressure for varied DFN orientation for Model I zoneset polygon at the end of the simulation. Elliptical drainage area is no longer present. Figure 100 displays the gas recovery factor for varied DFN orientation. Recovery factor was higher for DFN models since they resulted in the larger fracture area then in the Base Case. All simulation results are listed in Table 29.

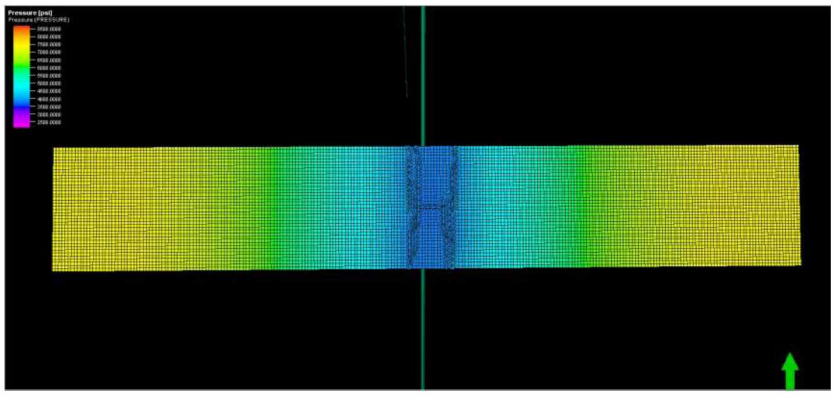

(a) DFN orientation of 0 degrees

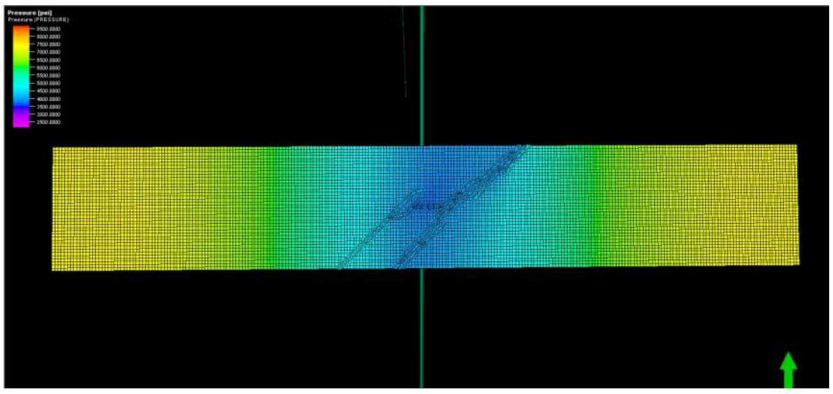

(b) DFN orientation of 45 degrees

Figure 99: 3D pressure resuls for varied DFN orientation at the end of the simulation (Model I) [psi]

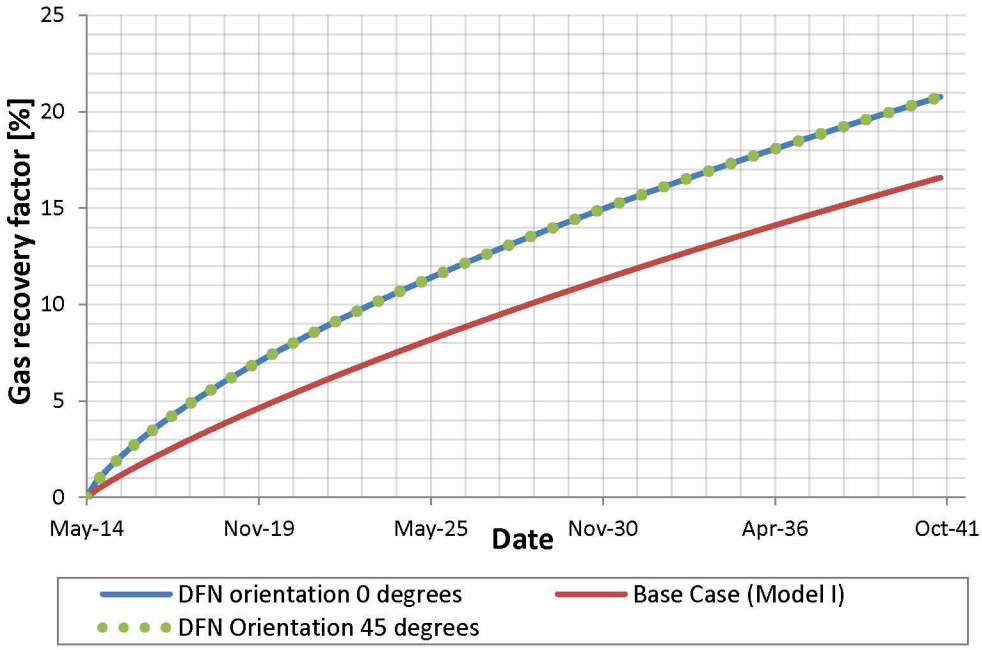

Figure 100: Effect of DFN orientation on gas recovery factor (Model I) [psi]

Table 29: Simulation results for varied DFN orienatation (Model I)

	DFN orientation 0	**DFN orientation 45**	**Base Case**
Pressure [psi]			
Initial value	8676.6	8676.6	8676.6
Final value	5948.7	5866.8	6114.1
Cumulative gas production [MMSCF]			
Final value	190.4	197.7	151.0
Gas production rate [MSCF/day]			
Maximum value	202.2	233.4	59.3
Final value	12.2	12.4	11.1
Gas in place [BSCF]			

Table 29: Simulation results for varied DFN orientation (Model I) continued

Initial value	0.92	0.91	0.92
Final value	0.72	0.71	0.76
Recovery factor [%]			
Final value	21.7	22.0	17.4

Figures 101 through 103 show model average pressure, gas production rate and gas cumulative production respectively.

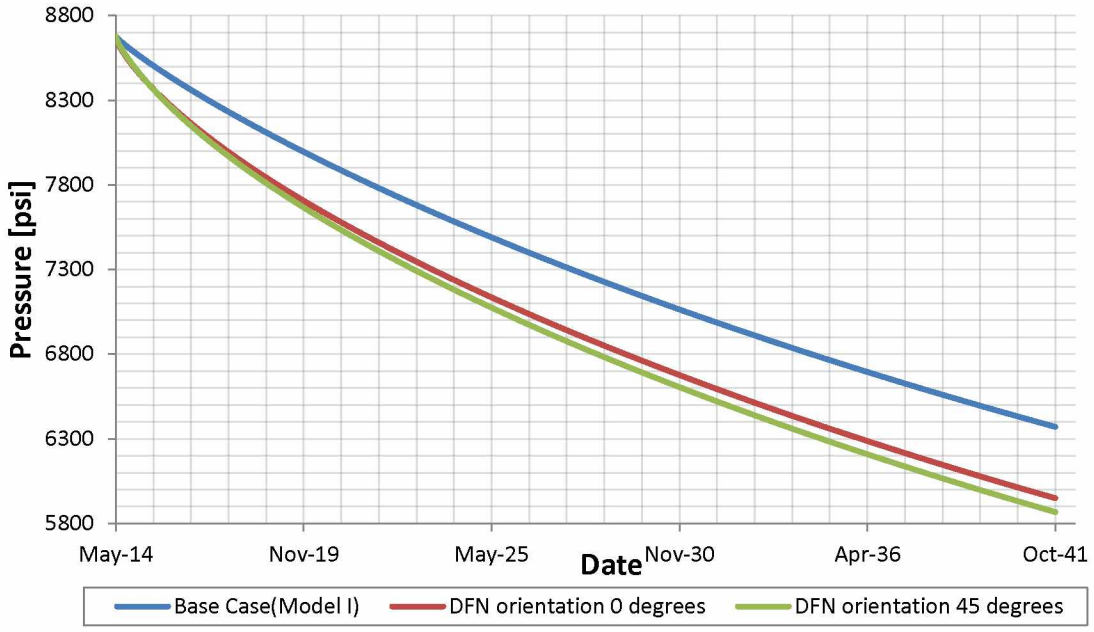

Figure 101: Model average pressure result for varied DFN orientation (Model I) [psi]

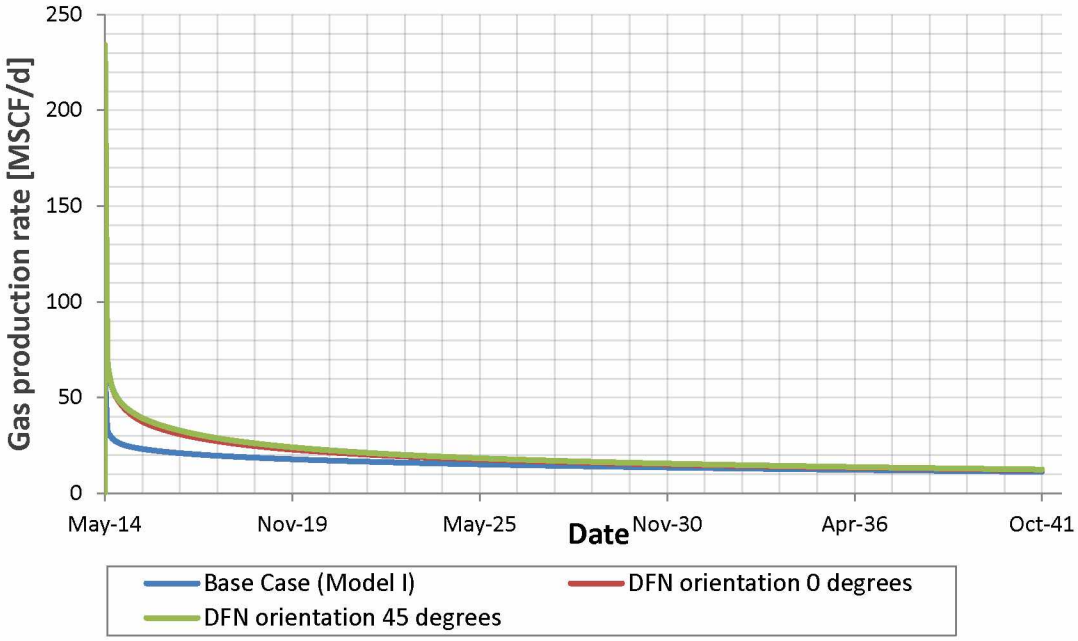

Figure 102: Gas rate result for varied DFN orientation (Model I) [MSCF/day]

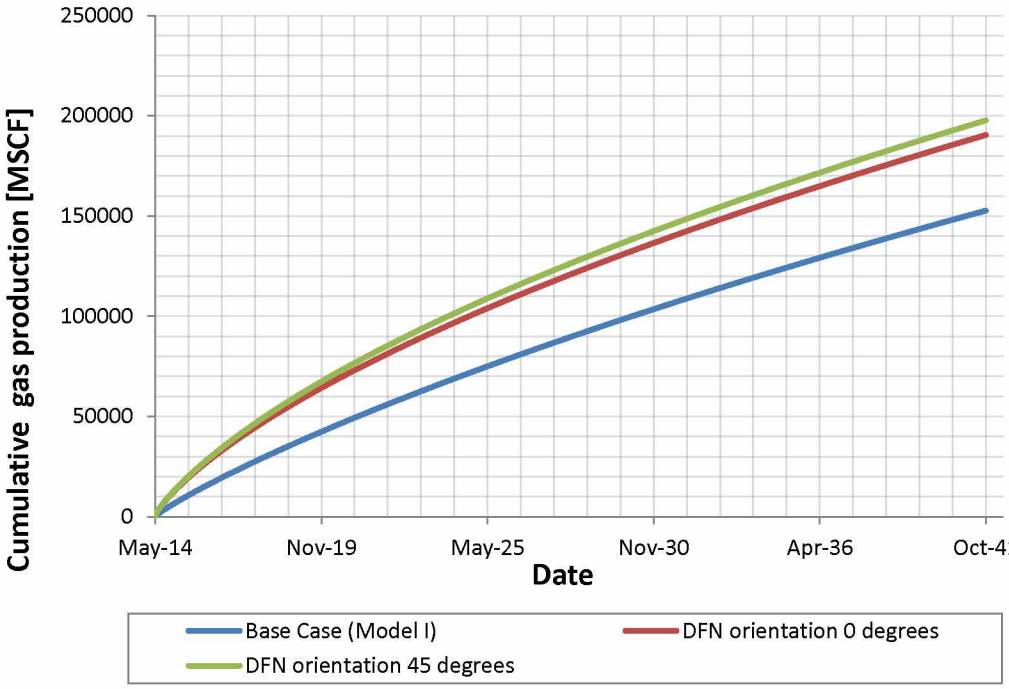

Figure 103: Cumulative gas production for varied DFN orientation (Model I) [MSCF]

4.12.2.2 Model II

Figure 104 shows the top view of pressure results for the varied DFN orientations for Model II at the end of the simulation. There is no significant difference between the two cases. Figure 105 shows the gas recovery factor. Base Case (No DFN) has the highest recovery factor because it resulted in the higher fracture area than the cases with natural fracture networks. Figures 106-108 show model average pressure, gas production rate and cumulative gas produced as versus pressure. Table 30 lists all simulation results for this case.

:

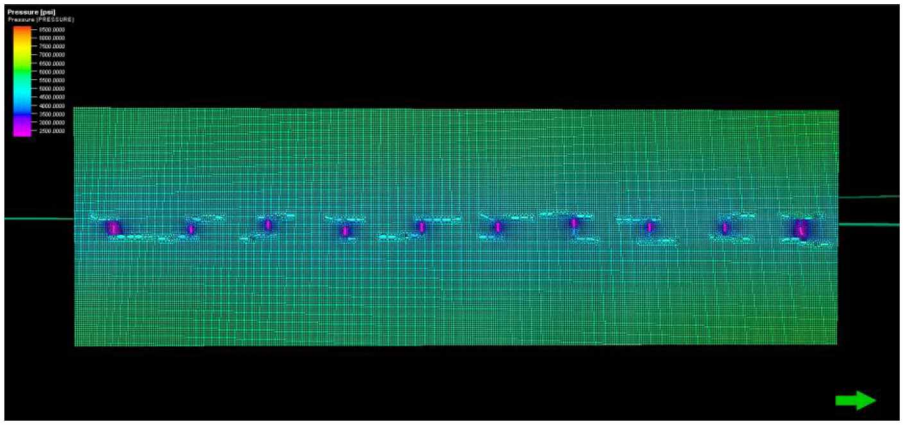

(a) DFN orientation 0 degrees

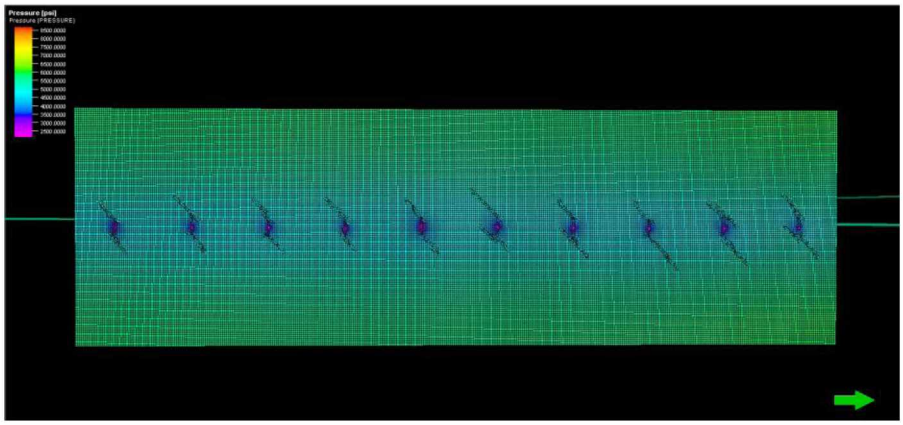

(b) DFN orientation 45 degrees

Figure 104: Top view of 3D pressure results for varied DFN orientation at the end of the simulation (Model II) [psi]

Table 30: Simulation results for varied DFN orientation (Model II)

	DFN orientation 0	DFN orientation 45	Base Case
Pressure [psi]			
Initial value	8688.5	8688.5	8687.9
Final value	5124.7	5192.8	4905.6
Cumulative gas production [MMSCF]			
Final value	1422.2	1400.6	1502.8
Gas production rate [MSCF/day]			
Maximum value	653.7	691.5	729.3
Final value	88.4	91.7	95.0
Gas in place [BSCF]			
Initial value	5.1	5.2	5.2
Final value	3.7	3.8	3.7
Recovery factor [%]			
Final value	27.5	26.9	28.8

Figures 106-108 show models average pressure, gas production rate and cumulative gas production plots, which confirm results reflected in Table 30 and the gas recovery plot.

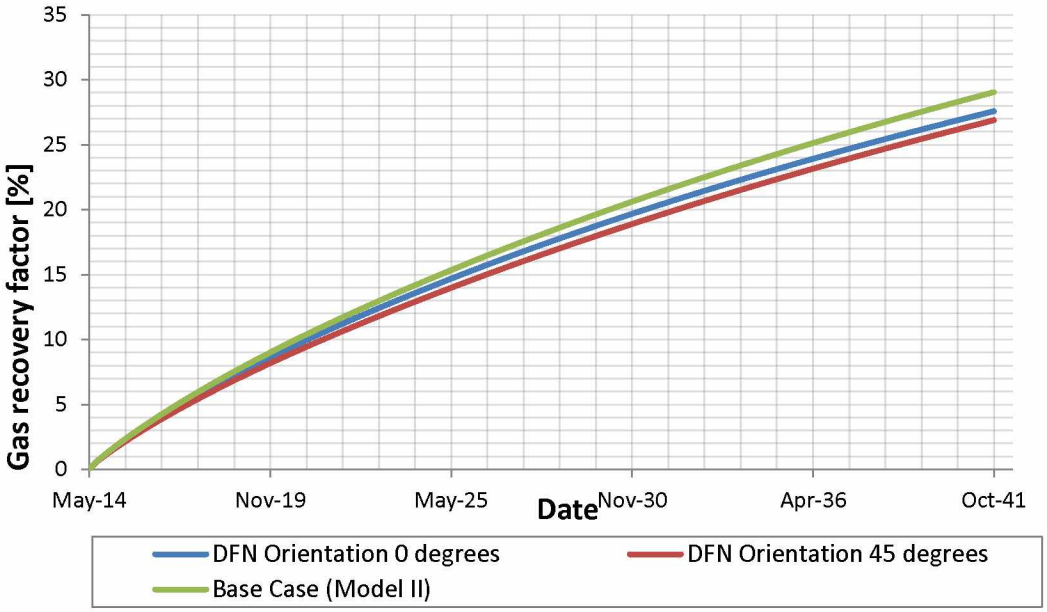

Figure 105: Effect of varied DFN orientation on the gas recovery factor

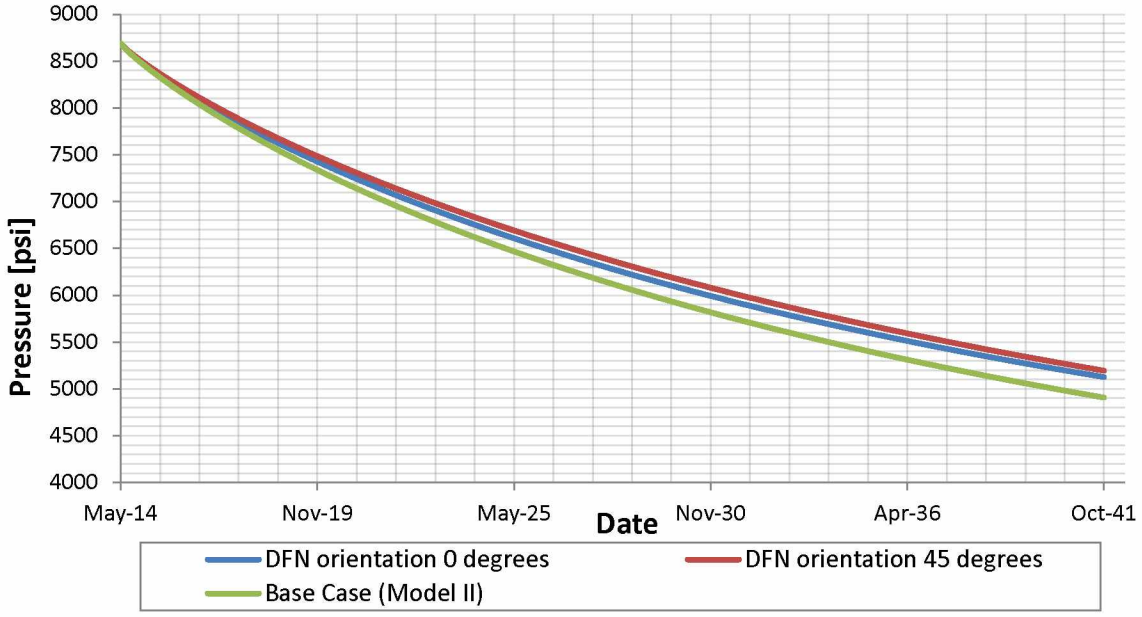

Figure 106: Model average pressure results for varied DFN orientation (Model II) [psi]

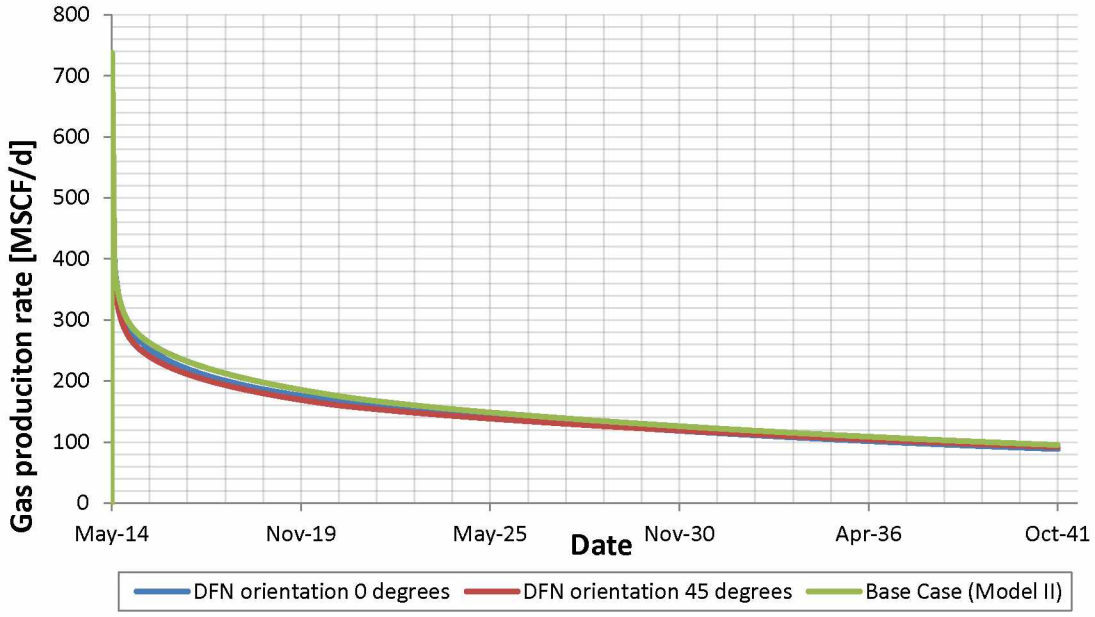

Figure 107: Gas production rate for varied DFN orientation (Model II) [MSCF/day]

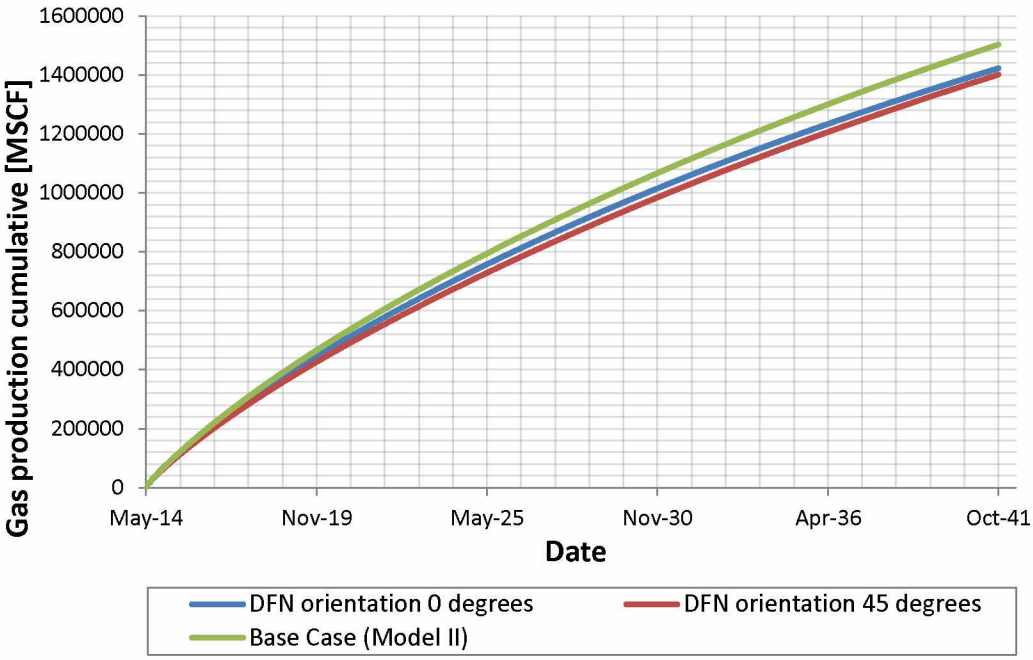

Figure 108: Cumulative gas production for varied DFN orientation (Model II) [MSCF]

4.12.3 Effect of DFN Fracture Spacing

4.12.3.1 Model I

Figure 109 shows the top view of pressure results for varied DFN fracture spacing at the end of the simulation. DFN fracture spacing of 10 ft does not have elliptical drainage area due to a larger propped fracture area. Figure 110 shows the gas recovery factor. Natural fracture spacing of 10 ft gives the highest recovery factor due to the largest propped fracture area. Table 31 lists all simulation results for varied DFN fracture spacing sets. Figures 111 through 113 show model average pressure, gas production rate and cumulative gas production results.

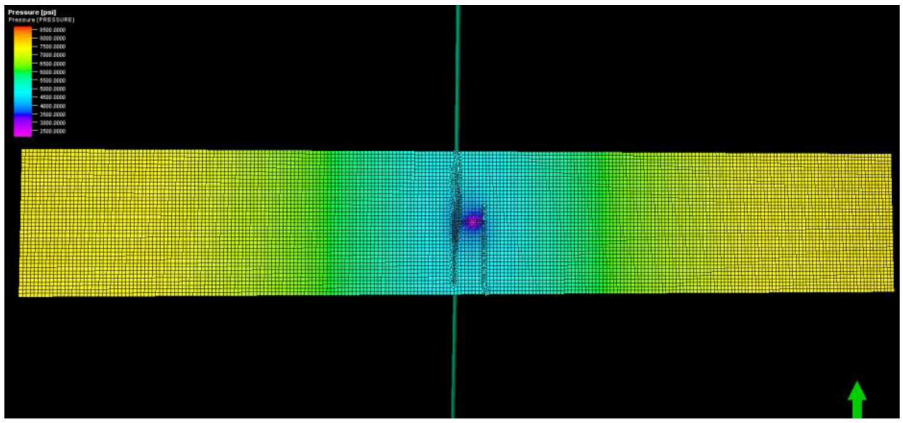

(a) DFN fracture spacing 1 ft

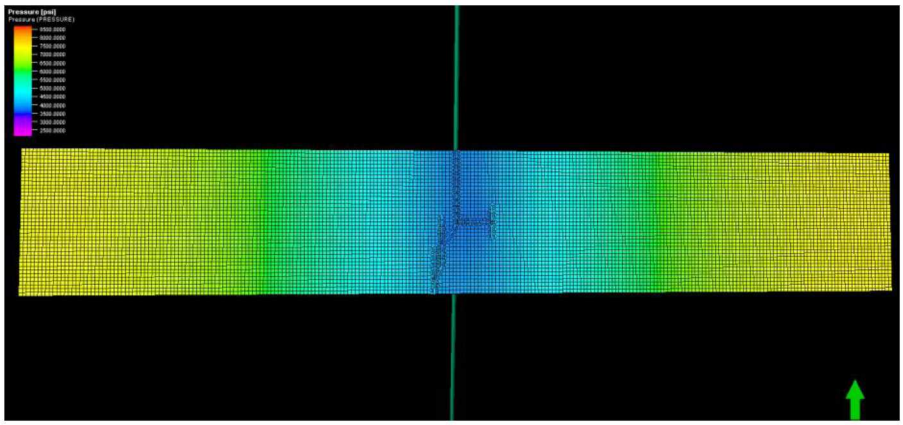

b) DFN fracture spacing 10 ft

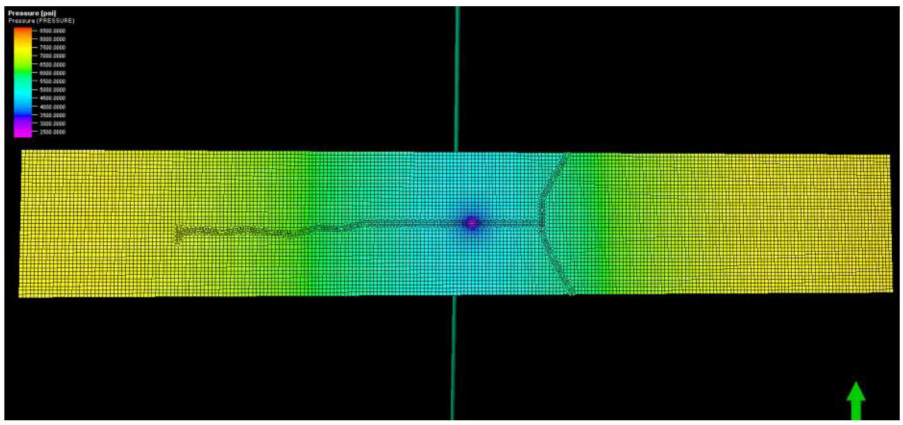

c) DFN fracture spacing 100 ft

Figure 109: Top view 3D pressure results for varied DFN fracture spacing at the end of the simulation [psi]

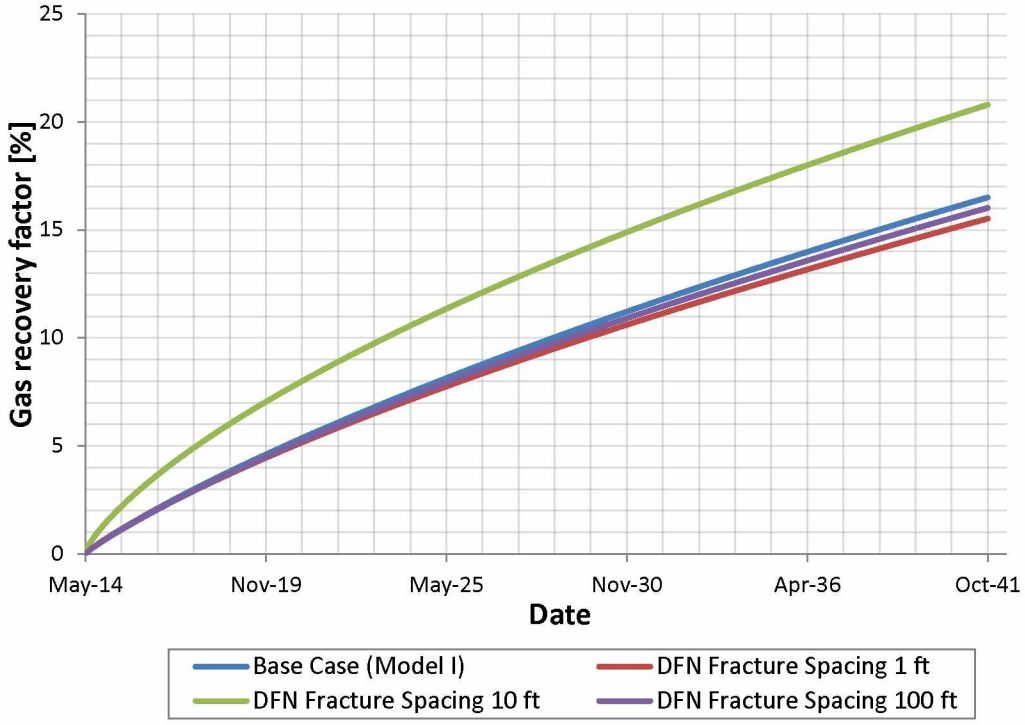

Figure 110: Gas recovery factor for varied DFN fracture spacing (Model I) [%]

Table 31: Simulation results for varied DFN fracture spacing (Model I)

	DFN Fracture Spacing 1 ft	**DFN Fracture Spacing 10ft**	**DFN Fracture Spacing 100 ft**	**Base Case**
Pressure [psi]				
Initial value	8676.6	8676.6	8676.6	8676.6
Final value	6535.1	5967.4	6465.3	6114.1
Cumulative gas production [MMSCF]				
Final value	142.4	191.1	146.8	151.0
Gas production rate [MSCF/day]				
Maximum value	60.1	291.8	54.7	59.3
Final value	10.4	12.3	10.8	11.1
Gas in place [BSCF]				
Initial value	0.92	0.92	0.92	0.92
Final value	0.78	0.73	0.77	0.76
Recovery factor [%]				
Final value	15.2	20.7	16.3	17.4

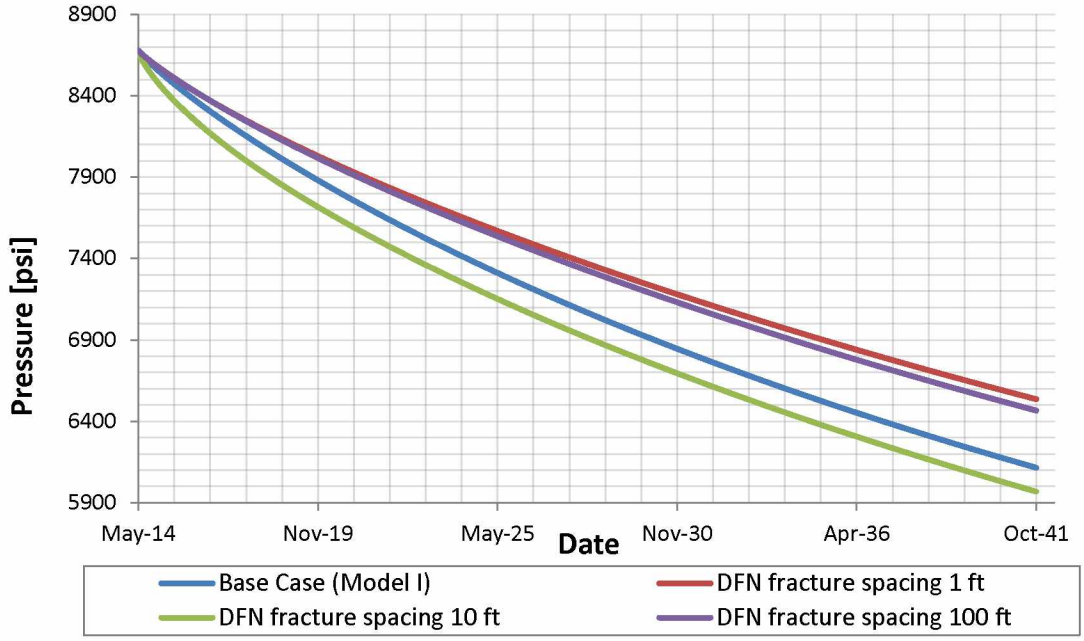

Figure 111: Model average pressure results for varied DFN fracture spacing (Model I) [psi]

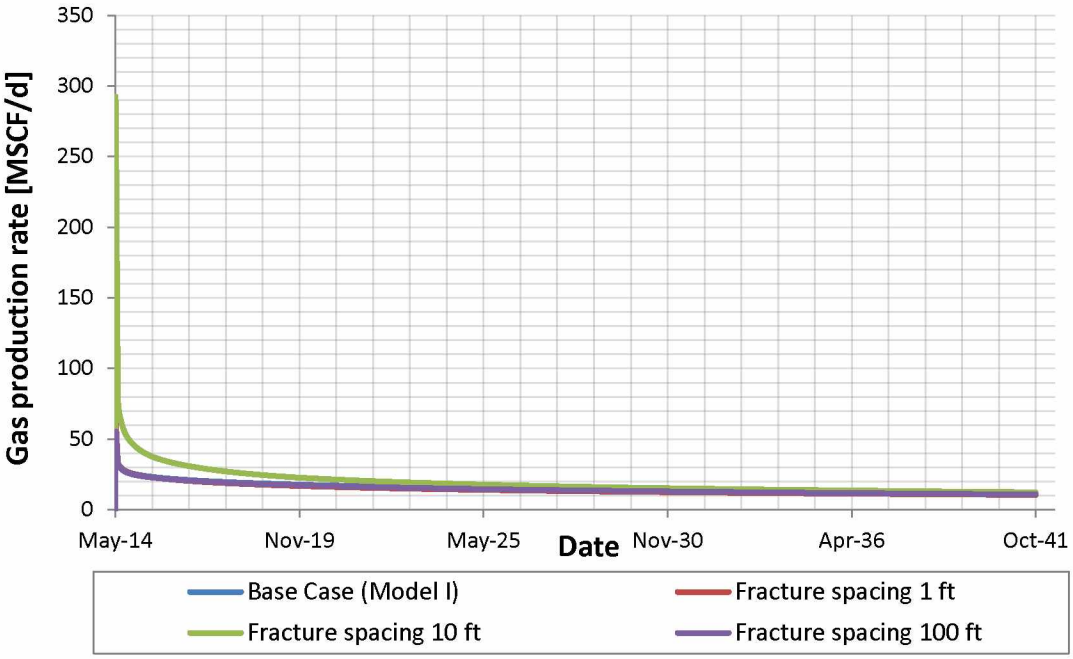

Figure 112: Gas production rate for varied DFN fracture spacing (Model I) [MSCF/day]

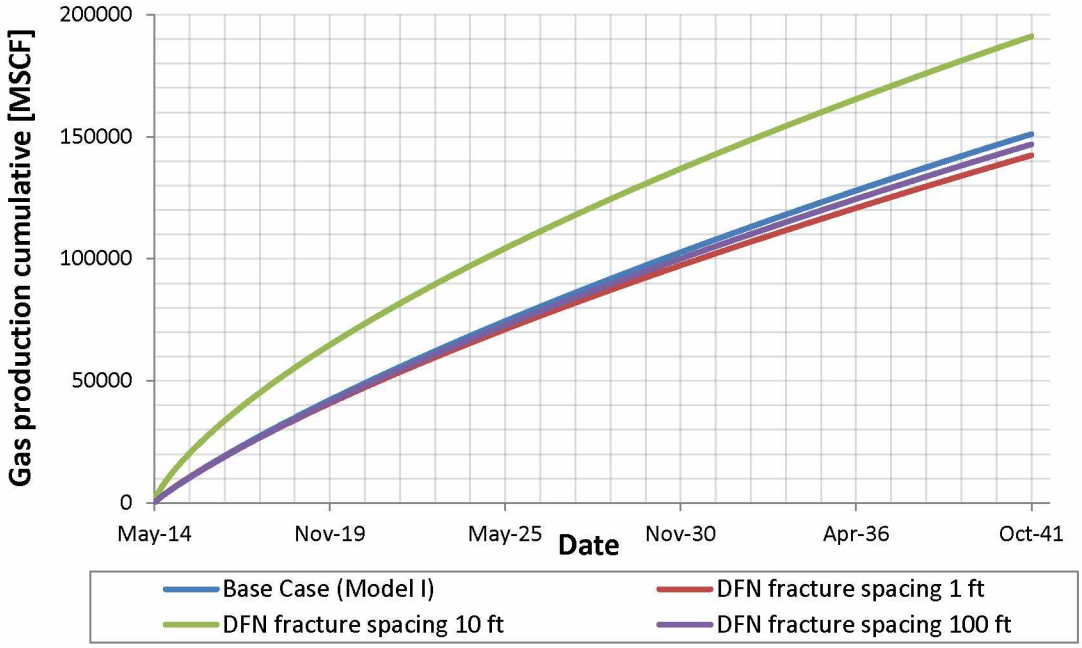

Figure 113: Cumulative gas production results for varied DFN fracture spacing (Model I) [MSCF]

4.12.3.2 Model II

Figure 114 displays the top view of pressure results for varied DFN fracture spacing at the end of the simulation. Elliptical drainage area is present in the center of the fractures.

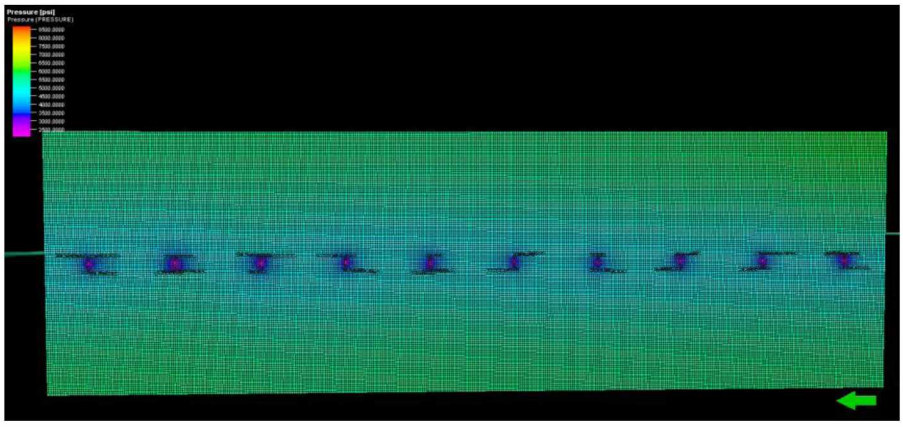

a) DFN fracture spacing 1 ft

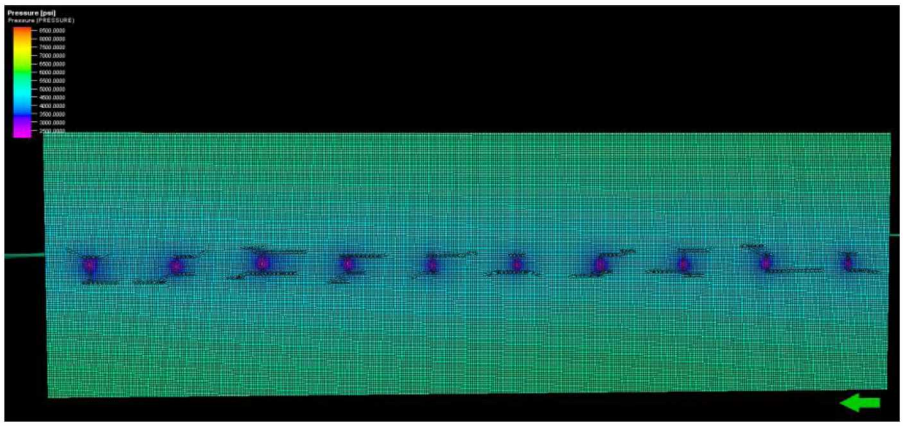

b) DFN fracture spacing 10 ft

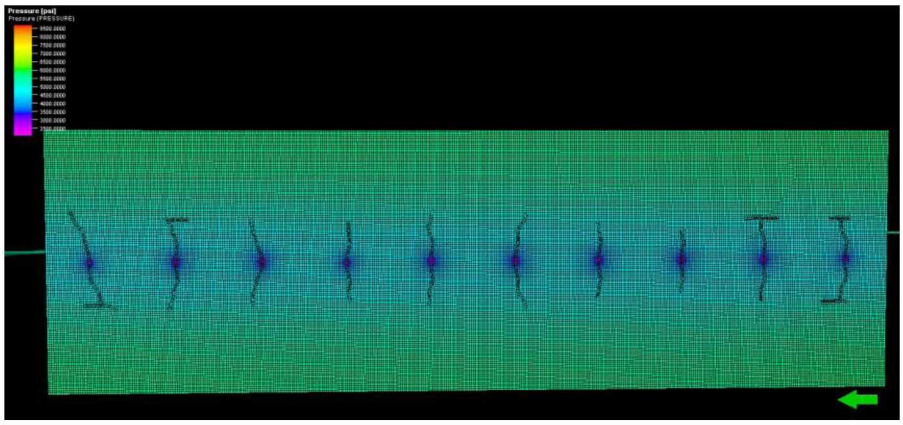

c) DFN fracture spacing 100 ft

Figure 114: Top view of pressure results for varied DFN fracture spacing (Model II) [psi]

Table 32 shows simulation results for varied DFN fracture spacing. Base case had the largest gas cumulative production followed by the case with DFN fracture spacing of 10 ft, which had the largest propped fracture area among all DFN fracture spacing cases. Figure 115 shows the effects of the DFN fracture spacing on the gas recovery factor. Base case (no DFN) had the largest recovery factor followed by DFN fracture spacing of 10 ft.

Table 32: Simulation results for varied DFN fracture spacing (Model II)

	DFN Fracture Spacing 100 ft	**Fracture Spacing 10 ft**	**Fracture Spacing 1 ft**	**Base Case**
Pressure [psi]				
Initial value	8688.5	8688.5	8688.5	8687.9
Final value	5258.1	5078.7	5308.2	4905.6
Cumulative gas production [MMSCF]				
Final value	1368.7	1460.2	1342.9	1502.7
Gas production rate [MSCF/day]				
Maximum value	636.9	695.6	638.9	729.3

Table 32: Simulation results for varied DFN fracture spacing (Model II) continued

Final value	91.2	93.6	89.0	95.0
Gas in place [BSCF]				
Initial value	5.2	5.2	5.2	5.2
Final value	3.9	3.8	3.9	3.7
Recovery factor [%]				
Final value	25.0	26.9	25.0	28.8

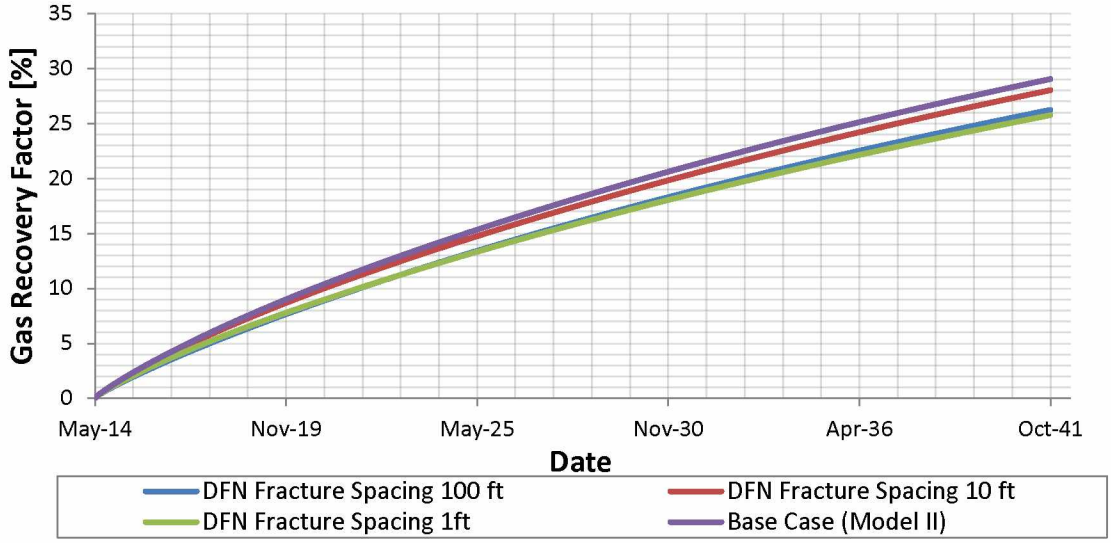

Figure 115: Effect of varied DFN fracture spacing on the gas recovery factor (Model II) [%]

Figures 116-118 show average model pressure, gas production rate and cumulative gas production.

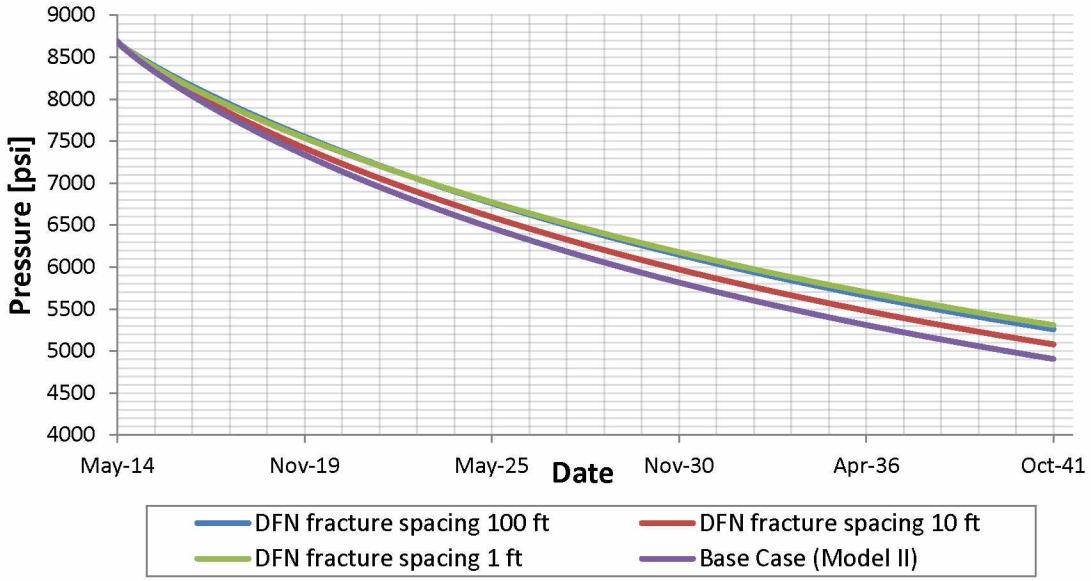

Figure 116: Model average pressure results for varied DFN fracture spacing (Model II) [psi]

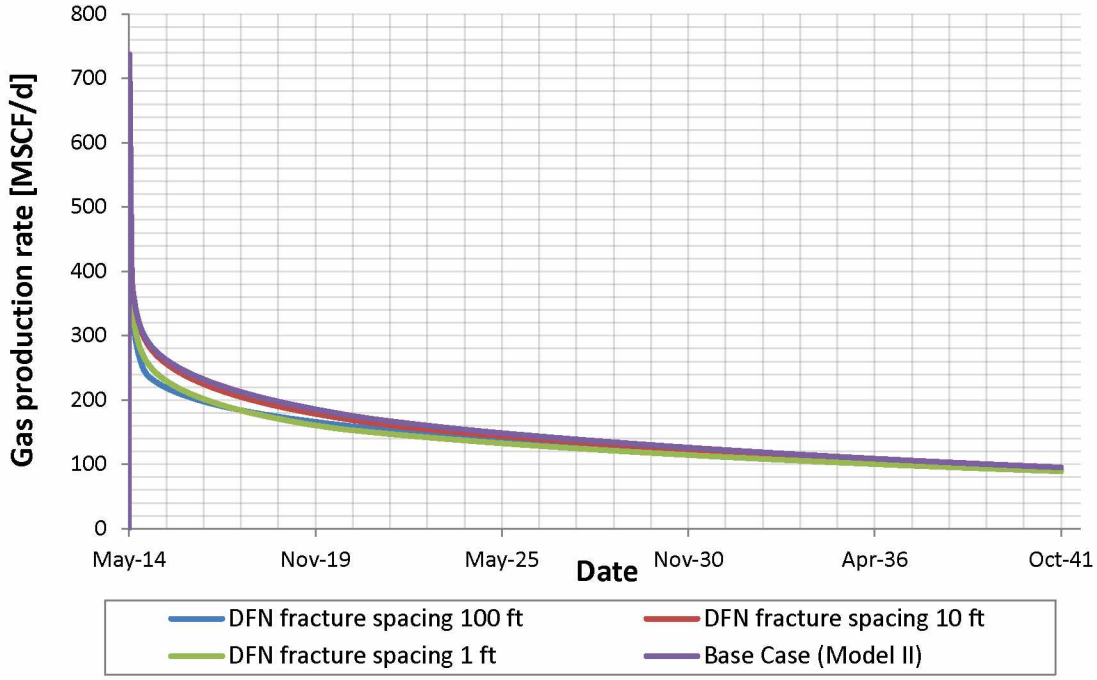

Figure 117: Gas production rate for varied DFN fracture spacing (Model II) [MSCF/day]

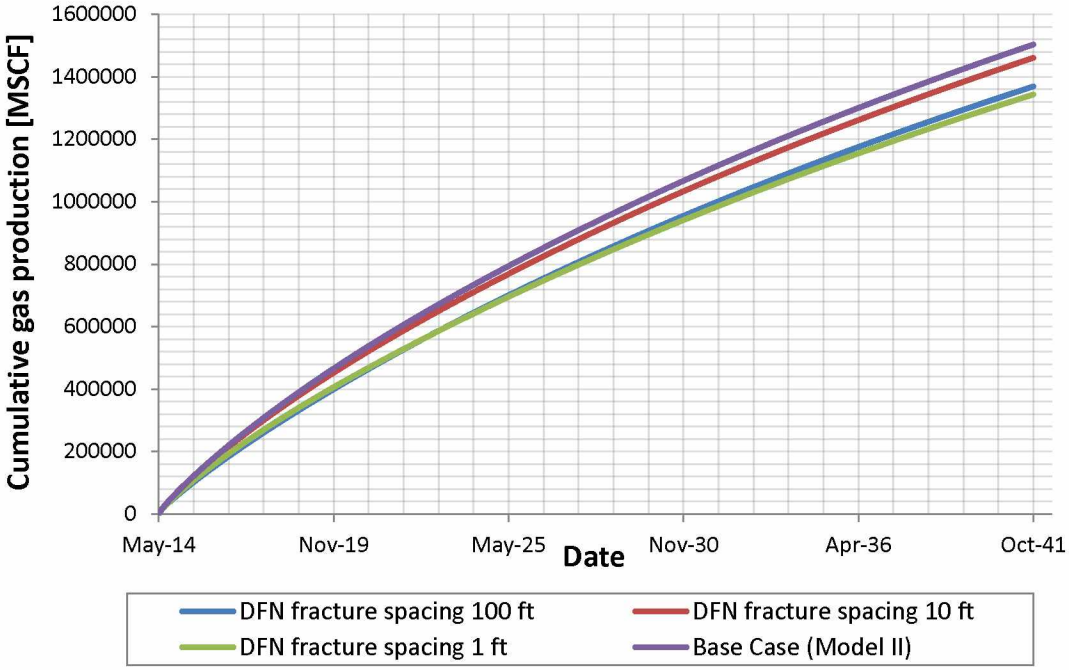

Figure 118: Cumulative gas production for varied DFN fracture spacing (Model II) [MSCF]

4.12.4 Effect of DFN Length

4.12.4.1 Model I

Figure 119 shows the top view of pressure results for varied DFN fracture length sets at the end of the simulation. Elliptical drainage area is present. Table 33 lists all simulation results for this case. Base Case had the most of cumulative gas produced followed by DFN length of 75 ft. Base Case and DFN length 75 ft had almost the same gas recovery factor. Figures 120 – 123 show the gas recovery factor, average model pressure, gas production rate, cumulative gas production and gas in place results.

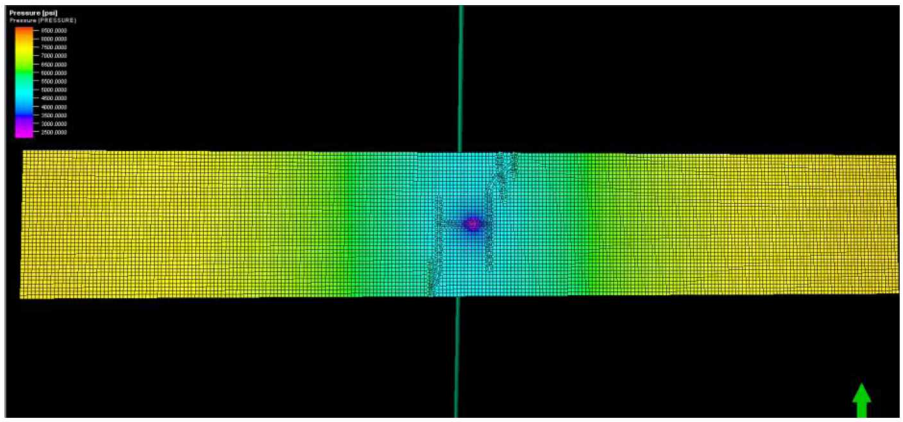

(a) DFN length 25 ft

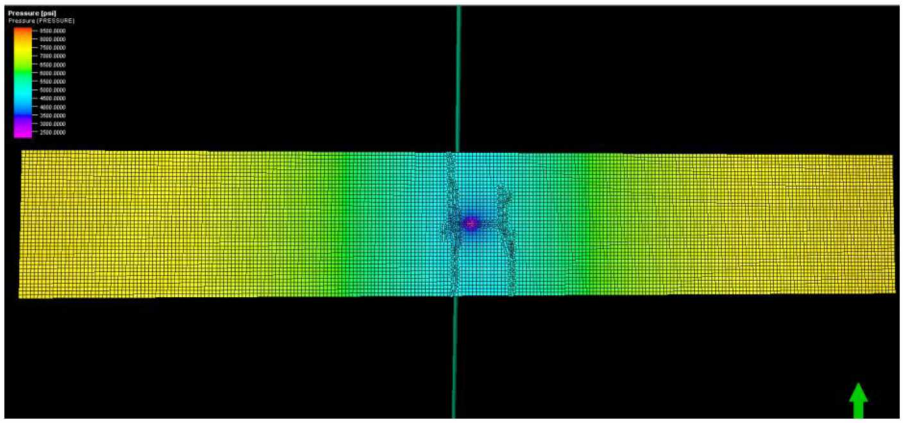

(b) DFN length 50 ft

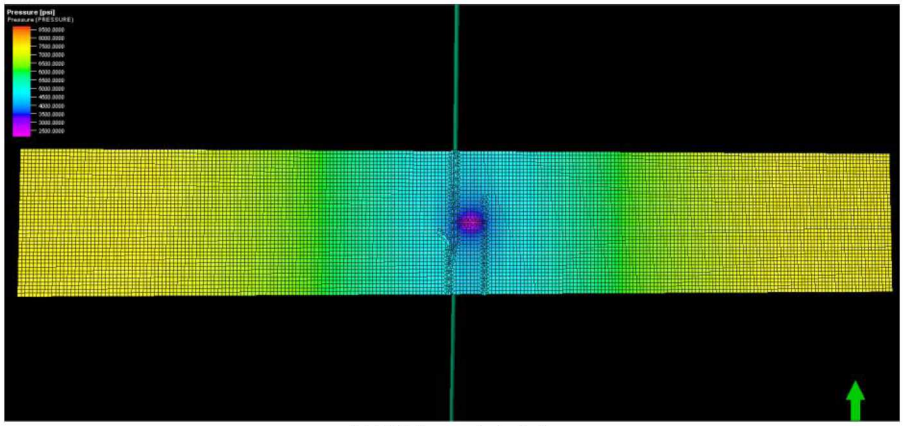

DFN length 75 ft

Figure 119: Top view of 3D pressure results for varied DFN length at the end of the simulation (Model I) [psi]

Table 33: Simulation results for varied DFN length (Model I)

	DFN Fracture Length 25 ft	DFN Fracture Length 50 ft	DFN Fracture Length 75 ft	Base Case
Pressure [psi]				
Initial value	8676.6	8676.6	8676.6	8676.6
Final value	6677.3	6659.1	6423.89	6114.1
Cumulative gas production [MMSCF]				
Final value	131.6	132.6	151.4	151.0
Gas production rate [MSCF/day]				
Maximum value	53.4	50.9	71.7	59.3
Final value	9.7	9.7	11.1	11.1
Gas in place [BSCF]				
Initial value	0.92	0.92	0.92	0.92
Final value	0.79	0.78	0.77	0.76
Recovery factor [%]				
Final value	14.1	15.2	16.3	17.4

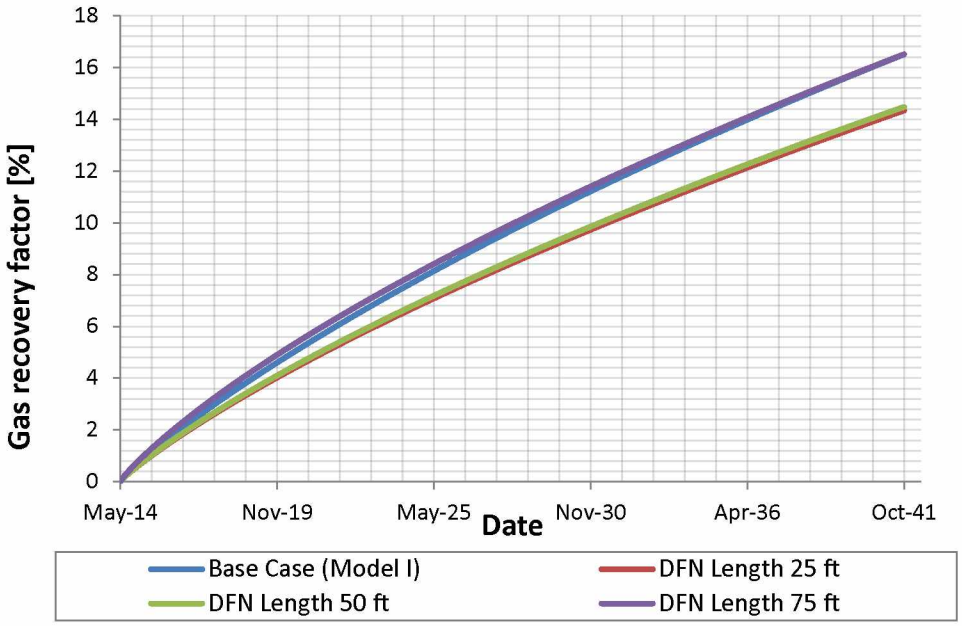

Figure 120: Effect of DFN length on the gas recovery factor (Model I)

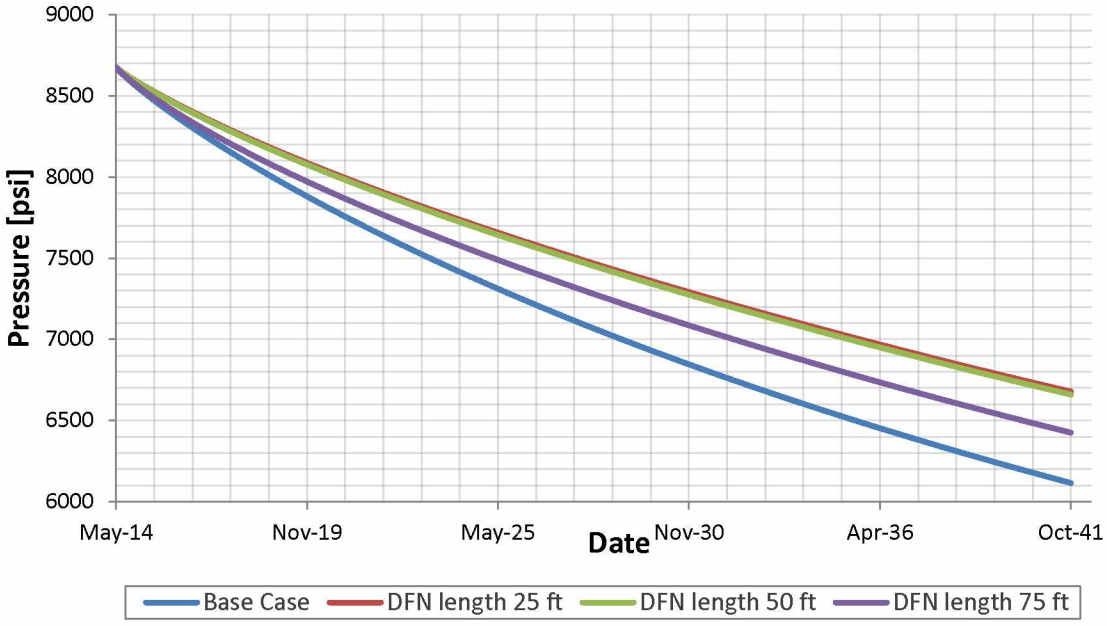

Figure 121: Model average pressure for varied DFN length (Model I) [psi]

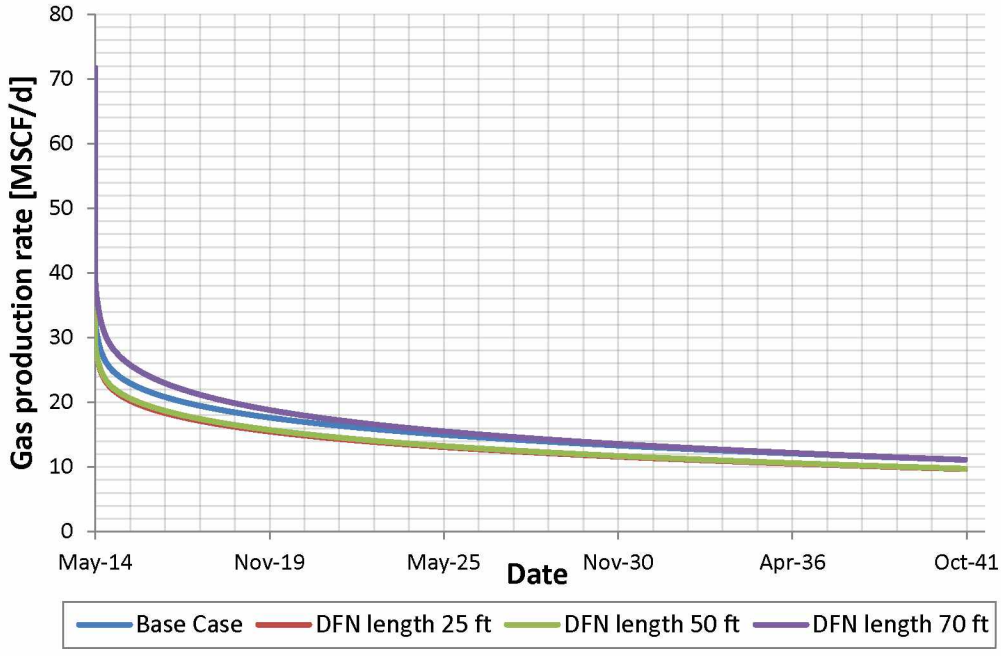

Figure 122: Gas production rate for varied DFN length (Model I) [MSCF/day]

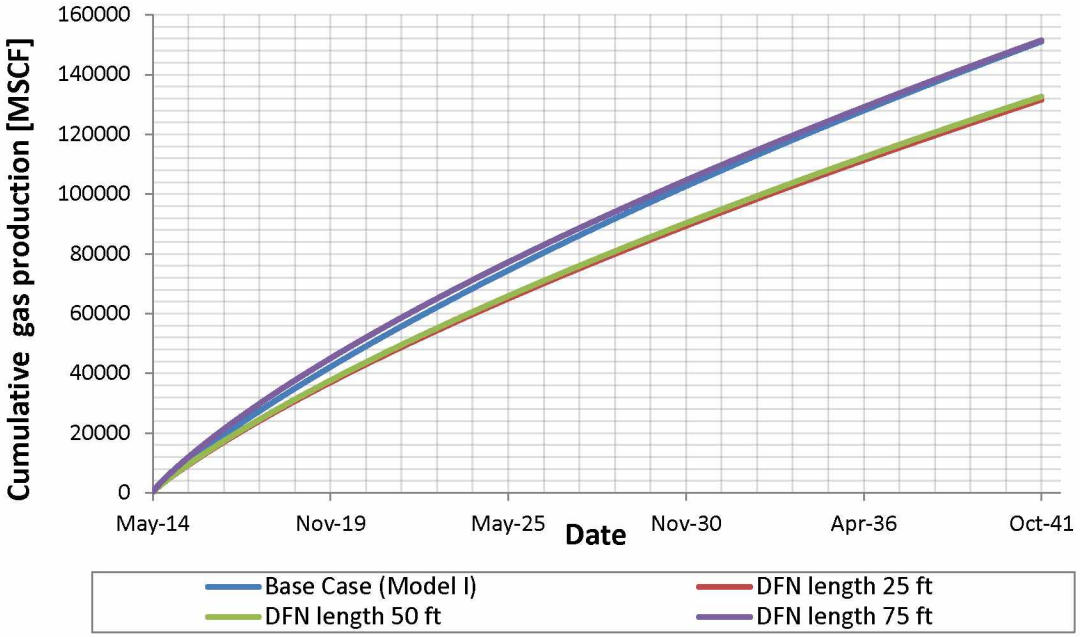

Figure 123: Gas production cumulative results for varied DFN length (Modeling I) [MSCF]

4.12.4.2 Model II

Figure 124 shows top view of pressure results for varied DFN length sets for Model II at the end of the simulation. DFN length of 50 ft has the highest pressure drop out of all cases in this study due to having large propped fracture area.

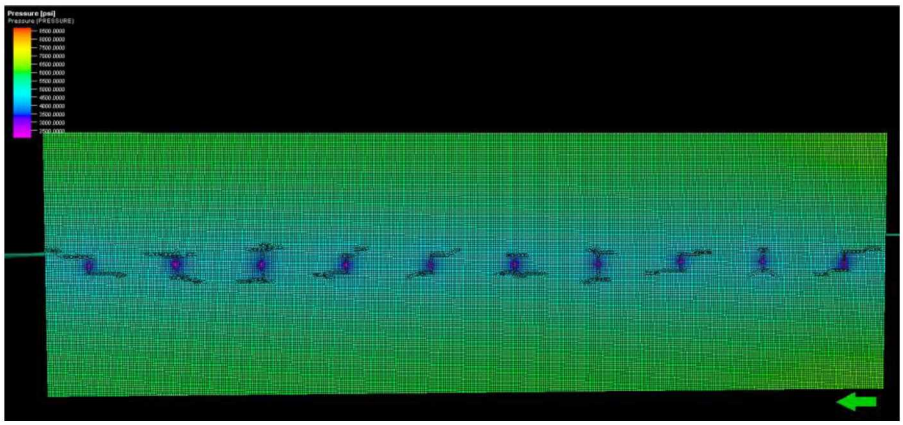

(a) DFN length 25 ft

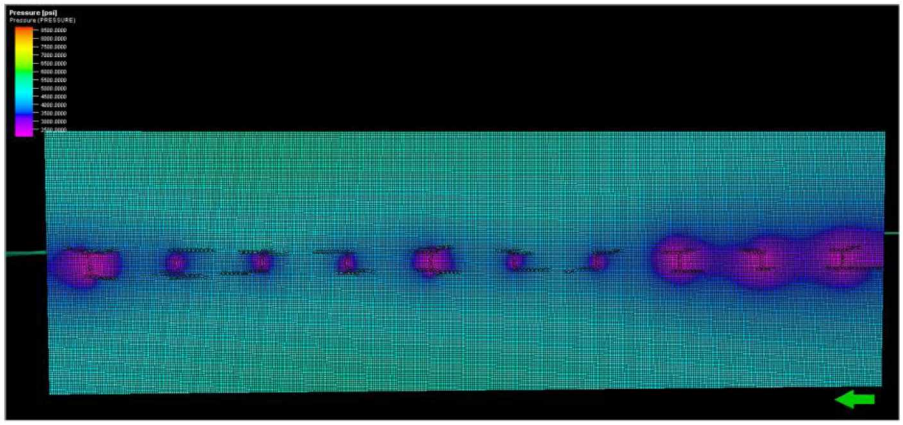

(b) DFN length 50 ft

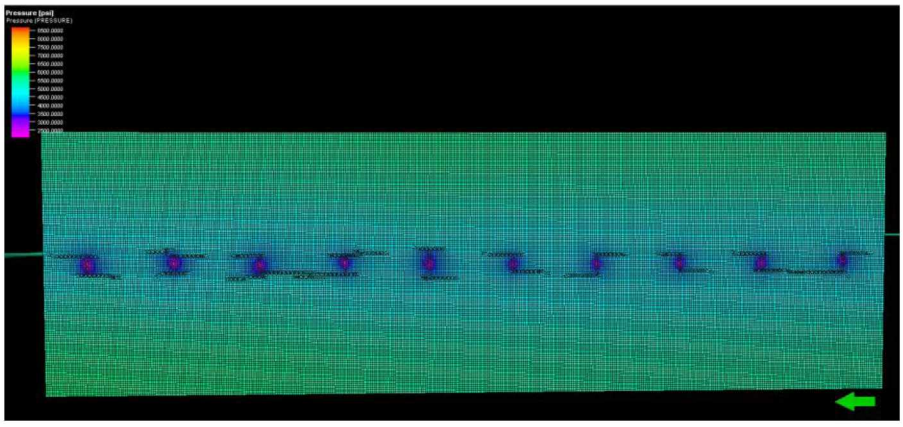

(c) DFN length 70 ft

Figure 124: Top view of pressure results for varied DFN length at the end of the simulation (Model II) [psia]

Table 34 lists all simulation results for varied DFN length sets for Model II. DFN length 50 ft had the highest gas production cumulative in all cases due to having the largest fracture

area. Figure 125 shows the effect of DFN on the gas recovery factor. Figures 126-128 show the model average pressure, gas production rate and cumulative gas production results.

Table 34: Simulation results for varied DFN length (Model II)

	DFN Fracture Length 25 ft	DFN Fracture Length 50 ft	DFN Fracture Length 75 ft	Base Case
Pressure [psi]				
Initial value	8688.5	8688.6	8688.5	8687.9
Final value	5618.2	4444.6	5104.6	4905.6
Cumulative gas production [MMSCF]				
Final value	1189.5	1823.6	1446.8	1502.7
Gas production rate [MSCF/day]				
Maximum value	523.7	2212.5	695.4	729.3
Final value	82.7	104.8	93.5	95.3
Gas in place [BSCF]				
Initial value	5.2	5.2	5.2	5.2
Final value	4.0	3.4	3.8	3.7
Recovery factor [%]				
Final value	23.1	34.6	26.9	28.8

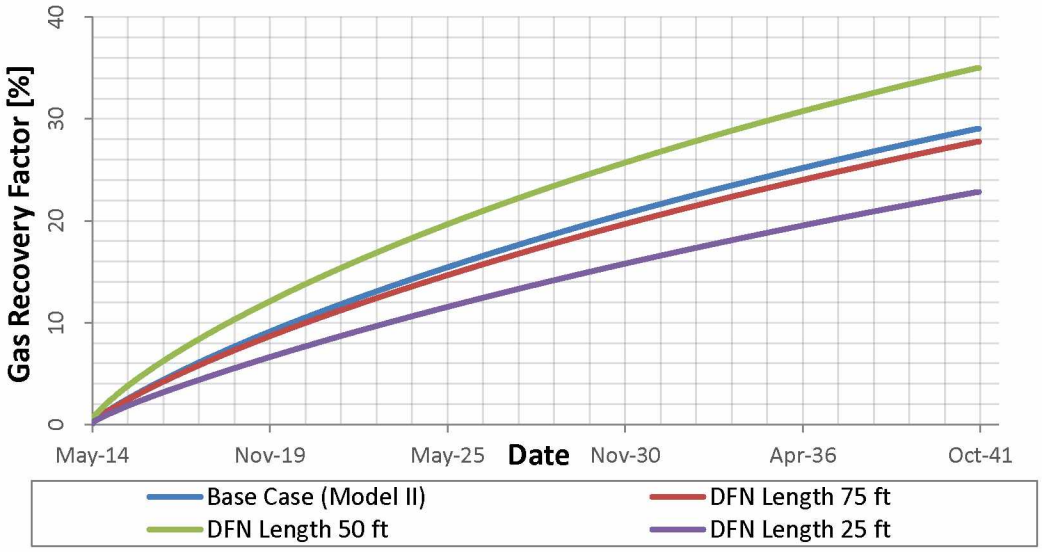

Figure 125: Effect of DFN length on the gas recovery factor (Model II) [%]

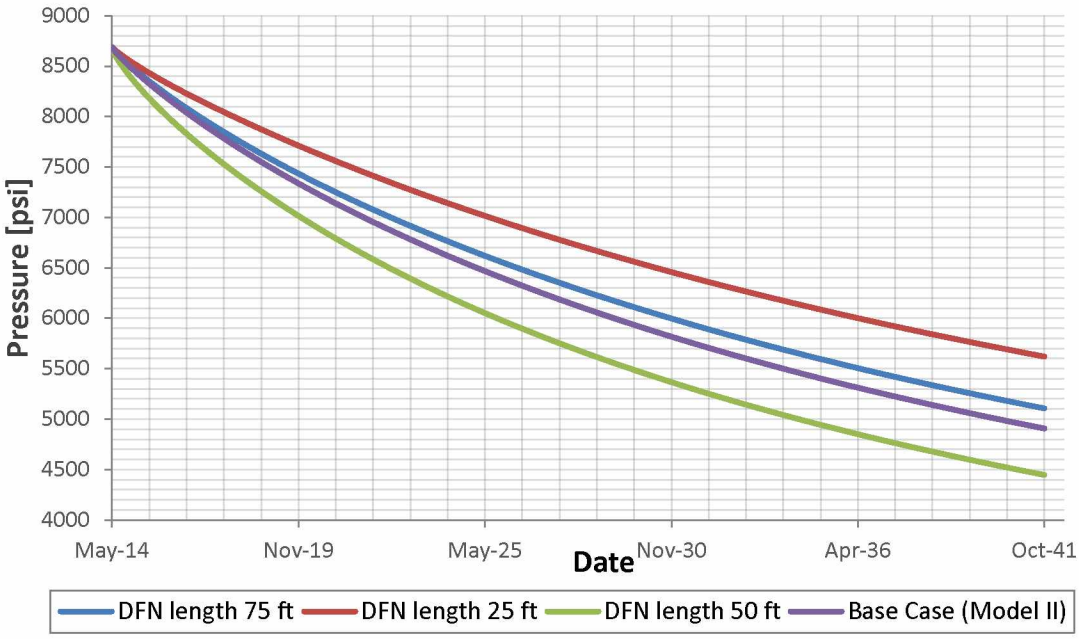

Figure 126: Field pressure results for varied DFN length (Model II) [psi]

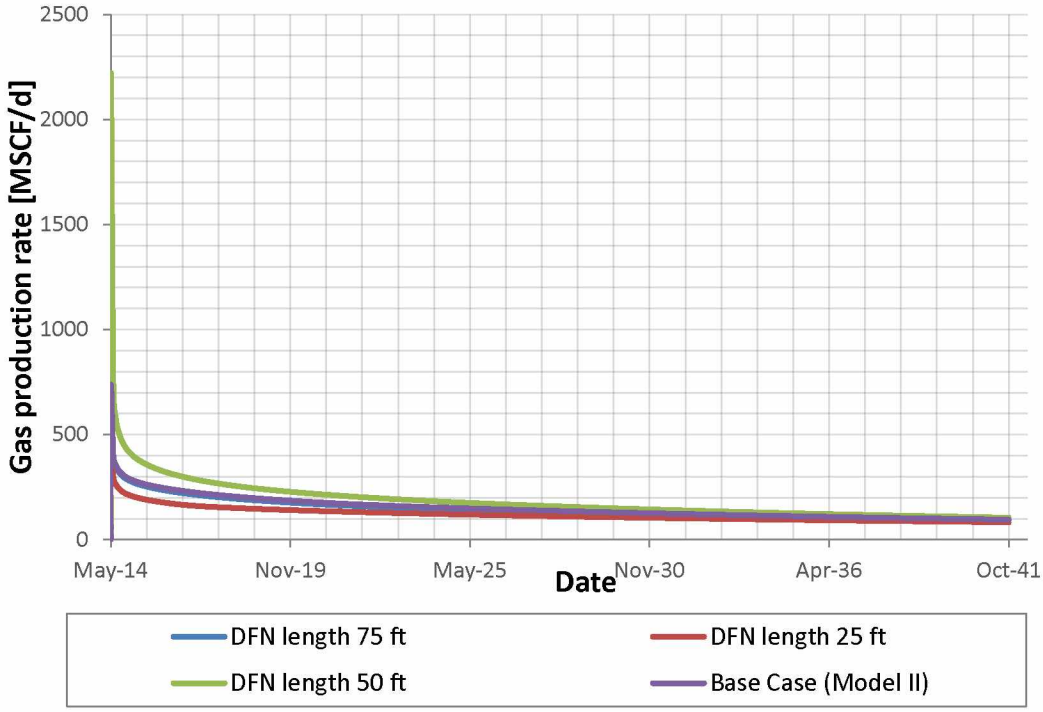

Figure 127: Gas production rate for varied DFN length (Model II) [MSCF/day]

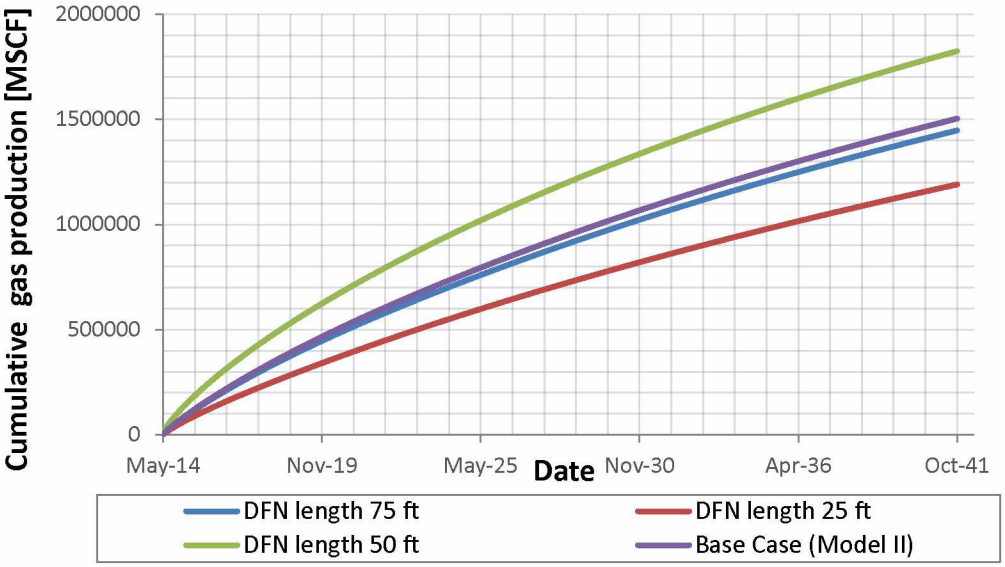

Figure 128: Cumulative gas production results for varied DFN length (Model II) [MSCF]

Chapter 5. Conclusions and Recommendations

5.1 Conclusions

Two simulation models were built in this study using Eagle Ford shale properties– one for the single fracture (Model I) and one for multiple fractures (Model II). Different rock compaction tables were assigned to the matrix, unpropped and propped fracture network zones. Non-Darcy flow and gas adsorption/desorption were excluded in the base case models and were later included in the technical sensitivity studies. While Model I gives good approximate solutions and realistic trends of the model behavior, Model II should be used for more accurate examination. The main pitfalls of Model I are neglect of stress shadowing effect of the neighboring fractures and inability to display the fracture network propagation beyond fracture spacing.

The presence of fracturing fluid, in the fracture and more importantly in the nearby matrix, results in smaller gas production rate and final recovery due to decreasing gas relative permeability and increasing non-Darcy effects.

For a fixed production time and constant bottom hole pressure, higher matrix porosity leads to lower gas recovery factor but higher cumulative gas production compared to low porosity cases. This means that high porosity case needs longer time to reach a given recovery factor.

Higher matrix, fracture and unpropped zone permeability produces higher gas recovery factor.

Smaller fracture spacing leads to increase in the gas recovery factor.

Neglecting non-Darcy flow leads to overestimation of the gas recovery factor. Using the two correlations used in this study for the non-Darcy flow does not produce large difference in the results.

Neglecting gas desorption/adsorption leads to the underestimation of the cumulative gas recovery.

There is no linear correlation between varied DFN orientation, fracture spacing and length with well performance. Propped fracture area in this case is the largest determinant in the gas cumulative production. However, DFN has a significant effect on the gas recovery factor and should not be neglected. In addition, dense DFN network can terminate the hydraulic fracture propagation in its early stage and encourage its growth out of the boundary zone. Moreover, less dense longer DFN oriented in favorable conditions can propagate further from the well than a planar fracture and can increase SRV.

5.2 Recommendations

This study used Eagle Ford Shale data as an analog to the Shublik formation. To get more accurate results for Shublik, logs, microseismic data along with core samples from Shublik formation, if available, should be used.

In hydraulic fracture design smaller proppant should be selected to prevent screenout. Proppant size 30/70 and 100 mesh is recommended to use.

Larger slickwater volumes should be used in the treatment schedule to ensure better connection of the natural fracture network with the hydraulic fracture network and ensure larger propped fracture area.

A hybrid treatment schedule with non-Newtonian schedule should be examined to see if it minimizes the fracturing fluid flowback.

In order to simulate fracturing fluid flowback, water injection should be done stage-by-stage, as was done by Zanganeh (2014), instead of injecting fracturing fluid after the whole fracture network already propagated.

Natural fractures in shale can be present oriented in different directions. This phenomenon can be accurately modeled in the hydraulic fracture simulator by introducing more than one DFN with varied orientations. The effects of DFN on the gas recovery after determining primary, secondary and maybe sedentary DFN based on micro seismic data for the Shublik formation should be examined.

Most wells in Alaska are drilled using oil-based mud in order to drill through permafrost layer to avoid water freezing and plugging the pores. Oil-based mud can change wettability of the formation, which in turn can change cumulative gas and water production. The effects of oil-wet and water-wet Corey constants on cumulative gas production in Shublik formation should be examined.

Furthermore, additional technical sensitivity studies could be done to accurately account for the effect of the flowback on the gas production: the effects of flowback incorporating DFN, the effects of fracturing fluid flowback with incorporated non-Darcy flow and gas adsorption/desorption and the effects of permeability jail and capillary pressures on the flowback if permeability jail is present. Permeability jail is the saturation region where, in low permeability rocks, the relative permeabilities to both gas and water are so low, that neither phase has any effective flow capacity. Moreover, additional factors such as auto shut-in time, varied grid alignment with the well azimuth, different pumping schedule (such as HiWAY), completions method adjusted to the Arctic climate (such as sliding sleeves instead of plug-in-perf completions method), water evaporation/condensation and tubing size could affect gas production.

This page intentionally left blank for the purposes of print publication.

References

Assessment of Potential Oil and Gas Resources in Source Rocks of the Alaska North Slope, 2012. (n.d.). In *USGS* (Fact sheet 2012-2013 ed.). U.S. Department of the Interior.

Andrade Perdomo, J. F., Civan, F., Devegowda, D., and Sigal, R. F. (2010, January 1). Accurate Simulation of Shale-Gas Reservoirs. Society of Petroleum Engineers. doi:10.2118/135564-MS

Ajayi B., Aso, I.I., Terry I.J., Walker K., Wutherich K., Caplan J., Gerdom D., Clark B., Ganguly U., Li X., Xu Y., Yang H., Liu H., Luo Y., and Waters G. 2013. "Stimulation Design for Unconventional Resources." Oilfield Review. Summer 2013: 25, no. 2. Schlumberger. http://www.slb.com/~/media/Files/resources/oilfield_review/ors13/sum13/04_stim_design.pdf

Aurenhammer , F. (1991). *Voronoi Diagrams – A Survey of a Fundamental Geometric Data Structure*. ACM Computing Surveys, 23(3):345–405, 1991

Barasia, A., and Pankaj, P. (2014, April 2). Tail-In Proppant and its Importance in Channel Fracturing Technique. Society of Petroleum Engineers. doi:10.2118/169227-MS

Bazan, L. W., Larkin, S. D., Lattibeaudiere, M. G., and Palisch, T. T. (2010, January 1). Improving Production in the Eagle Ford Shale With Fracture Modeling, Increased Fracture Conductivity, and Optimized Stage and Cluster Spacing Along the Horizontal Wellbore. Society of Petroleum Engineers. doi:10.2118/138425-MS

Britt, L. K., Smith, M. B., Haddad, Z. A., Lawrence, J. P., Chipperfield, S. T., and Hellman, T. J. (2006, January 1). Waterfracs: We Do Need Proppant After All. Society of Petroleum Engineers. doi:10.2118/102227-MS

Blome, C.D., 1986, Paleogeographic significance of Upper Triassic and Lower Jurassic Radiolaria from Cordilearn terranes: Abstracts, Fourth North American Paleontological Convention, August 12-15, 1986. p. A5.

Blome, C.D., 1987, Paleogeographic significance of lower Mesozoic radiolarians from the Brooks Range, Alaska, in Tailleur, I., and Weimer, P., eds., Alaskan North Slope Geology: Anchorage, Pacific Section, Society of Economic Paleontologists and Mineralogists and the Alaska Geological Society, p. 371-380.

Bodnar, D.A., 1984, Stratigraphy, age, depositional environments, and hydrocarbon source rock evaluation of the Otuk Formation, north-central Brooks Range, Alaska [unpublished MS thesis]: University of Alaska, Fairbanks, 231 p.

Brunauer, S., Deming, L.S., Deming, E.W and Teller, E. (1940). On a Theory of the van der Waals Adsorption of Gases, Journal the American Chemical Society, Vol. 62, No. 7, pp. 1723-1732. ISSN 00027863.

Civan, F., and Evans, R. D. (1991, January 1). Non-Darcy Flow Coefficients and Relative Permeabilities for Gas/Brine Systems. Society of Petroleum Engineers. doi:10.2118/21516-MS

Chaudhary, A. S., Ehlig-Economides, C. A., and Wattenbarger, R. A. (2011, January 1). Shale Oil Production Performance from a Stimulated Reservoir Volume. Society of Petroleum Engineers. doi:10.2118/147596-MS

Chong, E., Syihab, Z., Putra, E., and Schechter, D. (2004, January 1). A Unique Grid-Block System for Improved Grid Orientation. Society of Petroleum Engineers. doi:10.2118/88617-MS

Cipolla, C.L., 2009, "Modeling Production and Evaluating Fracture Performance in Unconventional Gas Reservoirs," JPT, Distinguished Author Series, pp. 84-90, September.

Cipolla, C. L., Lolon, E. P., Erdle, J. C., and Rubin, B. (2010, August 1). Reservoir Modeling in Shale-Gas Reservoirs. Society of Petroleum Engineers. doi:10.2118/125530-PA

Cooke, C.E. Jr. 1973. Conductivity of Fracture Proppants in Multiple Layers. Journal of Petroleum Technology, 1101-1107.

Corey, A.T, 1954. The Interrelation between Gas and Oil Relative Permeabilities. Prod. Monthly, 19 (1): 38.

Daniels, J. L., Waters, G. A., Le Calvez, J. H., Bentley, D., and Lassek, J. T. (2007, January 1). Contacting More of the Barnett Shale Through an Integration of Real-Time Microseismic Monitoring, Petrophysics, and Hydraulic Fracture Design. Society of Petroleum Engineers. doi:10.2118/110562-MS

Dawson, W. C. 2000. Shale Microfacies: Eagle Ford Group (Cenomanian-Turonian) North-Central Texas Outcrops and Subsurface Equivalents. Gulf Coast Association of Geological Societies Transactions. 50. 607-621.

Detterman, R.L., 1970, Sedimentary history of the Sadlerochit and Shublik Formations in northeastern Alaska, in Adkison, W.L., and Brosge, M.M., eds, Proceedings of the Geological Seminar on the North Slope of Alaska:, Pacific Section, American Association of Petroleum Geologists, p. O1-O13.

Dingus, A.S., 1984, Paleoenvironmental reconstruction of the Shublik Formation on the North Slope of Alaska [unpublished MS thesis]: University of California, Berkeley, 108 p.

Dong, Z., Holditch, S. A., and McVay, D. A. (2012, January 1). Resource Evaluation for Shale Gas Reservoirs. Society of Petroleum Engineers. doi:10.2118/152066-MS

Economides, M.J, Hill D., and Ehlig-Economides, C. 1994. *Petroleum Production Systems.* Prentice Hall, Inc. Simon and Schuster Company/ A Viacom Company.

Ehlig-Economides, C. A., and Economides, M. J. (2011, January 1). Water As Proppant. Society of Petroleum Engineers. doi:10.2118/147603-MSEIA (U.S. Energy Information Administration), 2011, "Review of Emerging Resources: U.S. Shale Gas and Shale Oil Plays", July.

EIA (U.S. Energy Information Administration), 2015, "Shale gas and tight oil provides largest share of U.S. natural gas production in 2013", April. http://www.eia.gov/todayinenergy/detail.cfm?id=15811

Fan, L., Thompson, J. W., and Robinson, J. R. (2010, January 1). Understanding Gas Production Mechanism and Effectiveness of Well Stimulation in the Haynesville Shale Through Reservoir Simulation. Society of Petroleum Engineers. doi:10.2118/136696-MS

Fisher, M. K., Wright, C. A., Davidson, B. M., Goodwin, A. K., Fielder, E. O., Buckler, W. S., and Steinsberger, N. P. (2002, January 1). Integrating Fracture Mapping Technologies to Optimize Stimulations in the Barnett Shale. Society of Petroleum Engineers. doi:10.2118/77441-MS

Forchheimer, P., 1901, "Wasserbewgung durch Boden", Zeitschirift des Vereines Deustscher Ingenieuer, 45 edition.

Forsyth, P. A. (1990, November 1). A Control-Volume, Finite-Element Method for Local Mesh Refinement in Thermal Reservoir Simulation. Society of Petroleum Engineers. doi:10.2118/18415-PA

Freeman, C., Moridis, G. J., Ilk, D., and Blasingame, T. (2010, January 1). A Numerical Study of Transport and Storage Effects for Tight Gas and Shale Gas Reservoir Systems. Society of Petroleum Engineers. doi:10.2118/131583-MS

Gu, H. and Weng, X. 2010. Criterion For Fractures Crossing Frictional Interfaces At Non-orthogonal Angles. Paper ARMA 10-198 presented at the 44th U.S. Rock Mechanics Symposium and 5th U.S.-Canada Rock Mechanics Symposium, Salt Lake City, Utah, USA, 27030, June.

Gu, H., Weng, X., Lund, J. B., Mack, M. G., Ganguly, U., and Suarez-Rivera, R. (2011, January 1). Hydraulic Fracture Crossing Natural Fracture at Non-Orthogonal Angles, A Criterion, Its Validation and Applications. Society of Petroleum Engineers. doi:10.2118/139984-MS

Gunasekera, D., Cox, J., and Lindsey, P. (1997, January 1). The Generation and Application of K-Orthogonal Grid Systems. Society of Petroleum Engineers. doi:10.2118/37998-MS

Haghshenas, B., Soroush, M., Brohi, I., and Clarkson, C. R. (2014, April 1). Simulation of Liquids Rich Shale Gas Reservoirs With Heavy Hydrocarbon Fraction Desorption. Society of Petroleum Engineers. doi:10.2118/168968-MS

Hallam, S. D., and Last, N. C. (1991, June 1). Geometry of Hydraulic Fractures From Modestly Deviated Wellbores. Society of Petroleum Engineers. doi:10.2118/20656-PA

Houseknecht, D.W., 2003, "Brookian Stratigraphic Plays in the National Petroleum Reserve – Alaska (NPRA)". U.S. Geological Survey. Open-File Report 03-039. http://pubs.usgs.gov/of/2003/of03-039/

Houseknecht, D.W., and Bird, K.J., 2004, Sequence stratigraphy of the Kingak Shale (Jurassic-Lower Cretaceous), National Petroleum Reserve in Alaska: American Association of Petroleum Geologists Bulletin, v.88, p.279-302.

Houseknecht, D.W., 2012b "Assessment of Potential Oil and Gas Resources in Source Rocks (Shale) of the Alaska North Slope 2012 – Overview of Geology and Results." USGS. http://www.arcticgas.gov/sites/default/files/documents/2012-usgs-north-slope-shale-assessment.pdf

Houseknecht, D., Rouse, W., Garrity, C., Whidden, K., Dumoulin, J., Schenk, C., and Pollastro, R. (n.d.). Assessment of Potential Oil and Gas Resources in Source Rocks of the Alaska North Slope, 2012. In *USGS* (Fact sheet 2012-2013 ed.). U.S. Department of the Interior. http://pubs.usgs.gov/fs/2012/3013/pdf/fs2012-3013_2-28-2012.pdf

Heinemann, Z.E., and Brand, C.W.: "Gridding Construction for Reservoir Simulation," paper presented at the First International Forum on Reservoir Simulation, Alpach, Austria, Sept, 12-16,1998.

Hulm, E.J., 1999, Subsurface facies architecture and sequence stratigraphy of the Eileen sandstone, Shublik Formation, and Sag River sandstone, Arctic Alaska [unpublished MS thesis]: University of Alaska Fairbanks, p.105.

Hughes, W.B., Miller, D.E., and Holba, A.G., 1983, North Slope, Alaska, oil-rock correlation study, in Magoon, L.B., and Claypool, G.E., eds., Alaska North Slope Oil-Rock Correlation Study – a Compilation of Abstracts: American Association of Petroleum Geologists Short Course: Dallas, TX, April 17, 1983, p. 379-402.

Hutton, E., Agboada, D. K., Whalen, M.T., and Hanks, C.L. 2012. Upper Triassic Shublik Formation of North Alaska - An Eagle Ford Type Shale Reservoir Play?. Presented at AAPG Annual Convention and Exhibition. Long Beach, CA.

IHS Energy. 2011. Enerdeq, http://energy.ihs.com/Products/Enerdeq/.

Ikewun, P. O. (2012). *Production optimization and forecasting of shale gas wells using simulation models and decline curve analysis*. MS thesis, UAF

Inamdar, A. A., Ogundare, T. M., Malpani, R., Atwood, W. K., Brook, K., Erwemi, A. M., and Purcell, D. (2010, January 1). Evaluation of Stimulation Techniques Using Microseismic Mapping in the Eagle Ford Shale. Society of Petroleum Engineers. doi:10.2118/136873-MS

Jurus, W. J., Whitson, C. H., and Golan, M. (2013, September 30). Modeling Water Flow in Hydraulically-Fractured Shale Wells. Society of Petroleum Engineers. doi:10.2118/166439-MS

King, G. E. (2012, April 1). Hydraulic Fracturing 101: What Every Representative, Environmentalist, Regulator, Reporter, Investor, University Researcher, Neighbor, and Engineer Should Know About Hydraulic Fracturing Risk. Society of Petroleum Engineers. doi:10.2118/0412-0034-JPT

Kresse, O., Cohen, C., Weng, X., Wu, R., and Gu, H. (2011, January 1). Numerical Modeling of Hydraulic Fracturing In Naturally Fractured Formations. American Rock Mechanics Association.

Kupecz, J.A., 1995, Depositional settling, sequence stratigraphy, diagenesis, and reservoir potential of a mixed-lithology, upwelling deposit: The Upper Triassic Shublik Formation, Prudhoe Bay, Alaska: American Association of Petroleum Geologists Bulletin, v.79, p.1301-1319.

Langmuir, I., 1916 "The construction and fundamental properties of solids and liquids," Journal of the American Chemical Society, 38 (11): 2221-2295.

Le Calvez, J. H., Craven, M. E., Klem, R. C., Baihly, J. D., Bennett, L. A., and Brook, K. (2007, January 1). Real-Time Microseismic Monitoring of Hydraulic Fracture Treatment: A Tool To Improve Completion and Reservoir Management. Society of Petroleum Engineers. doi:10.2118/106159-MS

Leahy-Dios, A., Das, M., Agarwal, A., and Kaminsky, R. D. (2011, January 1). Modeling of Transport Phenomena and Multicomponent Sorption for Shale Gas and Coalbed Methane in an Unstructured Grid Simulator. Society of Petroleum Engineers. doi:10.2118/147352-MS

Li, D., and Engler, T. W. (2001, January 1). Literature Review on Correlations of the Non-Darcy Coefficient. Society of Petroleum Engineers. doi:10.2118/70015-MS

Lock, B.E and Peschier, L. 2006. Boquillas (Eagle Ford) Upper Slope Sediments, West Texas: Outcrop Analogs for Potential Shale Reservoirs. Gulf Coast Association of Geological Societies Transactions. 56. 491-508.

Madden, B., and Vossoughi, S. (2013, October 22). US Shale Gas and Tight Oil Boom - The Opportunities and Risks for America. Society of Petroleum Engineers. doi:10.2118/165770-MS

Magoon, L.B., and Bird, K.J., 1988, Evaluation of petroleum source rocks in the National Petroleum Reserve in Alaska using organic carbon content, hydrocarbon content, visual kerogen, and vitrinite reflectance data, in Cryc, G., ed., Geology and Exploration of National Petroleum Reserve in Alaska 1974 to 1982: U.S. Geological Survey Professional Paper 1399, p. 381-450.

Magoon, L.B., and Claypool, G.E., 1983, Petroleum source rock richness, type and maturity for four rock units on the Alaskan North Slope – are they sources for the two oil types?, U.S. Geological Survey Polar Research Symposium – Abstracts with Program. U.S. Geological Survey Circular 911, p. 30-31.

Martin, R., Baihly, J. D., Malpani, R., Lindsay, G. J., and Atwood, W. K. (2011, January 1). Understanding Production from Eagle Ford-Austin Chalk System. Society of Petroleum Engineers. doi:10.2118/145117-MS

Mayerhofer, M. J., Lolon, E., Warpinski, N. R., Cipolla, C. L., Walser, D. W., and Rightmire, C. M. (2010, February 1). What Is Stimulated Reservoir Volume? Society of Petroleum Engineers. doi:10.2118/119890-PA

Maxwell, S. C., Urbancic, T. I., Steinsberger, N., and Zinno, R. (2002, January 1). Microseismic Imaging of Hydraulic Fracture Complexity in the Barnett Shale. Society of Petroleum Engineers. doi:10.2118/77440-MS

Mengal, S. A., and Wattenbarger, R. A. (2011, January 1). Accounting For Adsorbed Gas in Shale Gas Reservoirs. Society of Petroleum Engineers. doi:10.2118/141085-MS

Meyer, B. R., and Bazan, L. W. (2011, January 1). A Discrete Fracture Network Model for Hydraulically Induced Fractures - Theory, Parametric and Case Studies. Society of Petroleum Engineers. doi:10.2118/140514-MS

Mikhailov, D.N., Economides, M.J., and Nikolayevskiy, V.N., 2011. Fluid Leakoff Determines Hydraulic Fracture Dimensions: Approximate Solution for Non-Newtonian Fracturing Fluid. International Journal of Engineering Science, volume 49, issue 9, September 2011, pp 809-822. http://doi:10.1016/j.ijengsci.2011.03.021

Mirzaei, M., and Cipolla, C. L. (2012, January 1). A Workflow for Modeling and Simulation of Hydraulic Fractures in Unconventional Gas Reservoirs. Society of Petroleum Engineers. doi:10.2118/153022-MS

Moore, T.E., Wallace, W.K., Bird K. J., Karl, S. M., Mull, C. G., and Dilon, J. T., 1994. "Geology of Northern Alaska." The Geology of North America. Vol. G-1, The Geology of Alaska. The Geological Society of America. pp 49- 128.

Murphy, E. E., Praznik, G., Quirein, J., Galford, J. E., Witkowsky, J. M., and Chen, S. (2013, November 11). A Workflow to Evaluate Mineralogy, Porosity, TOC, and Hydrocarbon Volume in the Eagle Ford Shale. Society of Petroleum Engineers. doi:10.2118/167012-MS

Nagel, N., Zhang, F., Sanchez-Nagel, M., Lee, B., and Agharazi, A. (2013, November 5). Stress Shadow Evaluations for Completion Design in Unconventional Plays. Society of Petroleum Engineers. doi:10.2118/167128-MS

Nolte, K. G., and Economides, M. J. (1991, September 1). Fracture Design and Validation With Uncertainty and Model Limitations. Society of Petroleum Engineers. doi:10.2118/18979-PA

Olson, J. E. (2008, January 1). Multi-fracture propagation modeling: Applications to hydraulic fracturing in shales and tight gas sands. American Rock Mechanics Association.

Palagi, C. L., and Aziz, K. (1994, April 1). Use of Voronoi Grid in Reservoir Simulation. Society of Petroleum Engineers. doi:10.2118/22889-PA

Palisch, T.: "Proppant Selection In Unconventional Reservoirs", presentation, November 8, 2012. http://www.zenzebra.net/palisch/proppants.pdf

Parrish, J.T., 1987. Lithology, geochemistry, and depositional environment of the Shublik Formation (Triassic), northern Alaska, in Tailleur, I.L., and Weimer, P., eds., Alaskan North Slope Geology: Anchorage, Pacific Section, Society of Economic Paleontologists and Mineralogists and the Alaska Geological Society, p. 391-396.

Parrish, J.T., Droser M.L., Bottjer D.J., 2001. A Triassic Upwelling Zone: The Shublik Formation, Arctic Alaska, U.S.A. Journal of Sedimentary Research, March 2001, vol. 71, no. 2 272-285. Doi: 10.1306/052600710272

Patton, W.W., Jr., and Matzko, J.J., 1959, Phosphate deposits in northern Alaska, U.S. Geological Survey Professional Paper 302A, 17p.

Pedrosa, O.A., and Aziz, K.: "Use of a Hybrid Grid in Reservoir Simulation," SPERE (Nov. 1986) 611-621

Pena, A., Gutierrez, L., Archimio, A., D'Huteau, E. (2010, October 1). New treatment creates infinite fracture conductivity. *E&P*.

Prats, M. (1961, June 1). Effect of Vertical Fractures on Reservoir Behavior-Incompressible Fluid Case. Society of Petroleum Engineers. doi:10.2118/1575-G

Renshaw, C.E. and Pollard, D.D. 1995. An experimentally verified criterion for propagation across unbounded frictional interfaces in brittle, linear elastic materials. Int. J. Rock Mech. Min. Sci and Geomech. Abstracts 32 (3): 237-249. http://dx.doi.org/10.1016/0148-9062(94)00037-4.

Rossen, W. R., and Kumar, A. T. A. (1994, January 1). Effect of Fracture Relative Permeabilities on Performance of Naturally Fractured Reservoirs. Society of Petroleum Engineers. doi:10.2118/28700-MS

Rubin, B. (2010, January 1). Accurate Simulation of Non Darcy Flow in Stimulated Fractured Shale Reservoirs. Society of Petroleum Engineers. doi:10.2118/132093-MS Schiller, L., and Naumann, A., 1933. A drag coefficient correlation. VDI Zeitschrift 77: 318-320.

Saboorian-Jooybari, H., and Pourafshary, P. (2015, January 26). Non-Darcy Flow Effect in Fractured Tight Reservoirs: How Significant Is It at Low Flow Rates and away from Wellbores? Society of Petroleum Engineers. doi:10.2118/172948-MS

Sen, Z., 1995. Applied hydrology for scientists and engineers. By CRC Press.

Sobernheim, D., "Honing unconventionals technology for the Middle East". Energy in the Middle East 2012. Retrieved November 29, 2015, from http://www.slb.com/~/media/Files/industry_challenges/unconventional_gas/industry_articles/201211_pe_honing_ur_tech_middle_east.pdf

Tailleur, I.L, 1964, Rich oil shale from northern Alaska, U.S. Geological Survey Professional Paper 475-D, p. D131-D133.

Texas RRC. 2015."Eagle Ford Shale Information." Retrieved November 29, 2015 from http://www.rrc.state.tx.us/oil-gas/major-oil-gas-formations/eagle-ford-shale/

Thompson, J. M., Okouma Mangha, V., and Anderson, D. M. (2011, January 1). Improved Shale Gas Production Forecasting Using a Simplified Analytical Method-A Marcellus Case Study. Society of Petroleum Engineers. doi:10.2118/144436-MS

Waite, L.E., 2009. Edwards (Stuarts City) Shelf Margin of South Texas: New Data, New Concepts. Tulsa Geological Society. January.

Walton, I., McLennan, J., The Role of Natural Fractures in Shale Gas Production, An ISRM specialized Conference, Bunger, McLennan, and Jeffrey. Brisbane, Australia, May 2013. http://dx.doi.org/10.5772/56404

Wang, C., 2013. "Pressure Transient Analysis of Fractured Wells in Shale Reservoirs." MS Thesis. Colorado School of Mines. p. 9. http://digitool.library.colostate.edu///exlibris/dtl/d3_1/apache_media/L2V4bGlicmlzL2R0bC9kM18xL2FwYWNoZV9tZWRpYS8yMTI1ODM=.pdf

Warpinski, N. R. (2009, January 1). Stress Amplification and Arch Dimensions In Proppant Beds Deposited by Waterfracs. Society of Petroleum Engineers. doi:10.2118/119350-MS

Weng, X., Kresse, O., Cohen, C.E., Wu, R., and Gu, H. (2011, November 1). Modeling of Hydraulic-Fracture-Network Propagation in a Naturally Fractured Formation. Society of Petroleum Engineers. doi:10.2118/140253-PA

Wu, R., Kresse, O., Weng, X., Cohen, C.E., and Gu, H. (2012, January 1). Modeling of Interaction of Hydraulic Fractures in Complex Fracture Networks. Society of Petroleum Engineers. doi:10.2118/152052-MS

Wu, Y.S. and Wang, C., (2014, April 1). Modeling Analysis of Transient Pressure and Flow Behavior at Horizontal Wells with Multi-Stage Hydraulic Fractures in Shale Gas Reservoirs. Society of Petroleum Engineers. doi:10.2118/168966-MS

Wu, Y.S., Wang, C., Li, J., and Fakcharoenphol, P. (2012, January 1). Transient Gas Flow in Unconventional Gas Reservoirs. Society of Petroleum Engineers. doi:10.2118/154448-MS

Xu, W., Le Calvez, J. H., and Thiercelin, M. J. (2009, January 1). Characterization of Hydraulically-Induced Fracture Network Using Treatment and Microseismic Data in a Tight-Gas Sand Formation: A Geomechanical Approach. Society of Petroleum Engineers. doi:10.2118/125237-MS

Xu, W., Thiercelin, M. J., Ganguly, U., Weng, X., Gu, H., Onda, H., and Le Calvez, J. (2010, January 1). Wiremesh: A Novel Shale Fracturing Simulator. Society of Petroleum Engineers. doi:10.2118/132218-MS

Yu W. and Seperhnoori, K. 2014. Simulation of Gas Desorption and Geomechanics Effects for Unconventional Reservoirs. Fuel, 116: 455-464.

Zanganeh, B., 2014. Understanding Reservoir Engineer Aspects of Shale Gas Development on the Alaska North Slope. MS thesis, University of Alaska, Fairbanks, Alaska (May 2014)

Zhang, X. and Jeffrey, R.G. 2006. The role of friction and secondary flaws on deflection and reinitiating of hydraulic fractures at orthogonal preexisting fractures. Geophys. J.Int.166(3): 1454-1465. http://dx.doi.org/10.1111/j.1365-246X.2006.03062.x.

Zhang, X., Thiercelin, M. J., and Jeffrey, R. G. (2007, January 1). Effects of Frictional Geological Discontinuities on Hydraulic Fracture Propagation. Society of Petroleum Engineers. doi:10.2118/106111-MS

This page intentionally left blank for the purposes of print publication.

Appendix A. Nomenclature.

A = drainage area, ft^2, acres

B_g = gas formation volume factor, res ft^3/SCF

B_w = water formation volume factor, res bbl/STB

Burst pressure = psi

C_f = end-of-job slurry concentration, ppg

C_g = gas compressibility, psi^{-1}

C_l = leakoff coefficient, $ft/min^{1/2}$

Collapse pressure = psi

Conductivity, mD-ft

C_p = proppant concentration, bl/ft^2

D = diameter, ft

β - Forchheimer coefficient

E = Young's modulus, psi

F_{CD} = dimensionless fracture conductivity

Fluid volume, gal

g = acceleration of gravity, ft/sec2

G = adsorbed volume, scf/ton

GIP = gas in place, SCF

GIIP = initial gas in place, SCF

h = reservoir thickness, ft

h_f = fracture height, ft

ID = inner diameter, in

K = permeability, mD

K_f = fracture permeability, mD

K_h = horizontal permeability, mD

K_v = vertical permeability, mD

K_{rg} = gas relative permeability, dimensionless

K_{rw} = water relative permeability, dimensionless

L = horizontal well length, ft

M_p = mass of proppant, lb

OD = outer diameter, in

P = reservoir pressure, psi

P_L = Langmuir pressure, psi

Pressure gradient = psi/ft

Proppant concentration, PPA (proppant added per gallon)

Proppant mass, lb

Pump rate, lb/min

Pump time, min

S_w = water saturation, fraction

S_{wc} = connate water saturation, fraction

S_{iw} = initial water saturation, fraction

Slurry volume, bbl

t = time, hr, sec

T = temperature, ^oF

u = velocity, ft/sec

V = volume, ft^3

V_b = bulk volume, ft^3

V_L = Langmuir volume

V_p = pore volume, ft^3

W = fracture width, in

Weight = lb/ft

w_p = propped fracture width, in

x_f = fracture half-length, ft

z = elevation, ft

Z = gas compressibility (gas deviation factor), dimensionless

γg = gas gravity, fraction

γo = oil gravity, fraction

η = efficiency, dimensionless

μ = viscosity, cp

ν = Poisson's ratio, dimensionless

ρ = density, lb/ft^3

σ = stress, psi

φ = porosity, fraction

This page intentionally left blank for the purposes of print publication.

Appendix B. Definitions.

Average fracture conductivity [mD.ft] - product of fracture permeability times fracture width for a finite-conductivity fracture.

Average fracture height [ft] – average value height for the whole fracture.

Average fracture width [in] – the average value of the fracture width.

Average propped fracture height [ft] – the height of the propped fracture.

Efficiency [%] - fluid efficiency is the ratio of the stored volume within the fracture to the total fluid injected.

Estimated closure time [min] – time it takes for the fracture to close.

Final extension of HFN in the direction of max stress [ft] – final extension of Hydraulic Fracture Network (HFN) in the direction of the maximum horizontal stress.

Final extension of HFN in the direction of min stress– final extension of Hydraulic Fracture Network (HFN) in the direction of the minimum horizontal stress.

Fracture width at wellbore [in] – the width of the fracture at the wellbore.

Maximum BH pressure [psi] – maximum bottom hole pressure - the pressure of a well at the bottom of the hole or wellbore.

Maximum fracture height [ft] – maximum value height for the whole fracture.

Maximum surface pressure [psi] – pressure at the surface, which is used to calculate BHTP – Bottom Hole Treatment Pressure.

Total leak-off volume [ft^3] - leak off volume is the volume of the fluid absorbed by the formation.

Total propped fracture surface area [ft^2] - fracture surface area is the area of the fractures in contact with the reservoir that serve as channels that convey gas to the wellbore. This area stays propped with a proppant after part of the fracture closes.

Total fracture surface area [ft^2] - fracture surface area is the area of the fractures in contact with the reservoir that serve as channels that convey gas to the wellbore.

Total fracture volume [ft^3] - the volume of fluid injected minus the volume of fluid that leaks off into the formation.

Appendix C. Abbreviations.

BHP – Bottom Hole Pressure

CVFE – Control Volume Finite Element

DFN – Discrete Fracture Network

HFN – Hydraulic Fracture Network

HiWAY - "*HiWAY is a new hydraulic fracturing technique that changes the way a hydraulic fracture increases the effective near-wellbore reservoir conductivity. It decouples fracture conductivity from a proppant pack permeability by creating stable flow channels. Instead of flowing through the proppant pack, hydrocarbons flow through these channels, enormously increasing conductivity*" (Pena et al., 2010).

MD – Measured Depth

PEBI – Perpendicular Bisection

PKN – Perkins-Kern-Nordgren – one of the most common 2D models used in fracture treatment design

PPA – Proppant Added Per Gallon

ppm – parts per million

SRV – Stimulated Reservoir Volume

SCF – Standard Cubic Feet

TVD – True Vertical Depth

UFM – Unconventional Fracture Model

This page intentionally left blank for the purposes of print publication.

Appendix D. Material Balance Equation for the Injection Case

Material Balance Equation for the gas well can be stated as:

$$G(B_g - B_{gi}) + GB_{gi}\left(\frac{C_f + C_w S_{wi}}{1 - S_{wi}}\right)\Delta P_t + W_e + W_I B_{Iw} + G_I B_{Ig} = G_p B_g + W_p B_w \qquad \text{(AD-1)}$$

Where G is gas in place, Bg is gas volume formation factor, Bgi is initial gas volume formation factor, Cf is rock compressibility factor, Cw is water compressibility factor, Swi is initial water saturation, We is water drive, W_I is water injected, B_{IW} is injection water volume formation factor, G_I is gas injected, $B_I g$ is injected gas volume formation factor, Gp is gas produced, Wp is water produced and Bw is produced water formation factor.

In a given well there is no aquifer, gas injection, gas production and water production. In addition the pressure change between initial and final stage is small, so one can safely assume the same gas formation volume factor for both stages. This assumption cancels the first term in the left side of the equation.

After simplifying the equation using the assumptions above, the equation becomes:

$$GB_{gi}\left(\frac{C_f + C_w S_{wi}}{1 - S_{wi}}\right)\Delta P_t + W_I B_{Iw} = 0 \qquad \text{(AD-2)}$$

Rearrange the above equation to solve for the final pressure:

$$P_{final} = \frac{GB_{gi}\left(\frac{C_f + C_w S_{wi}}{1 - S_{wi}}\right)P_{initial} - W_I B_I}{GB_{gi}\left(\frac{C_f + C_w S_{wi}}{1 - S_{wi}}\right)} \qquad \text{(AD-3)}$$

Substitute the numerical values into the equation to get the final value for the final pressure:

$$\begin{aligned} P_{final} = {} & \frac{915504\ MSCF * 0.47\ \frac{RB}{MSCF}\left(\frac{10 * 10^{-6} psi^{-1} + 4.9 * 10^{-6} * 0.15994}{1 - 0.15994}\right)8676.6\ psi}{915504\ MSCF * 0.47\ \frac{RB}{MSCF}\left(\frac{10 * 10^{-6} psi^{-1} + 4.9 * 10^{-6} * 0.15994}{1 - 0.15994}\right)} \\ & - \frac{590\ STB * 1.01\ \frac{RB}{STB}}{915504\ MSCF * 0.47\ \frac{RB}{MSCF}\left(\frac{10 * 10^{-6} psi^{-1} + 4.9 * 10^{-6} * 0.15994}{1 - 0.15994}\right)} \\ & = 8678.2\ psi \end{aligned} \qquad \text{(AD-4)}$$

This exercise was done to prove that the injection profile in Section 4.1 is possible. In reality there is still uncertainty involved due to different rock compaction tables for the matrix, propped and unpropped zones, slightly varied gas volume formation factor, water formation volume factor, water compressibility constant and numeric calculation method done by Mangrove.